Lokalisatie van de epileptische focus
met behulp van functionele-connectiviteitsanalyse

Epileptic Focus Localization Using Functional Brain Connectivity

Pieter van Mierlo

Promotoren: prof. dr. S. Vandenberghe, prof. dr. K. Vonck, prof. dr. ir. S. Staelens
Proefschrift ingediend tot het behalen van de graad van
Doctor in de Ingenieurswetenschappen: Biomedische Ingenieurstechnieken

Vakgroep Elektronica en Informatiesystemen
Voorzitter: prof. dr. ir. J. Van Campenhout
Faculteit Ingenieurswetenschappen en Architectuur
Academiejaar 2012 - 2013

UNIVERSITEIT
GENT

ISBN 978-90-8578-605-4
NUR 954
Wettelijk depot: D/2013/10.500/38

Department of Electronics and Information Systems
Faculty of Engineering and Architecture
Ghent University

MEDISIP
IBiTech - iMinds
Campus Heymans, Block B
De Pintelaan 185
9000 Ghent
Belgium

Promotors:
Prof. dr. Stefaan Vandenberghe
Prof. dr. Kristl Vonck
Porf. dr. ir. Steven Staelens

Board of examiners:
Prof. dr. ir. Jan Van Campenhout, Ghent University, chairman
Dr. ir. Peter Van Hese, Ghent University, secretary
Prof. dr. Bert Aldenkamp, Maastricht University
Dr. Geertjan Huiskamp, University Medical Center Utrecht
Prof. dr. ir. Hans Hallez, University of Leuven
Prof. dr. Daniele Marinazzo, Ghent University
Prof. dr. Stefaan Vandenberghe, Ghent University
Prof. dr. Kristl Vonk, Ghent University Hospital
Prof. dr. ir. Steven Staelens, Antwerp University

This work was funded by a PhD grant of the Institute for the Promotion of Innovation through Science and Technology in Flanders (IWT-Vlaanderen).

Acknowledgements

First of all I want to thank my 3 promotors, **prof. dr. Stefaan Vandenberghe**, **prof. dr. Kristl Vonck** and **prof. dr. ir. Steven Staelens**. **Stefaan**, I want to thank you for adopting me as PhD student when Steven left to Antwerp University. You have given me the opportunity to develop my research skills within the fruitful atmosphere of MEDISIP. Also thanks for your growing interest in EEG and the stimulation of the neuroscience group. The friendly atmosphere you promote at MEDISIP makes it a unique creative environment. **Kristl**, I want to express my gratitude for learning me so much about epilepsy. Allowing me to follow the very interesting epilepsy staff meetings and especially for providing much feedback on my articles. I could not have achieved the publication in Epilepsia without your help. **Steven**, I want to thank you for guiding me during the first years of my PhD and for giving me the opportunity to start working at MEDISIP. Even when you left to Antwerp University, you still showed much interest in my work and gave me feedback when needed.

I wish to thank all colleagues of MEDISIP during the past years. A special thanks goes to the colleagues sharing the office. The one and only **Vincent**, I'm very pleased we developed such a great friendship over the years with many highlights. The many festival visits and ski trips where always lot's of fun. We share the same passion for neuroscience. I am grateful for the numerous scientific discussions and brain storm sessions we had at the office and in the many bar visits. I hope that we can maintain our fruitful collaboration once you will be working at the neurology department. **Pieter**, for finally being able to print. I want to thank you for always keeping up the spirit in the office and the numerous fun nights we had. I'm confident you will defend your PhD in the near future and I wish you all the luck. **Victoria**, for always being friendly, coping with us in the office and allowing me the be the second last to start working in the morning. **Tony**, it's always more fun when you're at

the office. Thank's for the many quotes with your juicy Antwerp accent and your greasy laugh. **Nathalie**, for being so enthusiastic about your research and organizing many MEDISIP parties. **Erwann**, for the many laughs we had and for the badminton games. **Longske**, for being the quietest colleague ever.

Ewout, for being the most relaxed guy in the world. You showed me how to combine work with the good things in life. Thanks for the legendary trips to Kyoto, Vancouver and the Video. **Roel, aka Rolen**, for separating the sheep (Leonie) from the goats. It's a pleasure to have you as a friend and it's always fun when we explore the nightlife together. Thanks for the scientific Friday night drinks. Also for the crazy two weeks in Karlruhe, the trip to Lisbon and the one to Vancouver. **Gregor**, for sharing the EEG research passion and for the fruitful discussions. Thanks for the amazing trips to Banff, Beijing, Paris and Seattle and also for introducing me to Julieke. **Chris**, for always being helpful and the nice visits to Der Vogel in Karlsruhe. **Benedicte** and **Scharon**, for always being so helpful during the many small animal studies. **Bert**, for sharing the promotor leaving situation. **Karel**, for your amazing flexibility. **Karen**, for coping with so many guys at MEDISIP during the start of your PhD. Now, the female/male ratio is luckily better. Thanks Karel, Karen and Molly for the many pleasant lunches at the cafeteria.

I would also like to thank **Anne-Marie**, **Ayfer**, **Saskia**, **Inge** and **Aaike** for their helpfulness during the last years. You make the lives of a PhD student a lot easier. Furthermore, I thank **Shandra**, **Carmen**, **Lara**, **Faruk**, **Radek** and **Samuel** to reinforce the MEDISIP team. I hope you will enjoy the working environment as much as I do. I think MEDISIP is a wonderful environment with many interesting persons with different backgrounds. I also want to thank the **MEDISIP cycling team**: Roel, Gregor, Stefaan, Vincent, Molly and Bert for the cycling trips we did together. I hope we can keep on doing this in the future. Also thanks to Steven for the Merckx bike.

I would also like to thank the colleagues of Biommeda for contributing to the nice atmosphere at the 5th floor of block B. Especially **prof. dr. Patrick Segers** and **prof. dr. ir Pascal Verdonck** for the nice new year lunches of IBiTech. Furthermore, I would like to thank the **CEO's of FEops** for showing how successful a university spin-off can be. I would also like to express my gratitude to **prof. dr. ir. Ignace Lemahieu** for providing nice parking facilities at the University Hospital.

This work could not have been achieved without the help of several colleagues of LKEN. A special thanks goes to **Evelien** for the continuing support and the very nice collaboration. It's always a pleasure to work with you. Furthermore, I want to thank **prof. dr. Paul Boon** for keeping interest in my work and introducing me into the epilepsy society. **Robrecht**, for fruitful collaboration and the nice scientific discussions and **prof. dr. Alfred Meurs** and **prof. dr. Dirk Van Roost** for always being supportive.

I specially want to thank **Hans** for the guidance during my first years as a PhD student. You were very supportive and always open for discussion and proving feedback. I also want to thank **prof. dr. Daniele Marinazzo** for the critical methodological discussions and transferring his knowledge about connectivity. **Margarita**, for having such in interest in my work and even promoting my work in London. Thanks for the nice informal discussions and the trip to the beautiful and very vivid Delmenhorst. **Dr. Laura Astolfi**, for the interest in my work and for paving the connectivity path. **Dr. Geertjan Huiskamp** and **dr. ir. Peter Van Hese** for the constructive comments made after reading my book and the constructive discussions. I also want to thank **dr. Sara Assecondi** for introducing me into the field of brain connectivity.

I wish to thank the colleagues of the 'speech therapy' group. **Prof. dr. Patrick Santens** and **prof. dr. Miet De Letter** for setting up the nice collaboration. **Annelies** and **Sarah** for showing interest in EEG analysis and being so enthusiastic to learn how to process data.

Ik wil ook het agentschap voor innovatie door wetenschap en technologie bedanken voor de financiële steun de afgelopen jaren.

Verder wil ik ook mijn huisgenoten van de voorbije jaren bedanken. Bedankt **Fran** en **Kim** dat ik na mijn studies bij jullie mocht intrekken en voor de leuke momenten. Een zeer grote dankjewel aan mijn **huisdier Lodeke** en **Eva, aka Schevinho**, om samen ons appartement te delen. Voor de super toffe sfeer, gezeligheid en de ginsdagen. Ook wil ik **Sofie** bedanken voor in te trekken bij huisdier en mezelf. Ik hoop dat we nog een lange tijd samen zullen wonen.

Verder wil ook mijn fantastische vrienden bedanken: **Stefke**, **Natalie**, **Gégéke**, **Lieven**, **Seppe**, **Max** en **Vis** voor de vele leuke reizen, feestjes en Dour festivalbezoeken. Ook de **magische vrienden** voor de jaarlijkse uitstap naar de Ronde van Vlaanderen en voor de legendarische trip naar de Rode Duivels. Verder wil ik ook **Ronny** en **Sheila**, **Filip** en **Eline**, **Safke** en **Sanne** en **Lynn** bedanken voor de leuke uitjes.

Uiteraard zou ik dit werk niet kunnen bereikt hebben zonder de steun

van mijn familie. Vooral mijn **moeder** en **vader**, voor de blijvende nieuwsgierigheid naar mijn onderzoek en voor het geven van alle kansen waarvan ik kon dromen. Ook om me te leren wat echt belangrijk is in het leven en me te maken tot wie ik ben. **An**, voor de toffe jeugd die we samen beleefden en de eeuwige steun. **Bart**, om er te zijn voor mijn zus. Ik hoop dat de kindjes er rap zullen zijn :). En dan rest mij nog om mijn **Julieke** te danken. **Julieke**, bedankt om er altijd te zijn voor me en de vreugde die je brengt in mijn leven. Ik hoop dat we lang van elkaar kunnen blijven genieten. De toekomst lacht ons toe!

Pieter
Juni 2013
(Vancouver) Gent

"Little is known about the functions of the brain, but we can perceive that as the intellectual powers become highly developed, the various parts of the brain must be connected by the most intricate channels of intercommunication."

Charles Darwin, The Descent of Man.

Table of Contents

Table of Contents i

List of Figures vii

List of Tables xi

List of acronyms xiii

English summary xxi

Nederlandstalige samenvatting xxvii

1 Introduction 1
- 1.1 Context . . . 1
- 1.2 Outline . . . 3

2 The brain, electroencephalography and epilepsy 7
- 2.1 Introduction . . . 7
- 2.2 The brain . . . 7
  - 2.2.1 The neuron . . . 8
  - 2.2.2 Neuronal physiology . . . 8
  - 2.2.3 Structural anatomy . . . 12
  - 2.2.4 Brain functions . . . 14
- 2.3 Neuroimaging . . . 15
  - 2.3.1 Different modalities . . . 16
  - 2.3.2 Spatial and temporal resolution of the functional neuroimaging techniques . . . 20
  - 2.3.3 Multimodal neuroimaging . . . 20
- 2.4 Electroencephalography . . . 21
  - 2.4.1 Generators of the EEG . . . 21
  - 2.4.2 Recording the EEG . . . 23

2.4.3 EEG rhythms . . . 24
2.4.4 Artifacts . . . 26
2.4.5 EEG source imaging . . . 27
2.4.5.1 Forward problem . . . 27
2.4.5.2 Inverse problem . . . 31
2.4.6 Applications . . . 35
2.5 Epilepsy . . . 36
2.5.1 Definition, prevalence and incidence . . . 36
2.5.2 Classification . . . 36
2.5.3 Seizures . . . 37
2.5.4 Epileptiform activity in the EEG . . . 37
2.5.5 Treatment . . . 39
2.6 Refractory epilepsy . . . 39
2.6.1 Definition . . . 39
2.6.2 Treatment . . . 40
2.6.2.1 Epilepsy surgery . . . 40
2.6.2.2 Electrical stimulation . . . 42
2.6.3 Presurgical evaluation . . . 43
2.6.3.1 Multi-modal neuroimaging . . . 43
2.6.3.2 Scalp Video-EEG Monitoring . . . 43
2.6.3.3 Structural Magnetic Resonance Imaging . . . 44
2.6.3.4 Invasive Video-EEG Monitoring . . . 44

3 Brain connectivity 47
3.1 Introduction . . . 47
3.2 Structural connectivity . . . 48
3.3 Functional connectivity . . . 49
3.3.1 Linear measures . . . 50
3.3.1.1 Correlation coefficient . . . 50
3.3.1.2 Cross correlation and Coherence . . . 50
3.3.1.3 Spectral density function and Partial Coherence . . . 51
3.3.2 Nonlinear measures . . . 51
3.3.3 Information-based measures . . . 52
3.4 Effective connectivity . . . 53
3.4.1 Linear effective connectivity measures . . . 53
3.4.1.1 Autoregressive modeling . . . 53
3.4.1.2 G-causality index . . . 57
3.4.1.3 Directed Coherence . . . 57
3.4.1.4 Directed Transfer Function . . . 58

3.4.1.5 Partial Directed Coherence 58
3.4.2 Nonlinear effective connectivity measures 59
3.4.3 Information theory based effective connectivity measures 60
3.5 Properties of the different connectivity measures 61
3.6 Simulations 63
3.6.1 Direct transmission 64
3.6.2 Indirect transmission 67
3.6.3 Hidden source 70
3.6.4 Unconnected signal 73
3.6.5 Discussion 76
3.7 Graph analysis 77
3.8 Localization of the epileptogenic focus based on connectivity analysis of EEG signals 78
3.8.1 Pioneering work 78
3.8.2 Recent studies 82

4 Framework to localize the seizure onset zone from intracranial EEG recordings based on effective brain connectivity 85
4.1 Introduction 85
4.2 Method 87
4.2.1 Time-variant autoregressive modeling 87
4.2.2 Estimation of the TVAR coefficients using Kalman filtering 88
4.2.2.1 State-space model 88
4.2.2.2 State-space model representation of the TVAR model 89
4.2.2.3 Estimation procedure of the TVAR coefficients 89
4.2.3 TVAR model to the frequency domain 91
4.2.4 Integration of the time-variant power spectrum into the effective connectivity measures 92
4.2.4.1 The integrated Adaptive Directed Transfer Function (iADTF) 93
4.2.4.2 The masked Adaptive Directed Transfer Function (mADTF) 94
4.2.4.3 The full-frequency Adaptive Directed Transfer Function (ffADTF) 95
4.3 Simulation Setup 95
4.3.1 Simulated model 95

4.3.2 Performance evaluation of the connectivity measures 96
4.3.3 Performance of connectivity measures on simulated model . . . 98
4.3.4 Results . . . 98
4.4 Proof of concept in 1 patient . . . 101
4.5 Discussion . . . 104
4.6 Conclusion . . . 110
4.7 Original contributions . . . 111

5 Seizure onset zone localization in the intrahippocampal kainic acid rat model of epilepsy 113
5.1 Introduction . . . 113
5.2 Method . . . 114
5.2.1 Estimation of the TVAR model coefficients . . . 114
5.2.1.1 Sliding window . . . 114
5.2.1.2 Kalman filtering . . . 115
5.2.2 The spectrum weighted Adaptive Directed Transfer Function (swADTF) . . . 115
5.2.3 Graph analysis . . . 116
5.3 Simulations . . . 117
5.3.1 Setup . . . 117
5.3.2 Processing . . . 119
5.3.3 Simulation results . . . 119
5.4 Pre-clinical experiment . . . 121
5.4.1 Animal models of epilepsy . . . 121
5.4.2 The intrahippocampal kainic acid rat model of epilepsy 122
5.4.3 Intracranial EEG recordings of seizures in rats . . . 123
5.4.3.1 Choice of parameters: p, WL and UC . . . 123
5.4.4 SOZ localization from the ictal IEEG recordings . . . 124
5.4.5 Results . . . 127
5.5 Discussion . . . 131
5.6 Conclusion . . . 133
5.7 Original contributions . . . 134

6 Seizure onset zone localization in 8 patients 135
6.1 Introduction . . . 135
6.2 Dataset and Method . . . 135
6.2.1 Patient data . . . 135
6.2.2 From IEEG to out-degree . . . 136
6.2.3 The outcome parameters . . . 140

6.3 Results . . . 140
6.3.1 Overall results . . . 141
6.3.2 Individual patient results . . . 141
6.3.2.1 Patient 1 . . . 143
6.3.2.2 Patient 2 . . . 145
6.3.2.3 Patient 3 . . . 147
6.3.2.4 Patient 4 . . . 149
6.3.2.5 Patient 5 . . . 151
6.3.2.6 Patient 6 . . . 153
6.3.2.7 Patient 7 . . . 155
6.3.2.8 Patient 8 . . . 157
6.4 Discussion . . . 159
6.5 Conclusion . . . 161
6.6 Original contributions . . . 162

7 Seizure onset zone localization from scalp EEG recordings 163
7.1 Introduction . . . 163
7.2 Method . . . 164
7.2.1 Estimating multiple synchronous sources from scalp EEG recordings . . . 164
7.2.1.1 Precorrelated and orthogonally projected multiple signal classification . . . 165
7.2.2 Source selection . . . 167
7.3 Simulations . . . 167
7.3.1 From simulated brain network to EEG . . . 167
7.3.2 From EEG to source locations . . . 169
7.3.3 Source location selection . . . 170
7.3.4 Setup . . . 170
7.3.5 Results . . . 171
7.3.5.1 Localization of sources . . . 171
7.3.5.2 Source selection . . . 171
7.4 Patient data . . . 172
7.5 Discussion . . . 174
7.6 Conclusion . . . 179
7.7 Original contributions . . . 179

8 General conclusions 181
8.1 Summary . . . 181
8.2 Future research possibilities . . . 183
8.3 Final conclusion . . . 184

References 187

List of Publications 213

List of Figures

2.1 The anatomy of a neuron. 9
2.2 The mechanisms of electrotonic conduction and the propagation of an action potential along an axon. 11
2.3 The structural anatomy of the brain. 13
2.4 The 4 brain lobes (frontal, temporal, parietal and occipital) and the naming of the sulci and gyri. 14
2.5 The Brodmann areas of the brain. 16
2.6 Overview of the different structural and functional neuroimaging techniques. 17
2.7 The spatial and temporal resolution of different functional neuroimaging methods. 20
2.8 The pyramidal neurons and their organization in the cerebral cortex. 22
2.9 The 10-20 system to record scalp EEG. 24
2.10 EEG rhythms: example of delta, theta, alpha, beta and gamma activity. 25
2.11 EEG source imaging 28
2.12 A subject specific head model. 29
2.13 The dipole representation of postsynaptic current at the apical dendrite. 30
2.14 Epileptiform activity in the EEG. 38
2.15 Treatment options for epilepsy patients. 39
2.16 Subdural grid and strip electrodes placed on top of the cortex. The depth electrode has many contacts and is placed inside the brain's parenchyma. 45
2.17 First recording of IEEG traces in 1949 by Jasper and Penfield. 46

3.1 The difference between structural, functional and effective brain connectivity. 48

3.2 Structural brain connectivity investigates the white matter fiber tracts. 49
3.3 The properties of the coherence (COH), partial coherence (PC), directed coherence (DC), directed transfer function (DTF) and partial directed coherence (PDC) shown in 2 graph examples. 63
3.4 Simulated model of direct transmission during a seizure. . . 64
3.5 Estimated functional connectivity pattern of the direct transmission model using the coherence and the partial coherence. 65
3.6 Estimated effective connectivity pattern of the direct transmission model using the directed coherence, directed transfer function and the partial directed coherence. 66
3.7 Simulated model of indirect transmission during a seizure. . 67
3.8 Estimated functional connectivity pattern of the indirect transmission model using the coherence and the partial coherence. 68
3.9 Estimated effective connectivity pattern of the indirect transmission model using the directed coherence, directed transfer function and the partial directed coherence. 69
3.10 Simulated model when the 4 recorded signals are driven by a hidden source. Here A is the hidden source and x_1, x_2, x_3 and x_4 are the recorded signals. 70
3.11 Estimated functional connectivity pattern of the hidden source model using the coherence and the partial coherence. 71
3.12 Estimated effective connectivity pattern of the hidden source model using the directed coherence, directed transfer function and the partial directed coherence. 72
3.13 Simulated model where x_4 is unconnected and has similar spectral properties as the other signals. Signal x_1 drives signals x_2 and x_3. 73
3.14 Estimated functional connectivity pattern of the simulated model with x_4 as unconnected signals using the coherence and the partial coherence. 74
3.15 Estimated effective connectivity pattern of the simulated model with x_4 is unconnected using the directed coherence, directed transfer function and the partial directed coherence. 75

4.1 Illustration of the simulated model. 96

4.2 The values of the integrated ADTF, masked ADTF and full-frequency ADTF for 1 simulation with SNR = 10 dB, model order p = 5 and update coefficient UC = 0.006 during the start of the simulated seizure. 100
4.3 The ROC-curve for the integrated, masked and full-frequency ADTF with model order set to 5 and SNR equal to 10 dB. 100
4.4 EER-points for the integrated, masked and full-frequency ADTF at different model orders and SNR range: [-5 dB, 10 dB]. 101
4.5 A CT image merged with a MR image showing the location of the intracranial electrodes. 103
4.6 The connectivity pattern during 1 seizure onset. 105
4.7 Sum of the sample based connections during 4 seizures and 29 subclinical seizures between the different contact points of the intracranial strips and depth electrodes. 106
4.8 Merged post-operative MR image and pre-operative CT image showing the electrode positions with respect to the resected brain area. 107

5.1 Simulation scheme of the different spreading patterns during the onset of a seizure. 118
5.2 The EERs for the iADTF, ffADTF, swADTF calculated using the sliding window technique (SL) or using the Kalman filtering algorithm (KF) for the 6 different simulation models. 120
5.3 The EERs for the connectivity measures estimated with Kalman filtering for all 6 models. 121
5.4 The subdivision of the animal models of epilepsy 122
5.5 The kainic acid rat model of temporal lobe epilepsy. 123
5.6 The implantation of the two depth electrode into the left (dl) and right (dr1 dr2) hippocampus shown in a coronal slice representation of the brain. The rat also had a epidural electrode over the frontal cortex (not shown in figure). . . . 124
5.7 Spectrograms of an example IEEG seizure epoch estimated out of the TVAR coefficients using different parameters. . . 125
5.8 An example of a recorded seizure in the intrahippocampal kainic acid rat model of epilepsy (fr: right frontal, dr1 and dr2: right hippocampus, dl: left hippocampus). 126

5.9 The out-degrees for the different connectivity measures for all seizures of rat3 (fr: frontal cortex; dr1, dr2: right hippocampus; dl: left hippocampus). 129
5.10 The connections in the frequency domain over time between signal fr, dr1, dr2 and dl for seizure 3 (originating from left hippocampus) of rat3. 130

6.1 Results of the connectivity analysis in pat. 1. 143
6.2 Connectivity patterns during seizure 3 in pat. 1. 144
6.3 Results of the connectivity analysis in pat. 2. 145
6.4 Connectivity patterns during seizure 1 in pat. 2. 146
6.5 Results of the connectivity analysis in pat. 3. 147
6.6 Connectivity patterns during seizure 3 in pat. 3. 148
6.7 Results of the connectivity analysis in pat. 4. 149
6.8 Connectivity patterns during seizure 1 in pat. 4. 150
6.9 Results of the connectivity analysis in pat. 5. 151
6.10 Connectivity patterns during seizure 2 in pat. 5. 152
6.11 Results of the connectivity analysis in pat. 6. 153
6.12 Connectivity patterns during seizure 1 in pat. 6. 154
6.13 Results of the connectivity analysis in pat. 7. 155
6.14 Connectivity patterns during seizure 4 in pat. 7. 156
6.15 Results of the connectivity analysis in pat. 8. 157
6.16 Connectivity patterns during seizure 2 in pat. 8. 158

7.1 The steps in the POP-MUSIC algorithm. 166
7.2 The simulation setup to generate the EEG. 168
7.3 Loreta analysis of simulated EEG. 170
7.4 Source localization results with POP-MUSIC. 171
7.5 Source selection results. Source selection is based on energy or on connectivity measures (iADTF, ffADTF and swADTF). 172
7.6 SOZ localization from scalp EEG recordings during seizure 1. 175
7.7 SOZ localization from scalp EEG recordings during seizure 2. 176
7.8 SOZ localization from scalp EEG recordings during seizure 3. 177

List of Tables

2.1 Efficacies of epilepsy surgery from 1887 until now. 41

3.1 The properties of the different connectivity measures 62
3.2 Earliest publications in the field of connectivity between EEG signals in epilepsy. 81

5.1 Identification of the driver of 230 seizures in 11 rats by the different connectivity measures. 128

6.1 Clinical patient characteristics. 137
6.2 Details of the IVEM data. 138
6.3 Seizure specific results of all patients. 142

List of acronyms

A

AAMI	Average Amount of Mutual Information
ADTF	Adaptive Directed Transfer Function
AED	AntiEpileptic Drug
AIC	Akaike Information Criterion
AR	AutoRegressive
ASL	Arterial Spin Labeling

B

BCG	BallistoCardioGraphic
BEM	Boundary Element Method
BOLD	Blood Oxygen Level Dependent

C

COH	COHerence
CSF	CerebroSpinal Fluid
CT	X-ray Computed Tomography
CTA	Computed Tomography Angiography
CTP	Computed Tomography Perfusion

D

DBS	Deep Brain Stimulation
DTF	Directed Transfer Function
DTI	Diffusion Tensor Imaging
DWI	Diffusion Weighted Imaging

E

ECG	ElectroCardioGraphy
ECoG	ElectroCorticoGraphy
EEG	ElectroEncephaloGraphy
EER	Equal Error Rate
EOG	ElectroOculoGraphy
EP	Evoked Potential
ERP	Event-Related Potential
ESI	EEG Source Imaging

F

FDG	FluoroDeoxyGlucose
FEM	Finite Element Method
FDM	Finite Difference Method
ffADTF	full-frequency ADTF
fMRI	functional Magnetic Resonance Imaging
FN	False Negative
FP	False Positive
fT	femtoTesla

G

GABA	Gamma-AminoButyric Acid

H

HMPAO	HexaMethylPropyleneAmine Oxime

I

iADTF	integrated ADTF
ICA	Independent Component Analysis
IED	Interictal Epileptiform Discharge
IEEG	Intracranial EEG
IFCN	International Federation of Clinical Neurophysiology
ILAE	International League Against Epilepsy
IPI	Initial Precipitating Insult
IVEM	Invasive Video-EEG Monitoring

K

KA	Kainic Acid

L

LFP	Local Field Potential

M

mADTF	masked ADTF
MI	Mutual Information
MRA	Magnetic Resonance Angiography
MRI	Magnetic Resonance Imaging
MRS	Magnetic Resonance Spectroscopy
MUSIC	MUltiple SIgnal Classification
MVAR	MultiVariate AutoRegressive

N

NIRS	Near-InfraRed Spectroscopy

P

PA	Phase Analysis
PC	Partial Coherence
PDC	Partial Directed Coherence
PET	Positron Emission Tomography
POP-MUSIC	Pre-correlated and Ortogonaly Projected MUSIC
PSD	Power Spectral Density

R

RAP-MUSIC	Recursively Applied and Projected MUSIC
REM	Rapid Eye Movement

S

SBC	Schwarz Bayesian Criterion
SE	Status Epilepticus
SNR	Signal-to-Noise Ratio
SOZ	Seizure Onset Zone
SPECT	Single Photon Emission Computed Tomography
SUA	Single Unit Activity
SVEM	Scalp Video-EEG Monitoring
swADTF	spectrum weighted ADTF

T

TLE	Temporal Lobe Epilepsy
TN	True Negative
TP	True Positive

U

UC	Update Coefficient

V

VNS	Vagus Nerve Stimulation

W

WMN	Weighted Minimum Norm

English summary

Nederlandstalige samenvatting

English summary

The aim of the research in this dissertation is to localize the epileptic focus from electroencephalographic (EEG) recordings using the concept of brain connectivity. Brain connectivity investigates the structural and functional links between brain regions. In this dissertation we use EEG signals to study the functional interactions between different brain regions during epileptic seizures.

EEG is a non-invasive technique that records the electric brain activity with electrodes placed at the scalp of the patient. The high temporal resolution of EEG allows to investigate the electrical brain activity in real time. In clinical practice EEG is most frequently used as a supporting tool in the diagnosis and treatment of patients with epilepsy.

Epilepsy is a chronic neurological disorder that is characterized by recurrent seizures and that affects around 1% of the world population. During a seizure there is an abnormal manifestation of neuronal activity in the brain. The well known seizures are the tonic clonic seizures, in which the patient is shaking while being unconscious. But not all seizures represent themself in this manner. The symptoms of a seizure are very diverse and depend on the involved brain areas. The brain area from which the clinical seizures start is called the seizure onset zone (SOZ).

Fortunately, up to 70% of the patients can be adequately treated with antiepileptic drugs. The remainder 30% is not rendered seizure free or has adverse side effects from the medication. For this patient group the treatment with highest efficacy is resective surgery of the estimated epileptogenic focus. The epileptogenic focus is defined as the area of cortex that is necessary and sufficient for initiating seizures and whose removal (or disconnection) is necessary for complete abolition of seizures. Whether or not a patient is eligible for epilepsy surgery is assessed during the presurgical evaluation. A number of clinical investigations are performed to define the epileptogenic focus and to determine possible overlap with eloquent tissue,

i.e. a region of cortex that is indispensable for defined cortical functions.

The two cornerstone investigations during the presurgical evaluation are scalp video-EEG monitoring (SVEM) and structural Magnetic Resonance Imaging (MRI). During the SVEM the patient is continuously monitored with video and scalp EEG in a specially equipped hospital room for approximately one week. The seizure semiology seen on the video recordings as well as how the seizure activity is represented in the EEG helps to classify the type of epilepsy and to localize the SOZ. Seizure activity is represented as a periodic waveform in the EEG. The precise localization of the SOZ helps to delineate the epileptogenic focus. During the structural MRI investigation high resolution anatomical images of the patient's brain are acquired to reveal anomalies.

The absence of structural anomalies, non-localizing SVEM, or conflicting findings between these 2 investigations results into referral of the patient to invasive Video-EEG monitoring (IVEM). Around 15% to 25% patients included in the presurgical evaluation need IVEM. Here intracranial electrodes are implanted on top of or inside the brain to reveal brain activity that cannot be registered with scalp EEG recordings. The epileptologists analyze the intracranial EEG (IEEG) traces recorded during seizures, namely the ictal IEEG traces, visually to localize the SOZ. They evaluate the amplitude and the relation between the IEEG signals to identify abnormal synchronous activity and relate these to the epileptogenic focus. However, this visual analysis and spatial interpretation of many simultaneously recorded IEEG signals by the epileptologist has its limitations. Precise identification of initial, sometimes very subtle IEEG changes, to determine the SOZ is time consuming and requires extensive and specific expertise. Also because of the fast propagation of an epileptic seizure, the SOZ can be difficult to pinpoint and can be overestimated in size.

The main objective of this dissertation is to develop a more quantitative and objective method to localize the SOZ from ictal IEEG recordings. We investigate the directional functional interactions between the ictal EEG traces recorded from the various brain regions to localize the SOZ. This directional functional connectivity is named effective connectivity. In the last part of this dissertation we explore how to localize the SOZ from ictal scalp EEG recordings.

The fundamental frequency of the seizure activity noticed in the IEEG may vary from seizure to seizure and from patient to patient. Due to this heterogeneous frequency content during different seizures it is challenging to design a framework suitable to pinpoint the SOZ applicable to all seizure

types and patients. Furthermore, seizures are intrinsically nonstationary requiring advanced techniques to investigate the dynamic functional interactions between brain regions.

In an initial phase we designed a framework capable of deriving the time-variant effective connections between multiple IEEG signals. This is achieved by modeling the nonstationary signals in a time-variant multivariate autoregressive (TVAR) model. In this model the signals are modeled as a linear combination of their past samples plus uncorrelated white noise in one single system. Kalman filtering can be used to estimate the TVAR coefficients. They reveal the causal relations between all signals and indicate how the past samples of a signal influence the present samples of the other signals. This allows to investigate causality between the signals. We transformed the coefficients to the spectral domain to investigate the effective connections at frequencies that are prominent in the IEEG during seizures.

Three different time-variant effective connectivity measures are calculated from the TVAR coefficients: the integrated Adaptive Directed Transfer Function (iADTF), the masked ADTF (mADTF) and the full-frequency ADTF (ffADTF). All three measures incorporate the frequency content of the signals in a different manner into the connectivity pattern. For the iADTF all frequencies in the considered frequency band contribute equally to the connectivity pattern, while the mADTF only looks at the 5% frequencies that are most prominent in the IEEG signals. The ffADTF weights the frequencies in a more appropriate manner: the connections are weighted with respect to the spectral power in the receiving signal.

By simulations we investigated the performance of the different ADTF measures to reveal the connections during a time-variant nonstationary seizure onset. We showed that incorporating the frequency content of the signals into the connectivity pattern was beneficial for signal-to-noise ratios (SNRs) above 0 dB. At these SNRs the mADTF and ffADTF outperformed the iADTF. The ffADTF had the best overall behavior with a sample based sensitivity and specificity higher than 90% for SNRs above 0 dB. Furthermore, we showed the feasibility of using ffADTF analysis to localize the SOZ from ictal IEEG recorded with 52 electrode contacts in 1 patient. We were able to correctly localize the SOZ based on the connectivity patterns derived from 4 seizures and 29 subclinical seizures. We showed that the connectivity pattern was consistent over the majority of seizure epochs.

In a second phase the spectrum weighted ADTF (swADTF) was introduced in the framework. This is an effective connectivity measure that

stresses connections with high spectral power in both the receiving and the sending signal. Simulations revealed that the newly developed swADTF outperformed the other considered connectivity measures, the iADTF and the ffADTF, for SNRs above 2 dB. We applied the iADTF, ffADTF and swADTF to investigate the capability of localizing the SOZ in a small animal model of epilepsy. We analyzed spontaneous seizures recorded in the intrahippocampal kainic acid model of temporal lobe epilepsy. Healthy rats were injected with kainic acid into the right hippocampus resulting in a status epilepticus, i.e. a severe seizure that can last several hours. After a latent period ranging from several days to weeks, the rats showed spontaneous seizures. In total 230 seizures recorded in 11 rats with 4 electrode contacts were analyzed. We defined the SOZ based on connectivity analysis and compared this to the scoring of an expert electrophysiologist. Our results indicated that swADTF analysis is the preferred technique for localizing the SOZ from ictal IEEG recordings in these rats compared to the iADTF and ffADTF. In 90% of all seizures the method was capable to correctly localize the SOZ.

In a third phase we studied the added value of our method to localize the SOZ from ictal IEEG recordings in 8 patients. Inclusion criteria for the patients in this study were focal ictal onset on IVEM and subsequent resective surgery rendering the patient seizure-free during a minimum follow-up of 2 years. For each patient swADTF analysis was performed to the ictal IEEG recordings to localize the SOZ. We compared the results of the connectivity analysis with the results of the visual identification analysis of the epileptologist and the resected brain tissue. We showed that in all patients the result corresponded with the visual analysis of the epileptologist. In all patients with post-operative imaging available (n=7/8) the results were concordant with the resected brain tissue. Furthermore, we showed that the seizure specific connectivity pattern was consistent over multiple seizures in each patient, indicating that the different seizures originated from the same epileptic brain region.

Thus far we can conclude that swADTF analysis outperforms the other connectivity measures for SNRs above 2 dB. We showed the applicability of the swADTF to localize the SOZ from ictal IEEG recordings both in a small animal model of epilepsy and in patients. The method does not require any prior information about the placement of the electrodes and is readily applicable in a clinical setting to assist the epileptologist.

In a final phase we investigated the feasibility to couple the developed framework to EEG source imaging (ESI) to localize the SOZ from ictal

scalp EEG recordings. ESI was used to estimate the electric neuronal activity of different brain regions over time. Afterwards connectivity analysis was performed to define the driving brain source. By simulations we revealed that investigating the connectivity pattern between the estimated sources is beneficial to localize the SOZ from ictal scalp EEG recordings. Furthermore, we showed the feasibility to localize the SOZ using ESI and ADTF analysis in 1 patient. We could correctly localize the SOZ in all 3 seizures in this patient. This shows the potential of the developed method to localize the SOZ from ictal scalp EEG recordings. However, more research is needed to assess the added value of connectivity measures in EEG source localization.

Overall we can conclude that in this dissertation a framework was developed (using the concept of effective connectivity) to localize the SOZ from ictal IEEG recordings. The method was validated in a small animal model of epilepsy and in 8 patients. The methods is readily applicable in a clinical setting and has the potential to improve the accuracy of SOZ localization during the presurgical evaluation in patients with refractory epilepsy. In the final part we showed the feasibility to couple the designed connectivity framework to ESI to localize the SOZ from ictal scalp EEG recordings.

Nederlandstalige samenvatting

Het hoofddoel van dit proefschrift is de lokalisatie van de epileptische focus op basis van electroencefalografische (EEG) signalen met behulp van connectiviteitsanalyze. De connectiviteit in de hersenen kan opgedeeld worden in structurele en functionele connectiviteit. Structurele connectiviteit onderzoekt de anatomische verbindingen tussen de hersenregio's, terwijl functionele connectiviteit de correlatie van neuronale activiteit onderzoekt. In dit proefschrift gebruiken we functionele connectiviteit tussen de EEG signalen zodoende de epileptische focus te bepalen in patiënten met epilepsie.

EEG is een niet-invasieve techniek die de hersenactiviteit opneemt d.m.v. elektroden die bevestigd worden op de hoofdhuid van de patiënt. De hoge temporele resolutie van EEG laat toe om de neuronale activiteit in ware tijd op te nemen. De meest voorkomende klinische toepassing van EEG is de diagnosticering en behandeling van patiënten met epilepsie.

Epilepsie is een chronische neurologische aandoening die gekarakteriseerd wordt door spontane aanvallen. Ongeveer 1% van de wereldbevolking heeft epilepsie. Tijdens een aanval is er abnormale synchrone neuronale activiteit in de hersenen. De meest bekende aanvallen zijn de tonisch-clonische aanvallen, waarbij de patiënt schokkend bewusteloos op de grond ligt. Maar er bestaan ook andere soorten aanvallen met minder uitgesproken symptomen. Welke symptomen een aanval veroorzaakt hangt af van welke hersenregio's betrokken zijn bij de aanval. Dit kan leiden tot heel uiteenlopende symptomen gaande van staren, niet meer kunnen praten tot bewusteloosheid. De hersenregio die de klinische aanvallen veroorzaakt wordt de *seizure onset zone (SOZ)* genoemd.

Gelukkig kan ongeveer 70% van de epilepsiepatiënten beholpen worden met anti-epiletische medicatie. De overige 30% is niet volledig aanvalsvrij

of heeft ongewenste bijwerkingen van de medicatie. De meest doeltreffende behandeling van deze patiënten is de chirurgische verwijdering van de epileptogene focus. Dit is de regio van de cortex die noodzakelijk is voor het veroorzaken van de aanvallen en wiens verwijdering noodzakelijk is voor aanvalsvrijheid van de patiënt te bekomen. Tijdens de prechirurgische evaluatie wordt nagegaan of de patiënt in aanmerking komt voor een resectieve hersenoperatie. Een aantal klinische testen worden uitgevoerd om de epileptogene focus te bepalen en om overlap met functioneel hersenweefsel te onderzoeken.

De 2 belangrijkste onderzoeken tijdens de prechirurgische evaluatie zijn video EEG monitoring (VEM) en magnetische resonantie beeldvorming van de anatomie van de hersenen. VEM is een onderzoek waarbij de patiënt gedurende ongeveer 1 week opgenomen wordt in het ziekenhuis en continu gemonitord wordt zowel door video als EEG. De klinische semiologie van de aanvallen en de elektrische aanvalsactiviteit geregistreerd met het EEG helpt bij de classificatie van het type epilepsie alsook bij de bepaling van de SOZ. Aanvalsactiviteit wordt in het EEG weergegeven als een periodieke golfvorm. De exacte lokalisatie van de SOZ is belangrijk om de epileptogene zone te bepalen. Bij het structurale magnetische resonantie beeldvorming wordt gezocht naar anatomische afwijkingen in de hersenen van de patiënt.

Bij de afwezigheid van structurele letsels, niet-lokaliseerbare elektrische activiteit en semiologie tijdens de VEM, of tegenstrijdige resultaten van beide onderzoeken wordt de patiënt doorverwezen naar de invasieve video EEG monitoring (IVEM). Hierbij worden elektroden rechtstreeks in de hersenen geplaatst zodoende de elektrische hersenactiviteit in kaart te brengen die niet opgemerkt kan worden met elektroden op de hoofdhuid. De epileptoloog analyseert het intracranile EEG (IEEG) visueel om de SOZ te lokaliseren. Hierbij worden de amplitude en de relatie tussen de verschillende IEEG signalen bestudeerd en gerelateerd aan de SOZ. Deze visuele analyse van de epileptoloog heeft echter beperkingen. Identificatie van initile, soms heel discrete, IEEG ontladingen die helpen bij het bepalen van de SOZ is moeilijk en zeer tijdrovend. Hiervoor is ook gespecialiseerde vakkennis nodig. Omdat de aanval zeer rap kan spreiden naar naburige regio's kan het ook moeilijk zijn om de SOZ exact te bepalen. Dit kan leiden tot een overschatting van de SOZ.

Het hoofddoel van dit proefschrift is om een meer objectieve en kwantitatieve manier te ontwikkelen om de SOZ te lokaliseren uit ictale IEEG opnames. Hiervoor onderzoeken de gerichte functionele connectiviteit tussen de ictale IEEG signalen opgenomen door de intracanile elektroden geplaatst

in verschillende hersenregio's. Deze gerichte functionele connectiviteit wordt effectieve connectiviteit genoemd. In het laatste deel van dit proefschrift onderzoeken we of we de SOZ kunnen lokaliseren op basis van ictale EEG opgenomen met elektroden op de hoofdhuid.

De signaalfrequentie van een aanval zichtbaar in het EEG varieert van aanval tot aanval en is patiënt specifiek. Omwille van deze heterogene frequentie-inhoud tijdens verschillende aanvallen is het uitdagend om een raamwerk te creeren om de SOZ te lokaliseren dat toegepast kan worden op alle types van aanvallen en in alle patiënten. Omdat aanvallen ook niet-stationair zijn, moeten geavanceerde technieken gebruikt worden die de dynamische interactie tussen de verschillende hersenregio's in beeld kunnen brengen.

In een initile fase werd het raamwerk ontwikkeld dat in staat is om het dynamische effectieve connectiviteitspatroon tussen signalen te berekenen. Dit werd verwezenlijkt door de niet-stationaire signalen te modeleren met een tijdsvariant multivariaat autoregressief (TVAR) model. In dit model worden de signalen gemodeleerd als een lineaire combinatie van hun verleden bemonsteringswaarden plus ongecorreleerde witte ruis. Kalman filtering werd gebruikt om deze cofficinten te schatten. Ze onthullen de causale interacties tussen de signalen door te schatten hoe het verleden van de signalen de huidige bemonsteringswaarden benvloedt. We transformeerden de cofficinten naar het frequentie domein m.b.v. de Fourier transformatie om de connecties bij bepaalde signaalfrequenties, die prominent aanwezig zijn in het IEEG tijdens de aanvallen, na te gaan.

Drie verschillende tijdsvariante effectieve connectiviteitsmaten werden gemplementeerd op basis van de TVAR cofficinten: de *integrated Adaptive Directed Transfer Function (iADTF), masked ADTF (mADTF) and full-frequency ADTF (ffADTF)*. Deze connectiviteitsmaten incorporeren de frequentie-inhoud van de IEEG signalen op een verschillende manier in het uiteindelijke connectiviteitspatroon. Voor de iADTF zijn alle frequenties in de beschouwde frequentieband evenwaardig, terwijl de mADTF slechts 5% van de frequenties in de frequentieband beschouwt die het meest voorkomen in de beschouwde IEEG signalen. De ffADTF heeft een meer natuurlijke weging waarin alle connecties gewogen worden op basis van de frequentie-inhoud van de ontvangende signalen.

Door middel van simulaties van een niet-stationair aanvalsbegin onderzochten we de performantie van de verschillende ADTF connectiviteitsmaten. We toonden aan dat het incorporeren van de frequentie-inhoud van de iEEG signalen in het connectiviteitspatroon voordelig was voor signaal-

ruisverhoudingen (SNR) hoger dan 0 dB. Bij deze SNRs presteerden de mADTF en ffADTF beter dan de iADTF. De ffADTF had de beste performantie met een sensitiviteit en specificiteit hoger dan 90% voor SNRs boven 0 dB. Bovendien toonden we de toepasbaarheid van ffADTF-analyse aan om de SOZ te lokaliseren op basis van ictaal IEEG opgenomen met 52 elektrode contacten in 1 patiënt. We konden de SOZ correct lokalizeren in 4 aanvallen en 29 subklinische aanvallen. Verder toonden we ook aan dat het connectiviteitspatroon consistent was over de beschouwde aanvallen.

In een tweede fase werd een nieuwe tijdsvariante effectieve connectiviteitsmaat ontwikkeld, namelijk de *spectrum weighted ADTF (swADTF)*. Deze connectiviteitsmaat benadrukt connecties bij frequenties met hoge frequentie-inhoud zowel in het zendende als het ontvangende signaal. Simulaties toonden aan dat de swADTF een betere performantie had dan de overige connectiviteitsmaten voor SNRs boven 2 dB. We pasten iADTF, ffADTF en swADTF analyse toe in een diermodel van epilepsie om de performantie van SOZ lokalisatie na te gaan. We analyseerden spontane aanvallen in het intrahippocampaal kainaat model voor temporale kwabepilepsie in ratten. Hierbij wordt in gezonde ratten in de rechter hippocampus kainaat genjecteerd. Hierdoor ontstaat een status epilepticus, zijnde een zware aanval die enkele uren kan duren. Na een latente periode van een aantal dagen tot een aantal weken vertonen de ratten spontane aanvallen. In totaal werden 230 aanvallen geanalyseerd opgenomen in 11 ratten met 4 elektrode contacten. We lokaliseerden de SOZ m.b.v. connectiviteitsanalyse en vergeleken de resultaten met de scoring van een ervaren elektrofysioloog. Onze resultaten toonden aan dat swADTF analyse de geprefereerde methode is om de SOZ te lokaliseren in deze ratten in vergelijking met de iADTF en ffADTF. In 90% van alle aanvallen kon de swADTF de correcte SOZ aanduiden.

In een derde fase bestudeerden we de meerwaarde van de ontwikkelde methode om de SOZ the lokaliseren op basis van ictale IEEG opnames in 8 patiënten. Inclusie criteria voor de patiënten in deze studie waren focaal aanvalsbegin zichtbaar op IEEG tijdens de IVEM en de patiënten zijn aanvalsvrij na resectieve chirurgie met een opvolging van minstens 2 jaar. Voor elke patiënt werd swADTF-analyse uitgevoerd op het ictale IEEG om de SOZ te lokaliseren. We vergeleken de resultaten van de connectiviteitsanalyze met de resultaten van de visuele identificatie van de IEEG opnames door de epileptoloog alsook met de gereseceerde hersenregio. We toonden aan dat in alle patiënten de resultaten overeenstemden met de visuele analyze van de epileptoloog. In alle patiënten met post-operatieve beeldvorming ter beschikking ($n = 7/8$) kwamen de resultaten overeen met de gereseceerde

hersenzone. Tevens toonden we aan dat het verkregen connectiviteitspatroon gelijkaardig was over meerdere aanvallen in dezelfde patiënt. Wat erop wijst dat de aanvallen vanuit dezelfde focus begonnen.

Voorlopig kunnen we concluderen dat swADTF-analyze een betere performantie heeft dan de andere connectiviteitsmaten voor SNRs boven 2 dB om de SOZ te lokaliseren. We toonden aan dat swADTF-analyze van ictale IEEG opnames kan gebruikt worden voor SOZ lokalisatie in een diermodel van epilepsie alsook in patiënten. De methode vereist geen voorkennis over de plaatsing van de elektroden en kan ogenblikkelijk toegepast worden in de klinische praktijk om de epileptoloog te ondersteunen.

In een finale fase onderzochten we de geschiktheid om het ontwikkelde raamwerk te koppelen aan EEG bronlokalisatie om de SOZ te lokaliseren op basis van ictaal EEG. We gebruikten EEG bronlokalisatie om de neuronale activiteit in verschillende hersenregio's te schatten. Nadien werd het ontwikkelde connectiviteitsraamwerk gebruikt om de SOZ to lokaliseren. Door middel van simulaties toonden we aan dat het incorporeren van connectiviteitsanalyze voordelig is om de SOZ te lokaliseren uit ictale EEG opnames. Tevens toonden we de toepasbaarheid aan van de ADTF-analyse gekoppeld aan EEG bronlokalisatie om de SOZ te lokaliseren uit ictale EEG opnames in 1 patiënt. We konden de SOZ correct lokaliseren in de 3 onderzochte aanvallen. Dit toonde het potentieel van de methode om de SOZ te lokaliseren op basis van ictale EEG opnames aan. Verder onderzoek dient gedaan te worden om de bijdrage van connectiviteitsanalyze in SOZ lokalisatie na te gaan.

Als algemene conclusie kunnen we stellen dat in dit proefschrift een raamwerk werd ontwikkeld om de SOZ te lokaliseren op basis van ictale IEEG opnames. De methode werd gevalideerd in een diermodel voor epilepsie en in 8 patiënten. De methode kan ogenblikkelijk toegepast in de klinische praktijk om de epileptoloog te ondersteunen en heeft het potentieel om de accuraatheid van SOZ lokalisatie te verbeteren tijdens de prechirugische evaluatie in patiënten met epilepsie. In een laatste fase werd ook aangetoond dat de methode gekoppeld kan worden aan EEG bronlokalisatie om de SOZ uit ictale EEG opnames te schatten.

Chapter 1

Introduction

1.1 Context

In this dissertation we investigate the use of brain connectivity to help treating patients with epilepsy. Brain connectivity is a rapidly advancing research field that tries to unravel the wiring and functioning of the human brain: How are the different brain regions structurally connected and how are they functionally interconnected to perform complex tasks? These structural and functional brain networks can be investigated using neuroimaging techniques.

The anatomical connections between brain regions can be imaged using Magnetic Resonance Imaging (MRI). A special MRI technique, diffusion weighted imaging, allows to image the diffusion of water molecules in the brain. Based on the movements of the water molecules, the white matter fiber tracts can be reconstructed using a technique called tractography.

The functional brain network can be investigated with functional neuroimaging techniques. Positron Emission Tomography (PET) and Single Photon Emission Computed Tomography (SPECT) are techniques that image the distribution of an injected radiotracer. Based on the kind of tracer that is injected these techniques can image the glucose metabolism, the perfusion or the oxygen level of the brain regions. Functional MRI (fMRI) is used to image the oxygenation level in the blood of the brain without the need of injecting a tracer. All previous techniques are based on hemodynamic principles and therefore indirectly investigate the neuronal activity of the brain regions.

The electrophysiological techniques, including electroencephalography

(EEG) and Magnetoencephalography (MEG), directly record the electrical signal of neuronal activity in the brain. In EEG multiple electrodes are placed on the scalp of the subject to record the electric field at different positions. In MEG highly sensitive magnetometers are placed around the head to record the magnetic field. Both techniques have a very high temporal resolution in the order of ms. This makes EEG and MEG valuable techniques to study time varying functional brain networks.

Currently there is a lot of research done in the field of brain connectivity. Many studies are performed using state of the art techniques to analyze the functional brain network during a specific task or condition. These studies provide useful insights about the functioning of the brain and may influence clinical treatments in the future. However, few of these studies have direct clinical impact. Therefore the aim of this dissertation is to develop a framework based on functional connectivity to help treating patients with epilepsy. We want to build a framework based on state of the art technique that is directly applicable in a clinical setting.

Epilepsy is a neurological disease characterized by recurrent seizures and has an incidence of approximately 1%. The treatment of the patients aims to suppress these seizures. This can be achieved in 70% of the patients with antiepileptic drugs. For the remaining 30% other treatment options need to be considered. Currently, the treatment with the highest efficacy is the surgical resection of the epileptic focus, i.e. the area responsible for causing epileptic seizures. The aim of this dissertation is to localize the epileptic focus based on functional brain networks derived from EEG recordings.

In several patients who are considered for epilepsy surgery, intracranial electrodes are placed on top of the neocortex or even inside the brain's parenchyma to reveal brain activity that is not noticeable in scalp EEG recordings. By using intracranial electrodes detailed brain activity of the implanted brain regions can be recorded. The epileptologist analyses these recorded intracranial EEG signals to define the brain region where the seizures start, i.e. the seizure onset zone (SOZ). This analysis happens visually and is therefore prone to human mistakes. The seizure activity also spreads rapidly making it difficult for the epileptologist to identify the SOZ. The work in this dissertation aims to localize the SOZ from ictal EEG recordings in a more objective manner. By investigating the functional connectivity pattern between the brain regions during the seizures we will localize the SOZ.

1.2 Outline

In chapter 2 we introduce the essential background to frame the work in this dissertation. We start by describing the brain's anatomy and functioning. Next the different neuroimaging technique that can be used to investigate brain anatomy and functioning are introduced. Here we especially focus on the different functional neuroimaging techniques. One of those techniques, EEG is used throughout this thesis and is therefore described in extensive detail. We explain how EEG can be recorded and what the recordings can tell us about brain functioning. Furthermore, we introduce EEG source imaging to localize the brain activity from the recorded scalp potentials.

The main application area of EEG is epilepsy. We describe epilepsy in detail and focus on the patient group that cannot be cured with antiepileptic drugs, namely the refractory epilepsy patients. The possible treatments, with emphasis on resective surgery, are discussed. An overview is given of the pre-surgical evaluation protocol that investigates whether the patient is eligible for epilepsy surgery. The two cornerstone investigations of the pre-surgical evaluation, scalp video EEG monitoring and structural magnetic resonance imaging, are addressed. The invasive video EEG monitoring in which intracranial electrodes are implanted in the brain to record brain activity that is not revealed by scalp EEG recordings is also introduced.

In chapter 3 we introduce the three types of brain connectivity: structural, functional and effective. First, structural connectivity is introduced, which reveals how the brain regions are physically linked to each other. Afterwards, functional and effective connectivity, that both show the correlation between the activity of different brain regions are described. Effective connectivity reveals the directional interactions between different brain regions, while functional connectivity does not. The connectivity measures can be categorized into linear, nonlinear and information theory based measures. For each category we give examples of functional and effective connectivity measures and how to compute them. We perform several small simulations to show the properties of the different connectivity measures. Subsequently, we introduce graph analysis and how it helps to deduct useful information from the connectivity graphs. Finally, we give an extensive overview of the literature dealing with the localization of the epileptic focus based on connectivity analysis of EEG signals.

In chapter 4 the framework to localize the SOZ from intracranial EEG recordings based on effective connectivity is introduced. The effective connectivity is investigated by means of autoregressive models. The coefficients

of the autoregressive model reveal the causal relations between the signals and can be used to calculate effective connectivity measures. In this chapter we introduce the Kalman filtering algorithm to calculate time-variant autoregressive coefficients. This allows to investigate the causal relations between multiple nonstationary signals. The time-variant coefficients are then used to estimate three effective connectivity measures: the integrated Adaptive Directed Transfer Function (iADTF), the masked ADTF and the full-frequency ADTF. The connectivity measures differ in the way they incorporate the frequency content of the investigated signals. The performance of the connectivity measures is examined using simulations. Afterwards connectivity analysis is applied to intracranial EEG recordings in 1 patient as a proof of concept. The connectivity pattern during 4 seizures and 27 subclinical seizures is studied and the results are compared to post-operative findings.

In chapter 5 the sliding window technique is compared with the Kalman filtering technique to see which technique is the preferred one to estimate time-variant TVAR coefficients. Furthermore, we introduce a new effective connectivity measure, the spectrum weighted ADTF (swADTF), that incorporates the signals' frequency content in a more appropriate manner. Simulations of a seizure onset are performed to investigate the performance of the connectivity measures at multiple signal-to-noise ratios. We applied the connectivity measures to seizures in the intrahippocampal rat model of epilepsy to localize the SOZ. The analysis is performed during 230 seizures recorded in 11 rats and results (which brain region is the SOZ) are compared with the scoring of an expert electrophysiologist.

In chapter 6 the connectivity analysis is performed in 8 patients to localize the SOZ. The patients had seizures with focal ictal onset and were rendered seizure free after resective surgery. We calculate the effective connectivity pattern during the first 20s of seizure activity to investigate the causal relations between multiple signals in the frequency domain. Afterwards graph analysis was done to localize the SOZ of each seizure specifically. The results are compared to the visual SOZ localization done by the epileptologist and with post-operative results.

In chapter 7 we investigate the use of the previously developed framework to localize the SOZ from ictal scalp EEG recordings. Because during a seizure multiple brain regions are simultaneously active, an inverse technique to localize correlated sources is used. The technique localizes the brain regions showing ictal activity and also provides a time course depicting the neuronal activity of each region. These time courses are then used

to investigate the brain network. The proposed technique is tested using simulations and applied to the scalp EEG of 1 patient. Afterwards the results are compared with post-operative findings.

In the final chapter, chapter 8, general conclusions are made and possible future research is discussed. We end this dissertation with a final conclusion.

Chapter 2

The brain, electroencephalography and epilepsy

2.1 Introduction

In this chapter the background to understand the work in the dissertation is described. First we will give a description of the anatomy and physiology of the brain. Then we introduce the neuroimaging techniques that are used to investigate the anatomy and functioning of the brain. Subsequently electroencephalography (EEG) is described, a technique that records the electric field of the brain. A short overview of the possible applications is also given. In the last part of this chapter we will introduce epilepsy and the treatment for patients that do not respond to antiepileptic drugs.

2.2 The brain

The brain is the most complex human organ and forms the central nervous system (CNS) together with the spinal cord. The CNS integrates and processes the information received from all body parts and coordinates their activity. A brief introduction to the anatomy of the brain and how brain regions communicate with each other is given below.

2.2.1 The neuron

The basic building block of the human brain is the neuronal cell or the neuron. The brain contains approximately 86 billion neurons interconnected to each other in a complex network [12]. Each neuron connects with 5000-200.000 other neurons. Three types of neurons exist: motor neurons (for conveying motor information), sensory neurons (for conveying sensory information), and interneurons (that convey information between different neurons). The main function of a neuron is to transmit received signals across its length.

A neuron consists of the soma (cell body), one axon and up to a thousand dendrites, as illustrated in fig. 2.1. The soma is the control center, manufacturing and recycling plant of the neuron and houses the nucleus with genetic material. The dendrites and the axon conduct information to and from the soma. The dendrites receive signals from other neurons while the axon sends outgoing signals to dendrites of other neurons or even to muscle cells. The interconnection between the soma and the axon is called the axon hillock. The axon can vary in length from a few mm up to just over 1m. Many axons are surrounded by a myelin sheath, a phospholipid layer acting as an electric insulator allowing rapid communication over a large distance. The periodic gaps in the insulating myelin sheath on the axon are called the nodes of Ranvier. The place where two neurons interconnect is called a synapse. The synaptic cleft is a small gap between the presynaptic axon terminal (one of the several end branches of the axon) and the postsynaptic dendrite.

2.2.2 Neuronal physiology

The neuronal cell membrane has sodium (Na^+) and potassium (K^+) voltage gated channels and Na^+/K^+pumps. The Na^+voltage-gated channels open at -55 mV and close at +40 mV, while the K^+voltage gated channels open at +40 mV and close at -80 mV. The Na^+/K^+pumps ensure that there is a higher concentration of Na^+outside the neuron's membrane compared to the inside and that there is more concentration of K^+inside the neuron's membrane compared to the outside. Together with the high permeability of the cell membrane to $K^+$and the low permeability to Na^+, this results in a resting potential of approximately -70 mV across the cell membrane. The cell is less positive at the inside compared to the outside.

The communication between the neurons is based on electrical and chemical conduction. The signal is transferred within a neurons from the dendrites

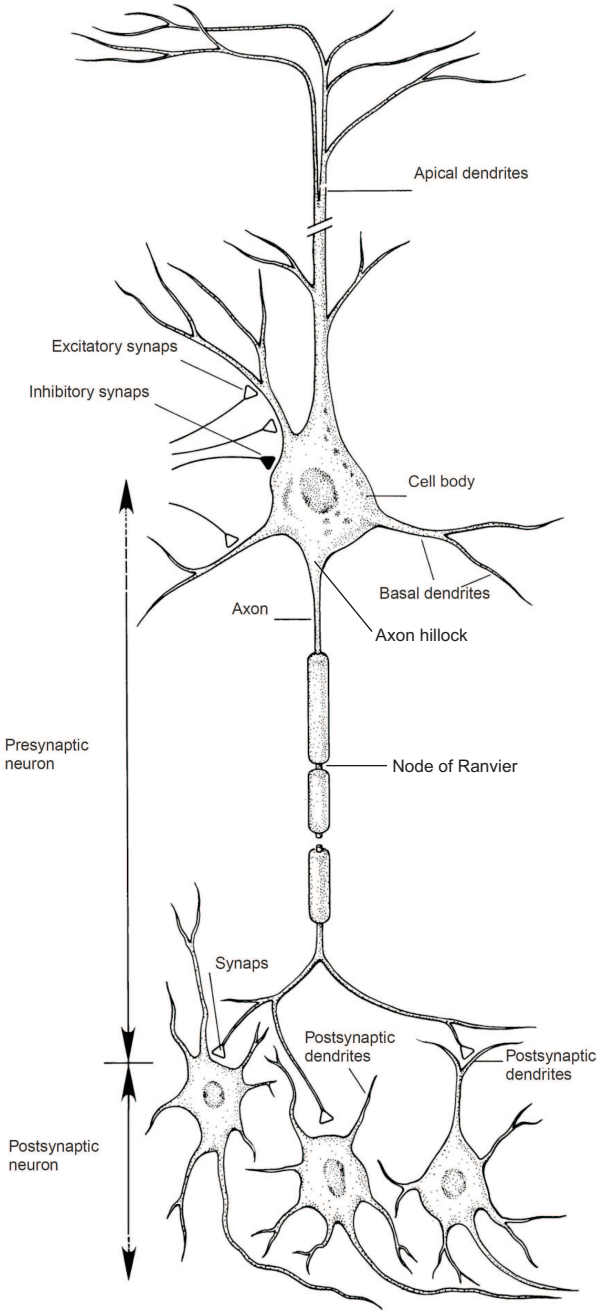


Figure 2.1: The anatomy of a neuron.

to the soma to the axon using electrical conduction, which is mainly based on the movements of $K^+$and Na^+ions. At the synapse between two neurons chemical conduction is used. The chemical conduction between the presynaptic axon terminal and the postsynaptic dendrite is based on neurotransmitters such as dopamine, glutamate and gamma-aminobutyric acid (GABA). The axon terminal contains these neurotransmitters and they are released into the synaptic cleft when the neuron has fired.

A synapse can either be excitatory or inhibitory. When neurotransmitters bind on receptors of the postsynaptic dendrite of a excitatory or inhibitory synapse the probability that the postsynaptic neuron will fire is increased or decreased respectively. The binding of the excitatory and inhibitory neurotransmitters causes an opening of Na^+channels or opening of K^+channels on the postsynaptic dendrite respectively. This results in an influx of Na^+or an outflux of K^+respectively due to the concentration gradients of $Na^+$and K^+. The inflow of positive Na^+ions causes a temporary depolarization of the postsynaptic membrane potential (it becomes more positive) which is called an excitatory postsynaptic potential (EPSP). The outflow of positive K^+ions results in a temporary hyperpolarization of the postsynaptic membrane potential (it becomes more negative) which is called an inhibitory postsynaptic potential (IPSP). Due to electrotonic conduction the ions will spread in the cell body and reach the axon hillock. The mechanism of electrotonic conduction is shown in the upper panel of fig. 2.2. If the number of EPSPs is larger (either from multiple EPSPs from different dendrites in space or from EPSPs from the same dendrite over a period of time) compared to the number of IPSPs the potential at the axon hillock will rise. If the axon hillock potential reaches -55 mV the neuron will fire. It will transmit the signal along its axon.

Electrotonic conduction which is used to transmit the signal from the dendrite to the axon hillock is fast, but the effects dissipates over distance. This makes it not suitable to transmit signals along the axons. Here transmission is based on action potentials (AP). An AP is a short-lasting event in which membrane potential rapidly rises and falls. The AP travels along the axon from the axon hillock to the axon terminal.

The mechanisms of the propagation of an AP is explained in the bottom panel of fig. 2.2. The increase in cell membrane voltage at the axon hillock to -55 mV opens the Na^+channel and leads to an influx of Na^+. This increases the cell membrane potential rapidly and due to electrotonic conduction the next Na^+channel (away from the soma) of the axon will open. When +40 mV is reached in the first Na^+channel it will close and

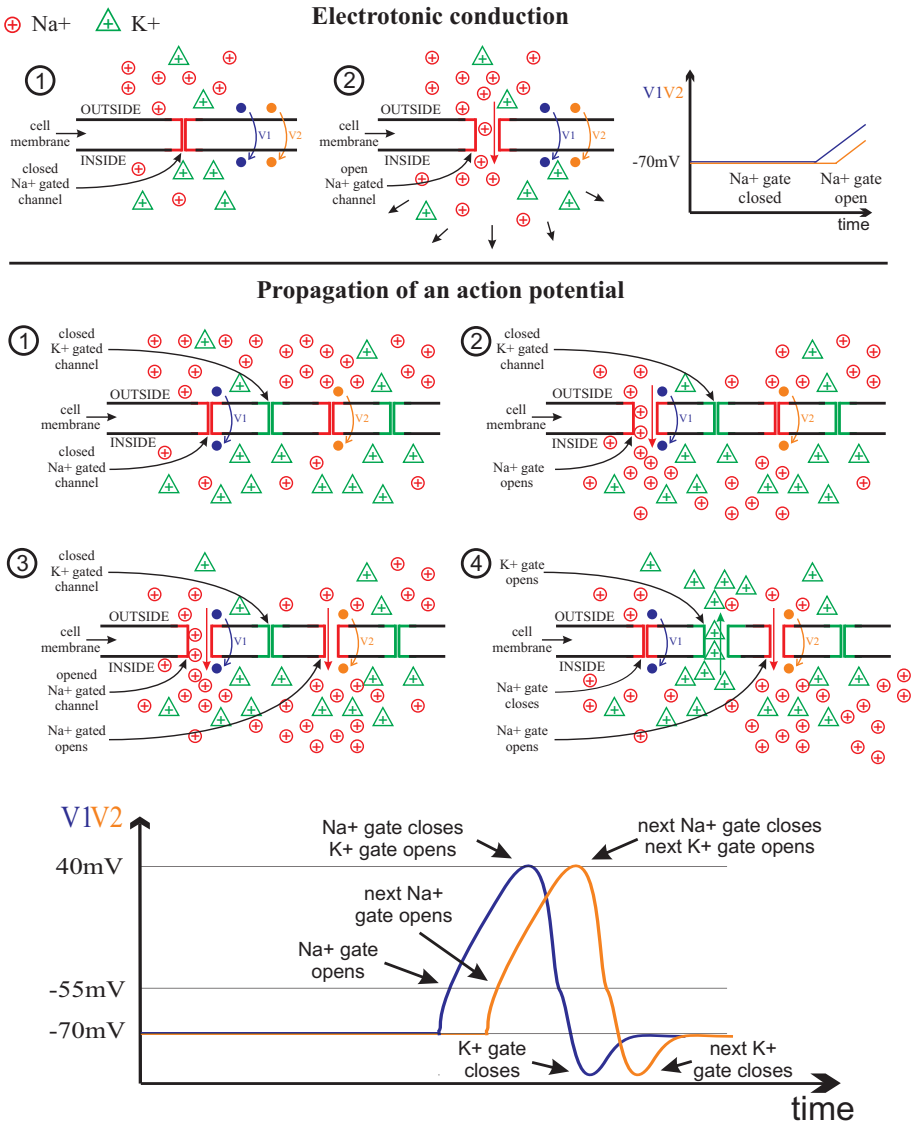


Figure 2.2: The mechanisms of electrotonic conduction and the propagation of an action potential along an axon.

the K^+channel at the same location will open. This results into an outflux of K^+ions until -80 mV is reached. Afterwards the Na^+/K^+pumps and the membrane permeability for $Na^+$and K^+will restore the resting state potential of -70 mV. The propagation of an AP along an axon is good for covering distance because there is no dissipation of energy over distance.

However, the propagation of an AP requires energy and is slow compared to electrotonic conduction. Therefore long axons are myelinated and use both electrotonic conduction and propagating AP to transmit signals across their length. Electrotonic conduction happens at the parts that are covered by myelin sheaths. The myelin sheaths allow rapid electrical transmission over large distances but the signal decreases over distances. The mechanism of the action potential boosts the signals at the Nodes of Ranvier. This is slower than electrotonic conduction and requires more energy but is able to preserve signal strength. This is called saltatory conduction (from the Latin *saltare*: to jump). When the AP reaches the axon terminal neurotransmitters are released into the synapse resulting in a EPSP or IPSP. The EPSP and IPSP can excite or inhibit the next neuron. For more information about electrophysiology of neurons we refer the reader to [151, 91].

2.2.3 Structural anatomy

The brain comprises on average 86.1 $\pm$ 8.1 billion neurons and 84.6 $\pm$ 9.8 billion nonneuronal cells [12]. The brain tissue can be divided into gray matter and white matter. Gray matter contains the neurons' cell bodies while white matter contains the axons. The myelin sheaths produce the distinct white color of the white matter. To maximize the surface area within a fixed space, the brain's surface evolved into a folded surface. The gyri are the convolutions that are separated by the 'grooves', named the sulci (or fissures).

The brain is protected against trauma by the skull and three meninges. The meninges are 3 membranes covering the brain: the dura mater, the arachnoid and the pia mater (from the outside to the inside). The meninges protect the brain from rubbing against the bone of the skull. The cerebrospinal fluid (CSF) between the pia mater and the arachnoid acts as a protective cushion for the cortex. Furthermore it brings nutrients to, and removes waste from, the brain. The ventricles are four spaces within the brain that are filled with CSF. This allows a circulation of CSF and they also protects the brain from trauma. The anatomy of the brain is shown in fig. 2.3.

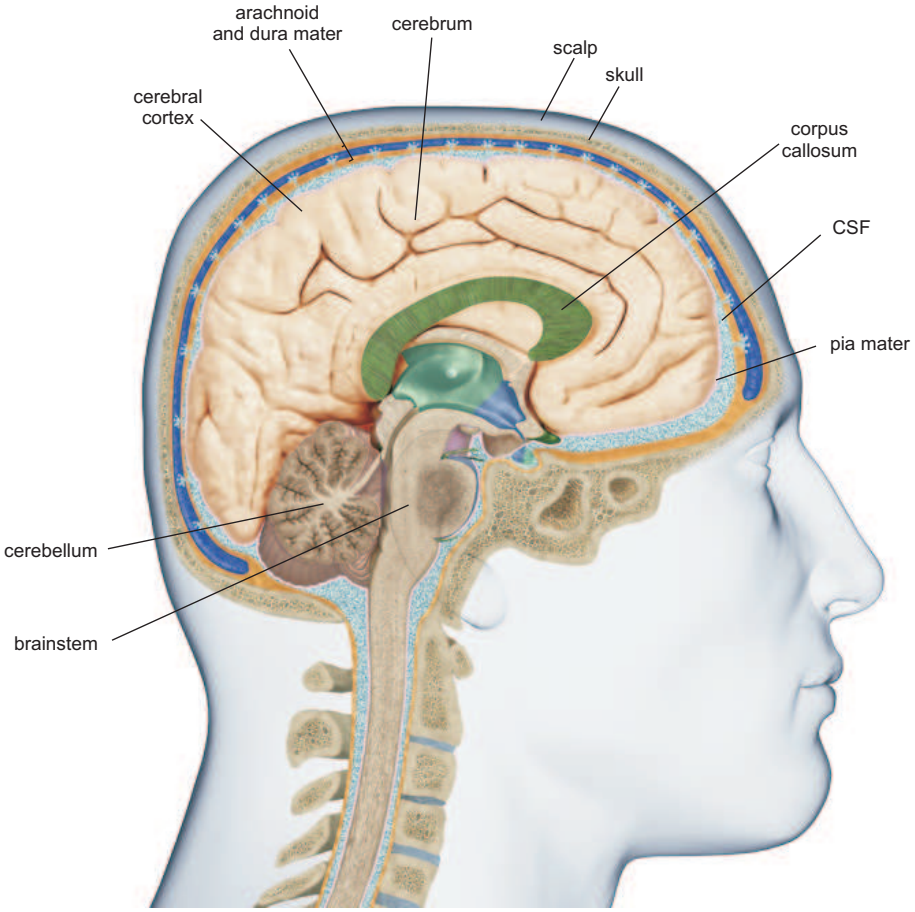


Figure 2.3: The structural anatomy of the brain. Figure adapted from [42].

The brain can be subdivided into the cerebellum, the cerebrum and the brainstem. The cerebellum is the separate structure attached to the bottom of the brain and the cerebrum is the upper part that contains the cerebral cortex. Only 19% of all neurons are located in the cerebral cortex which presents 82% of total brain mass [12]. The cerebrum is further divided into two hemispheres (left and right) by the medial longitudinal fissure. Each hemisphere of the cerebrum has four lobes: frontal, temporal, parietal and occipital (as illustrated in fig. 2.4). The cerebral cortex, the outermost sheet of neural tissue of the cerebrum, can be divided into 52 Brodmann areas based on the neuron's cytoarchitecture, or structure and organization of cells [38].

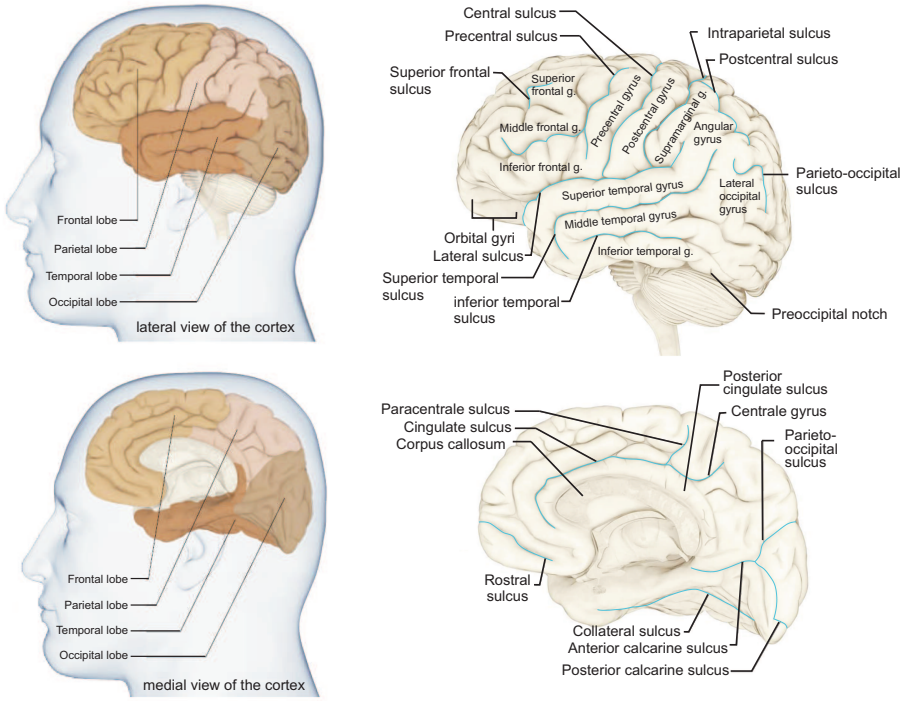


Figure 2.4: The 4 brain lobes (frontal, temporal, parietal and occipital) and the naming of the sulci and gyri. Figure adapted from [42].

2.2.4 Brain functions

The frontal lobe is mainly involved in executive functions, thinking, planning, organizing and problem solving, emotions and behavioral control and personality. It also includes the motor cortex responsible for the execution of movements and Broca's area responsible for speech production, named after Paul Broca. The central fissure and the Sylvian fissure separate the frontal from the parietal and temporal lobe respectively. The parietal lobe is involved in perception, making sense of the world (sensory cortex), arithmetic and spelling. The occipital lobe is used for vision and the temporal lobe for memory (hippocampus, circuit of papez [159]) and listening (auditory cortex). The temporal lobe includes Wernicke's area that is involved in the understanding of written and spoken language.

In the early days most functions of brain areas were discovered by injury to these areas resulting in a specific loss of ability. Three small examples illustrate this [42]. In 1848 Phineas Gage, a well respected railroad foreman,

had an accident when he was compressing explosive powder with a tamping rod. The rod flew into his head and made a hole in the skull and the front of his brain. Phineas survived, became blind in one eye but had remarkable little damage to most of his faculties. However, his behavior changed dramatically. The once conscientious, polite and thoughtful man became reckless, rude and socially irresponsible. This behavior was linked by his physician to the brain damage. Modern reconstructions of the position of the rod showed that the damaged brain area is now know to be central to moral sensitivity. In 1861, the French physician Paul Broca described a patient whom he named *Tan*, as it was the only word he could say. When Tan died, Broca examined his brain and found damage to part of the left frontal cortex. This part of the brain became known as *Broca's Area*. He also reported the loss of ability to speak after injury to the posterior inferior frontal gyrus of the brain in 2 patients [58]. In 1876, the German neurologist Carl Wernicke discovered that damage to the left posterior section of the superior temporal gyrus (*Wernicke's Area*) also caused language problems, but rather a problem in understanding words than producing them. The area is named after Carl Wernicke who was able to link the left posterior section of the superior temporal gyrus and the reflexive mimicking of words and their syllables that associated the sensory and motor images of spoken words [62].

As mentioned in previous section the brain can be divided based on the cytoarchitecture into the Brodmann areas. Most of them have been associated with a specific function as illustrated in fig. 2.5. For some areas the function is still unknown.

2.3 Neuroimaging

Neuroimaging refers to imaging the structure, function or pharmacology of the brain. It can be divided into structural and functional neuroimaging. The most common structural neuroimaging techniques are computed tomography (CT) and magnetic resonance imaging (MRI), while the most common functional neuroimaging techniques are positron emission tomography (PET), single photon emission computed tomography (SPECT), functional magnetic resonance imaging (fMRI), electroencephalography (EEG), magnetoencephalography (MEG) and near infrared spectroscopy (NIRS). Below we will briefly introduce each technique. An overview of the different techniques is given in fig. 2.6.

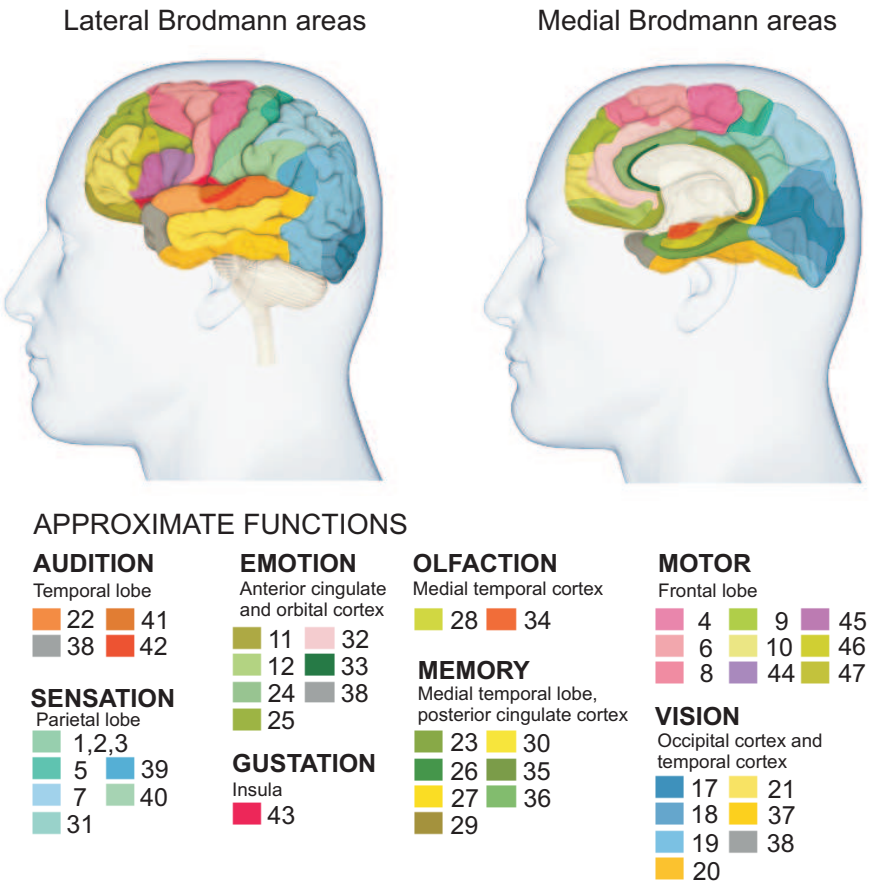


Figure 2.5: The Brodmann areas of the brain. Figure adapted from [42].

2.3.1 Different modalities

Computed Tomography (CT) is a technique in which X-rays are used to make tomographic images of the brain. The technique was introduced in the 1970s by Allan McLeod Cormack and Godfrey Newbold Hounsfield who received the Nobel prize for Physiology or Medicine for their work in 1979. The technique allows detailed anatomic images of the brain useful for diagnostic and research purposes. In clinical practice CT is used to reveal brain abnormalities such as hemorrhage, atrophy (a decrease in brain substance), scar tissue, tumors, abnormal blood vessels or abnormal spinal fluid circulation. CT can also image contrast agents that are injected into the patient's venous system shortly before acquisition. This allows to in-

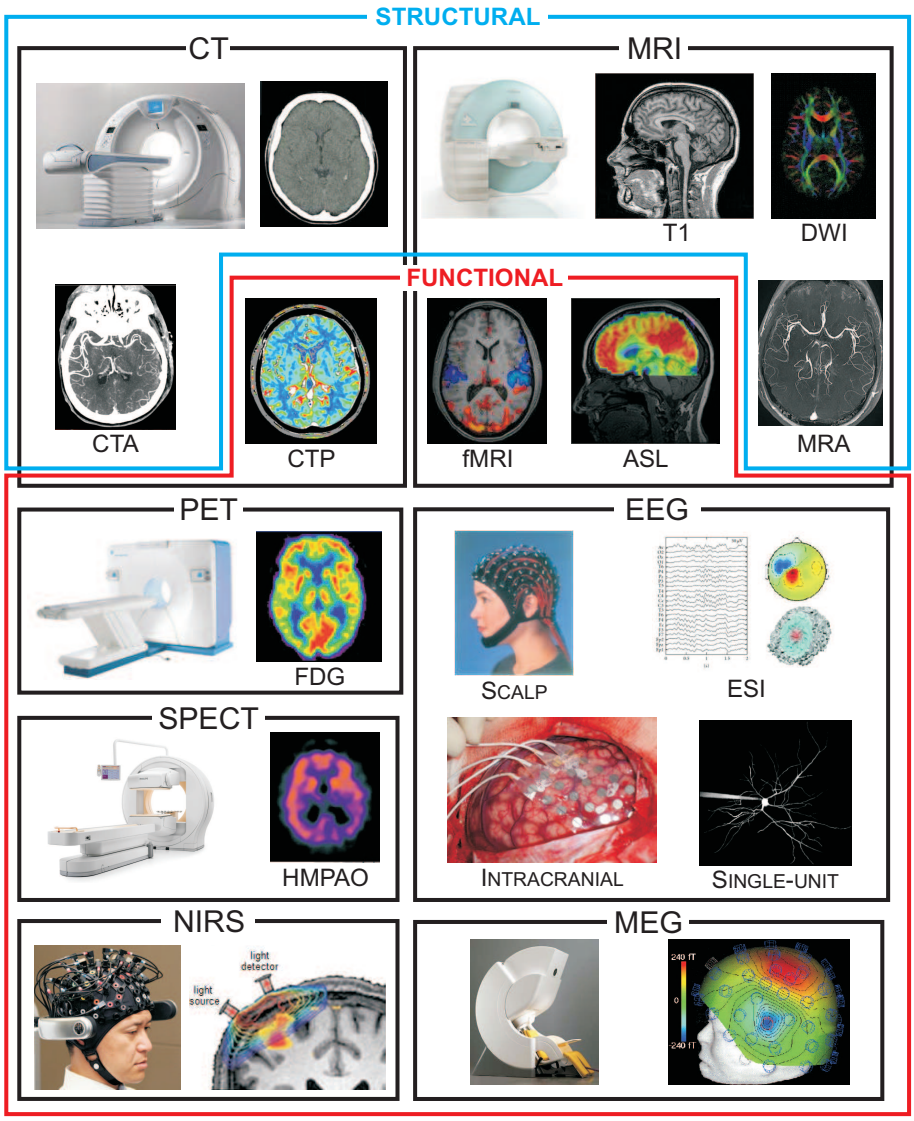


Figure 2.6: Overview of the different structural and functional neuroimaging techniques.

vestigate the perfusion of the brain with CT perfusion (CTP) and to study the lumen of blood vessels in the brain using CT angiography (CTA).

Magnetic Resonance Imaging (MRI) is a noninvasive technique using magnetic fields and radiowaves to image the protons of atoms inside the brain. The technique was developed in the 1980s by researchers including Peter Mansfield and Paul Lauterbur, who were awarded the Nobel Prize for Physiology or Medicine in 2003. MRI allows producing a high resolution 2D or 3D image of the brain. By using different MRI acquisitions, different properties of tissue can be visualized. To provide excellent contrast between gray and white matter T1-weighted images are used. In T1 weighting tissue will appear brighter if it contains more fat. This makes white matter brighter compared to the gray matter. T1-weighted sequences are used to reveal brain anomalies such as atrophy and cortical dysplasia. In T2-weighted imaging the fluids are bright, making this an excellent technique to visualize edema. In diffusion weighted imaging (DWI), the MR signal is related to the diffusion of the water molecules in the brain. In combination with specific algorithms this allows to investigate the directionality of the white matter tracts.

The MRI scanner can also be used as a functional neuroimaging tool. Functional MRI (fMRI) [153] uses blood-oxygenation-level-dependent (BOLD) contrast to indirectly investigate neuronal activation through its effect on the oxygenation level of the blood. Another technique is arterial spin labeling (ASL) MRI that investigated the perfusion in the brain. MR angiography (MRA) images the blood flow in the brain and does not necessarily require the injection of a contrast dye as is the case in CTA.

Positron Emission Tomography (PET) is a nuclear imaging technique that images the distribution of an injected radiotracer, which consists of a molecule of interest labeled with a positron emitting radionuclide. The most commonly used PET tracer is ^{18}F-fluorodeoxyglucose (^{18}F-FDG), a glucose analogue that reveals regional glucose uptake. It is used to investigate the metabolic rate of the different brain regions. The technique is most commonly used in oncology to image tumors and look for metastases. In neurology the technique can be used to localize the seizure focus in patients with epilepsy, which is sometimes reflected by local hypometabolism.

Single Photon Emission Computed Tomography (SPECT) is another nuclear imaging technique and images the distribution of a radiotracer labeled with a single photon emitting isotope. In neurology the most commonly used tracer is ^{99m}Tc-HMPAO (Technetium - hexamethylpropylene amine oxime) to image the perfusion in the brain. The tracer uptake time

is within 30 to 60s and the patient can be imaged several hours later. It it used to asses the regional cerebral blood flow at time of injection. In epilepsy patients the tracer can be injected at the time of a seizure and the patient can be imaged afterwards when the seizure has stopped. Hyperperfusion may indicate the seizure focus.

Electroencephalography (EEG) is a technique that images the electric field produced by the brain. Electrodes are placed on the scalp of the subject and the potential differences between the electrodes are registered over time. Because of the different electrical conductivities of the scalp, skull, CSF, gray and white matter the field is distorted and attenuated. A special technique called EEG source imaging (ESI) can be used to estimate the electrical source distribution in the brain. The electric field can also be measured inside the skull with intracranial electrodes, resulting in the intracranial EEG (IEEG). This technique is used to reveal brain activity that cannot be captured with scalp EEG. IEEG measures the local field potentials (LFP) at the location of the electrodes. An advanced microelectrode can be used to record single unit activity (SUA), this is the electrical activity produced by 1 single neuron. EEG is most commonly used to diagnose epilepsy and localize the epileptic focus. Furthermore it is used in sleep studies, to estimate the prognosis in coma patients and as an adjunct test for brain death. For more information about EEG we refer the reader to the next section.

Magnetoencephalography (MEG) images the magnetic field produced by the electrical currents in the brain. The magnetic field of the brain is very small in the order of 10 to 1000 femtotesla (fT) while the urban environment noise is around 10^8 fT. Therefore, MEG requires that the magnetic field is acquired in a special shielded magnetic room with highly sensitive magnetometers. MEG has the advantage over EEG that the magnetic field is not distorted by the scalp and the skull rendering the use for complex methods to image the underlying source distribution in the brain unnecessary. On the other hand MEG is only sensitive to tangential sources (originating in the sulci), while EEG is sensitive to both tangential and radial sources. The clinical use of MEG is situated in the field of epilepsy to reveal information about the epileptic focus.

Near-Infrared Spectroscopy (NIRS) is a recent non-invasive technique that uses near-infrared light to evaluate increases or decreases in oxygenated hemoglobin or deoxygenated hemoglobin in tissues below the body surface. Compared to fMRI the technique is portable and less intrusive but it is less sensitive to deeper sources and does not have the same spatial resolution.

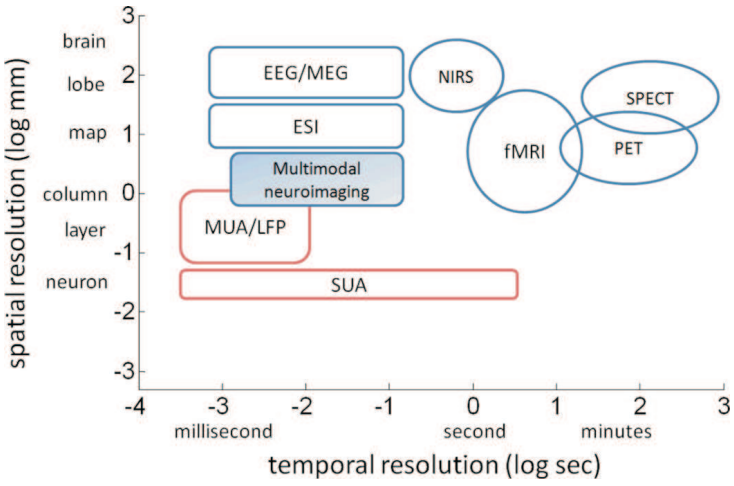


Figure 2.7: The spatial and temporal resolution of different functional neuroimaging methods (adapted from [101]).

2.3.2 Spatial and temporal resolution of the functional neuroimaging techniques

The different neuroimaging techniques are based on different neurophysiological phenomena and have diverse temporal and spatial resolutions. An estimate of the spatial and temporal resolution of different functional imaging modalities is shown in fig. 2.7. EEG and MEG have superior temporal resolution compared to fMRI, PET, SPECT and NIRS. However, they have limited spatial resolution (order of cm). The spatial resolution of NIRS is comparable to that of EEG and MEG, while fMRI has a high spatial resolution in the order of mm. PET and SPECT have poor spatial and temporal resolution but are highly sensitive and specific in the imaging of tumors, metabolism and perfusion.

2.3.3 Multimodal neuroimaging

Much effort is put nowadays in the design of hybrid imaging scanners like PET/MRI [102], SPECT/MRI [218] and even MEG/MRI [214]. The hybrid scanners are due to technical difficulties not yet routinely available in clinical practice. Other combinations with less technical issues are EEG/fMRI and EEG/MEG, and are already used in clinical practice especially in the field of epilepsy. In EEG/fMRI the high spatial resolution of fMRI is coupled to the high temporal resolution of EEG. EEG/MEG provides a simultaneous mea-

surement of the electric and magnetic field produced by the brain resulting in more accurate source imaging.

EEG can also be measured in a PET/MRI scanner resulting in a tri-modality set-up combining EEG, fMRI and PET. Structural MR images can be acquired to provide an anatomic reference for the fMRI, PET and EEG activity. This way electrophysiologic measurements can be combined with imaging of brain metabolism and neuronal activation reflected in the oxygen level in the blood. Multimodal neuroimaging is not commonly used in clinical practice yet, but shows promising potential to help in diagnosis and treatment.

2.4 Electroencephalography

Electroencephalography (EEG) was already shortly introduced in the previous section as one of many neuroimaging techniques. The main advantage of EEG is its high temporal resolution. This makes it an excellent technique to investigate the neuronal activity of different brain regions over time. In this dissertation EEG signals will be used as input to investigate the functional connections between brain regions. This section describes the generators of the EEG, how to record different EEG rhythms and introduces EEG source imaging (ESI). Some common artifacts and the main applications are also described. The section is mainly based on [17, 91, 151, 93, 92, 192].

2.4.1 Generators of the EEG

Because the electric field changes induced by one neuron are minimal and the electrodes are placed on the scalp, a large number of neurons need to be synchronously active before activity can be recorded by the EEG electrodes. An AP causes a membrane potential change of approximately 70 mV to 110 mV for about 0.3 ms in the axons. Because of the very small time interval it is unlikely that the action potentials of neighboring synchronously firing neurons can be summed. The amplitude of postsynaptic potentials is 0.1 - 10 mV, last for about 10 - 20 ms and is restricted to the soma and the dendrites. This is a much smaller change in amplitude, but due to the longer time course there is a higher probability that this period will overlap in neighboring neurons and their activity can be summed.

Before the electrical activity originating from postsynaptic potentials can be recorded at the scalp some criteria need to be fulfilled ([95, 17]). Thousand or millions of neurons should have the same kind of stimulus (excitatory

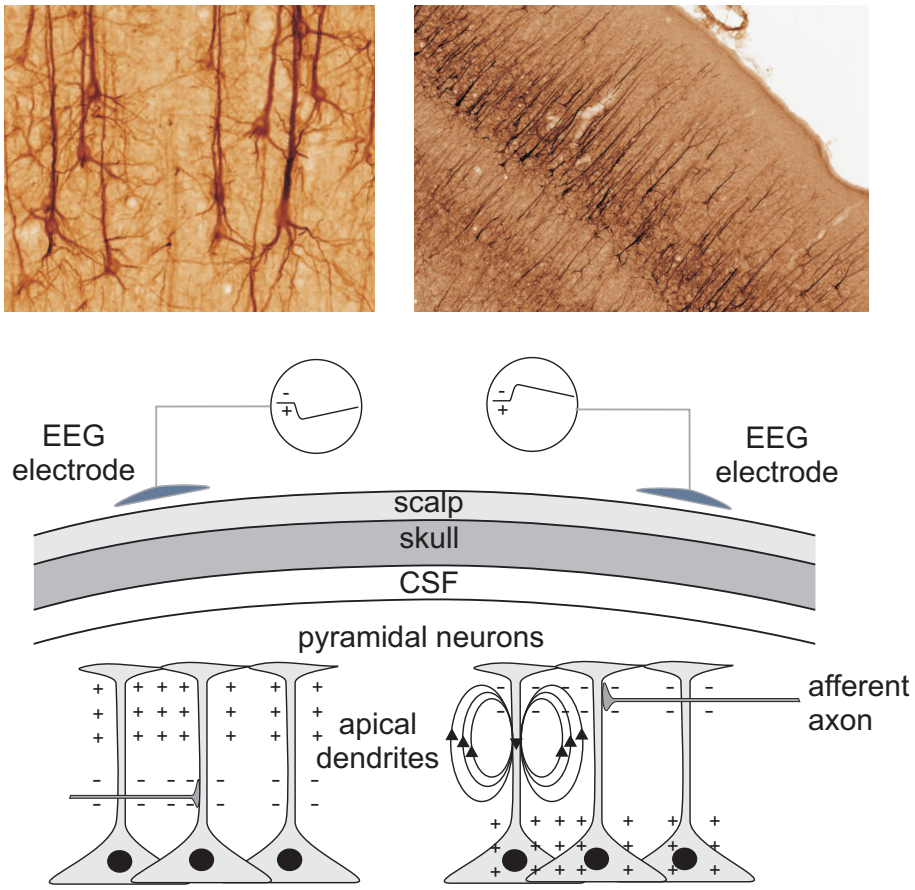


Figure 2.8: The pyramidal neurons and their organization in the cerebral cortex.

or inhibitory) which corresponds approximately to a patch of 5mm by 5mm of 4mm thick cortex. Moreover, the dendrites need to be spatially aligned so that they amplify each others extracellular potential fields created by the postsynaptic potentials.

The pyramidal cells are organized in such a way that the neighboring dendritic trees lie parallel to each other and orthogonal to the cortical surface. Pyramidal neurons and their organization in the cerebral cortex are shown in fig 2.8. They consist of a pyramidally shaped soma and long apical dendrites oriented perpendicularly to the cortical surface. They are believed to be the main generators of the recorded EEG.

The brain is surrounded by the meninges, CSF, skull and scalp as shown in fig. 2.3. The difference in conductivity between the tissues attenuates and

blurs the neuronal electrical signals measured on the scalp. The resulting EEG recordings are in the range of around 100 μV.

2.4.2 Recording the EEG

In 1924 the first scalp EEG was recorded by Hans Berger. Berger made the first EEG recording on July 6 1924, during a neurosurgical operation on a 17-year-old boy, performed by the neurosurgeon Nikolai Guleke. He reported on the topic in 1929 [27], using the terms alpha and beta waves.

EEG captures the time-variant electrode potentials of the brain at certain predefined standard positions. An internationally accepted standard is the so called 10-20 system (fig. 2.9) [117]. The amount and exact placement of the electrodes depend on the application. The electrodes are placed on the scalp and conductivity gel is used to reduce the scalp-electrode impedance. An impedance below 5 $k\Omega$ is adequate to record scalp potentials. The position of the electrodes is based on anatomical landmarks such as inion (the lowest point of the skull from the back of the head and normally indicated by a prominent bump), nasion (the distinctly depressed area between the eyes, just above the bridge of the nose) and the pre-auricular points (the point in front of the auricle of the ear) in such a way that the entire brain is covered. The spatial sampling depends on the number of electrodes that is used. In clinical practice usually 27 to 32 electrodes are used, although there is a trend towards the use of higher number of electrodes to achieve better spatial sampling.

Each electrode contact has a specific label. Electrodes covering the frontal, temporal, parietal and occipital lobe have as label 'F', 'T', 'P' and 'O' respectively. The central electrodes have label C, the ones at the earlobe have label 'A' (auricular) and the ones on the forehead have label 'Fp' (frontal polar). The electrodes over the midline of the brain have a 'z' as last character. Those covering the left hemisphere have an odd number and those covering the right hemisphere an even number as last character. This way we know that electrode T4 monitors the right temporal lobe. An example of recorded EEG traces is shown in fig. 2.9. The EEG is recorded with a single reference, but can also be represented as a bipolar montage showing the potential difference over time between adjacent electrodes.

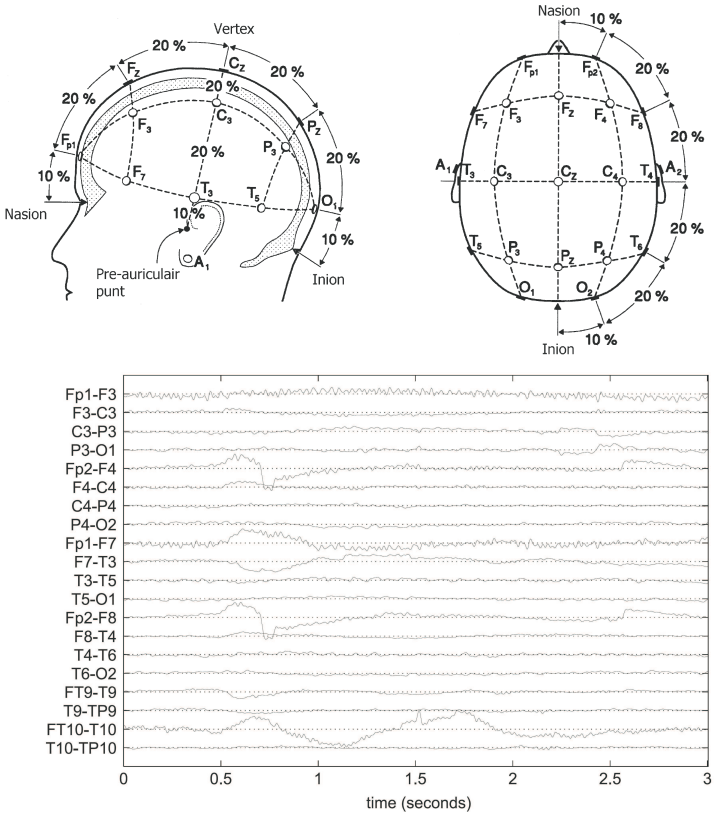


Figure 2.9: The 10-20 system to record scalp EEG.

2.4.3 EEG rhythms

Based on their amplitude and frequency, EEG signals can be used to identify normal and abnormal brain conditions. The EEG signals depend on the age, physical and mental conditions of the subject. Generally speaking the EEG signals can be divided according to the observed frequency content into 5 rhythms [183] (fig. 2.10):

- Delta rhythm: frequencies less than 4 Hz. This rhythm is observed when the adult is in deep sleep. The EEG signals have large amplitudes. When this rhythm is present in an awake adult it may indicate brain disease.

- Theta rhythm: frequencies between 4 and 7 Hz. The theta rhythm is encountered during drowsiness and in certain sleep stages.

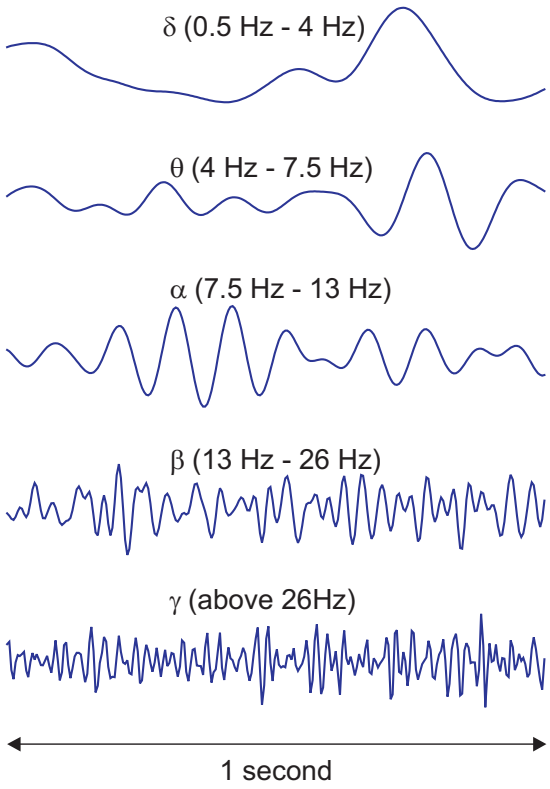


Figure 2.10: EEG rhythms: example of delta, theta, alpha, beta and gamma activity.

- Alpha rhythm: frequencies between 8 and 13 Hz. This is most prominent in relaxed and awake subjects with eyes closed. The activity is suppressed when the eyes are open. This activity is typically localized in the occipital lobe.
- Beta rhythm: frequencies between 14 and 30 Hz. The rhythm is associated with alertness and also in certain sleep stages. Low frequencies in this band correspond to a relaxed yet focused adult. Higher frequencies are encountered when the person is thinking and alert. It is primarily present in the frontal and central regions.
- Gamma rhythm: frequencies higher than 30 Hz. Gamma waves are related to the state of active information processing of the cortex.

Broadly speaking, when the cortex analyzes information, the activity of its neurons is relatively high but also relatively unsynchronized. Each little

group of neurons is being activated by a different aspect of the cognitive task that the cortex is performing. The activity of these groups is not synchronized, and the amplitude of the EEG is small, resulting in high-frequency beta and gamma waves.

During non-rapid eye movement (REM) sleep, cortical neurons do not process any information. They are stimulated by a rhythmic pulse arising from the thalamus. The thalamus plays an important role in regulating states of sleep and wakefulness. The rhythmic pulse results in highly synchronized activity of the neurons, leading to EEG signals with high amplitude and low frequency, the delta waves.

2.4.4 Artifacts

EEG traces are commonly contaminated by extracerebral sources. These artifacts can either be physiological (caused by the subject) or extraphysiological (caused by environmental sources). Common physiological artifacts are ocular, muscle and cardiogenic artifacts.

Ocular artifacts are generated by the potential difference (of approximately 0.4 - 1 mV between the cornea and the retina of the eye [110]. This can be seen as a small dipole. When the eye moves, the dipole will change position and orientation accordingly. This will produce high amplitude changes on nearby placed electrodes (Fp1, Fpz and Fp2). During eye blinks, the eye slightly moves but more importantly the eyelid makes contact with the cornea. This contact leads to alterations in conductance that propagate through the superficial layer of the face and head and decreases rapidly with distance from the eyes [156]. The ocular activity can be monitored with the electrooculogram (EOG) that records the electric field from electrodes placed next to the eyes. These signals can be used for artifact filtering. A popular way of filtering ocular artifacts without the need of EOG recordings is by using Independent Component Analysis (ICA) [125].

Muscle artifacts are produced by muscle contractions and are superimposed on the EEG. They are related to chewing, biting, grinding and clenching of the teeth, swallowing, frowning, sniffling, movement of the tongue et cetera.

Cardiogenic artifacts are caused by contraction of the heart muscle. The electrode potential arising from the heart muscles is high in amplitude compared to the measured EEG. It can be measured at the scalp due to volume conduction. The heart activity can be monitored with the electrocardiogram

(ECG). These recordings can help to filter the cardiogenic artifacts.

The most common extraphysiological artifacts are the power line artifact (50 Hz in Europe) and electrode- or equipment related artifacts. For example a loose electrode will result in a change of the impedance and this will produce high voltage artifacts. The electrode behaves like an antenna and will pick up a lot of environmental noise.

During EEG/fMRI measurements two other types of artifacts are seen due to the high magnetic field of the MRI scanner: the gradient artifact and the ballistocardiographic (BCG) artifact. The gradient artifact is due to the switching of the gradient coils during the fMRI sequence and has an amplitude in the order of mV. Luckily the artifact is very deterministic and can easily be removed by average template subtraction. The BCG artifact is caused by the blood flow in the scalp arteries leading to electrode movements. The artifact occurs during the heartbeat and can be removed using average template subtraction over several heartbeats or using more advanced techniques like the canonical correlation approach [9].

2.4.5 EEG source imaging

EEG source imaging (ESI) estimates the electrical source distribution inside the brain that corresponds most likely to the recorded scalp potentials. It comprises two subproblems: the forward problem and the inverse problem. The forward problem estimates the scalp potentials given an electrical source distribution, while the inverse problem estimates the source parameters out of the recorded scalp potentials based on the solution of the forward problem. A schematic representation of both subproblems is shown in fig. 2.11. The following section is mainly based on [192, 92].

2.4.5.1 Forward problem

The forward problem calculates the scalp potentials for a given electrical source distribution (= source model) based on a realistic volume conductor model of the head (= head model).

Head model

The head model provides a description of the anatomy of the head and of the electrical conductivities of each tissue type. In the most simple head model, the head is approximated by concentric spheres where each sphere corresponds to a certain tissue type. These head models are called spherical head models. More complex head models can be built based

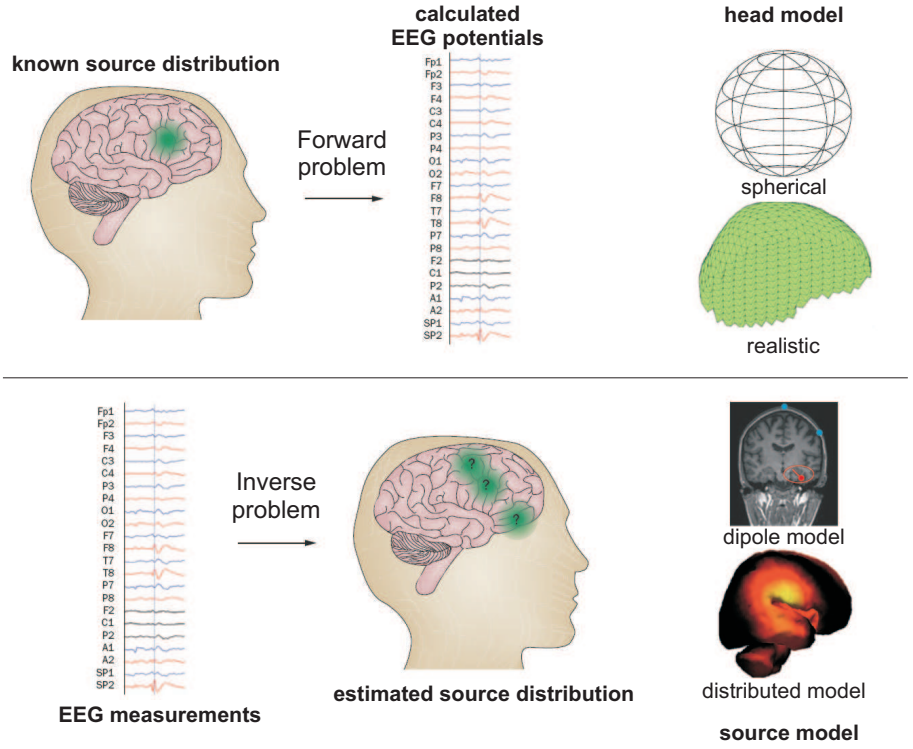


Figure 2.11: EEG source imaging exist out of two problems. The forward problem calculates the scalp potentials given an source distribution based on a head model and the electrode positions. The inverse problem estimates the source distribution that best explains the calculated potentials using the solution of the forward problem. Figure adapted from [113].

on high resolution anatomical Magnetic Resonance (MR) images (usually T1 and T2 weighted images) of the brain. The different tissues: white matter, gray matter, cerebrospinal fluid (CSF), skull, air, and scalp can be segmented from these images. The skull can be further divided into compact bone and spongy bone. Each tissue has a specific corresponding conductivity value. An example of a subject specific head model and typical conductivity values used in literature [83, 77, 98, 25] are depicted in fig. 2.12. The advantage of simple spherical head models is that the solution can be calculated analytically, which is not the case for the complex models in which iterative techniques need to be used.

Source model

The most simple source model is a current dipole. It represents the post-

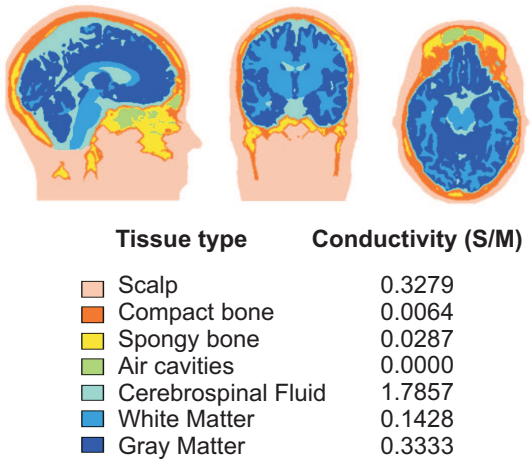


Figure 2.12: A subject specific head model.

synaptic current at the apical dendrite (fig. 2.13). It has 6 parameters: the position $\mathbf{r} = [x\, y\, z]$, the orientation (ϕ and θ) and the intensity (I). The orientation and intensity are described by the dipole moment, i.e. the product of the charge and the displacement vector $\mathbf{s}$, given by: $\mathbf{d} = I\mathbf{s} = [d_x\ d_y\ d_z]$. The dipole models the synchronous electrical activity of a group of pyramidal neurons with there apical dendrites oriented similar to the dipole [50, 97, 173]. A dipole is the basic building block of more complex source models. If the brain activity is limited to one specific brain area this can be represented by the single dipole model. If the brain activity is limited to several brain areas this can be represented by a source model consisting of several dipoles, namely the multiple dipole model. The number of unknowns equals 6 times the number of dipoles as for each dipole the position, the orientation and the intensity need to be estimated.

In distributed source models a dipole is assigned to each brain voxel. The orientation of the dipoles is chosen the same way as the orientation of the apical dendrites of the pyramidal neurons, perpendicular to the surface of the cortex [45]. The number of unknowns is in the range of 10^4 [17].

The advantage of current dipole source models is that there are less unknowns than measured data points, which can be easily solved. Unfortunately we need to define the number of dipoles a priori which can bias or corrupt the results. Distributed source models do not suffer from this drawback, but here the number of unknowns is much higher than the measured data points, which makes the problem ill-posed.

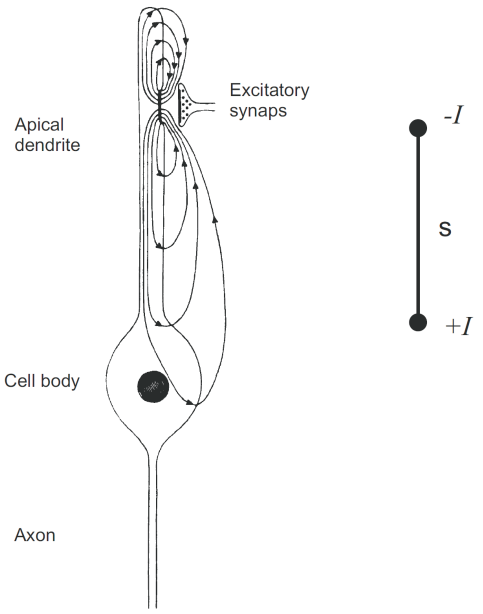


Figure 2.13: The dipole representation of postsynaptic current at the apical dendrite. Here an excitatory synapse is considered, which has the current sink (-I) at the synapse and the current source (+I) at the cell body of the neuron with interdistance equal to s. For an inhibitory synapse the sink and source will switch positions.

Solving the forward problem

The potentials at M electrodes $\mathbf{V} = [V(\mathbf{r_1})\, V(\mathbf{r_2}) \ldots V(\mathbf{r_M})]^T$ caused by one dipole with position $\mathbf{r_d} = [x_d\ y_d\ z_d]$ and dipole moment $\mathbf{d} = [d_x\ d_y\ d_z]$ can be calculated as:

$$\mathbf{V} = \mathbf{L}(\mathbf{r_d})\mathbf{d} \tag{2.1}$$

where $\mathbf{L}(\mathbf{r_d})$ is called the lead field matrix, that depends on the dipole position $\mathbf{r_d}$, the head model and the electrode positions, $\mathbf{V}$ are the EEG measurements and $\mathbf{d}$ the dipole moment.

Three numerical techniques exist to estimate the lead field matrix for each dipole position given the head model and the electrode positions: the boundary element method (BEM) [18], the finite difference method (FDM) [144] and the finite element method (FEM) [44]. The BEM only allows volume conductors with homogeneous isotropic compartments. It calculates the potentials at each boundary of two compartments. The FEM and FDM

method allow more complex volume conductor models. For more detailed information about all three methods we refer the reader to [92].

2.4.5.2 Inverse problem

The inverse problem estimates the electrical source distribution given the lead field matrices and measured electrode potentials. It was shown that given a potential distribution at the scalp an infinite number of source configurations exist [215]. Therefore, source models are needed to confine the solution space to a unique solution. We will present several techniques to estimate the source distribution from the measured scalp EEG. The techniques are either based on a dipole source model, where the number of unknowns is much smaller than the measured data points, or on distributed source models, where the number of unknowns is much larger than the number of measured data points. First we will describe the dipole model and afterwards the distributed source models

Single dipole model at one time point

The inverse problem for a single dipole model given the measured scalp potentials $\mathbf{V} \in \mathbb{R}^{M\times 1}$ is solved by minimizing the relative residual energy (RRE):

$$RRE = \frac{\|\mathbf{V} - \mathbf{L}(\mathbf{r})\mathbf{d}\|}{\|\mathbf{V}\|} \tag{2.2}$$

with $\|.\|$ being the L_2-norm. The dipole parameters $\mathbf{r}$ and $\mathbf{d}$ are optimized so that they minimize the RRE, i.e. the energy that cannot be explained by the model. This 6D problem can be reduced into a 3D problem because the optimal dipole moment at position $\mathbf{r}$ is given by [149, 173]:

$$\mathbf{d}_{opt}(\mathbf{r}) = \mathbf{L}(\mathbf{r})^{\dagger}\mathbf{V} \tag{2.3}$$

with $\mathbf{L}^{\dagger}$ the Moore-Penrose pseudo-inverse of matrix $\mathbf{L}$ [147]. This reduces eq.2.2 to a minimization problem with respect to parameter $\mathbf{r}$:

$$RRE = \frac{\|\mathbf{V} - \mathbf{L}(\mathbf{r})\mathbf{L}(\mathbf{r})^{\dagger}\mathbf{V}\|}{\|\mathbf{V}\|} \tag{2.4}$$

This can be solved using a 3D scanning approach or optimization techniques like the Nelder-Maede simplex method [150].

Single dipole at multiple time points

If we now consider an EEG epoch $\mathbf{V} \in \mathbb{R}^{M \times N}$ with N time points. A possible solution is to decompose the measurements using a singular value decomposition (SVD) and use the most prominent topography for dipole estimation. The SVD of the measured scalp potentials $\mathbf{V}$ is

$$\mathbf{V} = \mathbf{U}\mathbf{\Sigma}\mathbf{D}^T \tag{2.5}$$

where $\mathbf{U}$ represents the topographies, $\mathbf{\Sigma}$ is the matrix containing the singular values and $\mathbf{D}$ contains the time series corresponding to the topographies. The first column of $\mathbf{U}$ is the topography that corresponds to the highest singular value. We can estimate the dipole corresponding with that topography by finding the $\mathbf{r}$ corresponding to the minimum RRE of an adapted version of eq.2.4 as follows:

$$RRE = \frac{\|\mathbf{U}(:,\mathbf{1}) - \mathbf{L}(\mathbf{r})\mathbf{L}(\mathbf{r})^{\dagger}\mathbf{U}(:,\mathbf{1})\|}{\|\mathbf{U}(:,\mathbf{1})\|} \tag{2.6}$$

Multiple dipole model

The measured EEG epoch $\mathbf{V} \in \mathbb{R}^{M \times N}$ can be modeled as a sum of multiple sources:

$$\mathbf{V} = A\mathbf{S}^T = [\mathbf{a_1}\ \mathbf{a_2} \ldots \mathbf{a_p}] \begin{bmatrix} \mathbf{s_1} \\ \mathbf{s_2} \\ \vdots \\ \mathbf{s_p} \end{bmatrix} \tag{2.7}$$

The data is modeled as a sum of contributions of different sources ($p < M$) each with a fixed topography $\mathbf{a_i} \in \mathbb{R}^{M \times 1}$ and time varying amplitude $\mathbf{s_i} \in \mathbb{R}^{1 \times N}$.

We need to find the topographies and corresponding sources that minimize the RRE. The optimal time series are given by $\mathbf{S}_{opt} = \mathbf{A}^{\dagger}\mathbf{V}$. This leads to a minimization problem with respect to $\mathbf{A}$.

$$RRE = \frac{\|\mathbf{V} - \mathbf{A}\mathbf{S}^T\|_F}{\|\mathbf{V}\|_F} = \frac{\|\mathbf{V} - \mathbf{A}\mathbf{A}^{\dagger}\mathbf{V}\|_F}{\|\mathbf{V}\|_F} \tag{2.8}$$

with $\|.\|_F$ being the Frobenius-norm.

Direct optimization methods exist to minimize the RRE. But due to the large number of unknowns (5 times the number of dipoles p), the optimiza-

tion methods tend to get trapped in a local minimum. Another problem is that the number of estimated dipoles need to be known a priori. A wrong estimation of this number p could lead to erroneous and even meaningless results.

To deal with these problem, one can resort to signal subspace technique. The multiple signal classification (MUSIC) algorithm [149, 148] replaces the simultaneous dipole search by p single dipole searches. We assume that the electrode potential measurement can be written as:

$$\mathbf{V} = \mathbf{A}\mathbf{S}^T + \mathbf{N} \tag{2.9}$$

where $\mathbf{N}$ is additive white noise with zero mean and σ^2 variance. All matrices $\mathbf{A}$, $\mathbf{S}$ and $\mathbf{N}$ are full rank (p). This means that the topographies as well as the corresponding time series are linearly independent. The spatial covariance matrix of the data can be written as:

$$\mathbf{R_V} = E\left[\mathbf{V}\mathbf{V}^T\right] \tag{2.10}$$

$$= \mathbf{A}\mathbf{R_S}\mathbf{A}^T + \sigma^2\mathbf{I_M} \tag{2.11}$$

$$= [\mathbf{\Phi_S}\ \mathbf{\Phi_N}] \begin{bmatrix} \mathbf{\Sigma_S} & \mathbf{0} \\ \mathbf{0} & \mathbf{\Sigma_N} \end{bmatrix} \begin{bmatrix} \mathbf{\Phi_S} \\ \mathbf{\Phi_N} \end{bmatrix}^T \tag{2.12}$$

where $\mathbf{R_S}$ is the covariance matrix of the time series with rank p. $\mathbf{\Sigma_S}$ is a diagonal matrix containing the p largest eigenvalues and corresponding eigenvectors $\mathbf{\Phi_S}$ that span the signal subspace. The eigenvectors $\mathbf{\Phi_N}$ with corresponding eigenvalues in $\mathbf{\Sigma_N}$ span the noise subspace. The MUSIC algorithm searches for dipoles whose potential topography lies in the signal subspace. This means that $\mathbf{P_S}\mathbf{L}(\mathbf{r_i}, \mathbf{e_i}) = \mathbf{L}(\mathbf{r_i}, \mathbf{e_i})$ for $i = 1 \ldots p$. Here $\mathbf{P_S} = \mathbf{\Phi_S}\mathbf{\Phi_S}^T$ is the projection matrix onto the signal subspace and $\mathbf{L}(\mathbf{r_i}, \mathbf{e_i})$ is the topography that characterizes the fixed dipole with position $\mathbf{r_i}$ and orientation $\mathbf{e_i}$.

In practice the spatial covariance matrix is estimated as $\hat{\mathbf{R}}_\mathbf{V} = \frac{1}{N}\mathbf{V}\mathbf{V}^T$ and the SVD is used to estimate the signal and noise subspaces given the measured EEG data $\mathbf{V}$. The MUSIC algorithm can be summarized in following steps:

1. Calculate the SVD of matrix $\mathbf{V}$. Estimate the number of dipoles p based on the ordered eigenvalues. Calculate the projection matrix onto the signal subspace $\mathbf{P_S}$ out of the corresponding eigenvectors

2. Find the p maxima of following cost function:

$$C(\mathbf{r_d}, \mathbf{e_d}) = \frac{\|\mathbf{P_S}\mathbf{L}(\mathbf{r_d}, \mathbf{e_d})\|^2}{\|\mathbf{L}(\mathbf{r_d}, \mathbf{e_d})\|^2} \tag{2.13}$$

   This depends on 5 parameters, 3 for the dipole position and 2 for the dipole orientation. However the dipole orientation is given by the eigenvector that corresponds to the largest eigenvalue. This reduces the number of parameters to 3, which allows a 3D scanning approach. The cost function is evaluated on a 3D grid containing the brain voxels.

3. The matrix $\mathbf{A} = [\mathbf{L}(\mathbf{r}_1, \mathbf{e}_1)\, \mathbf{L}(\mathbf{r}_2, \mathbf{e}_2) \ldots \mathbf{L}(\mathbf{r}_p, \mathbf{e}_p)]$ can be constructed out of the topographies corresponding to the found dipole positions and orientations. The time series of the dipoles can be calculated as: $\mathbf{S} = \mathbf{A}^{\dagger}\mathbf{V}$.

The Recursively Applied and Projected MUSIC (RAP-MUSIC) algorithm [148] is based on the MUSIC approach. It uses a recursive procedure in which each source is found as the global maximizer of a different cost function. This is done by recursively scanning through the source space. In essence, the method works by applying a MUSIC search to a modified problem in which we first project both the estimated signal subspace and the array manifold vector away from the subspace spanned by the sources that have already been found.

Imaging methods

Inverse techniques based on single or multiple dipole models have much less parameters to be estimated than measured scalp potentials, making the problem overdetermined. Imaging methods are based on distributed source models with a dipole in each brain voxel. This problem is underdetermined, the number of parameters to estimate is much larger than the measured data points. To solve this underdetermined problem regularization techniques are needed [90, 179, 141]. The framework used to estimate the unknown dipole intensities $\mathbf{J} \in \mathbb{R}^{p\times 1}$ with $p \gg M$ is characterized by:

$$\hat{\mathbf{J}} = argmin\|\mathbf{V} - \mathbf{G}\mathbf{J}\|^2_{\mathbf{C}} + \lambda\|J\|^2_{\mathbf{B}} \tag{2.14}$$

with λ the regularization parameter and $\|.\|^2_{\mathbf{W}} = \mathbf{V}^{\mathbf{T}}\mathbf{W}\mathbf{V}$ a weighted norm defined by weighting matrix $\mathbf{W} \in \mathbb{R}^{M\times M}$. The first term defines the data fit, while the second term penalizes the complexity.

A closed solution for eq.2.14 is given by [28]:

$$\hat{\mathbf{J}}_\lambda = \mathbf{B}^{-1}\mathbf{G}^T(\mathbf{G}\mathbf{B}^{-1}\mathbf{G}^T + \lambda\mathbf{C}^{-1})^{-1}\mathbf{V} \tag{2.15}$$

where the choice of the matrices $\mathbf{B}$ and $\mathbf{C}$ define the different solutions, e.g. minimum norm [94, 99], weighted minimum norm [108], Laplacian weighted minimum norm (LORETA) [161] et cetera.

2.4.6 Applications

EEG is a relatively easy and inexpensive technique to record ongoing brain activity. It is often used in research to study neurophysiological phenomena both in healthy subjects and in patients. It is an established clinical tool for analyzing psychiatric and neurological disorders such as epilepsy, Alzheimer's disease and dyslexia. EEG is also used to prognosticate the outcome in coma patients and as an adjunct test for brain death.

In research, EEG is commonly used to investigate the brain response to a stimulus. An evoked potential (EP) is an electrical potential recorded from the nervous system following presentation of a stimulus, that can be distinguished from spontaneous potentials [143]. An event-related potential (ERP) is any measured brain response that is the direct result of a thought or perception [40]. Because EPs and ERPs have a much smaller amplitude (in the range of 10 μ V) compared to background EEG, many trials need to be averaged to reveal them. By averaging many trials the signal-to-noise ratio will increase and the evoked neurophysiological phenomena will be reflected in the EEG. The EP and ERP are characterized by an amplitude and latency. They are used to study the neurophysiological phenomena like naming objects, visual perception et cetera, but also to diagnose dyslexia [66], dementia [32], Parkinson's disease [166], multiple sclerosis [31], head injuries [60], stroke [46], Obsessive-Compulsive Disorder [96] and Alzheimer's disease [67].

Another application of EEG is the study of sleep. EEG is one of the modalities used during polysomnography to diagnose sleep disorders including narcolepsy, hypersomnia, periodic limb movement disorder, REM behavior disorder, parasomnias, and sleep apnea [6]. The EEG is used to differentiate the sleep stages and reveal related issues.

The most frequently used EEG application is the diagnosis and follow-up of patients with epilepsy. The recorded EEG traces are especially used to diagnose and classify the type of epilepsy. The epileptologists look for typical epileptiform manifestations in the EEG, like seizures and interictal

epileptiform discharges. The EEG can also be used for localizing the brain regions involved in the epilepsy. A nice overview of the clinical use of EEG source imaging in epilepsy is given by [113, 165].

2.5 Epilepsy

2.5.1 Definition, prevalence and incidence

Epilepsy is one of the most common neurological disorder affecting roughly 0.5 to 1% of the population worldwide. This means that in Europe approximately 4,4 million persons have epilepsy [69]. Epilepsy is characterized by recurrent, unprovoked seizures [68]. An epileptic seizure is defined as the manifestation(s) of epileptic (excessive and/or hyper synchronous), usually self-limited activity of neurons in the brain [29]. During a seizure, a sudden burst of uncontrolled electrical activity occurs in a group of neurons of the cerebral cortex [184]. Epilepsy is usually diagnosed after a person has had at least two seizures that were not caused by some known medical condition like alcohol withdrawal or extremely low blood sugar.

Epilepsy can develop at any age, but the incidence of epilepsy is highest during the first years of life and after the age of 65, due to the higher incidence of stroke at old age. During the adult years the incidence is lowest [105]. In most cases the etiology of epilepsy in a specific patient is unknown. Nevertheless, many factors can cause epilepsy: genetic factors, head trauma, tumors, stroke, dementia, meningitis, prenatal injury, oxygen deprivation and many more. This is called the initial precipitating insult (IPI) generating epilepsy. The process in which epilepsy develops until spontaneous seizures occur, is called epileptogenesis.

2.5.2 Classification

Depending on the etiology, epilepsy is either defined as idiopathic, symptomatic or cryptogenic [1]. Idiopathic is used when there is no association with an identifiable cause. Symptomatic when there is a cause (e.g. a congenital brain malformation or a tumor) for the epilepsy. Cryptogenic is used when there is presumably an underlying cause, but the cause is not yet identified.

The International League Against Epilepsy (ILAE) has recently proposed a new categorization based on the etiology into: genetic, structural/metabolic or of unknown cause [26].The concept of genetic epilepsy is that the epilepsy

is, as best as understood, the direct result of a known or presumed genetic defect(s) in which seizures are the core symptom of the disorder. For structural/metabolic epilepsy there is a distinct other structural or metabolic condition or disease that has been demonstrated to be associated with a substantially increased risk of developing epilepsy in appropriately designed studies. Of unknown cause is meant to be viewed neutrally and to designate that the nature of the underlying cause is as yet unknown.

2.5.3 Seizures

Epilepsy can be divided into two types based on the location in the brain where the seizure starts from and how it propagates. On the one hand, primary generalized seizures begin with a widespread electrical discharge that involves the entire brain. On the other hand, partial seizures begin with an electrical discharge in a limited area of the brain. Partial epilepsy can be further classified based on the involved brain lobe during the seizures into temporal, frontal, occipital and parietal lobe epilepsy. The clinical manifestation of the seizures has many forms depending on which brain areas are affected by the seizure. Ictal (during the seizure) and postictal (after the seizure) symptoms are patient and seizure specific. They diverge from auras, tonic-clonic movements to impairment or loss of consciousness. A summary of the ictal and postictal symptoms for temporal, frontal, occipital and parietal lobe epilepsy can be found in [157].

A life threatening condition in which the brain is in a persistent state of seizure activity is called status epilepticus (SE). SE is defined as a seizure that shows no clinical signs of arresting after a duration encompassing the great majority of seizures of that type in most patients [29].

A specific terminology is used to precisely denominate epileptic brain regions. The epileptogenic zone is the area of the cerebral cortex responsible for causing habitual seizures. Surgical removal of this brain area is required and sufficient to render the patient seizure free [132]. The irritative zone is defined as the area of cortical tissue that generates interictal electrographic spikes. The ictal onset zone, also called seizure onset zone (SOZ), is the area of cortex from which clinical seizures are (actually) generated [169].

2.5.4 Epileptiform activity in the EEG

During a seizure there is synchronous rhythmical brain activity. This is usually reflected in the EEG as a periodic waveform with higher amplitude



Figure 2.14: Epileptiform activity in the EEG. The left panel shows a 30 s long EEG epoch during a seizure of a patient with right mesial temporal lobe epilepsy. Rhythmic activity can be noticed especially at the electrodes covering the right hemisphere. The right panel shows an interictal epileptiform discharge noticed in a 5 s long EEG epoch in another patient. The spike-wave complex has phase reversal over F7-T3. Figure adapted from [107]

compared to the interictal periods. An example of seizure activity is shown in the left panel of fig. 2.14. The International Federation of Clinical Neurophysiology (IFCN) defines a seizure pattern in the EEG as a phenomenon consisting of repetitive EEG discharges with relatively abrupt onset and termination and characteristic pattern of evolution lasting at least several seconds. The component waves or complexes vary in form, frequency, and topography. They are generally rhythmic and frequently display increasing amplitude and decreasing frequency during the same episode. When focal in onset, they tend to spread subsequently to other areas. The EEG seizure patterns unaccompanied by clinical epileptic manifestations are called subclinical.

During the interictal period there can also be manifestations of epileptiform activity, namely interictal epileptic discharges (IEDs). They can be divided morphologically into sharp waves, spikes, spike-wave complexes, and polyspike-wave complexes. IEDs can occur in isolation or in brief bursts; bursts longer than a few seconds are likely to represent seizure activity rather than interictal discharges. An example of a spike-wave complex is shown in the right panel of fig. 2.14.

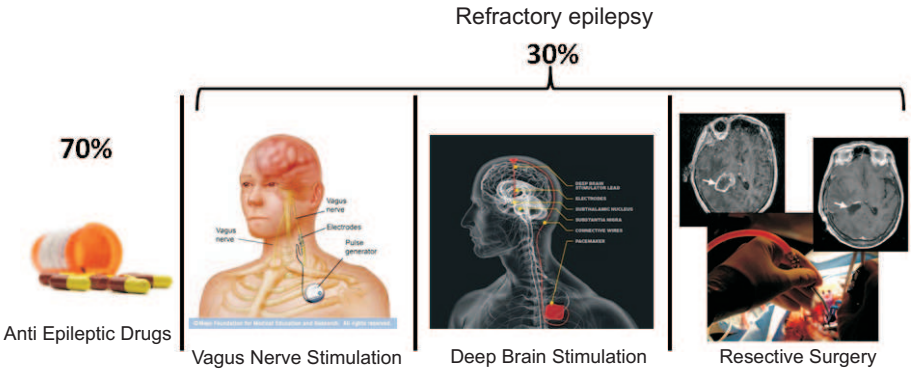


Figure 2.15: Treatment options for epilepsy patients. Approximately 70% can be cured using AEDs, for the remaining 30% epilepsy surgery, deep brain stimulation or vagus nerve stimulation is opted as treatment.

2.5.5 Treatment

The aim of the treatment of epilepsy is to suppress the seizures. Treatment with antiepileptic drugs (AEDs) are successful in 60-70% of epilepsy patients [37]. They go into remission, are seizure free, without unwanted AED related side-effects. In 40-60% of these succesfully treated patients AEDs can be withdrawn after a reasonable time [2].

2.6 Refractory epilepsy

2.6.1 Definition

The group that cannot be adequately treated with AEDs have farmaco-resistant or refractory epilepsy. The seizures are not (completely) suppressed or the patients suffers from adverse drug reactions. The ILAE defines refractory epilepsy as 'failure of adequate trials of two tolerated and appropriately chosen and used AED schedules whether as monotherapy or in combination to achieve sustained seizure freedom' [120]. In newly diagnosed patients, 50% of the patients will become seizure free on their first AED, 10% on their second AED, but no more than 5% on the third or a combination of two AEDs [119, 146, 145].

2.6.2 Treatment

Possible treatments for these refractory epilepsy patients are epilepsy surgery or electric stimulation such as deep brain stimulation or vagus nerve stimulation (fig. 2.15). To assess whether a patient is eligible for epilepsy surgery a battery of tests are performed. This is called the presurgical evaluation.

2.6.2.1 Epilepsy surgery

Pioneers

Trepanation was the surgical method performed during the antiquity and Middle ages on epileptics to create an outlet for pathogenic humors and vapors [233]. The first case of resective surgery other than trepanation aiming to render the patient seizure free is believed to be performed in 1886 by Victor Horsley. The 20-year old patient suffered from Jacksonian seizures, with onset in the left hand. The surgery rendered the patient seizure free. In 1887 Horsley published the results of 9 epilepsy surgery cases. In 1893 Krause was the first to report intraoperative electrical stimulation of the human cerebral cortex to help guide the surgery. He reported over 20 cases of epilepsy surgery in 1912. Foerster and Attenburger were the first to record an intraoperative electrocorticogram (ECoG) in 1934 and resected brain tissue that generated IEDs. Foerster and his pupil Penfield reported to have performed more than 100 surgeries to treat epilepsy. However, they only provided detailed results in 6 patients, which may not necessarily correctly represent the total population.

Penfield and Paine reported the results of cortical excision in the treatment of epileptics combined with the recording of EEG over a six-year period from 1945 through 1950 in 470 patients. They looked for intraoperative spiking activity in the ECoG, and tried to remove brain regions showing spiking activity. They concluded that the seizures were stopped in 41% of the cases, and the outcome was satisfactory in 35%. The case mortality has remained in the vicinity of 1.5% of the 470 patients that have been analysed. In 1994 Rossi et al. reported about 138 cases. The efficacy of epilepsy surgery during the early days (1887) up to now is given in table 2.1.

Surgical procedures

Nowadays ECoG and electrical stimulation mapping are used prior to surgery or intra-operatively. Eloquent tissue is spared as much as possible while trying to remove the complete epileptogenic focus. Eloquent cortex is a

Table 2.1: Efficacies of epilepsy surgery from 1887 until now (adapted from [133]). * Froester mentioned to have performed surgery in more than 100 cases, he only reported 6 cases. This cases do not necessarily reflect the whole population. It is likely that these patients were selected because of the favorable outcome.

Surgeon	year	# patients	complete cure	reduction in seizure freq	death	no changes or lost follow-up
Horsley	1887	9	22%	56%	22%	0%
Krause	1912	21	43%	19%	24%	14%
Foerster*	1930	6	83%	17%	0%	0%
Penfield	1950	470	41%	35%	2%	22%
Modern-day	1994	138	62%	23%	0%	15%

region of cortex that is indispensable for defined cortical functions [169]. The surgical procedures itself can be divided into resective, disconnective and radiosurgery.

In resective surgery the epileptogenic zone is resected. This can be a small focal lesion, a brain lobe or even one complete hemisphere. The most common resections are temporal lobe resections such as selective amygdalo-hippocampectomy, where the amygdala and the hippocampus are resected. Hemispherectomy can be an option in patients with one diseased hemisphere and having contralateral hemiparesis and/or hemianopsia [182]. Similar seizure freedom rates (typically from 60% to 80% [227]) are found for focal, lobar, multilobar resection or hemispherectomy.

In disconnective surgery the spreading from the epileptogenic zone to other brain regions is prevented by multiple subpial transsections or a callosotomy. The procedure of multiple subpial transsections is performed when the epileptogenic zone overlaps with eloquent brain tissue. The method aims at stopping the seizure spread while preserving the brain function of the epileptogenic zone. The seizure freedom rates are around 33% [54]. Corpus callosomoty is a palliative procedure in which the corpus callosum is severed. The communication between both hemispheres is cut. The patient will not be rendered seizure free, but the quality of life is often improved.

Another surgical method is radiosurgery or gamma-knife. Accurate radiation is applied to a volume of interest identified from MR images. The method enables treatment of brain areas that are not easily accessible by conventional brain surgery.

Optimal extent of resection

The optimal extent of the resection is not a clear cut case. Aggressive versus

limited resection is an often debated topic in epilepsy surgery [154]. Several questions can be posed. Can a limited resection lead to the same seizure freedom rates with less neurological complications? Does a wider/more aggressive resection lead to higher seizure freedom rates but yield a higher complication rate? If a smaller resection leads to lower seizure freedom rates, could it still yield a higher quality of life? So far there is evidence that a more limited resection can result in similar seizure freedom rates if we compare selective amygdalohippocampectomy to temporal lobectomy while resulting in higher cognitive outcome [176]. However, there is a void in studies comparing the extent of resection to quality of life outcome. But as imaging and post-processing techniques advance limited resection will become the more attractive option.

2.6.2.2 Electrical stimulation

In patients that are not eligible for epilepsy surgery treatment, electrical stimulation such as deep brain stimulation (DBS) and vagus nerve stimulation (VNS) can be opted as treatment. Unlike resective surgery these treatments are considered reversible.

Deep brain stimulation

In DBS one or more electrodes are placed in a target brain region or several target brain regions (for instance both hippocampi) and are stimulated to suppress seizures. A longitudinal study performed at Ghent University Hospital in 11 patients had the following results [217]. After a mean follow-up of 8.5 years (range: 67-120 months), 6/11 patients had a 90% seizure frequency reduction with 3/6 seizure-free for more than 3 years; three patients had a 40%-70% reduction and two had a $< 30\%$ reduction. In 3/5 patients switching to bilateral DBS further improved outcome. Uni- or bilateral mesial temporal lobe epilepsy DBS did not affect neuropsychological functioning. The precise mechanism of deep brain stimulation is still unknown.

Vagus nerve stimulation

In VNS an electrode is placed around the cranial nerve and stimulated to suppress seizures. It is indicated in patients with refractory epilepsy who are unsuitable candidates for epilepsy surgery or who have insufficient benefit from such a treatment. VNS reduces seizure frequency with $> 50\%$ in 1/3 of patients and has a mild side effects profile [216]. The precise mechanism of action of VNS is still unknown.

2.6.3 Presurgical evaluation

The question whether surgery can improve the quality of life of the patient is answered during the presurgical evaluation [63, 30, 169]. A multidisciplinary team of neurologists, neurosurgeons, radiologists, psychologists and engineers investigates whether surgery is beneficial for the patient. The current state, how many seizures the patient has and how they affect his quality-of-life, should be balanced against the risks of surgery and possible post-operative functional neurological deficits. The risks should be carefully considered with respect to the possible gain before suggesting epilepsy surgery. The presurgical evaluation is a highly demanding exercise in which the results of different neuroimaging techniques are combined in the interest of the patient's health.

2.6.3.1 Multi-modal neuroimaging

During the presurgical evaluation the patient's history, neurophysiological testing, scalp Video/EEG monitoring (SVEM) [152, 43], EEG source imaging (ESI), structural (and functional) Magnetic Resonance Imaging (MRI and fMRI) [39, 51], EEG/fMRI, magnetoencephalography (MEG) [188], interictal Positron Emission Tomography (PET) and ictal Single Photon Emission Tomography (SPECT) [121, 52] are combined to identify the epileptogenic focus and to define overlap between the epileptogenic zone and eloquent cortex. All results are gathered and a decision is taken in the best interest of the patient's health.

The two cornerstone investigations to identify the epileptogenic zone prior to epilepsy surgery are SVEM and structural MRI. The absence of structural anomalies, non-localizing SVEM, or conflicting results between these 2 investigations result into referral of patients to invasive Video-EEG monitoring (IVEM).

2.6.3.2 Scalp Video-EEG Monitoring

For SVEM, the patient is admitted to the hospital for several days. During this period scalp EEG is continuously recorded and the patient stays in a specially equipped room with video monitoring. The investigation of interictal spikes and seizures helps the classification of epilepsy and the localization of the irritative and ictal onset zone respectively. The video is used to identify specific movements and behavior of the patient during the seizures. This seizure semiology has a localizing value, although the

first clinical symptoms do not necessarily arise from the epileptogenic zone [169]. This can be the case if the epileptogenic zone is related to a negative symptom, like paresis or speech difficulty. When the patient is paralyzed during the seizure or has difficulties to talk, it will only be noticed if the patient is asked to perform an appropriate task, like moving a limb or naming an object during the seizure.

2.6.3.3 Structural Magnetic Resonance Imaging

The structural MRI protocol (T1, T2, DWI, ..) is used to reveal anomalies in the brain such as atrophy, focal cortical dysplasia and lesions. The most common observed anomalies in epilepsy are hippocampal sclerosis, developmental cortical dysplasia, cavernous angiomas and low-grade neoplasms [222]. The observation of these anomalies in the brain is not directly indicative for epilepsy. The relation between the lesion and the epileptogenic zone needs to be assessed. Here the semiology and the results from the SVEM can help.

2.6.3.4 Invasive Video-EEG Monitoring

In approximately 15 to 25% of the refractory epilepsy patients included in the presurgical evaluation protocol, IVEM is required to identify the ictal onset zone [41]. The electric field generated by the neurons is measured intracranially. Here electrodes are placed under the skull (in the cranium) to allow a more direct measurement of the brain's potential field and to reveal brain activity that cannot be observed with scalp EEG recordings. The intracranial electroencephalogram (IEEG) or electrocorticogram (ECoG) records electrical activity of various brain regions by means of strip or grid electrodes placed on the cortex and/or depth electrodes inserted deep within the brain's parenchyma (fig. 2.16). The term ECoG is preferred when only grids or strips are placed on the cortex and the brain is not penetrated.

IVEM is an invasive procedure that is accompanied by many risks (such as mortality, cerebrospinal fluid leaks, infections) [193] and should be carefully considered. There needs to by a clear hypothesis that is tested by the IVEM. IVEM either rejects or confirms the hypothesis. In IVEM only a limited number of electrodes can be implanted, making the choice of implanted regions very important. The implantation scheme defines the spatial sampling. The IVEM can show the spread of ictal activity instead of the initial onset if the actual SOZ is not covered by the electrodes.

The pioneer in the field of ECoG is the neurosurgeon Wilder Penfield

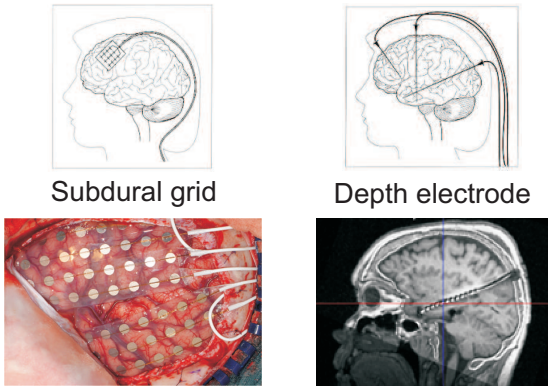


Figure 2.16: Subdural grid and strip electrodes placed on top of the cortex. The depth electrode has many contacts and is placed inside the brain's parenchyma.

from McGill University, Canada. During the late 40's and early 50's he recorded brain activity directly from the cortex in epileptics after the brain was exposed by a craniotomy. The recordings were used to identify epileptic brain tissue. Furthermore, Jasper and Penfield also used the ECoG traces to examine functionality of the human brain. The first published ECoG traces and the used set-up are shown in fig. 2.17. Here the effect of voluntary movement upon the electrical activity of the precentral gyrus was investigated [106].

The IEEG records the local field potentials created by a vast populations of neurons in the close approximation of the electrode. Practically, the spatial sampling of IEEG depends both on the impedance of the electrode and on the volume conduction properties of the brain tissue around it. Distant sources can be measured, but these are usually overshadowed by the local sources. For a nice review about the advantages and limitations of the IEEG we refer the reader to [123].

Nowadays IEEG traces are recorded from up to 100 electrode contacts with a high temporal resolution. The signals have a high signal-to-noise ratio because they are recorded directly from the cortex without attenuation caused by the skull and scalp. This makes IEEG signals very useful to investigate neuronal communication. How the brain regions functionally interact can be investigated using brain connectivity.

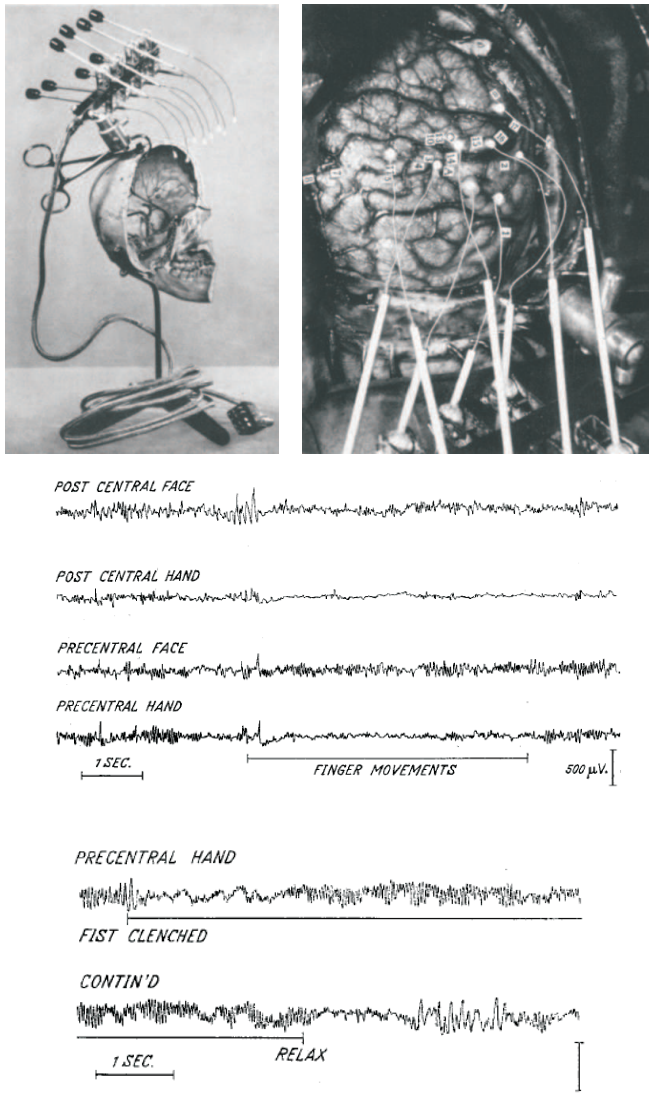


Figure 2.17: First recording of IEEG traces in 1949 by Jasper and Penfield. The effect of voluntary movement upon the electrical activity of the precentral gyrus was studied.

Chapter 3

Brain connectivity

3.1 Introduction

Brain functioning is network based, meaning that several brain regions intercommunicate to execute a specific task. How these intercommunications happen and which brain regions are involved is studied in the research domain of brain connectivity. Brain connectivity can reveal pathways between brain regions or reveal how information is processed, sent to, received by or shared between the different brain regions. In the following we will introduce the different types of brain connectivity and how they can be used in the diagnosis of patients with refractory epilepsy.

There are three types of brain connectivity: structural, functional and effective. Structural connectivity refers to the axonal connections (for instance the white matter tracts) between groups of neurons. Functional and effective connectivity examine the relationship between the neuronal activity of different brain regions at a given moment in time. Functional connectivity is defined as the study of temporal correlations between spatially distinct neurophysiological events [73, 124]. Effective connectivity is defined as the influence one neural system exerts over another [72]. In contrast to functional connectivity, the latter describes the directionality of interactions between brain regions. Meaning that effective connectivity can be seen as directed functional connectivity. The origin of functional and effective connectivity is discussed in [75, 101, 76]. The distinction between structural, functional and effective connectivity is shown in fig. 3.1.

The most commonly used brain signals to investigate functional and effective connectivity are EEG and fMRI time series. Here EEG has the advantage of its superior temporal resolution (in the order of ms) but unfortunately it

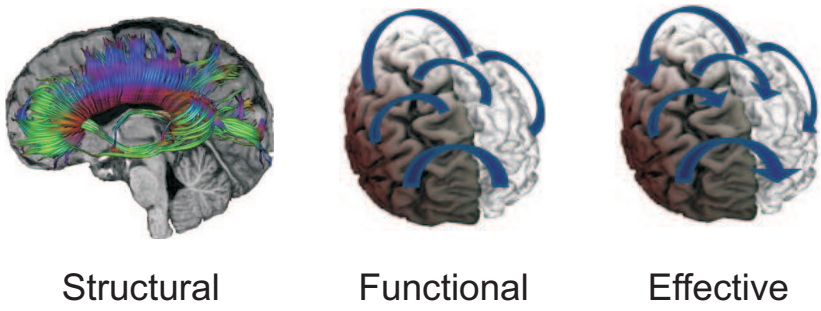


Figure 3.1: The difference between structural, functional and effective brain connectivity. Structural connectivity shows the white matter connections between the gray matter brain regions. Functional and effective connectivity show the connections between the neuronal activity of the brain regions. Effective connectivity shows the directionality of these connections, while functional connectivity does not.

is associated with a low spatial resolution (in the order of cm). The fMRI time series can be obtained with a very high spatial resolution (order of mm) but have a poor temporal resolution (order of s). In the remainder of the book we will focus on functional and effective connectivity obtained from EEG time series.

3.2 Structural connectivity

Structural connectivity shows the anatomical connections between brain regions. These are the fiber pathways between the brain regions. They can be imaged in vivo by assessing the diffusion of water molecules in the brain using diffusion weighted imaging (DWI) [24]. DWI can be applied in several different directions to examine the diffusion in each of these directions. This results in diffusion tensor imaging (DTI). The obtained directional information can be used to image the white matter fiber tracts using tractography as illustrated in fig. 3.2.

Structural brain connectivity is used to study neurological disorders. It visualizes abnormalities in the white matter fiber tracts that can be related to the disease. The structural brain connectivity can also help to preserve important anatomical connections during the surgical resection of a brain area.

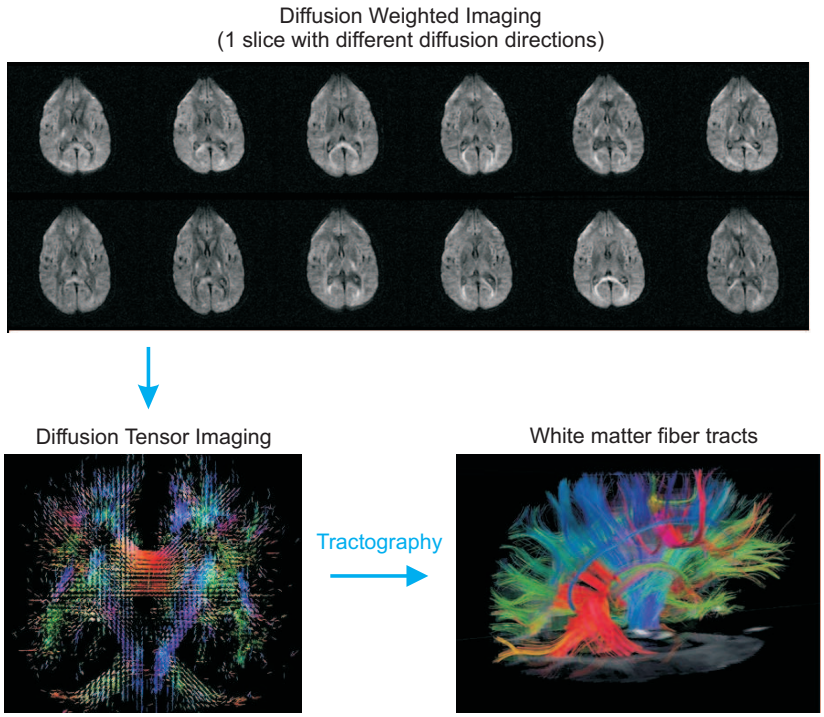


Figure 3.2: Structural brain connectivity investigates the white matter fiber tracts.

3.3 Functional connectivity

Functional brain connectivity investigates the correlations between neurophysiological signals without taken the directionality of the connections into account. The basic signals used to derive the functional connectivity pattern are EEG or fMRI time series that reflect the neuronal activity of different brain regions over time. For two time series $y(n)$ and $x(n)$ we can derive different functional connectivity measures. These measures are symmetric, meaning that the connection from signal x to y is the same as that from signal y to x. The functional connectivity measures can be subdivided into 3 categories based on [171, 162]: linear, nonlinear and information-based measures. In this section we will describe the linear measures in detail and give a more general overview of the nonlinear and information-based measures.

3.3.1 Linear measures

The linear dependency between two signals can be estimated in the time-domain by the correlation coefficient and in the frequency domain by the coherence. The linear dependencies between multiple signals in the frequency domain can be investigated by the partial coherence.

3.3.1.1 Correlation coefficient

The correlation coefficient (ρ_{xy}) is a simple functional connectivity measure to assess the interdependency between two time series (x and y). It examines the linear relation between two signals as follows:

$$\rho_{xy} = \frac{E[(x-\mu_x)(y-\mu_y)]}{\sigma_x \sigma_y} \tag{3.1}$$

$$= \frac{1}{N}\sum_{n=1}^{N} \frac{(x(n)-\mu_x)(y(n)-\mu_y)}{\sigma_x \sigma_y} \tag{3.2}$$

where N is the number of samples, E[x] is the expected value of x, σ_x and σ_y are the standard deviations and μ_x and μ_y are the mean values of signal x and y respectively. The resulting value lies between -1 and $+1$. The closer the absolute value is to 1, the higher the correlation.

3.3.1.2 Cross correlation and Coherence

The cross-correlation estimates the correlation between two signals in function of a time lag τ:

$$\rho_{xy}(\tau) = \frac{1}{N-\tau}\sum_{n=1}^{N-\tau} \frac{(x(n)-\mu_x)(y(n+\tau)-\mu_y)}{\sigma_x \sigma_y} \tag{3.3}$$

The Fourier transform of eq.3.3 leads to the cross spectral density function $S_{xy}(f)$. It is used to estimate the coherence, that shows the interconnections between two signals in the frequency domain:

$$C_{xy}(f) = \frac{|S_{xy}(f)|^2}{|S_{xx}(f)|\,|S_{yy}(f)|} \tag{3.4}$$

The cross spectral density of signal x and y is normalized by the individual autospectral density functions. Because of the normalization the value lies

between 0 and 1. If the value is close to 1 at a frequency f, then the two processes are maximally interdependent at that frequency. On the other hand, a value near 0 indicates independence of the two processes at frequency f.

3.3.1.3 Spectral density function and Partial Coherence

The coherence is a bivariate measure: it investigates only two signals simultaneously. The spectral density function for K signals $x_i(n)$, with $i = 1 \ldots K$, can be derived from all the cross spectral density functions of the pairwise combinations of channels. The spectral density function $S(f)$ is defined as:

$$\mathbf{S}(f) = \begin{bmatrix} S_{11}(f) & S_{12}(f) \cdots S_{1K}(f) \\ S_{21}(f) & S_{22}(f) \cdots S_{2K}(f) \\ \vdots & \vdots \quad \ddots \quad \vdots \\ S_{K1}(f) & S_{K2}(f) \cdots S_{KK}(f) \end{bmatrix} \tag{3.5}$$

The partial coherence was developed to differentiate direct and indirect interrelations: it calculates the coherence remaining between two time series after the influence of all the other time series is removed from each of the first two [109]. It can be constructed out of the spectral density function as follows:

$$PC_{ij}(f) = \frac{|M_{ij}(f)|^2}{|M_{ii}(f)|\,|M_{jj}(f)|} \tag{3.6}$$

where $M_{ij}(f)$ is the minor of the spectral density function $\mathbf{S}(f)$. This is the determinant of $\mathbf{S}(f)$ with i^{th} row and j^{th} column removed.

3.3.2 Nonlinear measures

Nonlinear methods are not designed to outperform linear methods but rather to provide complementary information under certain and rather strict assumptions. Nonlinear neural time series analysis was motivated by the fact that many crucial neural processes have nonlinear characteristics such as the regulation of voltage-gated ion channels which corresponds to a steep nonlinear step-function relating membrane potential to current flow [171].

Nonlinear measures can be used to investigate the phase synchronization between signals. A commonly used method to obtain the strength of phase

synchronization between different areas of the brain is the Phase Locking Value [122].

3.3.3 Information-based measures

Information-based techniques are able to capture both linear and nonlinear statistical dependencies between two time series. The common information between signals is investigated with information theory based tools. The basis of the information theory is the concept of entropy [180], that measures the uncertainty of a random variable. The Shannon entropy of a set of probabilities (p_i, with $i = 1 \dots M$) of signal x is defined as:

$$I_x = -\sum_{i=1}^{M} p_i log(p_i) \tag{3.7}$$

where p_i is the probability that signal x has the value x_i. The probability p_i can be obtained by calculating the histogram of signal x, with M being the number of histogram bins.

The concept of Shannon entropy is used to investigate the statistical dependencies between two signals x and y by means of their mutual information (MI):

$$MI_{XY} = \sum_{i,j} p_{ij} log \frac{p_{ij}}{p_i p_j} \tag{3.8}$$

with p_i and p_j the probabilities corresponding to signal x and y respectively and p_{ij} the joint probabilities of x and y. The probabilities p_i and p_j can be obtained from the individual histograms of the signals and the joint probabilities p_{ij} from the combined histogram of x and y. A drawback is that many samples and small histograms bins are required to obtain a correct estimate [167].

If there is no relation between the two variables x and y, $p_{ij} = p_i p_j$ which is the case for independent processes, then the Mutual information becomes zero. For two identical signals $x = y$, the MI will be equal to the Shannon entropy of the signal $I_x = I_y$.

3.4 Effective connectivity

In previous section we described connectivity measures capable of deriving the functional relations between the signals. These functional connectivity measures are not capable of revealing the direction of the interactions. In the following we will describe effective connectivity measures that are able to reveal the direction of information flow between the considered signals.

The effective connectivity pattern between brain regions can be investigated in various ways. The directional interactions can either be predefined as in model based techniques such as structural equation modeling [190] and dynamic causal modeling [74] or derived from the data (model free) as with Granger causality measures [88, 19, 36].

The concept of Granger causality was developed when Clive Granger adapted the definition of causality proposed by Norbert Weiner [228] into a practical form [89]. He applied it to the field of econometrics to study the relationships between economic indices. One time series is said to Granger cause a second one if inclusion of the past values of the first into the modeling of the second significantly reduces the variance of the modeling error. According to Granger causality, if a signal x_1 Granger-causes (or G-causes) a signal x_2, then past values of x_1 should contain information that helps to predict x_2 above and beyond the information contained in past values of x_2 alone. The Granger causality from signal x_1 to x_2 and the one from signal x_2 to x_1 can be investigated separately. This allows investigation of directional causal relations between multiple signals.

In this section we will focus on data-driven effective connectivity techniques. The data-driven measures can be subdivided like the functional connectivity measures into: linear, nonlinear and information-based measures. In this section we will introduce how to assess Granger causality by means of autoregressive modeling. We will describe the linear measures based on Granger causality in extensive detail and give a more general overview of the nonlinear and information-based measures. This section is mainly based on [171, 162, 116, 16].

3.4.1 Linear effective connectivity measures

3.4.1.1 Autoregressive modeling

Definition

Granger causality can be investigated with autoregressive (AR) models, in

which the signals are represented as a linear combination of their own past plus additional uncorrelated white noise. The Granger causality between signals x_1 and x_2 can be assessed by comparing the univariate AR model fitting with the bivariate model fitting. For signal x the univariate AR model is described as follows:

$$x(n) = \sum_{m=1}^{p} a(m)x(n-m) + e(n) \tag{3.9}$$

where p is the model order, $a(m)$ are the model coefficients and $e(n)$ is the residual.

For two signals (x_1 and x_2) we can construct following bivariate autoregressive model:

$$x_1(n) = \sum_{m=1}^{p} a_{11}(m)x_1(n-m) + \sum_{m=1}^{p} a_{12}(m)x_2(n-m) + e_1(n) \tag{3.10}$$

$$x_2(n) = \sum_{m=1}^{p} a_{21}(m)x_1(n-m) + \sum_{m=1}^{p} a_{22}(m)x_2(n-m) + e_2(n) \tag{3.11}$$

with a_{11}, a_{12}, a_{21} and a_{22} the model coefficients and e_1 and e_2 are the residuals of signals x_1 and x_2 respectively.

This can be rewritten in matrix formulation:

$$\begin{bmatrix} x_1(n) \\ x_2(n) \end{bmatrix} = \sum_{m=1}^{p} \begin{bmatrix} a_{11}(m)\, a_{12}(m) \\ a_{21}(m)\, a_{22}(m) \end{bmatrix} \begin{bmatrix} x_1(n-m) \\ x_2(n-m) \end{bmatrix} + \begin{bmatrix} e_1(n) \\ e_2(n) \end{bmatrix} \tag{3.12}$$

We can generalize eq.3.12 for K simultaneously recorded signals. This is called a multivariate autoregressive (MVAR) model, where the K signals are modeled as a linear combination of their own past plus additional uncorrelated white noise:

$$\mathbf{X}(n) = \sum_{m=1}^{p} \mathbf{A}(m)\mathbf{X}(n-m) + \mathbf{E}(n) \tag{3.13}$$

where $\mathbf{X}(n) = [\mathbf{x}_1(n)\ \mathbf{x}_2(n)\ \ldots\ \mathbf{x}_K(n)]^T$ is the signal matrix at time n, $\mathbf{E}(n) = [\mathbf{e}_1(n)\ \mathbf{e}_2(n)\ \ldots\ \mathbf{e}_K(n)]^T$ is the matrix containing the uncorrelated

white noise at time n, p is the model order and $\mathbf{A}(m)$ is the $K \times K$ coefficient matrix for delay m. The model order defines the number of past time points that are included to estimate the current sample. Element $\mathbf{A}_{ij}(m)$ estimates the influence of the sample $\mathbf{x}_j(n-m)$ on the current sample $\mathbf{x}_i(n)$. All coefficient matrices together provide knowledge about the directed information flow between all signals.

Estimation of the model parameters

The model order defines the time window used to estimate the current samples based on a linear combination of the past samples. It can be estimated using a criterion like the Akaike Information Criterion [3] or the Schwarz's bayesian Criterion [178]. Both criteria are based on the covariance of the residuals and an additional term penalizing overfitting.

The Akaike Information Criterion for MVAR model can be calculated as follows:

$$AIC(p) = ln\,|\mathbf{\Sigma_e}(p)| + \frac{2pK^2}{N} \tag{3.14}$$

and the Schwarz's Bayesian Criterion as follows:

$$SBC(p) = ln\,|\mathbf{\Sigma_e}(p)| + \frac{ln(N)pK^2}{N} \tag{3.15}$$

with $\mathbf{\Sigma_e}(p)$ the covariance matrix of the residuals, N the number of time points, p the model order and K the number of considered signals. Both above criteria need to be minimized, meaning that the model order corresponding with the minimum of the AIC function or the SBC function is chosen for further analysis.

Once the model order is selected based on one of the above criteria or empirically set to a certain value, the coefficients can be estimated with the ordinary least squares procedure or the method of moments (out of the Yule-Walker equations [158]).

Transformation to the frequency domain

The Fourier transformation of Eq.3.13 results in the relations between the signals in the spectral domain:

$$\mathbf{E}(f) = \mathbf{A}(f)\mathbf{X}(f) \tag{3.16}$$

where

$$\mathbf{A}(f) = -\sum_{m=0}^{p} \mathbf{A}(m)\, e^{-i\,2\,\pi\,\frac{f}{f_s}\,m} \tag{3.17}$$

with f_s the sampling frequency and $\mathbf{A}(0) = -\mathbf{I}$ ($\mathbf{I}$ the $K \times K$ identity matrix). $\mathbf{E}(f)$, $\mathbf{X}(f)$ and $\mathbf{A}(f)$ are the Fourier transform of the white noise, the multivariate dataset and the coefficient matrices, respectively. This equation can be rewritten as:

$$\mathbf{X}(f) = \mathbf{A}^{-1}(f)\,\mathbf{E}(f) = \mathbf{H}(f)\,\mathbf{E}(f), \tag{3.18}$$

where $\mathbf{H}(f)$ is defined as the transfer matrix of the MVAR model. $\mathbf{H}(f)$ is a $K \times K$ matrix, in which element $\mathbf{H}_{ij}(f)$ estimates the information flow from signal $\mathbf{x}_j$ to $\mathbf{x}_i$ at frequency f.

The power spectral density matrix, $\mathbf{S}(f)$, can be calculated out of the coefficients and residuals of the MVAR model as follows:

$$\begin{aligned}
\mathbf{S}(f) &= \mathbf{X}(f)\,\mathbf{X}^*(f) \\
&= \mathbf{H}(f)\,\mathbf{E}(f)\,\mathbf{E}^*(f)\,\mathbf{H}^*(f) \\
&= \mathbf{H}(f)\,\mathbf{\Sigma_e}\,\mathbf{H}^*(f) \\
&= \mathbf{H}(f)\,\sigma_e\mathbf{I}\,\mathbf{H}^*(f) \\
&= \sigma_e\mathbf{H}(f)\,\mathbf{H}^*(f),
\end{aligned} \tag{3.19}$$

where * denotes the conjugate transpose and $\mathbf{\Sigma_e}$ is the noise covariance matrix. Since we assume the error time series are uncorrelated white noise, the covariance matrix $\mathbf{\Sigma_e}$ will be a diagonal matrix approximated by $\sigma\mathbf{I}$. This allows to estimate the autospectrum of signal $\mathbf{x}_i$ as:

$$\hat{\mathbf{S}}_{ii}(f) = \sigma_e \sum_{k=1}^{K} \mathbf{H}_{ik}(f)\mathbf{H}^*_{ki}(f) = \sigma \sum_{k=1}^{K} |\mathbf{H}_{ik}(f)|^2 \tag{3.20}$$

Out of the parameters of the AR models we can derive several linear effective connectivity measures. In the time domain we can investigate the Granger causality between two signals by estimating the G-causality index. Saito and Harashima [170], and Geweke [79] translated the time domain approach of bivariate Granger causality to the frequency domain. Geweke extended this 2 years later to the multivariate case [80]. This allows investigating the causal relations in the different frequency bands between

multiple signals. The Granger causality is studied in the frequency domain by calculating the Directed Coherence, the Directed Transfer Function or the Partial Directed Coherence.

3.4.1.2 G-causality index

The bivariate Granger causality from y to x can be derived out of the univariate AR models and the bivariate model of x and y. It is defined as:

$$G_{xy} = ln\left(\frac{V_{x|x}}{V_{x|xy}}\right) \tag{3.21}$$

where $V_{x|x}$ is the variance of the residual in the univariate case and $V_{x|xy}$ is the variance of the residual in the bivariate model. If the past values of y do not improve the prediction of x, then $V_{x|x} \approx V_{x|xy}$ and $G_{xy} \approx 0$. A better prediction will decrease $V_{x|xy}$ and result in a value of G_{xy} bigger than 0. The Granger causality from x to y can be investigated accordingly.

3.4.1.3 Directed Coherence

Because the coherence and the partial coherence are not able to reveal the direction of the information flow, the Directed Coherence (DC) was constructed by Saito and Harashima in 1981. The basic consideration of the directed coherence is that the direction can be determined according to the temporal relations of time series, because a time delay must exist in information transmission [219]. The Directed Coherence reveals the direction of information flow from one channel y to another x:

$$\mathbf{DC}_{xy}(f) = \frac{\sigma_{xy}\mathbf{H}_{xy}(f)}{\sqrt{\sigma_{xx}^2\left|\mathbf{H}_{xx}\right|^2 + \sigma_{yy}^2\left|\mathbf{H}_{yy}\right|^2}} \tag{3.22}$$

It is based on the residuals and transfer matrix of a bivariate autoregressive model. The measure is bivariate, which requires that all pairwise combinations of recorded signals need to be investigated separately. This can be circumvented when we use MVAR modeling to investigate the Granger causality between the signals. In 1998 the Directed Coherence was extended

to the multivariate case by Baccala and Sameshima [15]:

$$\mathbf{DC}_{ij}(f) = \frac{\sigma_{ij}\mathbf{H}_{ij}(f)}{\sqrt{\sum_{j=1}^{K} \sigma_{jj}^2 \left|\mathbf{H}_{ij}\right|^2}} \tag{3.23}$$

which is based on the residuals and transfer matrix of a multivariate autoregressive model. For the number of signals K equal to 2 it is equal to eq.3.22.

3.4.1.4 Directed Transfer Function

The Directed Transfer Function (DTF) was defined by Kaminski and Blinowska in 1991 to differentiate indirect and direct information flows between multiple signals [116] as follows:

$$\mathbf{DTF}_{ij}(f) = \frac{\left|\mathbf{H}_{ij}(f)\right|^2}{\sum_{k=1}^{K} \left|\mathbf{H}_{ik}(f)\right|^2} \tag{3.24}$$

with corresponding normalization condition:

$$\sum_{k=1}^{K} \mathbf{DTF}_{ik}(f) = 1 \tag{3.25}$$

this indicates that the total incoming information flow into each channel is equal to 1 at each frequency. The construction of the DTF does solely include the transfer function $\mathbf{H}(f)$ and not the noise matrix $\mathbf{\Sigma}$. Therefore possible correlation of input noises among themselves, manifested in presence of non-diagonal elements in $\mathbf{\Sigma}$, should not influence the DTF.

3.4.1.5 Partial Directed Coherence

In 2001, Baccala and Sameshima constructed the Partial Directed Coherence, a multivariate directional connectivity measure that only shows the

direct interrelations between the signals [14]:

$$\mathbf{PDC}_{ij}(f) = \frac{|\mathbf{A}_{ij}(f)|^2}{\sum_{k=1}^{K} |\mathbf{A}_{kj}(f)|^2} \tag{3.26}$$

The construction of the PDC is based on the Fourier transform of the coefficients and does not require the inverse of it to calculate the transfer matrix. It has following normalization condition:

$$\sum_{k=1}^{K} \mathbf{PDC}_{kj}(f) = 1 \tag{3.27}$$

which indicates that the total outgoing flow from each channel equals 1 at each frequency.

3.4.2 Nonlinear effective connectivity measures

Nonlinear Granger causality can be assessed by using the kernel trick [181]. Kernel algorithms work by projecting data into a Hilbert space, and searching for linear relations in that space [211]. Marinazzo et al. [135] generalized Granger causality to the nonlinear case using the theory of reproducing kernel Hilbert spaces. The method investigates linear Granger causality in the feature space of suitable kernel functions, assuming an arbitrary degree of nonlinearity. For more information about nonlinear Kernel Granger causality we refer the reader to [134].

Another nonlinear effective connectivity measure is the nonlinear correlation coefficient h^2_{xy} [129, 163] coupled with the direction index D [223]. The nonlinear coefficient h^2_{xy} is defined as the maximum of following equation with respect to τ_{xy}:

$$h^2_{xy}(\tau_{xy}) = \frac{\sum_{k=1}^{N} y(k+\tau_{xy})^2 - \sum_{k=1}^{N} (y(k+\tau_{xy}) - f(x(k)))^2}{\sum_{k=1}^{N} y(k+\tau_{xy})^2} \tag{3.28}$$

where f is a nonlinear fitting curve which approximates the statistical rela-

tionship between signal x and y. In practice, this function can be obtained from the piece-wise linear approximation between the samples of the two time series.

The direction index is calculated out of the nonlinear correlation coefficients h^2_{xy} and h^2_{yx} and the corresponding time delay τ_{xy} and τ_{yx} respectively:

$$D = 1/2\left(\text{sgn}(\Delta h^2) + \text{sgn}(\Delta\tau)\right) \tag{3.29}$$

with $\Delta h^2 = h^2_{xy} - h^2_{yx}$ and $\Delta\tau = \tau_{yx} - \tau_{xy}$. D = +1 (respectively -1) denotes that y (respectively x) is dependent on and delayed with respect to x (respectively y). Conversely, D = 0 denotes either (i) a situation where there is a constant discrepancy between the information provided by the asymmetry (Δh^2) and by the time delay ($\Delta\tau$) or (ii) a situation where the sign of Δh^2 and the sign of $\Delta\tau$ continuously fluctuates over the considered time window [226].

3.4.3 Information theory based effective connectivity measures

The Shannon entropy was extended by taking the probability of obtaining a value at time n if the previous k values are incorporated. This defines the entropy rate of a signal x as:

$$h_x(k) = -\sum_{i=1}^{M} p(i_n, i_{n-1}, \dots, i_{n-k}) log\left(p(i_n|i_{n-1}, \dots, i_{n-k})\right) \tag{3.30}$$

where $p(i_n|i_{n-1}, \dots, i_{n-k})$ is the probability of obtaining value i_n of signals x given that the k previous values were equal to $i_{n-1}, \dots, i_{n-k}$.

The transfer entropy [177] from signal x to y is derived based on the entropy rate as follows:

$$T_{xy}(k,l) = \sum_{i,j} p(i_n, i_{n-1}, \dots, i_{n-k}, j_{n-1}, \dots, j_{n-l}) log \frac{p(i_n|i_{n-1}, \dots, i_{n-k}, j_{n-1}, \dots, j_{n-l})}{p(i_n|i_{n-1}, \dots, i_{n-k})} \tag{3.31}$$

The transfer entropy is an asymmetric measure, $T_{xy}(k,l)$ differs from $T_{yx}(k,l)$. If the l previous samples of signal y do not influence the estimation of the current sample of x, $p(i_n|i_{n-1}, \dots, i_{n-k}, j_{n-1}, \dots, j_{n-l}) \approx p(i_n|i_{n-1}, \dots, i_{n-k})$ and the transfer entropy from y to x will be close to zero.

3.5 Properties of the different connectivity measures

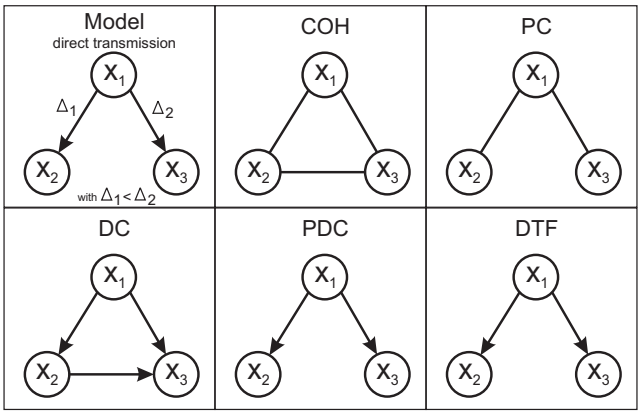
The connectivity measures can show the directionality of the connections (effective connectivity) or not (functional connectivity). They can either be bivariate or multivariate. Bivariate means that only 2 signals are considered at the same time. This means that all pairwise combinations of signals need to be investigated separately. Multivariate means that all signals are modeled within one single system, meaning that the influence between all signals is investigated simultaneously. The connections can be assessed in the time domain or in the frequency domain. The connectivity measures can either be linear, nonlinear or information theory based. The properties of the different considered connectivity measures are shown in table 3.1.

In this dissertation we will investigate the connections between IEEG signals during seizures. Because seizures are represented as periodic waveforms in the IEEG it is advantageous to look at connections in the frequency domain. In this thesis we will focus on linear connectivity measures that reveal connections in the frequency domain. These include the COH, PC, DC, PDC and the DTF. The theoretical behavior of these measures is illustrated in 2 different examples in fig. 3.3. A direct and an indirect transmission model are considered. We depicted the expected resulting graphs for the different measures based on their properties. The COH and PC are functional connectivity measures that do not reveal the directionality of the interactions. The effective connectivity measures DC, PDC and DTF reveal the direction of interaction between the channels. The COH and DC are both bivariate measures, meaning that they only consider 2 signal simultaneously. The PDC and DTF are both multivariate effective connectivity measures. The PDC only reveals the direct connections, while the DTF reveals both direct and indirect connections. This can be seen in the bottom panel of fig. 3.3 where the PDC reveals the direct connections from x_1 to x_2 and from x_2 to x_3 and the DTF shows the connections from x_1 to x_2 and x_3.

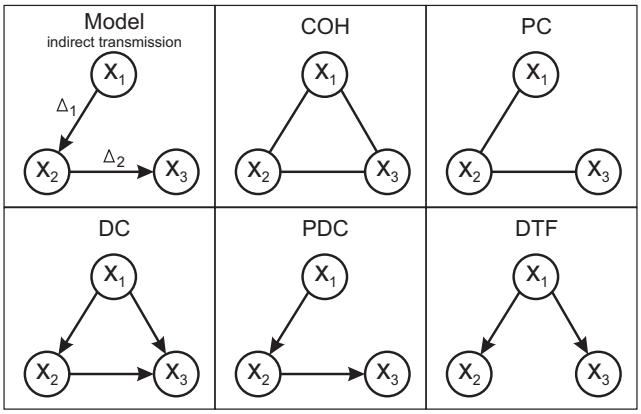
Table 3.1: The properties of the different connectivity measures

	func	eff	bi	multi	lin	nonlin	inf th	time	freq
Correlation coefficient	x		x		x			x	
Coherence (COH)	x		x		x				x
Partial Coherence (PC)	x			x	x				x
Phase Locking Value	x		x			x			x
Mutual Information	x		x				x	x	
G-causality index		x	x		x			x	
Directed Coherence (DC)		x	x		x				x
Directed Transfer Function (DTF)		x		x	x				x
Partial Directed Coherence (PDC)		x		x	x				x
KGC index		x		x		x		x	
Transfer Entropy		x	x				x	x	

Abbrevations: funct = functional, eff = effective, bi = bivariate, multi = multivariate, lin = linear, nonlin = nonlinear, inf th = information theory, freq = frequency



(a) Direct transmission



(b) Indirect transmission

Figure 3.3: The properties of the coherence (COH), partial coherence (PC), directed coherence (DC), directed transfer function (DTF) and partial directed coherence (PDC) shown in 2 graph examples. The upper graph shows how direct transmission between the signals (with delay Δ_1 and Δ_2) is revealed by the different connectivity measures. The bottom panel shows a graph example of indirect transmission between the signals and the resulting connectivity measures.

3.6 Simulations

In the previous section we showed the theoretical resulting graphs for a direct transmission and indirect transmission model. In this section we will use simulations to further investigate the properties of the different

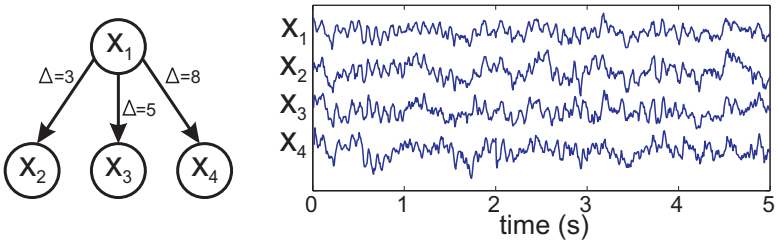


Figure 3.4: Simulated model of direct transmission during a seizure.

connectivity measures and to see which one is best suited to localize the seizure onset zone (SOZ) from ictal IEEG recordings. We will consider a simulation setup of a direct transmission, indirect transmission, a simulation setup in which a hidden source drives all channels and a simulation setup in which one signal is unconnected while having similar spectral properties compared to the other signals.

3.6.1 Direct transmission

To illustrate the properties of the considered measures we will simulate an ictal IEEG epoch with known underlying connectivity pattern. The simulated connectivity pattern is shown in fig. 3.4 in which signal x_1 is represented as $1/f$-noise plus a seizure component. The seizure activity is modeled as a sinusoid with decreasing frequency content from 12 Hz to 8 Hz. The signal x_1 is 5 s long with a sampling frequency of 512 Hz. Signal x_2, x_3 and x_4 are constructed by delaying signal x_1 with 3, 5 and 8 samples respectively plus adding $1/f$-noise. This results in a model with direct transmission from signal x_1 to the other signals. The resulting signals are shown in the right panel of fig. 3.4.

The signals are first resampled from 512 to 128 Hz and afterwards the COH, PC, DC, PDC and DTF are calculated. The results of the functional connectivity measure COH and PC are shown in fig. 3.5. On the diagonal the PSD of the different signals is plotted and the connectivity measures are shown in the off diagonal boxes. The PSD shows that there is a peak in power at the simulated seizure frequency (from 8 Hz to 12 Hz). Functional connectivity measures are symmetric, meaning that the connection from x_i to x_j is equal to the one from x_j to x_i. We find high COH values between all pairs of signals, with highest values at the seizure frequencies. The PC values for the connections involving signal x_1 are higher than the others. The

effective connectivity measures, DC, DTF and PDC, are calculated with a MVAR model of order 10. The results are shown in fig. 3.6. All three measures show the correct connections at the seizure frequency. The DC also reveals connections from x_2 to x_3 and x_4 and from x_3 to x_4. The DTF and PDC correctly show the connections from x_1 to the others. The values of the PDC are lower due to the normalization. The PDC is normalized in a way that the outgoing flow of each channel is 1. The DTF on the other hand is normalized with respect to the incoming flow resulting in high connectivity peaks around 10 Hz from x_1 to the other channels.

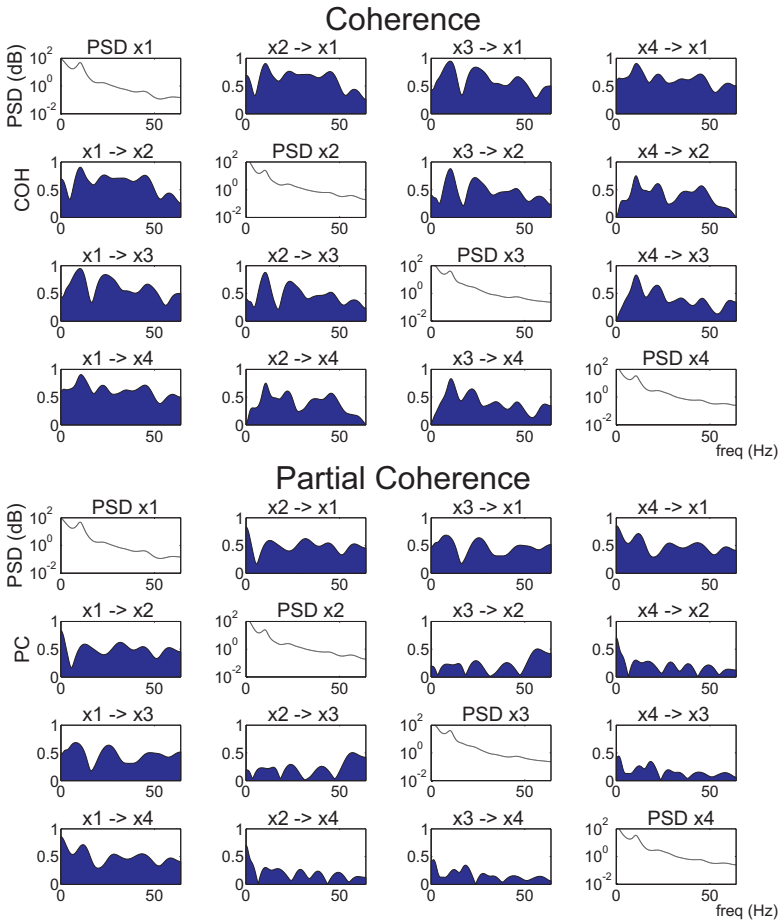


Figure 3.5: Estimated functional connectivity pattern of the direct transmission model using the coherence and the partial coherence.

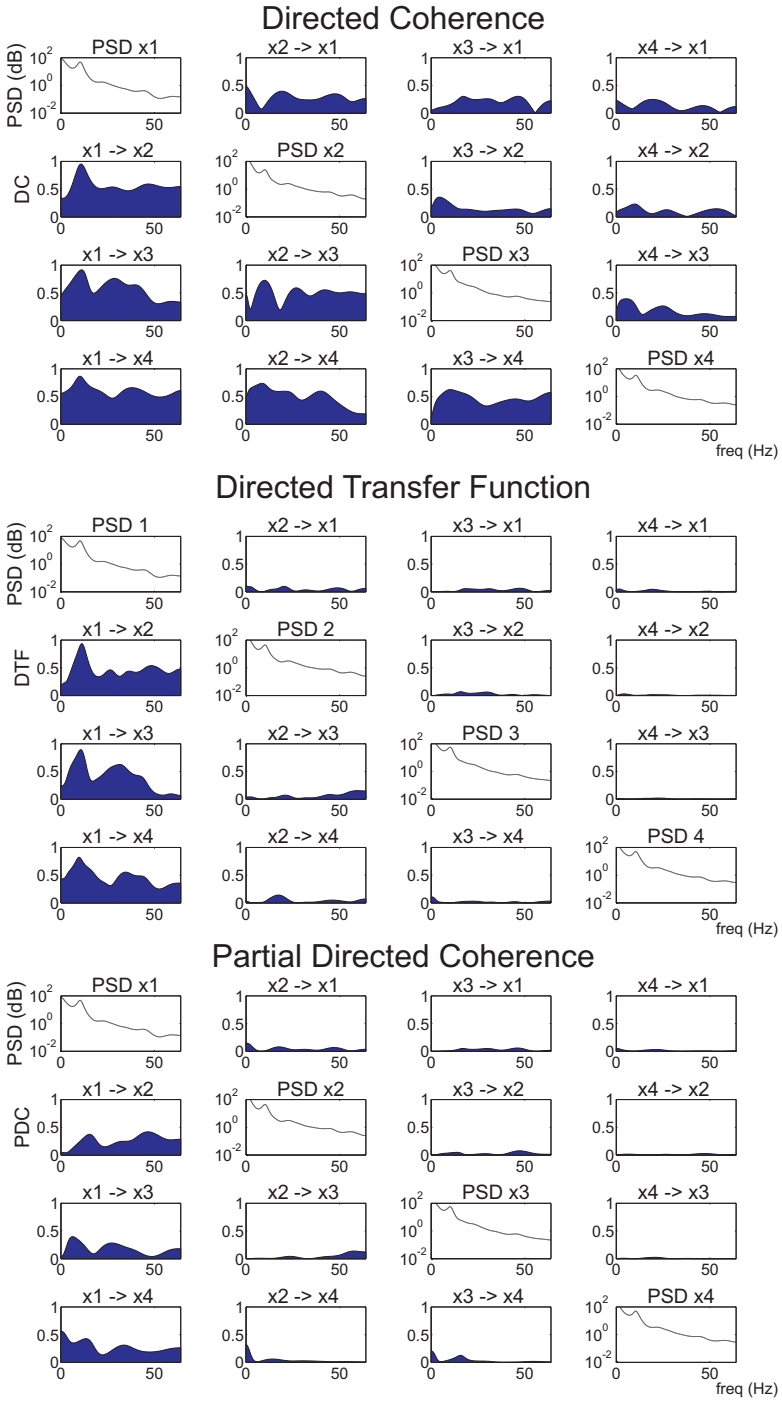


Figure 3.6: Estimated effective connectivity pattern of the direct transmission model using the directed coherence, directed transfer function and the partial directed coherence.

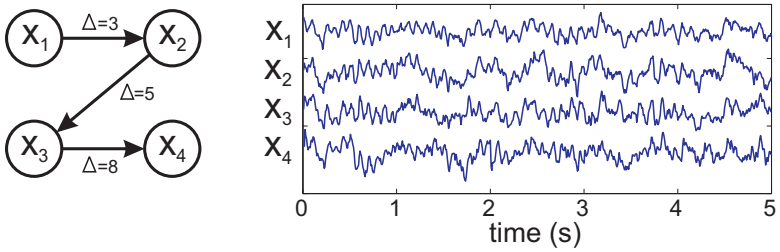


Figure 3.7: Simulated model of indirect transmission during a seizure.

3.6.2 Indirect transmission

In previous section we simulated direct transmission of information between the signals. In this section we will simulate a model representing indirect transmission of information. Signal x_1 is constructed in the same way as before. It exist of 1/f-noise plus a sinusoidal seizure component with decreasing frequency content. Signal x_2 is a delayed version of x_1 plus additional 1/f-noise. Signal x_3 is constructed out of x_2 and x_4 out of x_3. The indirect transmission simulation setup and the resulting signals are shown in fig. 3.7.

The connectivity measures were calculated from the simulated signals. The results for the functional measures are shown in fig. 3.8. The COH again has high values for all pair of signals especially around 10 Hz. The PC reveals high connections between x_1 and x_2, x_2 and x_3 and x_3 and x_4. The effective connectivity measures are shown in fig. 3.9. The DC shows high connectivity from x_1 to all other signals, x_2 to x_3 and x_4 and from x_3 to x_4. All connections have a peak around the seizure frequency. The DTF shows that the information around the seizure frequency peak originates from signal x_1. High connectivity is seen at that frequency from x_1 to all other channels. High values for the DTF are also seen at higher frequencies from x_2 to x_3 and x_4 and from x_3 to x_4. The PDC only shows the direct connections. From x_1 to x_2 a high information flow is observed around 10 Hz. This peak is not found in the other connections.

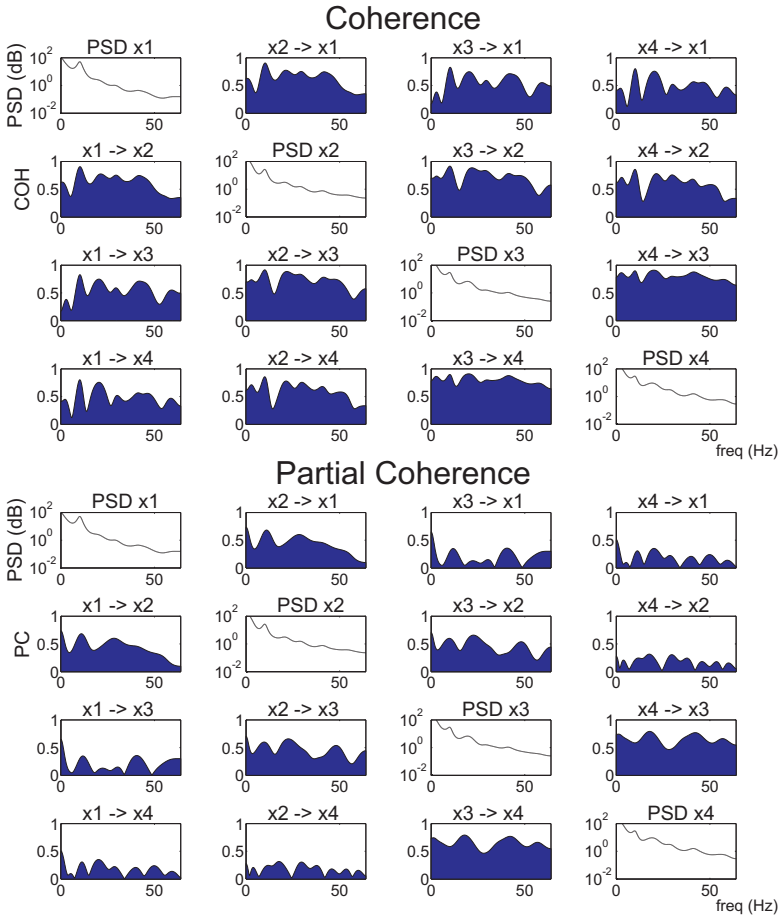


Figure 3.8: Estimated functional connectivity pattern of the indirect transmission model using the coherence and the partial coherence.

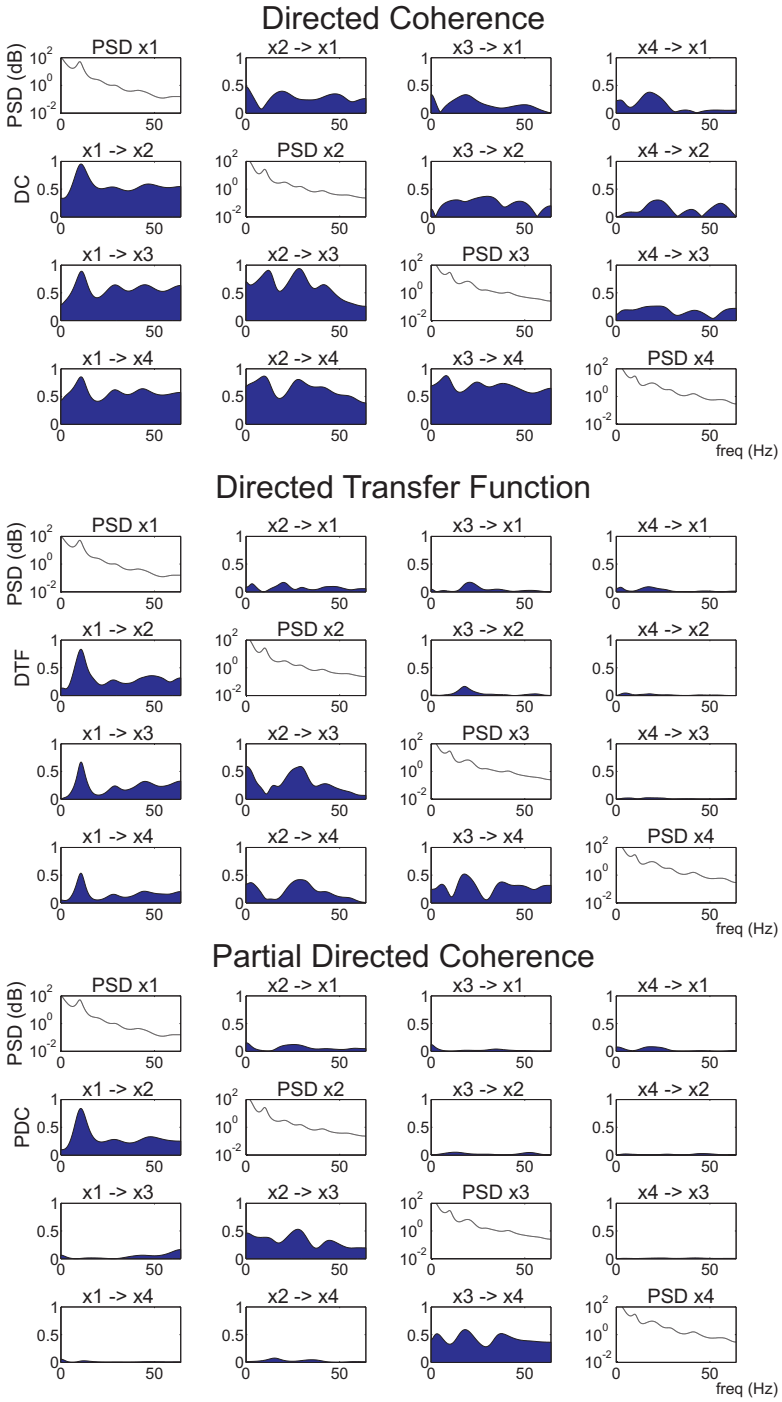


Figure 3.9: Estimated effective connectivity pattern of the indirect transmission model using the directed coherence, directed transfer function and the partial directed coherence.

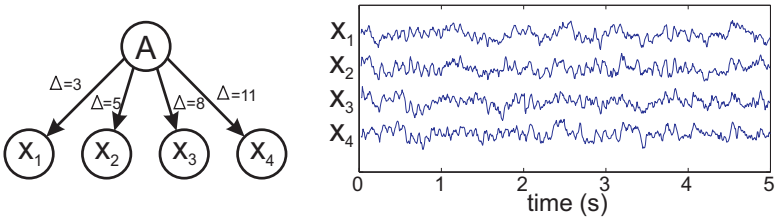


Figure 3.10: Simulated model when the 4 recorded signals are driven by a hidden source. Here A is the hidden source and x_1, x_2, x_3 and x_4 are the recorded signals.

3.6.3 Hidden source

In this simulation setup a hidden source drives the measured signals as illustrated in fig. 3.10. The signal of hidden source A is constructed as 1/f-noise plus a seizure component. The seizure activity is modeled as a sinusoid with decreasing frequency content from 12 Hz to 8 Hz. The signal of source A is 5 s long with a sampling frequency of 512 Hz. Signal x_1, x_2, x_3 and x_4 are constructed by delaying signal of source A with 3, 5, 8 and 11 samples respectively plus additional 1/f-noise. The resulting signals are shown in fig. 3.10.

The signals are resampled from 512 Hz to 128 Hz and the COH, PC, DC, DTF and PDC are calculated afterwards. In fig. 3.11 the functional connectivity measures, the COH and PC, are displayed. We notice high coherence values between all signals especially around 10 Hz. The PC has similar shape for all connections and does not provide much useful information. In fig. 3.12 the effective connectivity measures (the DC, the DTF and the PDC) are shown. There is time delay between the considered signals because the signal of source A is delayed with different number of samples to construct x_1, x_2, x_3 and x_4. The DC reveals directed connections from x_1 to all signals, from x_2 to x_3 and x_4 and from x_3 to x_4. The DTF shows the origin of information flow, resulting in connections from x_1 to the other signals. With the PDC the same connection as with the DTF are found, although the amplitude is smaller due to the normalization.

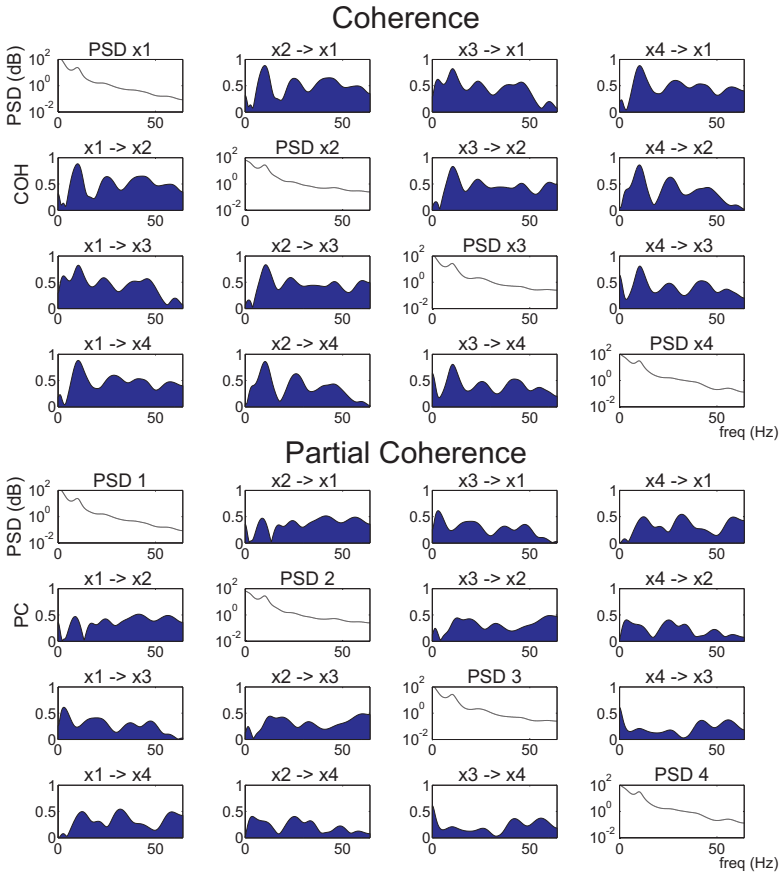


Figure 3.11: Estimated functional connectivity pattern of the hidden source model using the coherence and the partial coherence.

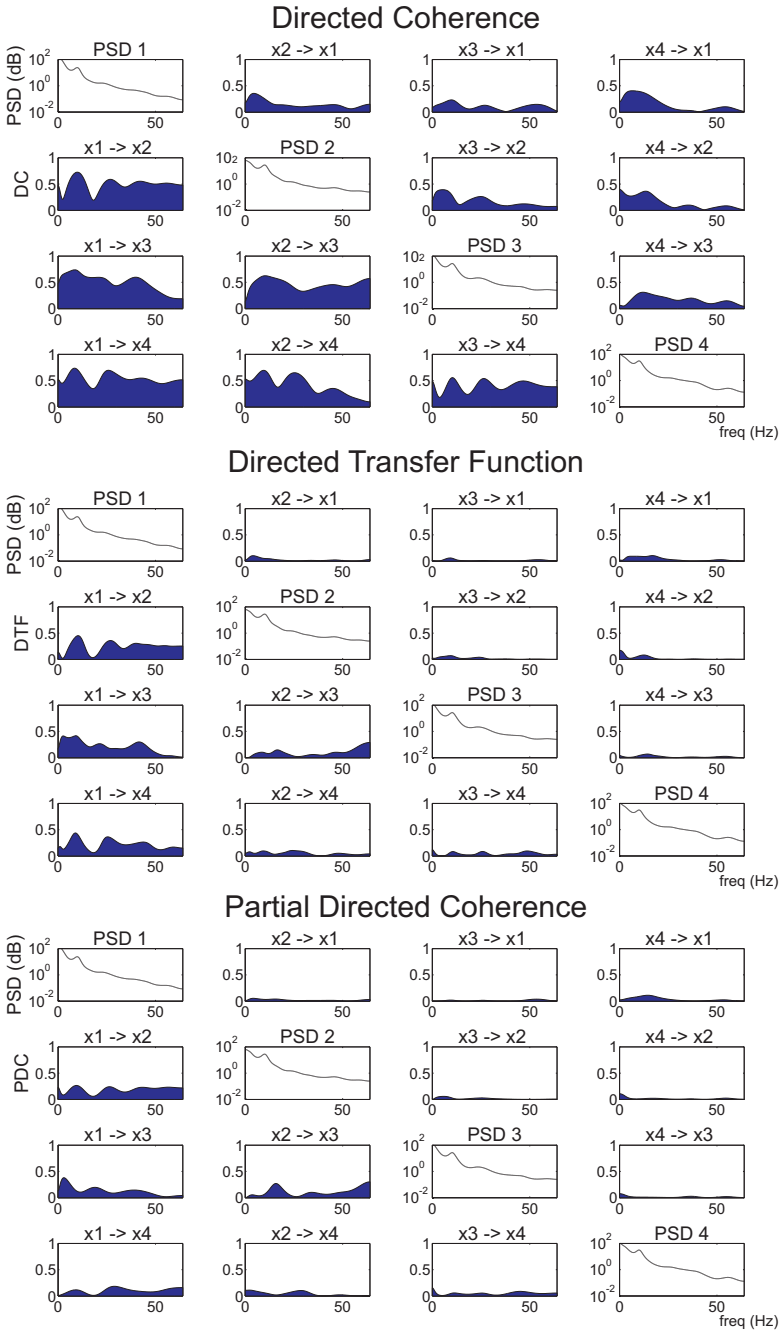


Figure 3.12: Estimated effective connectivity pattern of the hidden source model using the directed coherence, directed transfer function and the partial directed coherence.

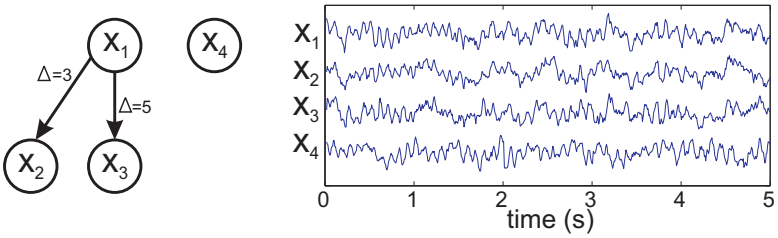


Figure 3.13: Simulated model where x_4 is unconnected and has similar spectral properties as the other signals. Signal x_1 drives signals x_2 and x_3.

3.6.4 Unconnected signal

As last simulation we consider a network of 3 signals and 1 unconnected signal with similar spectral properties. Signals x_1 is constructed as 1/f-noise plus a sinusoid ranging from 12 Hz to 8 Hz. Signal x_1 is delayed by 3 and 5 samples and additional 1/f-noise is added to construct signals x_2 and x_3, respectively. Signal x_4 is constructed as 1/f-noise plus a sinusoid ranging from 12 Hz to 7.5 Hz. The simulation scheme and the resulting signals are shown in fig. 3.13. All signals are 5 s long and have a sampling frequency equal to 512 Hz.

The signals are resampled from 512 Hz to 128 Hz and afterwards the different connectivity measures are calculated with the same parameters as in previous three simulations. The COH en PC are depicted in fig. 3.14. High values of coherence are found between all channels, even between x_1, x_2, x_3 and the unconnected channel x_4. Although stronger connections are observed between x_1, x_2 and x_3 than between x_4 and the other signals. The PC shows strong connections between x_1 and, x_2 and x_3. The effective connectivity measure are displayed in fig. 3.15. The DC nicely shows the connection from x_1 to x_2 and x_3, and from x_2 to x_3. The DTF shows the connections from x_1 to x_2 and x_3. The DTF values for the other connections are small compared to the corresponding DC values. The PDC shows the same connections as the DTF, but due to the normalization the peak at the connection from x_1 to x_2 and for connection x_2 to x_3 is not at the same frequency. While the DTF shows peaks for both connections at the same frequency, around 10 Hz.

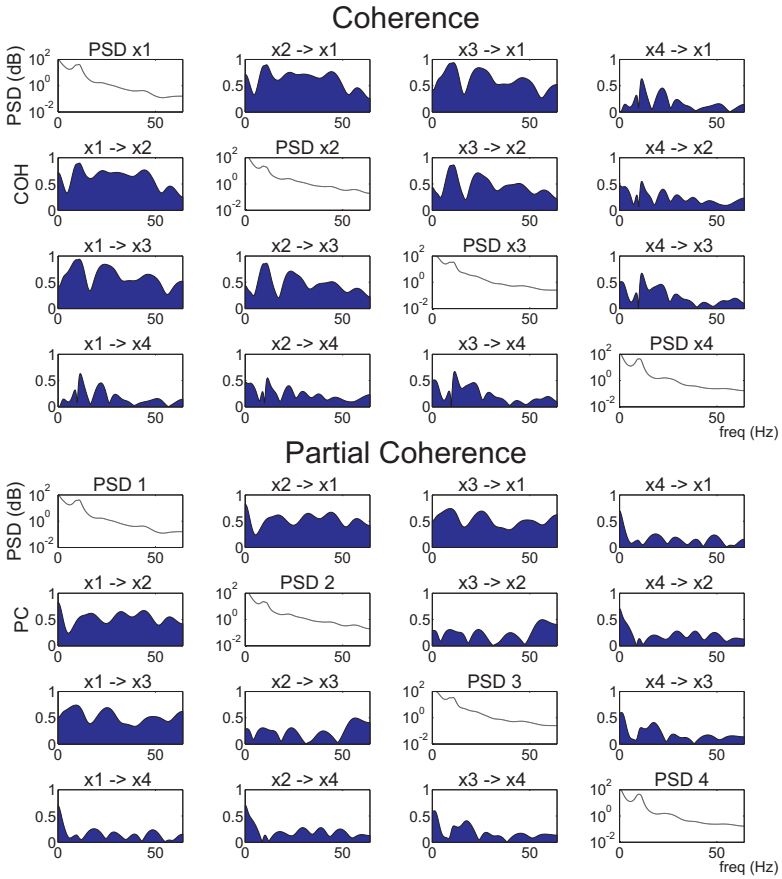


Figure 3.14: Estimated functional connectivity pattern of the simulated model with x_4 as unconnected signals using the coherence and the partial coherence.

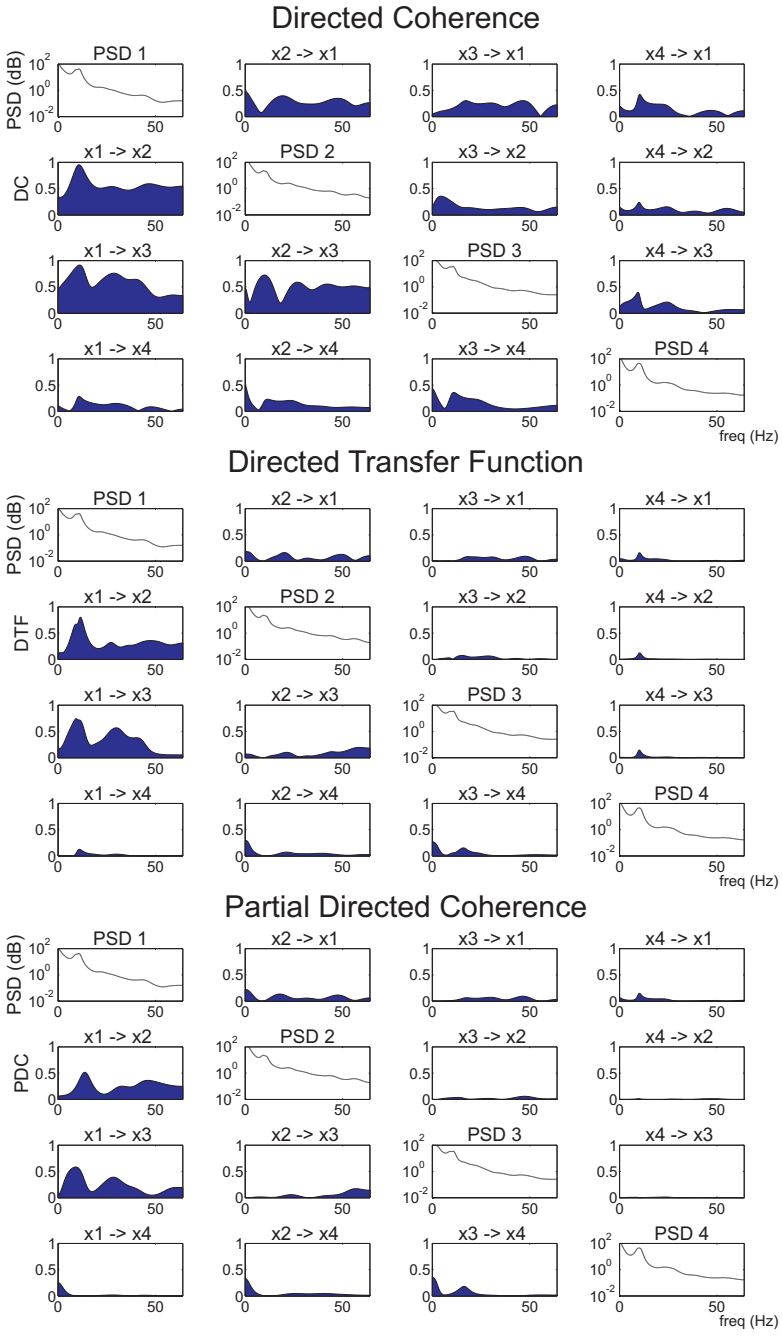


Figure 3.15: Estimated effective connectivity pattern of the simulated model with x_4 is unconnected using the directed coherence, directed transfer function and the partial directed coherence.

3.6.5 Discussion

We used 4 simulations to investigate the behavior of the different connectivity measures. In this dissertation we want to localize the SOZ from ictal IEEG recordings. This means that we want to investigate which of the measures is most suitable to depict the origin of information flow.

The coherence reveals in all 4 simulations connections between all pairs of channels, making it not suitable to reveal the simulated patterns. It does not express directionality, which makes it impossible to find the origin of information flow with the COH.

The partial coherence also does not express the directionality of the information flow. This is cumbersome to find the origin of information flow. If we consider the simulation model with the indirect information flow. Here we found connections between x_1 and x_2, x_2 and x_3 and x_3 and x_4. Because we don't have directionality of the connections we cannot depict the origin of information flow.

The directed coherence reveals the directionality of the connections. However, it is a bivariate measure which requires each pair of signals to be investigated separately. This means that both indirect and direct information flow will be revealed. Meaning that if there is a flow from x_1 to x_2 to x_3, there will be connections from x_1 to x_2 and x_3 and from x_2 to x_3. Here we are still able to identify the origin of information flow. Although many connections are seen, which can make the interpretation of graphs with many nodes cumbersome. Another disadvantage of the DC is that the variance of the noise terms is included in its calculation. This means that correlated noise in different channels could result in spurious connections.

The directed transfer function always reveals the origin of information flow and not any other connection at each frequency. It can be seen that in all simulations the correct information flow from x_1 to the other channels is seen around 10 Hz. The DTF measures the amount of information being transferred between two time series through all (direct and indirect) transfer pathways, relative to the total influence on the target. The DTF has a meaningful physical interpretation as it measures predictive information transfer as the amount of signal power transferred from one process to another, but cannot distinguish between direct and indirect influences measured in the frequency domain.

The partial directed coherence reveals the direct flow without looking for indirect information flow. It always reveals the correct connections if we compare it with the simulated network. The PDC measures directed

predictive information transfer from the source to the target through the direct transfer pathway only, relative to the total information leaving the source. The PDC clearly reflects the underlying interaction structure as it provides a one-to-one representation of direct causality, but is hardly useful as a quantitative measure because its magnitude quantifies the information transfer through the inverse spectral matrix elements (which are not easily interpreted in terms of power spectral density) [65].

The simulation setup in which a hidden source drives the measured signals revealed that connections are noticed between the signals with all connectivity measures. With the DTF connections are seen from signal x_1 to the other signals. This is because signal x_1 is less samples delayed compared to signals x_2, x_3 and x_4. This means that with the DTF signal x_1 will be considered as the origin of information flow. In practice this means that we are limited by the spatial sampling. If we don't record the source of the network, we might end up with a different origin of information flow. The signal with least delay will be considered as driver.

Overall we can conclude that the DTF is most suitable to identify the origin of information flow. Therefore in the remainder of this dissertation we will consider the DTF to localize the SOZ from ictal IEEG recordings.

3.7 Graph analysis

The connectivity measures estimate the amount of information flow between the signals. The signals can be represented as nodes (or vertices) in a graph and the values of the connectivity measures correspond to the edges. The graph is an abstract representation of the network. The graph can be very complex and difficult to interpret. Graph theory is the study of the properties of the graph to better understand the network. These properties can provide complex information about the graph and help to understand the relations between all signals.

Functional connectivity measures result in undirected graphs, while effective measures result in directed graphs. Furthermore, the graph can either be weighted or unweighted. Graphs in which edges either exist or do not exist, and in which all edges have the same significance are called unweighted graphs. When weights are assigned to each of the edges the corresponding graph is called a weighted graph. In the following we will restrict ourself to unweighted graphs.

The adjacency matrix for unweighted graphs is defined as follows: when

an edge exists from node j to i the corresponding entry of the adjacency matrix $A_{ij} = 1$, otherwise $A_{ij} = 0$. For functional connectivity measures this will be a symmetric matrix ($A_{ij} = A_{ji}$). The degree distribution is one of the core properties of graphs and can be calculated out of the adjacency matrix [187]. The in-degree and out-degree for node j is the number of incoming and outgoing connections of node j respectively:

$$IN_J = \sum_{k=1}^{K} A_{jk} \tag{3.32}$$

$$OUT_J = \sum_{k=1}^{K} A_{kj} \tag{3.33}$$

with K the number of nodes. The in-degree is equal to the out-degree for graphs based on functional connectivity measures. For more complex measures like the clustering coefficient, the path length and the betweenness centrality we refer the reader to [221, 187, 186].

3.8 Localization of the epileptogenic focus based on connectivity analysis of EEG signals

In this section we give a literature overview of the most important and pioneering studies of brain connectivity in epilepsy. First the pioneering work from 1970 to 1990 will be discussed followed by an overview of more recent studies.

3.8.1 Pioneering work

The first attempt to localize the epileptogenic focus out of IEEG recording was already performed in 1970 by Gersch and Goddard [78]. They examined three channels of intracranial recordings in the cat brain during generalized seizures produced by kindling of the piriform cortex. The coherence and partial coherence were used to analyze the seizures. They concluded that the kindling site could explain a great part of the coherence between various pairs of channels. This study used functional connectivity measures and was therefore not able to examine the causality between the signals.

Mary Brazier was the pioneer in analyzing human IEEG recorded seizures using effective connectivity measures. She used a method based on coherence and phase analysis to infer causal relations between two signals.

The coherence is used to estimate the strength of the connection while the phase is used to infer information about the directionality. Brazier reported in 1972 [34]: 'The path followed by spontaneous seizure activity in spreading to other structures is a feature peculiar to each individual (n = 4) and can be established for that patient by this method, possibly offering a more restricted therapeutic surgery than temporal lobectomy'. In 1975 Brazier et al. [35] related the depicted epileptogenic focus based on coherence and phase analysis of the scalp EEG with respect to the surgical outcome. They showed that the EEG improved post-operatively which correlated with the clinical improvements of the patients.

The pioneers during the late 1970s and during 1980s were Jean Gotman and Nicolaas Mars. In 1977 Mars et al. [138] investigated the coherence and phase spectra between EEG signals during seizures. They showed that in some cases consistent delay times were found but in many others this was not achieved. The Average Amount of Mutual Information (AAMI) method of analysis was developed to infer nonlinear relations between the signals [139]. It was successfully applied to localize the seizure origin in a kindling dog model of epilepsy [136]. The AAMI was also applied to EEG of 2 patients with focal onset and 1 with generalized seizures [137]. It was shown that high AAMI values characterized the site of the epileptogenic focus while high AAMI values were found for all electrodes for the patient with generalized epilepsy. Furthermore it was shown that the time delays were not consistent in any subject.

Gotman compared the EEG of two groups of patients (generalized corticoreticular and focal epilepsy) during bilateral synchronous spike-and-wave activity. Comparing the coherence and phase difference between the homologous EEG channels of the two hemispheres showed that in the group of focal epilepsy patients there was an interhemispheric time difference (mean of 15 ms from the affected hemisphere to the healthy) that was not found in the generalized epilepsy group [85]. In another study [86] he confirmed the finding that the area of the focus had a consistent time lead (range 5 - 30 ms) over the other recording sites in patients and showed the applicability of the method to a cat model of epilepsy with known focus (penicillin focus and kindling). He concluded that the method is capable of assessing the presence of an epileptic focus even when only widespread seizure activity is recorded and that it allows to make inferences about the possible routes of propagation of seizure activity. Furthermore he studied the relationship between the two hemispheres in patients with intracranial electrodes during seizures (n = 8) [87]. He showed that interhemispheric coherence was generally low throughout seizures, with highest values being reached early in

the seizure at the time of spread, or at the very end. The time delays most often indicated a lead from the side of onset except in 2 of 3 patients with bilateral independent onsets. Here interhemispheric time leads were always from the same side, independently of the side of onset.

Lieb et al. [127] analyzed the intra- and inter-hemispheric connectivity during ictal discharges recorded with depth electrodes in 10 patients by using the coherence and phase analysis method. They reported: 'Although strong intra-hemispheric coherences and linear phase spectra reliably emerged in both the epileptogenic and non-epileptogenic hemispheres during seizure onset and contralateral spread, these relationships were usually not observed for inter-hemispheric comparisons. Only 3 of 10 patients demonstrated some degree of consistency in the emergence of significant wideband coherences and linear phase spectra between left and right mesial temporal sites during the inter-hemispherics propagation of ictal discharges'. The coherence and phase analysis was used by Duckrow and Spencer [59] to study synchronization mechanisms particularly at the onset of seizures.

Table 3.2 gives a chronological overview of these early publications applying connectivity analysis to EEG signals in epilepsy. Most studies used a bivariate, effective connectivity measure, either the coherence coupled with phase analysis or the average amount of mutual information.

Table 3.2: Earliest publications in the field of connectivity between EEG signals in epilepsy. The studies investigated functional or effective connectivity from scalp or depth recordings using a bivariate or multivariate measure. COH & PA: coherence and phase analysis, AAMI: average amount of mutual information

author	year	species	measure	findings	func	eff	scalp	depth	bi	multi
Gersch and Goddard	1970	cat	(partial) COH	the kindling site could explain a great part of the coherence between various pairs of channels	X			X	X	X
Brazier	1972	human	COH & PA	spreading pattern is peculiar to each individual		X		X	X	
Brazier et al.	1975	human	COH & PA	EEG improves post-operatively		X	X		X	
Mars et al.	1977	human	COH & PA	in some cases consistent delay times were found but in many others this was not achieved		X	X		X	
Gotman	1981	human	COH & PA	time difference found for focal epilepsy group and not for generalized corticoreticular epilepsy		X	X		X	
Mars et al.	1983	dog	AAMI	succesfully found prepiriform cortex as onset site		X		X	X	
Gotman	1983	cat / human	COH & PA	method is capable to assess the presence of an epileptic focus even when only widespread seizure activity is recorded		X	X		X	
Mars et al.	1985	human	AAMI	high AAMI values characterize the site of the epileptogenic focus		X			X	
Gotman	1987	human	COH & PA	interhemispheric coherence between IEEG channels low troughout seizures, highest values early in the seizure at the time of spread		X		X	X	
Lieb et al.	1987	human	COH & PA	strong intra-hemispheric coherences and linear phase spectra reliably emerged in both the epileptogenic and non-epileptogenic hemispheres during seizure onset and contralateral spread but not observed for inter-hemispheric comparisons		X	X		X	

3.8.2 Recent studies

Several more recent studies investigated the difference in performance of linear vs. nonlinear measures. Allen et al. [7] investigated the difference between interhemispheric synchronization during generalized spike-and-wave discharges with linear measures (coherence and phase analysis, and linear cross-correlation) and with the nonlinear cross-correlation. They found no significant time difference information with the nonlinear techniques compared to their linear counterpart. Quiroga et al. [167] studied the synchronization between left and right hemisphere rat EEG channels by using nonlinear interdependences, phase synchronizations, mutual information, cross correlation, and the coherence function. They concluded that despite the difference in connectivity measures, the results are qualitatively the same. In 2008 the linear correlation, mutual information and phase synchronization were used to reveal synchronization clusters during interictal activity that was recorded intraoperatively [155]. They showed that synchronous intraoperative ECoG activity emerges from specific cortical areas that are highly differentiated from the rest of the temporal cortex. Methodologically linear correlation and phase synchronization performed better than mutual information.

The group of Fabrice Bartolomei and Fabrice Wendling performed many studies investigating the network during temporal lobe epilepsy (TLE) seizures. Using the coherence they were able to classify TLE seizures into 4 distinct categories, i.e. medial (M), medial-lateral (ML), lateral-medial (LM), and lateral (L) [22]. They used the nonlinear correlation coefficient coupled to the direction index to investigate the degree and direction of coupling between medial and neocortical areas during TLE seizures in patients with the M, ML, and LM subtypes [20]. The same connectivity measure was used to study epileptogenic networks that might be responsible for the triggering of seizures [223]. The nonlinear correlation method was also used to analyze different periods (before, during and after rapid discharges that occur during seizure onset) with or without the occurrence of prior spiking [21]. They showed that if there was prior spiking, the hippocampus was always the leader, while if there was no prior spiking the entorhinal cortex was most often the leading structure. During the rapid discharges period there was a significant decrease of correlation values. This corresponded with earlier findings based on correlation analysis [224]. Furthermore, they found a correlation between the strength of coupling from the entorhinal cortex to the hippocampus and the degree of atrophy in the entorhinal cortex [23]. A nice overview of these studies can be found in [226].

All previously mentioned studies are bivariate, meaning that each pairwise combination of all channels had to be investigated separately. In 1994 Franaszczuk et al. [71] analyzed the onset of mesial TLE seizures and the propagation pattern using the Directed Transfer Function (DTF) of recorded IEEG traces in 3 patients. This is the first study using a multivariate connectivity measure to estimate the epileptogenic focus from human IEEG recordings. The DTF method was able to localize deep mesial structures as the source of seizure activity for these patients. Moreover, they demonstrated that the DTF method can provide information regarding flow that is not readily apparent from visual inspection. The DTF has also been used to investigate kainic acid (KA) induced epileptogenesis in rats [140]. They concluded that KA-induced epileptiform discharges are cortical and hippocampal events, with the frontal cortex expressing low frequency rhythms and the hippocampus high frequency rhythms. In 1998 Franaszczuk and Bergey [70] used the integrated DTF, the summation of the DTF over a predefined frequency band to reveal patterns during mesial and lateral onset temporal lobe seizures. They showed the potential of the integrated DTF to determine patterns of flow of activity, even during periods when visual analysis of the intracranial ictal EEG may not allow for definitive source localization. The integrated DTF was proven to be a valuable measure to localize the epileptogenic focus out of the ictal IEEG recordings [229, 232, 111].

Another multivariate effective connectivity measure used for localization of the epileptogenic focus is the partial directed coherence (PDC) [16]. In 2004 PDC analysis of scalp EEG traces coupled to graph analysis (strongly connected subgraphs) provided correct focal localization. Another PDC study showed enhanced frontocentral EEG connectivity in photosensitive generalized epilepsies during rest and during intermittent photic stimulation [213]. Furthermore PDC analysis coupled to graph theory (betweenness centrality) has also been used to localize the epileptogenic focus in epilepsy secondary to type II focal cortical dysplasia [212].

Chapter 4

Framework to localize the seizure onset zone from intracranial EEG recordings based on effective brain connectivity

4.1 Introduction

The treatment with highest efficacy for refractory epilepsy patients is resective surgery of the epileptogenic focus. This requires accurate and precise localization of the epileptogenic focus which is intended during the pre-surgical evaluation. In 15-25% of the patients in the pre-surgical protocol IVEM is required for the delineation of the seizure onset zone (SOZ) and to determine the overlap with eloquent tissue. In clinical practice the IEEG recorded during the IVEM is visually analyzed by epileptologists. They evaluate the amplitude and the geometrical relationship between the signals to identify abnormal synchronous activity that is reflective of the epileptogenic focus. However, this visual analysis and spatial interpretation of many simultaneously recorded IEEG signals by the epileptologist has its limitations. Precise identification of initial, sometimes very discrete IEEG changes, to determine the SOZ is time consuming and requires extensive and specific expertise. Also because of the fast propagation of an epileptic seizure the SOZ can be difficult to pinpoint which can lead to an overestimation of the

size of the SOZ.

In this chapter we will introduce a framework that is able to localize the SOZ from ictal IEEG recordings. The proposed technique investigates the causal relationship in the spectral domain between the intracranial signals by using the concept of effective brain connectivity. The performance of the framework is first tested on simulations and it is afterwards applied to identify the SOZ in 1 patient during 4 seizures and 29 sub-clinical seizures.

Until now, connectivity studies in epilepsy mostly used bivariate measures (section 3.8). This means that each pairwise combination of channels requires separate investigation, which can be cumbersome when many signals are considered simultaneously. Some patients have over 50 different electrode contacts to investigate the brain activity of different regions. This would lead to over 1225 signal pairs requiring separate investigation. For this reason we based our framework on multivariate measures, in which all signals are considered within one single system. This also allows to investigate indirect information flows between the signals.

The designed framework is based on the DTF, because it is a multivariate effective connectivity measure capable of showing the indirect connections in the frequency domain. This makes it feasible to trace the origin of the information flow. The DTF is calculated out of the coefficients of a MVAR model fitted to the data and is therefore designed to be applied to stationary epochs. The DTF has already been applied to various biomedical signals: fMRI time-series [53], scalp EEG for sleep studies [115, 114, 48, 49, 172] and Event Related Potentials [57, 126, 142, 81, 13]. In the field of epilepsy it has been used to localize the epileptogenic focus during stationary seizure epochs [71, 70, 231, 112] and to investigate kainic acid-induced epileptogenesis in rats [140]. It was demonstrated that DTF analysis can be a useful auxiliary tool for determining surgical resection areas prior to epilepsy surgery. However, these studies analyzed one or two epoch of 3 - 10 s of EEG during the seizure and assumed that the seizure was stationary in the considered time-windows. This contradicts the fact that seizures are highly non-stationary. Furthermore, the earliest seizure spread is of utmost importance and this is intrinsically non-stationary.

To investigate non-stationary signals a time-dependent version of the DTF was recently introduced by two groups [10, 230]. The Adaptive Directed Transfer Function (ADTF) is the extension of the DTF that is applicable to non-stationary signals. The effective connectivity pattern obtained by the ADTF shows the information flow between different channels at specified frequencies and how it changes over time. The ADTF has been used to

localize Event Related Potentials [10] and to localize the irritative zone from interictal spikes seen in the IEEG [230].

The fundamental EEG frequency during a seizure may vary from seizure to seizure and from patient to patient. Due to this heterogeneous frequency content during different seizures it is challenging to design a framework suitable to pinpoint the SOZ applicable to all seizure types and patients. In our framework we incorporate the frequency content of the signals more into the connectivity pattern, making it suitable to investigate different patients with variable EEG frequency content. Because the onset of a seizure is intrinsically non-stationary we investigated the applicability of the ADTF to localize the SOZ. We propose several connectivity measures derived from the ADTF that incorporate the signal frequency power and investigate their performance with straightforward simulations. As a proof of concept we show the applicability to localize the SOZ in 1 patient who had depth and grid EEG recordings.

4.2 Method

In this section we will first introduce time-variant multivariate autoregressive (TVAR) modeling and how the coefficients are estimated based on Kalman filtering. Afterwards we will show how different effective connectivity measures can be calculated based on these coefficients.

4.2.1 Time-variant autoregressive modeling

We will investigate Granger causality by using a time-variant multivariate autoregressive (TVAR) model. The TVAR model is an adaptation of the multivariate autoregressive (MVAR) model (eq. 3.13) in which the coefficients are allowed to vary over time. This allows to model non-stationary signals:

$$\mathbf{x}(t) = \sum_{m=1}^{p} \mathbf{A}_m(t)\mathbf{x}(t-m) + \mathbf{e}(t) \tag{4.1}$$

with K being the number of signals, p the model order, $\mathbf{x}(t) = [x_1(t) \quad x_2(t) \quad \ldots \quad x_K(t)]^T$ the $K \times 1$ signal matrix, $\mathbf{e}(t) = [e_1(t)\ e_2(t)\ \ldots\ e_K(t)]^T$ the $K \times 1$ matrix containing the uncorrelated white noise and $\mathbf{A}_m(t)$ the $K \times K$ coefficient matrix for delay m at time point t. Each element of the matrix $\mathbf{A}_m(t)$, $\mathbf{A}_{m,ij}(t)$, estimates the influence of

the sample $\mathbf{x}_j(t-m)$ on the current sample $\mathbf{x}_i(t)$. All coefficient matrices together provide knowledge about the directed information flow between all signals and how this changes over time. The model order defines the time window used to estimate the current samples based on a linear combination of the past samples. This TVAR model with time-varying parameters allows us to investigate non-stationary signals such as those observed at the onset of epileptic seizures.

4.2.2 Estimation of the TVAR coefficients using Kalman filtering

The estimation of the coefficients of the TVAR model is an ill-posed problem: there are more unknown parameters than measured data points. We estimate the time-varying coefficients using the Kalman filtering algorithm [8]. The Kalman filter is an algorithm for estimating the state of a state space model with a system equation and measurement equation. For an overview of the different ways to obtain the adaptive autoregressive coefficients with the Kalman filtering algorithm we refer the reader to [175]. We applied the standard Kalman algorithm implemented in the BioSig toolbox [174] to the data to obtain the autoregressive coefficients.

Below we address the mathematical derivation of the coefficients out of the considered EEG signals using the Kalman filtering algorithm. First we will introduce the state space model and how to represent the TVAR model as a state space model. Afterwards we will explain in detail the procedure to actually estimate the coefficients.

4.2.2.1 State-space model

Kalman filtering is an algorithm to estimate the state of a state-space model. The state-space model exists of a system equation (eq. 4.2) and an observation (measurement) equation (eq. 4.3).

$$\mathbf{z}(t) = \mathbf{G}(t|t-1)\mathbf{z}(t-1) + \mathbf{w}(t) \tag{4.2}$$

$$\mathbf{x}(t) = \mathbf{H}(t)\mathbf{z}(t) + \mathbf{v}(t) \tag{4.3}$$

where $\mathbf{x}(t)$ are the measurements, $\mathbf{v}(t)$ is the measurement noise, $\mathbf{z}(t)$ is the state vector and $\mathbf{w}(t)$ is the process noise at time point t. Matrix $\mathbf{G}(t|t-1)$ is the state transition matrix and $\mathbf{H}(t)$ is the observation matrix.

4.2.2.2 State-space model representation of the TVAR model

The TVAR model needs to be represented as a state-space model to apply the Kalman filtering algorithm [100]. This is achieved by using the following notation:

$$\mathbf{a}(t) = vec([\mathbf{A}_1(t), \mathbf{A}_2(t), ..., \mathbf{A}_p(t)]^T) \tag{4.4}$$

$$\mathbf{X}(t) = (\mathbf{x}^T(t-1), \mathbf{x}^T(t-2), ..., \mathbf{x}^T(t-p)) \tag{4.5}$$

$$\mathbf{C}(t) = \mathbf{I}_K \otimes \mathbf{X}(t)^T \tag{4.6}$$

where p is the model order, $\mathbf{a}(t)$ is the $pK^2 \times 1$ coefficient vector, $\mathbf{I}_K$ is the $K \times K$ identity matrix, $\mathbf{X}(t)$ is a $1 \times Kp$ vector containing the p previous measurements, $\otimes$ represents the Kronecker product and $\mathbf{C}(t)$ is the $pK^2 \times K$ matrix representing previous measurements.

Suppose the autoregressive coefficients follow a multivariate random walk model. By supposing this we assume that the state transition matrix $\mathbf{G}(t|t-1)$ is equal to the identity matrix. Out of eq. 4.2 and eq. 4.3 we find following system and measurement equation:

$$\mathbf{a}(t) = \mathbf{a}(t-1) + \mathbf{w}(t) \tag{4.7}$$

$$\mathbf{x}(t) = \mathbf{C}^T(t)\mathbf{a}(t) + \mathbf{v}(t) \tag{4.8}$$

Here $\mathbf{a}(t)$ is the state vector and $\mathbf{C}^T(t)$ is the measurement matrix. The vector $\mathbf{w}(t)$ (dimensions $pK^2 \times 1$) is the state process noise modeled as zero-mean white Gaussian noise with covariance matrix $\mathbf{Q}(t)$, $\mathbf{v}(t)$ is a $K \times 1$ vector containing zero-mean white Gaussian measurement noise with covariance matrix $\mathbf{R}(t)$.

4.2.2.3 Estimation procedure of the TVAR coefficients

The Kalman filtering algorithm consists of a prediction step, followed by an update step. The prediction step consists of

$$\mathbf{P}(t|t-1) = \mathbf{P}(t-1|t-1) + \mathbf{Q}(t-1) \tag{4.9}$$

$$\hat{\mathbf{a}}(t|t-1) = \hat{\mathbf{a}}(t-1) \tag{4.10}$$

where $\mathbf{P}(t|t-1)$ is the one step ahead prediction of the state covariance matrix, $\mathbf{P}(t-1|t-1)$ is the estimated covariance matrix of the state vector, $\hat{\mathbf{a}}(t-1)$ is the estimate of the state vector $\mathbf{a}(t-1)$ and $\hat{\mathbf{a}}(t|t-1)$ is the one step ahead prediction of the state vector. The initial value of $\mathbf{P}_{0|0}$ is the $pK^2 \times pK^2$ identity matrix and $\mathbf{Q}_0 = \lambda \mathbf{I}_L$. Here λ is the update coefficient (UC) and $\mathbf{I}_L$ is the $pK^2 \times pK^2$ identity matrix.

The update step of the Kalman filtering follows after the prediction step. The update step exists of:

$$\hat{\mathbf{v}}(t) = \mathbf{x}(t) - \mathbf{C}^T(t)\mathbf{a}(t) \tag{4.11}$$

$$\mathbf{R}(t) = (1-\lambda)\mathbf{R}(t-1) + \lambda \hat{\mathbf{v}}(t)\hat{\mathbf{v}}^T(t) \tag{4.12}$$

$$\mathbf{G}(t) = \mathbf{P}(t|t-1)\mathbf{C}(t)\left(\mathbf{C}^T(t)\mathbf{P}(t|t-1)\mathbf{C}(t) + \mathbf{R}(t)\right)^{-1} \tag{4.13}$$

$$\hat{\mathbf{a}}(t) = \hat{\mathbf{a}}(t|t-1) + \mathbf{G}(t)\hat{\mathbf{v}}(t) \tag{4.14}$$

$$\mathbf{Q}(t) = \lambda \mathbf{I}_L \tag{4.15}$$

$$\mathbf{P}(t|t) = \left(\mathbf{I}_L - \mathbf{G}(t)\mathbf{C}^T(t)\right)\mathbf{P}(t|t-1) \tag{4.16}$$

where $\hat{\mathbf{v}}(t)$ is the one-step prediction error, $\mathbf{R}(t)$ is the covariance matrix of the measurement noise, λ is the update coefficient, $\mathbf{G}(t)$ is the filter gain matrix and $\mathbf{I}_L$ is the $pK^2 \times pK^2$ identity matrix. The starting value for the covariance matrix of the measurement noise $\mathbf{R}_0$ is equal to the $K \times K$ identity matrix. The update coefficient $\lambda \in (0,1)$ is a constant which has to be set a priori. The filter gain matrix $\mathbf{G}(t)$ tells us how much the prediction $\hat{\mathbf{a}}(t|t-1)$ should be corrected for on time step t.

Two parameters influence the Kalman filter algorithm: the model order (p) and the update coefficient (UC). The model order defines how many previous samples are taken into account to update the state. The update coefficient defines how quickly the model will adapt to changes in the dataset. The lower the UC, the more robust the estimates of the parameters, but the

slower they will adapt to changes. A higher UC means that the coefficients will adapt more rapidly, but will also lead to less robust estimates.

4.2.3 TVAR model to the frequency domain

Once we have obtained the TVAR coefficients we can transform them to the frequency domain to investigate the connections at specific frequencies. At each time point we calculate the Fourier transform of the coefficient matrices in eq. 4.1 as follows:

$$\mathbf{A}(f,t) = -\sum_{m=0}^{p} \mathbf{A}_m(t) e^{-i2\pi \frac{f}{f_s} m} \tag{4.17}$$

with

$$\mathbf{A}_0(t) = -\mathbf{I}_K \tag{4.18}$$

By inverting matrix $\mathbf{A}(f,t)$ we get following system equation:

$$\mathbf{X}(f,t) = \mathbf{A}^{-1}(f,t)\mathbf{E}(f,t) = \mathbf{H}(f,t)\mathbf{E}(f,t) \tag{4.19}$$

where $\mathbf{X}(f,t)$, $\mathbf{A}(f,t)$ and $\mathbf{E}(f,t)$ is the Fourier transformation of the considered multivariate dataset, the coefficient matrices at time point t and the white noise, respectively. Matrix $\mathbf{H}(f,t)$ is called the time-variant transfer matrix of the system. The element $\mathbf{H}_{ij}(f,t)$ expresses the amount of information flow from signal $\mathbf{x}_j$ to $\mathbf{x}_i$ at frequency f at time point t.

The time-variant power spectral density (PSD) matrix, $\mathbf{S}(f,t)$ can be calculated out this matrix and the residuals of the TVAR model as follows:

$$\begin{aligned}
\mathbf{S}(f,t) &= \mathbf{X}(f,t)\,\mathbf{X}^*(f,t) \\
&= \mathbf{H}(f,t)\,\mathbf{E}(f,t)\,\mathbf{E}^*(f,t)\,\mathbf{H}^*(f,t) \\
&= \mathbf{H}(f,t)\,\mathbf{\Sigma_e}\,\mathbf{H}^*(f,t) \\
&= \mathbf{H}(f,t)\,\sigma_e^2\mathbf{I}\,\mathbf{H}^*(f,t) \\
&= \sigma_e^2\mathbf{H}(f,t)\,\mathbf{H}^*(f,t),
\end{aligned} \tag{4.20}$$

where * denotes the conjugate transpose and $\mathbf{\Sigma_e}$ is the noise covariance matrix. Since we assume that the residual time series are uncorrelated white noise, the covariance matrix $\mathbf{\Sigma_e}$ will be a diagonal matrix approximated by $\sigma_e^2\mathbf{I}$. This allows to estimate the autospectrum of signal $\mathbf{x}_i$ as:

$$\hat{\mathbf{S}}_{ii}(f,t) = \sigma_e^2 \sum_{k=1}^{K} \mathbf{H}_{ik}(f,t)\mathbf{H}_{ki}^*(f,t) = \sigma_e^2 \sum_{k=1}^{K} |\mathbf{H}_{ik}(f,t)|^2 \quad (4.21)$$

This indicates that the spectra of the signals are modeled by the time-variant transfer matrix. Since the transfer matrix is calculated out of the coefficients of the TVAR model, the model order p directly defines the resolution of the estimated spectra of the signals. A higher order results in a better delineation between the frequencies, but also makes the coefficient estimation procedure more underdetermined.

The TVAR model is capable of modeling the frequency content of non-stationary signals. Out of the coefficients of the TVAR model the time-varying Power Spectral Density matrix is calculated using eq. 4.20. This time-varying PSD matrix captures the non-stationary frequency content of the signals. We define the power of the TVAR model (P_{TVAR}) as the sum of autospectra of the signals:

$$P_{TVAR}(f,t) = \sum_{k=1}^{K} \hat{\mathbf{S}}_{kk}(f,t) \quad (4.22)$$

Because the PSD matrix is time dependent, the power of the TVAR system will also vary over time. The power of the TVAR model reflects which frequencies are most prominently modeled at each time point. It reflects at which frequencies most connections are seen.

4.2.4 Integration of the time-variant power spectrum into the effective connectivity measures

The time-variant version of the DTF 3.24 is called the Adaptive Directed Transfer Function (ADTF) [10, 230]:

$$\mathbf{ADTF}_{ij}(f,t) = \frac{|\mathbf{H}_{ij}(f,t)|^2}{\sum_{k=1}^{K} |\mathbf{H}_{ik}(f,t)|^2} \quad (4.23)$$

with following normalization condition:

$$\sum_{k=1}^{K} \mathbf{ADTF}_{ik}(f,t) = 1 \tag{4.24}$$

meaning that the incoming information flow into each channel is equal to 1 at each frequency at each time point. The ADTF shows the effective connectivity pattern between all signals at each frequency over time.

4.2.4.1 The integrated Adaptive Directed Transfer Function (iADTF)

To study the information flow between the signals in a certain frequency band, the DTF is integrated over the specific frequency band, leading to the integrated DTF (iDTF) [71]. The integrated DTF has been used in previous studies to localize the epileptic focus during stationary windows of a seizure [71, 70, 229]. However the onset of a seizure is non-stationary and cannot be studied by this measure. For this purpose the effective connectivity in a specific frequency band can be studied by the time variant version of the iDTF, namely the **integrated ADTF (iADTF)**, which is the integration of the ADTF over the considered frequency band.

$$\mathbf{iADTF}_{ij}(t) = \frac{1}{f_2 - f_1} \int_{f=f_1}^{f_2} \frac{|\mathbf{H}_{ij}(f,t)|^2}{\sum_{k=1}^{K} |\mathbf{H}_{ik}(f,t)|^2} \tag{4.25}$$

The values of the iADTF lie within the interval [0,1]. The normalization is performed in a way that the sum of incoming information flow into a channel at each time point is equal to 1:

$$\sum_{k=1}^{K} \mathbf{iADTF}_{ik}(t) = 1 \tag{4.26}$$

The iADTF has been used to investigate the network during a combined foot-lips movement task [11] and to localize interictal spikes [230, 229]. These authors showed that iADTF analysis of interictal spikes correlated with the location of the resected cortical regions in patients who were seizure-free following a surgical intervention.

The normalization of the iADTF does not take the power spectrum of the signals into account. Each term of the sum over frequencies in eq. 4.25 is normalized between 0 and 1. This means that each term of the sum is equally important, which implies that each frequency in the considered frequency band is equally important. We suggest to take the power spectrum of the signals into account in order to prioritize the frequencies containing much power.

4.2.4.2 The masked Adaptive Directed Transfer Function (mADTF)

In this section we propose to use the frequency content of the signals to mask the ADTF-values. The power of the TVAR model, $P_{TVAR}(f,t)$, in the considered frequency band $[f_1, f_2]$ is used to mask the ADTF values because it describes the frequencies which are prominent in the signal set. The power mask is constructed by only considering the 5% highest values of the power of the TVAR system at each time point in the considered frequency interval. We integrate the masked ADTF-values over the predefined frequency interval $[f_1, f_2]$ and name the new measure **the masked ADTF (mADTF)**.

$$\forall f \in [f_1, f_2]: \ \text{mask(f,t)} = \begin{cases} 1 \text{ if } \mathrm{P}_{TVAR}(\text{f,t}) >= \mathrm{p}_{95}(\mathrm{P}_{TVAR}(\text{f,t})) \\ 0 \text{ if } \mathrm{P}_{TVAR}(\text{f,t}) < \mathrm{p}_{95}(\mathrm{P}_{TVAR}(\text{f,t})) \end{cases} \quad (4.27)$$

$$\mathbf{mADTF}_{ij}(t) = \frac{1}{0.05(f_2 - f_1)} \int_{f=f_1}^{f_2} \mathbf{ADTF}_{ij}(f,t)\text{mask(f,t)} \quad (4.28)$$

where p_{95} is the 95^{th} percentile of the power of the TVAR system over frequencies at each time point. The value of mask(f,t) is 1 if the power of the TVAR model $P_{TVAR}(f,t)$ at that frequency belongs to the 5% of highest power values over all frequencies at that specific time point, otherwise the value is set to 0. So at each time point we only sum over 5% of the frequencies in the considered frequency band, namely those at which the TVAR power is the highest. The values of the mADTF lie within the interval [0,1]. The normalization is performed in a way that the sum of incoming information flow into a channel at each time point is equal to 1.

$$\sum_{k=1}^{K} \mathbf{mADTF}_{ik}(t) = 1 \quad (4.29)$$

The mask allows us to study the frequencies containing the highest power. The other frequencies in the frequency interval are disregarded.

4.2.4.3 The full-frequency Adaptive Directed Transfer Function (ffADTF)

The time-frequency mask only considers 5% of the frequencies in the predefined frequency interval at each time point and disregards the information flow at the other frequencies. We propose a new normalization of the ADTF to overcome the use of a time-frequency mask derived from the power of the TVAR model. Hereby we introduce a normalization which incorporates the frequency information of all the frequencies in the defined frequency interval based on the full frequency DTF introduced by Korzeniewska [118]. The ADTF is normalized at each time point by the total frequency content in the considered frequency band $[f_1, f_2]$ at that time point. This is different in comparison to the iADTF in eq. 4.25, where the normalization at each frequency disregards the frequency content at other frequencies of the interval. The full frequency ADTF considers all the frequencies in the predefined frequency interval, where the masked ADTF only considers 5% of the frequencies. The **full frequency ADTF (ffADTF)** is defined as:

$$\mathbf{ffADTF}_{ij}(t) = \int_{f=f_1}^{f_2} \frac{|\mathbf{H}_{ij}(f,t)|^2}{\sum_{k=1}^{K} \int_{f'=f_1}^{f_2} |\mathbf{H}_{ik}(f',t)|^2} \tag{4.30}$$

The values of the ffADTF lie within the interval [0,1]. The normalization is performed in a way that the sum of incoming information flow into a channel at each time point is equal to 1.

$$\sum_{k=1}^{K} \mathbf{ffADTF}_{ik}(t) = 1 \tag{4.31}$$

4.3 Simulation Setup

4.3.1 Simulated model

The simulation is designed to test if the ADTF is appropriate and which of the modified ADTF measures (iADTF, mADTF and ffADTF) is better suited to describe the directional flow that occurs during the onset of an

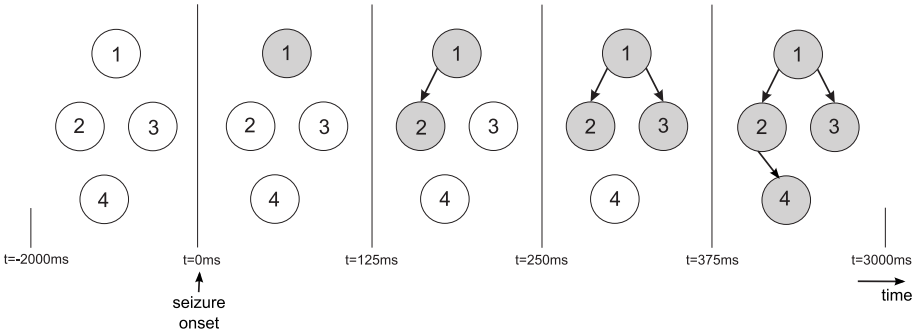


Figure 4.1: Illustration of the simulated model. The model consists of 4 signals, where a seizure onset was simulated at t=0ms at node 1. Afterwards a fast propagation was simulated.

epileptic seizure. Four signals are constructed during 5 different states with a sampling frequency of 256 Hz (fig. 4.1). The background noise of the signals is set to have a 1/f-spectral behavior. The seizure activity is modeled as a sinusoid with a frequency content varying from 12 Hz at t = 0 ms to 8 Hz at t = 3000 ms. The seizure starts at t = 0 ms in signal x_1, which represents the SOZ. The seizure is passed to signal x_2 at time t = 125 ms with a delay of 2 samples. At t = 250 ms the seizure propagates from signal x_1 to signal x_3. At time t = 375 ms the seizure propagates from x_2 to x_4. This means that the seizure starting in x_1 propagates to x_4 through x_2.

The amount of seizure activity that was added to the background noise in each node was defined by the Signal-to-Noise Ratio (SNR).

$$SNR = 10 log_{10} \frac{P_{signal}}{P_{noise}} \tag{4.32}$$

where P_{signal} and P_{noise} are the power of the epileptic activity and the background noise respectively.

4.3.2 Performance evaluation of the connectivity measures

In order to validate the performance of the different connectivity measures during simulations, a connectivity graph will be derived from the calculated connectivity values. This connectivity graph will be compared with the intrinsic connections of the simulated model. To derive a connectivity graph out of the calculated connectivity measures a significance level needs to be set to define which values of the *ADTF (with *ATDTF either the

iADTF, mADTF or ffADTF) are considered to represent a connection. If the calculated *ADTF-value is lower than the significance level, then no connection is derived. If the *ADTF-value is higher than the significance level, we assume there is a connection.

In the simulations a uniform threshold will be used as significance level. We will vary the value of the threshold from 0 to 1 to take the effect of the changing uniform threshold on the estimated connectivity pattern into account. This way we do not bias any calculated connectivity measure by assuming a fixed threshold value.

To validate the performance of the connectivity measures the sensitivity and specificity of the derived connections are calculated. The calculated connectivity graph is compared with the intrinsic connectivity graph of the simulated model at each sample. Because the *ADTF models the indirect flow we will compare the derived connections with a model in which all flow originates from signal x_1. The sensitivity is the proportion of actual positives which are correctly identified as such. We calculate the true positives (TP): the connections in the simulated model that are correctly identified by the connectivity measure, the false positives (FP): wrongly detected connections, the true negative (TN): there is no connection in the simulated model and no connection is derived with the connectivity measure, the false negatives: no connection is derived by the connectivity measure while there is a connection in the simulated model. The sensitivity is calculated out of the TP and FN as described by eq. 4.33. Specificity measures the proportion of negatives which are correctly identified and is calculated out of the TN and the FP as defined by eq. 4.34. This way we can quantify the performance of a connectivity measure during a simulation.

$$sens = \frac{TP}{TP + FN} \tag{4.33}$$

$$spec = \frac{TN}{TN + FP} \tag{4.34}$$

The Receiver Operating Characteristics curve (ROC-curve) is calculated out of the sensitivity and specificity for each model order and each SNR. This is the curve that describes the sensitivity vs. specificity as a function of the considered parameters (here the UC and the threshold). The ROC curve describes the behavior of the connectivity measure with respect to a changing parameter set. The Equal Error Rate point (EER point) is computed for the different measures. The EER is obtained as the intercept of the sensitivity vs. specificity curve with the line of equal sensitivity and

specificity. The EER equals 1 - sensitivity = 1 - specificity at the point where the sensitivity and the specificity are equal and which is closest to the point where sensitivity = 1 and specificity = 1. A lower EER indicates a better performance. These points define how well the method performs and allows to compare different connectivity measures.

4.3.3 Performance of connectivity measures on simulated model

The signals are constructed based on the model shown in fig. 4.1 with the SNR varying from -5 dB to 10 dB. We perform a decimation of the signals in the frequency domain from 256 Hz to 64 Hz. The downsampling does not only decreases the number of samples in each epoch but also allows a lower model order of the TVAR model to be used. This means that this downsampling leads to an enormous decrease in computation time without losing information in the desired frequency band. After the decimation the signals are normalized: the mean was set to 0 and the standard deviation was set to 1. This normalization is done to treat every signal equally and not bias results based on the amplitude of the signals.

The time-variant autoregressive coefficients are computed out of the pre-processed signals for a model order ranging from 1 to 5. The iADTF, mADTF and the ffADTF are calculated out of these coefficients in the pre-defined frequency interval [5, 30 Hz]. The ROC curve is calculated for each SNR and model order with two varying parameters: the update coefficient of the Kalman filter algorithm and the value used for the fixed uniform threshold. The update coefficient is evaluated in the empirically chosen interval $[0.001, 0.04]$. The uniform value for the significance threshold varied from 0 to 1 with stepsize 0.01. The simulation is repeated 160 times for each SNR to get a robust estimate for the sensitivity and specificity. The Equal Error Rate points (EER-points) are compared to see which measure is better suited to describe rapid propagation of a seizure between the different channels.

4.3.4 Results

The result of 1 simulation with SNR of 10 dB, model order 5 and the update coefficient equal to 0.006 is shown in fig. 4.2. The autospectra of the signals, depicted on the diagonal, reveal the epileptic activity starting at 12 Hz and decreasing over time. All 3 connectivity measures show a rising information flow from signal x_1 to all the other signals during this epileptic

activity. The pattern seen here is as we would expect: there is an increase in information flow from x_1 to the other channels. The increase in the mADTF and the ffADTF is more outspoken than the increase in the iADTF, but the mADTF and ffADTF values fluctuated more than the iADTF values.

There is a delay between the calculated and intrinsic connectivity between the signals of the model. This delay is related to the update procedure of the state in the Kalman filtering algorithm used to assess the autoregressive coefficients. A higher update coefficient enforces a quicker adaptation to a changing dataset which reduces this delay but introduces more fluctuations in the ADTF-values.

The sensitivity and specificity were calculated for all combinations of the update coefficient and the uniform thresholds at each different model order and SNR. The ROC-curve for a SNR equal to 10 dB and model order set to 5 is shown in fig. 4.3. The different points on the ROC-curve show the results for different combinations of the update coefficient and the uniform threshold. The EER-points for all three methods are also depicted in the same figure. In the figure we see that the masked and full-frequency ADTF outperform the results of the integrated ADTF. The EER-points of the ffADTF and mADTF correspond with a sensitivity and specificity which is approximately 3% higher than those of the iADTF. Furthermore, more points of the ROC-curve of the ffADTF and mADTF lie close to their EER-points compared with the iADTF. This means that the ffADTF and the mADTF are less sensitive to changes in the parameterset (UC and uniform threshold) compared to the iADTF.

The EER-points of the iADTF, mADTF and ffADTF are calculated for each combination of model order and SNR. The EERs corresponding to the EER-points are depicted in fig. 4.4. A lower EER indicates a better performance. The results of model order equal to 1 are 5% to 10% worse than results achieved with a higher model order. An increase in model order leads to an increase in frequency resolution. A model order equal to 1 is not sufficient to adequately describe the frequency content present in the signals (ranging from 12 Hz to 8 Hz). The results of a model order equal to 2 and higher are similar: the EER ranges from 0.2 for a SNR of -5 dB to 0.05 for a SNR of 10 dB. A higher SNR leads to a better estimation of the connectivity pattern as expected.

All 3 connectivity measures lead to results in the same range. However, the results of the mADTF and ffADTF are up to 3% better than those of the iADTF at high SNRs (from 5 dB to 10 dB). At low SNRs (-5 dB to 0 dB) the results of the iADTF and ffADTF are up to 3% better than those

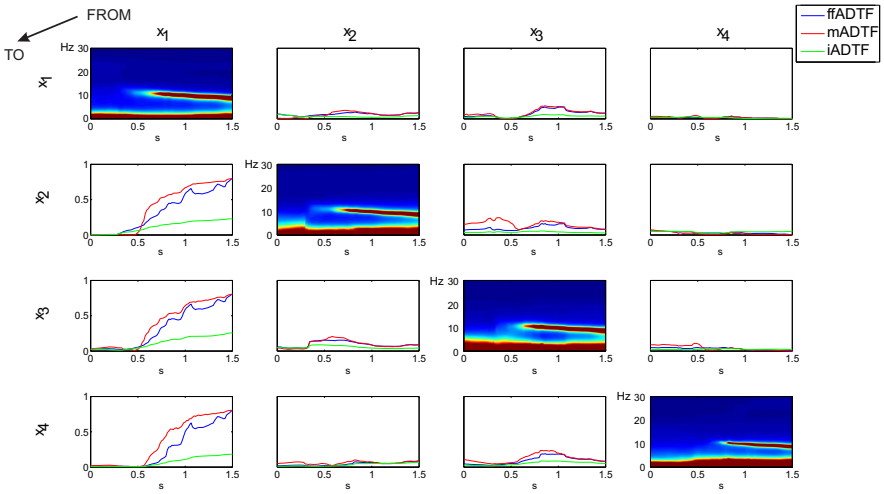


Figure 4.2: The values of the integrated ADTF, masked ADTF and full-frequency ADTF for 1 simulation with SNR = 10 dB, model order p = 5 and update coefficient UC = 0.006 during the start of the simulated seizure. On the diagonal the time-variant autospectra of the signals are depicted. The off diagonal plots express the information flow going from the signal indicated on top to the signal indicated on the left. We can see a rise in the connectivity measure around 0.5 s indicating information flow going from x_1 to x_2, x_3 and x_4.

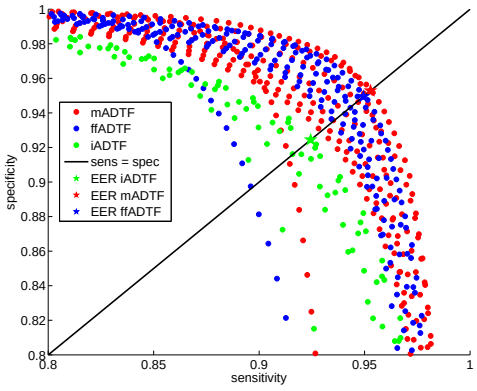


Figure 4.3: The ROC-curve for the integrated, masked and full-frequency ADTF with model order set to 5 and SNR equal to 10 dB. The EER-points are depicted as stars on the figure. The mADTF and ffADTF outperform the iADTF.

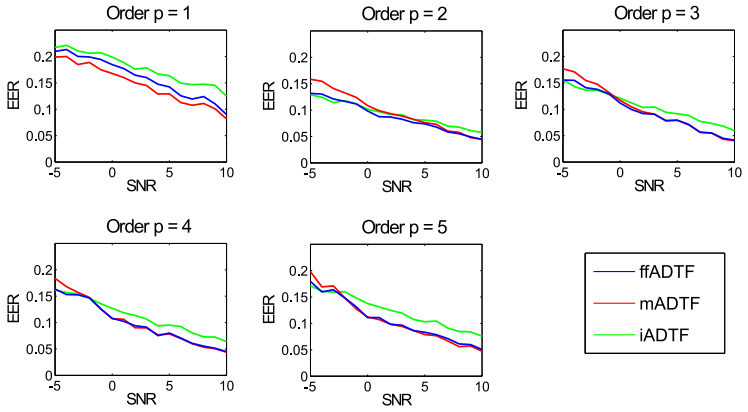


Figure 4.4: EER-points for the integrated, masked and full-frequency ADTF at different model orders and SNR range: [-5 dB, 10 dB].

of the mADTF. The mADTF behaves worse for low SNRs, because the frequencies containing the signal (12 Hz to 8 Hz) become more difficult to be distinguished from the frequencies containing much noise. For high SNRs the ffADTF and mADTF are able to prioritize the frequencies containing much signal over the frequencies containing noise which leads to better results. Overal the ffADTF leads to the best results and will be used to investigate the connectivity pattern out of IEEG recordings during the onset of multiple similar seizure onsets in 1 patient.

4.4 Proof of concept in 1 patient

We consider a dataset of 4 similar seizure onsets and 29 similar subclinical seizures recorded during the presurgical evaluation of a patient with refractory epilepsy. The onset of the seizures and subclinical seizures were marked by the neurologists. The IEEG epochs were selected starting from -2 s before until 8 s after the marked onset. During the seizure onsets there is no clinical manifestation of the seizure. The dataset contains 52 IEEG signals monitoring 8 regions of interest. The patient has 2 amygdalo-occipital depth electrodes with 12 contacts each, respectively LH1-12 and RH1-12. These electrodes monitor the electrical activity of the left and right amygdala and hippocampus respectively. The contacts LH1 to LH5 lie within the left amygdala and hippocampus, LH6 lies on the border of the hippocampus. Four subdural strips (electrodes fixated on a plastic patch) with 4 electrode contacts each are placed on the left and right temporobasal area (left an-

terior: LTA1-4, left posterior: LTM1-4, right anterior: RTA1-4 and right posterior: RTM1-4) and 2 subdural strip with 6 electrode contacts monitor the left and right temporolateral area (left: LTP1-6 and right: RTP1-6). The position of the contacts of the intracranial depth electrodes is shown in a coregistered CT-MR image (fig. 4.5). Four signals, RH5, RH6, RH11 and RH12, are omitted from the dataset due to visually identified artifacts present in the EEG channels.

The sampling frequency of the recorded intracranial EEG epochs is 256 Hz. The signals are decimated to 64 Hz and normalized. The fundamental frequency during all seizure is between 12 Hz and 8 Hz. The fundamental frequency decreases over time during the seizure onsets. The SNR of the epileptic activity compared to the background IEEG is approximately 3 dB. The parameters to perform the connectivity analysis are chosen based on the knowledge gained by the performed simulations of seizure spreading. The model order is set to 5 and the update coefficient is set to 0.001. The uniform threshold was determined by calculating the 99^{th} percentile of the ffADTF-values during 33 carefully selected background IEEG epochs of 10 s. This lead to a uniform threshold equal to 0.053. The ffADTF is applied to all IEEG recordings in the predefined frequency window ranging from 5 Hz to 30 Hz. The connectivity graphs were calculated for each seizure based on the ffADTF.

The presurgical evaluation lead to a selective amygdalo-hippocampectomy 6 years ago. The left hippocampus and amygdala were resected and the patient has been seizure free since.

Four seizure onsets and 29 subclinical seizures were analyzed based on the effective connectivity pattern obtained by the ffADTF. The results of the analysis of 1 seizure onset led to the graph shown in fig. 4.6. The spacing between the vertical lines is 1 second. The information flow is detected if the sample based ffADTF-values exceed the uniform threshold value for more than half of the samples during the considered time window of 1s for visualization purpose. The uniform threshold was set to 0.053 (the 99^{th} percentile of the ffADTF-values of the analyzed background IEEG epochs). Before window A no connections are identified. The seizure is detected by the system during time window A. The seizure starts spreading from LH4-6 to other contact points of the left amygdalo-occipital electrode and towards contact points on LTA and LTM. During the next windows the seizure information spreads to the contact points of all the other intracranial electrodes. The amount of information flow arising from the contact point of the left amygdalo-occipital electrode increases gradually over time. In

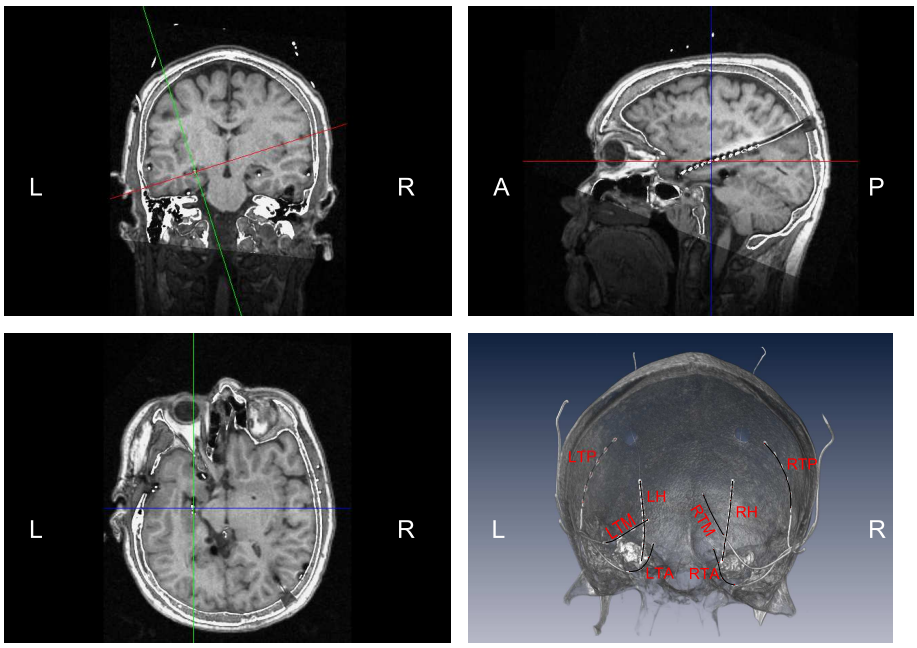


Figure 4.5: A CT image merged with a MR image showing the location of the intracranial electrodes. A rendering of the electrode positions is also shown in the right lower image for visualizing the strip and depth electrodes. Four subdural strips with 4 contact points are placed on the left and right temporobasal area (left anterior: LTA1-4, left posterior: LTM1-4, right anterior: RTA1-4 and right posterior: RTM1-4), two subdural strip with 6 contact points monitor the left and right temporolateral area (left: LTP1-6 and right: RTP1-6) and two amygdalo-occipital depth electrodes with each 12 contact points, respectively LH1-12 and RH1-12, monitor the electrical activity of the left and right amygdala and hippocampus. The intersection of the lines denotes the position of LH5.

window F spreading is seen from LH4-7 to the contact points of all the other electrodes. This shows that the seizure information in the considered frequency band is spread throughout the whole brain.

All the other seizures are analyzed with the same parameter set. In the 3 other seizure onsets as well as in the 29 subclinical seizures, information flow coming from contact points located in the left hippocampus to the other electrodes is observed. The information flow from the hippocampus to the other contact points of the left depth electrode is mainly arising from electrodes LH4, LH5 and LH6. The overall connections during all 4 seizure onsets and 29 subclinical seizures are shown in fig. 4.7. This figure shows the sum of the sample based connections between all the channels during

all seizure onsets and subclinical seizures. At each time point a connectivity graph is derived. Afterwards all the connections between all contact point pairs are summed. Most connections are seen from LH4, LH5 and LH6 to the other contact points of the left amygdalo-occipital depth electrode. There is also a high number of connections from LH4, LH5 and LH6 to the contact points of LTM and LTA. Overall we can clearly see more connections arising from electrode contact points LH4, LH5 and LH6 to all the other electrode contact points. We conclude that the information flow during the seizure onsets and subclinical seizures is mainly coming from LH4, LH5 and LH6 which are located in the left hippocampus and at the border of the left hippocampus respectively.

The left hippocampus and amygdala of the patient were resected approximately 6 years ago and the patient has been seizure free since. The contact points LH1 to LH5 are located in the resected area. Contact point LH6 lies on the border of the resected area (fig. 4.8). The figure shows the merged post-operative MR image and pre-operative CT image. These images were both registered to the pre-operative MR of the patient with depth electrodes implanted and merged afterwards.

The identified epileptogenic zone through connectivity analysis corresponds to the resected area. This indicates that our proposed method is able to correctly identify the left hippocampus as being responsible for the seizure without any history about the seizures and prior knowledge about the placement of the electrodes.

4.5 Discussion

The fundamental frequency of a seizure is patient dependent. In most seizures the fundamental frequency decreases during the seizure. This makes it difficult to predefine a frequency window corresponding to the fundamental frequency in which the connectivity analysis should be performed. During a seizure the power at the fundamental frequency increases drastically. Because of this it is advantageous to incorporate the power spectrum into the connectivity measures.

The integrated ADTF treats every frequency in the predefined frequency interval as equally important: it does not matter how much power the signals contain at that specific frequency. The integrated ADTF sums these values without prioritizing any frequency. This means that within the predefined frequency band all frequencies are considered to be equally important. However, some frequencies are more present in the signals during an epilep-

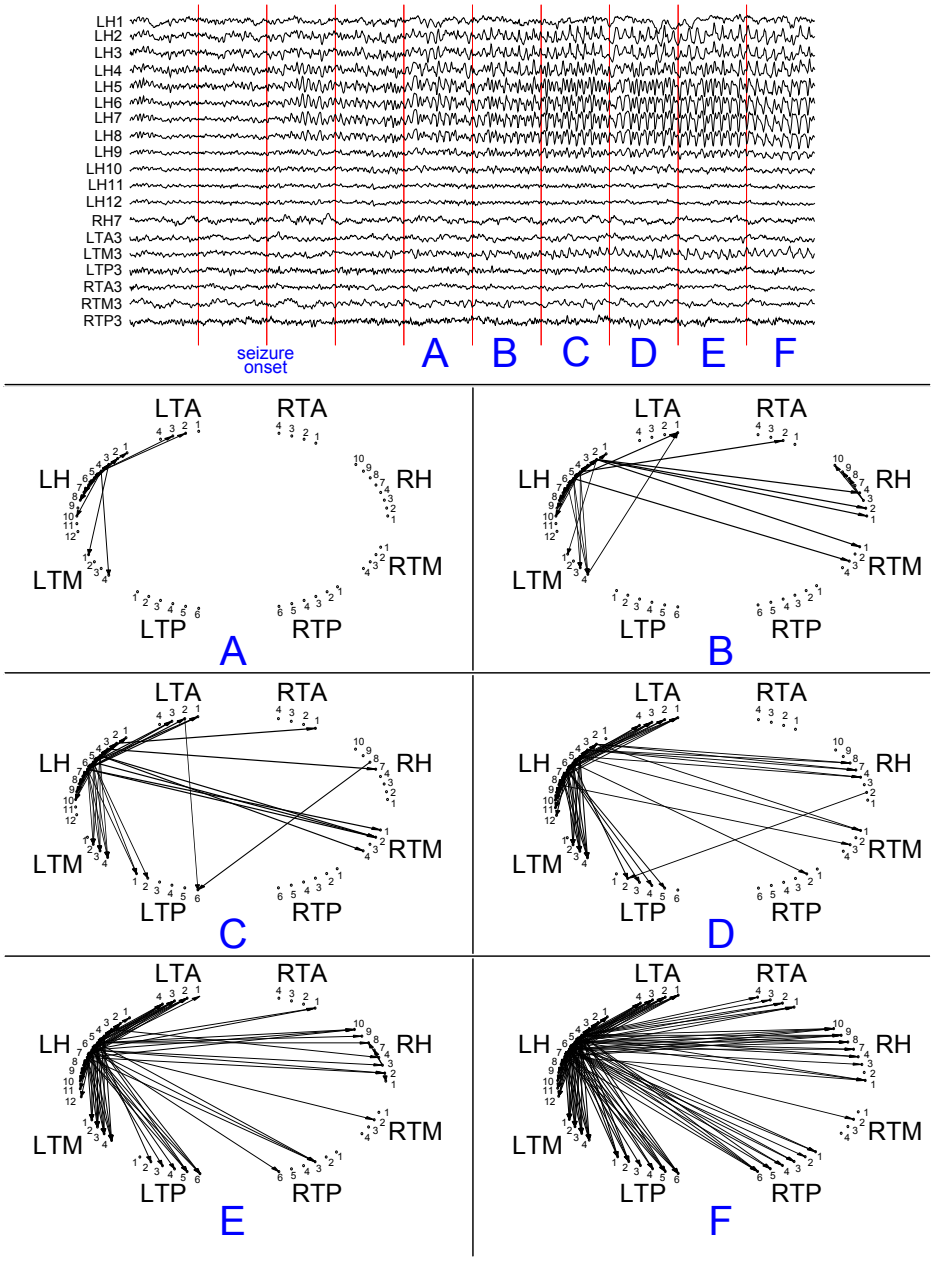


Figure 4.6: The connectivity pattern during 1 seizure onset. At the top the intracranial EEG signals during the seizure are shown. At the bottom each subgraph (denoted by a letter) corresponds to the effective connectivity graph during a 1 second interval defined by the red vertical lines marked on the IEEG signals. The arrows in the subgraph denote a directional connection from one contact point to another.

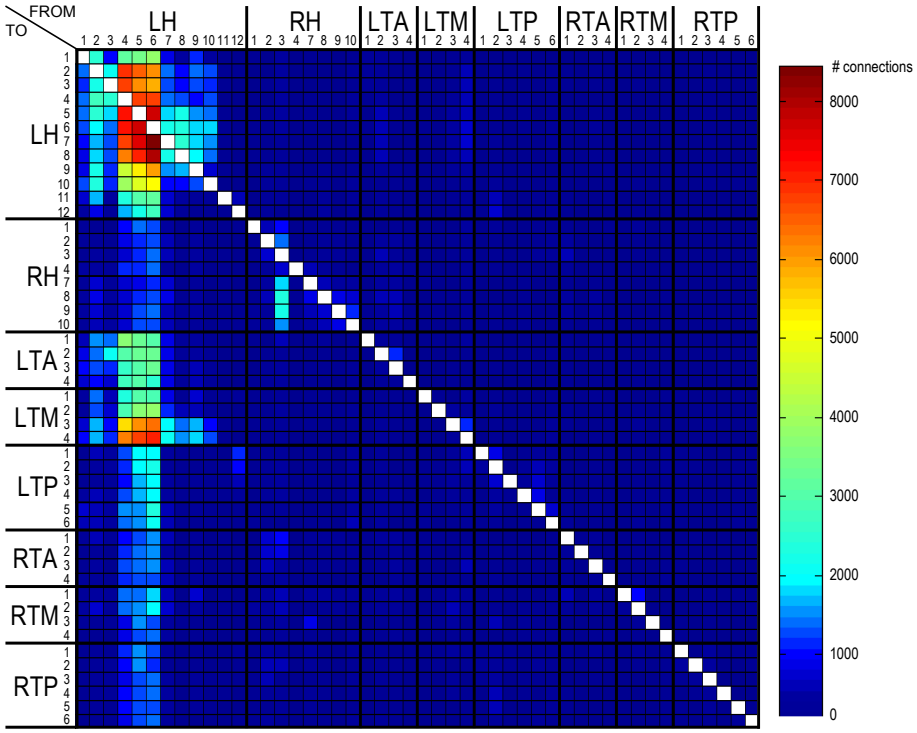


Figure 4.7: Sum of the sample based connections during 4 seizures and 29 subclinical seizures between the different contact points of the intracranial strips and depth electrodes. Most information flow can be seen from LH4, LH5 and LH6 to all other contact points.

tic seizure and should therefore be considered as more important. The proposed masked ADTF and the full frequency ADTF take the frequency information of the signals into account, prioritizing those frequencies which contribute the most to the power of the signals.

The choice of the frequency window in which the seizure is studied becomes irrelevant because the proposed connectivity measures, the mADTF and the ffADTF, automatically prioritize the fundamental frequency of the seizure. To take into account the harmonics corresponding with the fundamental frequency, the ffADTF is most suited. The mADTF provides a mask that only incorporates 5% of the frequencies, namely those with the highest spectral power in the TVAR model. These frequencies usually correspond to frequencies around the fundamental frequency and may disregards the harmonics. The ffADTF will weight the information flow at each frequency corresponding with the signal power at that frequency. This means that

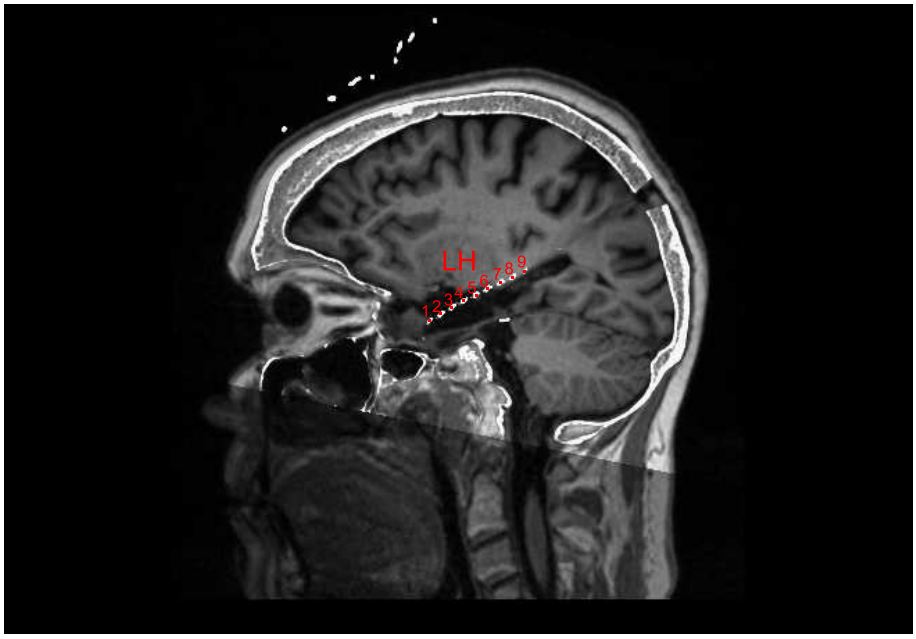


Figure 4.8: Merged post-operative MR image and pre-operative CT image showing the electrode positions with respect to the resected brain area. LH1 to LH5 laid within the resected area, LH6 laid on the border of the resected area.

the harmonics will never have a weight of 0 which can be the case for the mADTF.

In order to assess connections out of the ADTF-values a significance level needs to be set. Two statistical techniques exist to define the significance level under the null hypothesis that the value of the connectivity measure equals zero for time-invariant multivariate autoregressive models (MVAR models). A pointwise significance level based on the asymptotic distribution of the autoregressive coefficients for large sample sizes was established by Eichler for the DTF [61]. Another technique is to use a surrogate dataset to compute the significance level. A common used nonparametric statistical test using surrogate data is described by Theiler [189]. The nonparametric statistical test technique using surrogate data has been applied to the DTF by Ding [56].

Unfortunately the two previously mentioned techniques cannot be easily adapted to the time-variant models (TVAR models). The pointwise significance level is based on the asymptotic distribution of the autoregressive estimates for large sample sizes. We want the TVAR model to quickly adapt

to changes in the dataset, so we indirectly assume a small sample size. This leads to an inadequate estimation of the significance level. The surrogate dataset on the other hand takes into account the complete dataset at once. This means that the temporal information of the model is mixed in the surrogate data which is not desired. Because the above-mentioned techniques are not applicable to connectivity measures derived out of TVAR models, we decided to use a uniform threshold as significance level. The value of the threshold varied from 0 to 1 during the simulations to take the effect of the changing uniform threshold on the estimated connectivity pattern into account. This way we do not bias any calculated connectivity measure by assuming a fixed threshold value.

The use of a fixed threshold leads to an unweighted connectivity pattern analysis. The outgoing connections from each node are given the same strength if the corresponding ffADTF-values are higher than the uniform threshold. We give the same connection strength to all derived connections because we want to emphasize the spreading of the seizure instead of the connection strength between the brain areas.

The use of ROC-curves to compare different connectivity measures during simulations is emphasized. This quantifies the suitability of a connectivity measure applied to a specific situation, in our case the onset of an epileptic seizure. Because of the high sensitivity and specificity we showed that effective connectivity measures are suited to be applied to multichannel IEEG recordings.

By using ROC-curves during realistic simulations the effect of certain parameters can be easily investigated. By considering all possible values of the different parameters the intrinsic performance of the connectivity measure can be evaluated. Out of the ROC-curves the best operating point of the method can be derived. This leads to a good approximation of the parameters when applied to real datasets.

The update coefficient (UC) is a parameter of the Kalman filtering algorithm determining the adaptation speed of the update procedure for the state. The higher the UC, the quicker the autoregressive model will respond to changes in the dataset. However, a higher UC will also lead to more unwanted changes of the model caused by noise present in the dataset. An increase in UC will thus lead to an increase in true positives but also an increase in false positives. The false negatives as well as the true negatives will decrease in this case. This will lead to an increase in sensitivity but a decrease in specificity. A lower UC corresponds with an increase of false negatives and true negatives but a decrease of false positives and true positives.

This results in an increase in specificity and a decrease in sensitivity.

The uniform threshold is a parameter set to assess the connectivity graph out of the calculated values of the different ADTFs. A higher uniform threshold will lead to a decrease of true positives and an increase of false negatives, resulting in a decreasing sensitivity. In this case the number of true negatives will rise and the number of false positives will drop, which results in an increase of specificity. A lower uniform threshold leads to an increase of true positives and false positives, but a decrease of true negatives and false negatives. This leads to an increase in sensitivity but a decrease in specificity.

The model order can be seen as the frequency resolution of the system. A model order of 2 is sufficient to describe the desired frequency content in the simulated dataset. A higher model order enables the TVAR model to better describe and delineate high frequencies present in the signals. In the simulations the signal power can be adequately described using a model order equal to 2, which makes the use of a high order not necessary. In the realistic dataset more variable frequency content is present which implies the use of a higher model order. The model order is set to 5, because this gives us the desired frequency resolution with an acceptable computational time.

For the analysis of the real intracranial dataset a small update coefficient is used (0.001) because this leads to a decrease of false positives. On the other hand with a smaller UC less true positives will be seen, but still enough to pinpoint the area responsible for the seizure. We choose a low UC because we don't want the model to adapt to all the abrupt changes in the dataset. A connection will only be seen if the change in the dataset is maintained.

Previous studies [71, 70, 229] investigated a stationary window during a seizure. However, the leading region during this stationary window does not need to be the epileptogenic region responsible for the onset of the seizure. That is why is of uttermost importance to include the onset of the seizure in the effective connectivity analysis. This study is to our knowledge the first study to analyze the connectivity pattern during the non-stationary onset of an epileptic seizure. The short-windowed approach such as proposed by Ding et al. [57] is a time-variant extension of the DTF. However, due to the assumption that the data within the short window is stationary the results will be inferior to the results obtained by the proposed method using the Kalman filtering algorithm.

The same [5, 30 Hz] window was used to analyze all seizures and sub-

clinical seizures. The epileptic activity is clearly seen in the spectra of the signals estimated by time-variant autoregressive analysis. During a seizure the manifestation of the epileptic activity in the signals in the frequency band [5, 30 Hz] is much higher than the manifestation of the normative brain function. This ensures us that the patterns we derived model the epileptic activity present in the data.

The connectivity pattern derived during multiple seizure onsets is a helpful tool for the neurologist and neurosurgeon and could improve the accuracy of the epileptogenic focus localization. For example, the neurosurgeon can ablate the brain area around the electrode contact pinpointed by the connectivity analysis as the driver of the seizure. This way more brain tissue can be preserved and less functionality will be lost.

The connectivity analysis can easily be disturbed by artifacts in the considered signals. Fortunately intracranial signals have a high signal to noise ratio and contain very few artifacts.

The technique presented in this chapter makes it possible to calculate effective connectivity on-line. This could be useful for a Deep Brain Stimulation closed loop system to repress upcoming seizures. The on-line effective connectivity pattern could point to the leading brain region during an upcoming seizure, resulting in a stimulation pulse at that specific electrode. Another application of on-line effective connectivity analysis is the use of the connectivity measures in an invasive Brain-Computer-Interface application. In this way connectivity patterns can be linked to specific actions taken by the output device.

4.6 Conclusion

In this chapter the framework to estimate the SOZ out of ictal IEEG recordings is presented. Furthermore, the applicability of connectivity analysis based on the ADTF to locate the epileptogenic focus out of IEEG recordings of seizure onsets is investigated. Different normalizations of the ADTF (the iADTF, mADTF and ffADTF) are compared during simulations using sensitivity and specificity. We proved the benefit of incorporating the frequency content of the data into the connectivity measures.

We applied the ffADTF to 4 seizure onsets and 29 subclinical seizures of the same patient. The results obtained by the ffADTF were concordant with postsurgical finding. Our proposed method is able to correctly identify the left hippocampus as being responsible for the seizure without any history

about the seizures and any prior knowledge about the placement of the electrodes. We showed that the connectivity pattern during the seizure onset can provide useful information about seizure propagation and can possibly improve the accuracy of the presurgical evaluation in patients with refractory epilepsy.

4.7 Original contributions

The results of this chapter were presented at 1 national conference [194] and various international conferences [201, 202, 199]. The results were published in the A1 journal *NeuroImage* [209].

Chapter 5

Seizure onset zone localization in the intrahippocampal kainic acid rat model of epilepsy

5.1 Introduction

In the previous chapter we designed the framework to estimate the time-variant effective connectivity pattern of non-stationary signals. The framework uses Kalman filtering to estimate the time-variant TVAR coefficients. Three connectivity measures were introduced based on these coefficients, the iADTF, mADTF and the ffADTF. They differ in the way the frequency content of the signals are incorporated into the connectivity pattern. For the iADTF each frequency in the considered band is equally important, while the mADTF only considers 5% of the frequencies in the considered frequency band at each time point. The ffADTF has a weighting that stresses connections with high power spectral at the receiving signals. We showed by simulation that the ffADTF outperforms both the iADTF and the mADTF. Furthermore we showed the feasibility of ffADTF analysis to localize the SOZ in 1 patient from ictal IEEG recordings.

In this chapter a new time-variant effective connectivity measure is introduced, the spectrum weighted ADTF (swADTF). Here connections are stressed with high spectral power both in the receiving and in the sending signal. We will test the performance of the swADTF by simulations.

Furthermore we will investigate the applicability to localize the SOZ in a small animal model of epilepsy. We will compare the result of the developed method with the scoring of an expert electrophysiologist.

Additionally we investigated another technique to estimate the TVAR coefficients, namely the sliding window technique as proposed by Ding et al. [57]. They applied their methodology to visuomotor ERPs and showed that the technique is capable of revealing task-relevant patterns of cortical interdependency during different stages of cognitive processing. In this chapter we will compare the sliding window technique with the already implemented Kalman filtering algorithm. We will investigate which method is preferred to estimate the time-variant effective connectivity measures by simulation and in a small animal model of epilepsy to localize the SOZ from ictal IEEG recordings.

5.2 Method

In this section we will describe how the coefficients are estimated based either on the sliding window technique or the Kalman filtering technique. We will introduce the swADTF and show how graph analysis facilitates SOZ localization.

5.2.1 Estimation of the TVAR model coefficients

Two techniques to estimate the TVAR model coefficients will be used, the sliding window technique and the Kalman filtering algorithm.

5.2.1.1 Sliding window

The sliding window technique uses a sliding window with length WL that slides over the complete dataset. At each time point t_0 the epoch in the interval $[t_0 - \mathrm{WL} + 1, t_0]$ is selected and for each epoch a MVAR model is estimated. This explicitly assumes that the data in the considered epoch is stationary. By using a small WL the dynamics of the time series can be captured more optimally but the estimation of the coefficients is based on less samples which can result in more noisy estimates of the coefficients.

5.2.1.2 Kalman filtering

The Kalman filtering algorithm is an elegant technique to estimate the coefficients of the TVAR model [8]. We extended the implementation of the Kalman filtering algorithm explained in section 4.2.2 with a Kalman smoothing procedure [8]. The Kalman smoothing term was set to 100 and kept constant during the remainder of this chapter.

5.2.2 The spectrum weighted Adaptive Directed Transfer Function (swADTF)

By using either the described sliding window technique or the Kalman filtering, the integrated Adaptive Directed Transfer Function (iADTF) [57, 230, 11] can be calculated in a certain frequency band $[f_1, f_2]$ out of the time-variant transfer matrix (eq. 4.25). The normalization of the iADTF makes each frequency contribute equally to the results. This suggests that each frequency is equally important even if there is no spectral power at a particular frequency f_0 in signal $\mathbf{x}_i$ at time t_0. In this case the term $|\mathbf{H}_{ij}(f_0, t_0)|^2$ will be low, but the other terms at the same frequency $|\mathbf{H}_{ik}(f_0, t_0)|^2$ with $k = 1 \ldots K$ and $k \neq j$ may be even lower. This would lead to a high value of information flow (close to 1) although there is not much power in the signal $\mathbf{x}_i$ at that frequency f_0 at time t_0.

To overcome this issue another normalization method was proposed by Korzeniewska et al. [118] named the full frequency DTF with corresponding time-variant version, the full frequency ADTF (ffADTF) (eq. 4.30). The normalization is performed in such a way that $|\mathbf{H}_{ij}(f_0, t_0)|^2$ at each frequency is normalized with respect to the total power of the receiving signal $\mathbf{x}_i$ in the studied frequency band. This implies that there is a weighting that respects the power of the receiving signal $\mathbf{x}_i$ but neglects that of the sending signal $\mathbf{x}_j$.

A more complex normalization incorporation both 'sending and receiving' power spectra can be constructed as:

$$\mathbf{swADTF}_{ij}(t) = \int_{f=f_1}^{f_2} \frac{|\mathbf{H}_{ij}(f,t)|^2 \, \hat{\mathbf{S}}_{jj}(f,t)}{\sum_{k=1}^{K} \int_{f'=f_1}^{f_2} |\mathbf{H}_{ik}(f',t)|^2 \, \hat{\mathbf{S}}_{kk}(f,t)}$$

$$= \int_{f=f_1}^{f_2} \frac{|\mathbf{H}_{ij}(f,t)|^2 \sum_{l=1}^{K} |\mathbf{H}_{jl}(f,t)|^2}{\sum_{k=1}^{K} \int_{f'=f_1}^{f_2} \left|\mathbf{H}_{ik}(f',t)\right|^2 \sum_{s=1}^{K} \left|\mathbf{H}_{ks}(f',t)\right|^2} \tag{5.2}$$

We will call this time-variant connectivity measure the spectrum weighted ADTF (swADTF). Each element $|\mathbf{H}_{ij}(f_0, t_0)|^2$ is weighted by the power present in the sending signal, namely $\hat{\mathbf{S}}_{jj}(f_0, t_0)$. This additional term in the normalization implies that information flow can only be seen at a certain frequency if the power in the sending signal at that frequency is large enough.

All three time-variant variations of the DTF, namely the iADTF eq. 4.25, ffADTF eq. 4.30 and swADTF eq. 5.1, are normalized in such a way that the value at each time point t always lies between 0 and 1. A higher value indicates that there is more information flow. Furthermore, they are normalized in a way that the inflow into each signal is equal to 1 at each time point:

$$\sum_{k=1}^{K} *\mathbf{ADTF}_{ik}(t) = 1 \tag{5.3}$$

in which $*\mathbf{ADTF}$ is either the iADTF, ffADTF or swADTF.

5.2.3 Graph analysis

The different normalizations of the ADTF lead to time-variant connections with a strength in the interval [0, 1] between all signals. We assume that there is a connection from $\mathbf{x}_j$ to $\mathbf{x}_i$ at time t if the corresponding iADTF, ffADTF or swADTF-value is higher than a pre-defined threshold.

$$\begin{aligned} *\mathbf{ADTF}_{ij}(t) \geq \theta_{ij} &=> \mathbf{C}_{ij}(t) = 1 \; ; \; \forall \; i,j = 1 \; ... \; K \\ *\mathbf{ADTF}_{ij}(t) < \theta_{ij} &=> \mathbf{C}_{ij}(t) = 0 \; ; \; \forall \; i,j = 1 \; ... \; K \end{aligned} \tag{5.4}$$

The threshold θ can either be uniform (the same for all connections) or connection specific. The matrix $\mathbf{C}_{ij}(t)$ is the adjacency matrix and represents

the directed edges between all signals over time.

The out-degree of each signal, i.e. the number of outgoing connections from that signal to all the other signal, is calculated from the adjacency matrix. The out-degree of signal $\mathbf{x}_j$ at time t is noted as $\phi_J(t)$:

$$\phi_J(t) = \sum_{k=1,k\neq j}^{K} \mathbf{C}_{kj}(t) \tag{5.5}$$

The sum of the out-degree of signal $\mathbf{x}_j$ over the time points of an interval $[t_1, t_2]$ depicts the number of outgoing connections during that time interval:

$$\begin{aligned} \mathbf{\Phi}_J &= \int_{t=t_1}^{t_2} \phi_J(t) \\ &= \int_{t=t_1}^{t_2} \sum_{k=1,k\neq j}^{K} \mathbf{C}_{kj}(t) \end{aligned} \tag{5.6}$$

The higher this integrated out-degree, the more information flow arose from that signal in the considered time interval and thus the more likely this is the origin of information flow during that time interval.

5.3 Simulations

5.3.1 Setup

We simulated the onset of a seizure in 4 IEEG channels with 6 different spreading patterns over time (A, B, C, D, E and F). The overview of the simulation models is shown in fig. 5.1 panel A. The time series have a length of 8 s and a sampling frequency of 200 Hz. In all 4 channels 1/f-activity is present during the whole time series. At time point 0 s, seizure activity starts in channel 1 and spreads to channels 2, 3 and 4 at time t_1, t_2 and t_3 with a sample delay of δ_1, δ_2 and δ_3 respectively. How the channels are interconnected is defined by the simulation model. In model A, the connections are from channel 1 directly to channels 2, 3 and 4, while in model F there is a cascade flow from channel 1 to channel 2 to channel 3 and eventually to channel 4. The seizure activity is modeled as a sinusoid with fundamental frequency ranging from 12 Hz at time 0 s to 8 Hz at 5 s and its corresponding second and third harmonics. The SNR of the seizure

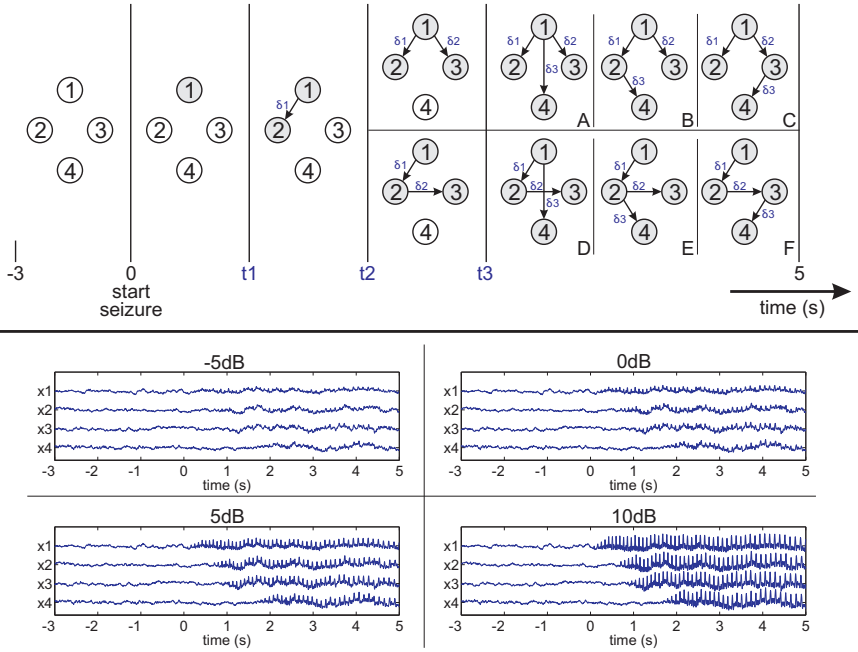


Figure 5.1: The upper panel depicts the simulation scheme of the different spreading patterns during the onset of a seizure. The nodes are depicted in white if only 1/f activity is present and in gray if there is 1/f activity plus seizure activity. During the first 3 s there is 1/f activity in all 4 channels. The seizure starts at time point 0 in signal 1 and spreads to signal 2 at time t_1 with sample delay δ_1. At time t_2 the seizure spreads to signal 3 either from signal 1 or from signal 2 with sample delay δ_2. At time t_3 the seizure spreads to signal 4 either from signal 1, 2 or 3 with sample delay δ_3. This results in 6 different possible spreading patterns over time (A, B, C, D, E and F). The lower panel depicts an example simulated dataset of model A at -5, 0, 5 and 10 dB.

activity to the 1/f-activity ranged from -5 dB to 10 dB. White measurement noise with a signal to noise variance of 0.08 [103] is added to all channels.

In total, 100 different values were generated for t_1, t_2, t_3, δ_1, δ_2 and δ_3. The values for the seizure spreading times t_1, t_2, t_3 were randomly chosen in the intervals [0 s, 1 s], [t_1, t_1+1 s] and [t_2, t_2+1 s] respectively. The values for the sample delays δ_1, δ_2 and δ_3 are randomly chosen between 1 and 5 samples. Out of these values each of the 6 simulation models was constructed for each SNR (-5 dB to 10 dB). This led to 100 different simulated IEEG datasets for each model (A, B, C, D, E and F) for each SNR level. Examples of the generated signals for model A at -5, 0, 5 and 10 dB are shown in fig. 5.1 panel B.

5.3.2 Processing

The simulated signals were decimated from 200 Hz to 100 Hz using a specific resampling procedure for time-variant autoregressive models [175] and normalized afterwards (mean set to 0 and standard deviation to 1). The iADTF, ffADTF and swADTF were computed with both the sliding window and the Kalman filtering technique with p = 8, WL = 100 or UC = 6*10^{-4} in the frequency band [3, 40 Hz] incorporating both second and third harmonic of the seizure activity.

The iADTF, ffADTF and swADTF values calculated for each simulated dataset can be thresholded using an a priori defined threshold to obtain the corresponding time-variant adjacency matrix. Since we want to avoid using prior information about the threshold, we considered all possible thresholds ranging from 0 to 1 with stepsize 0.01. In this way 101 adjacency matrices were obtained for each simulation. These time-variant adjacency matrices were compared to the simulated reference model, in which all information flow originated from channel 1.

The sample based sensitivity and specificity were calculated for all resulting adjacency matrices corresponding to each threshold value. The EER point was computed from these values. The lower the EER, the better the performance. For each model (A to F) and each SNR (-5 to 10 dB) the EERs were averaged over the 100 simulations.

5.3.3 Simulation results

The resulting EERs for each simulation model (A, B, C, D, E and F) at each SNR are shown in fig. 5.2. The subscript SL and KF indicate that the parameters of the TVAR model are estimated either with the sliding window technique or the Kalman filtering algorithm respectively. We notice that all 6 connectivity measures perform worse if there is more indirect flow in the model. More indirect flow leads to more erroneous connections especially for the measures calculated using the sliding window technique.

Overall we can clearly see that the sliding window technique is outperformed by the Kalman filtering algorithm. The EERs of the iADTF$_{KF}$, ffADTF$_{KF}$ and swADTF$_{KF}$ are always lower (perform better) than those of the iADTF$_{SL}$, ffADTF$_{SL}$ and swADTF$_{SL}$ respectively.

For SNR's higher than 2 dB the ffADTF$_{KF}$ and the swADTF$_{KF}$ outperform the iADTF$_{KF}$. This is because both connectivity measure prioritize frequencies with a higher spectral power in their normalization. Since these

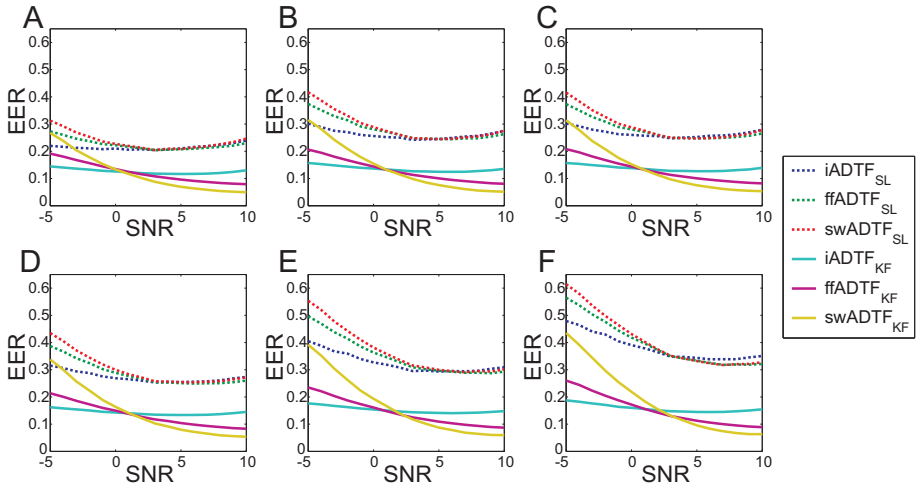


Figure 5.2: The EERs for the iADTF, ffADTF, swADTF calculated using the sliding window technique (SL) or using the Kalman filtering algorithm (KF) for the 6 different simulation models. The connectivity measures calculated with the Kalman filtering algorithm outperform those calculated with the sliding window technique. For high SNRs the swADTF$_{KF}$ performs the best.

frequencies correspond to the frequencies of the spreading seizure activity we gain in sensitivity and specificity. The largest gain is found for the swADTF$_{KF}$ at the highest SNRs. For low SNR values (smaller than 0) both ffADTF$_{KF}$ and swADTF$_{KF}$ prioritize the frequencies corresponding to noise and therefore perform worse than the iADTF$_{KF}$.

In real seizures however, the SNR tends to be higher than 2 dB. This suggests that the swADTF$_{KF}$ would perform better than the others in realistic ictal datasets. In fig. 5.3 the mean EER values for the iADTF$_{KF}$, ffADTF$_{KF}$ and swADTF$_{KF}$ for the 6 different simulation models are shown in the same axes. For a SNR higher than 3 dB, the swADTF$_{KF}$ outperforms both the iADTF$_{KF}$ and the ffADTF$_{KF}$. The difference in EER values between the 6 models stays the same for the iADTF$_{KF}$ over the different SNR levels. However, for the ffADTF$_{KF}$ and swADTF$_{KF}$ the difference in EER between the 6 models decreases with a higher SNR.

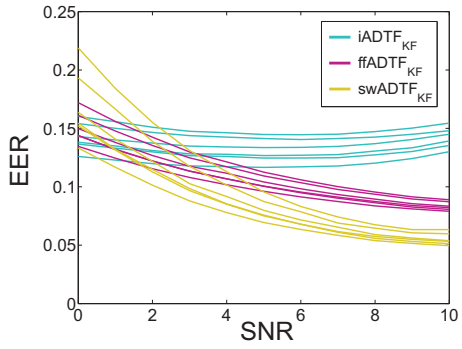


Figure 5.3: The EERs for the connectivity measures estimated with Kalman filtering for all 6 models. For a SNR higher than 3 dB the swADTF$_{KF}$ outperforms the iADTF$_{KF}$ and the ffADTF$_{KF}$. The ffADTF$_{KF}$ outperforms the iADTF$_{KF}$ for an SNR higher than 2 dB.

5.4 Pre-clinical experiment

5.4.1 Animal models of epilepsy

Although epilepsy can be classified into several groups, each patient will still have his own specific seizures. Meaning that the seizures of each patient differ and even intrapatient there are differences between multiple seizures. Also the epileptogenis in each patient is different and the patients usually come to the clinic after having at least one seizure. This makes it cumbersome to do a controlled group study and to study epileptogenesis.

An animal model of epilepsy is a model in which a precipitating controlled event triggers the epileptogenesis resulting in spontaneous seizures. Using an animal model of epilepsy has a number of advantages to study epilepsy: (i) the initial precipitating event triggering epileptogenesis can be controlled; (ii) epileptogenesis leading to spontaneous seizures can be studied; (iii) data can be acquired from the baseline period prior to the epileptogenesis; (iv) a controlled group study can be performed.

The animal models of epilepsy can be divided into genetic animal models and models where seizures are induced in healthy animals. An overview of different animal models of epilepsy adapted from [130] is shown in fig. 5.4. In healthy animals acute or chronic seizures can be induced electrically or chemically. However, not all models are shown in the figure, for instance models in which recurrent spontaneous seizures develop after traumatic brain injury, ischemic brain damage or febrile seizures [164] are not shown.

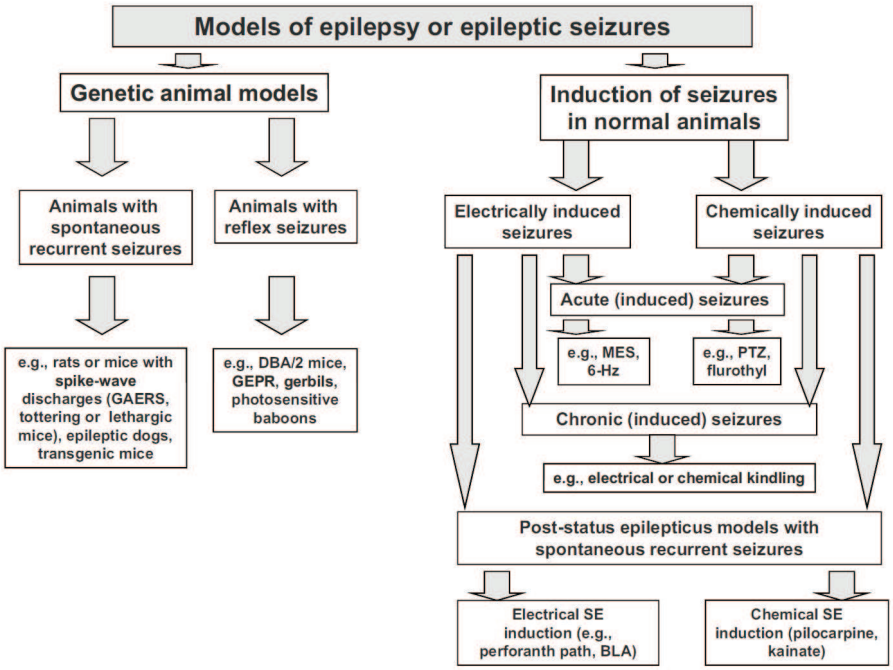


Figure 5.4: The subdivision of the animal models of epilepsy (adapted from [130]).

5.4.2 The intrahippocampal kainic acid rat model of epilepsy

The intrahippocampal kainic acid (KA) rat model is a model of temporal lobe epilepsy. It is a post-status epilepticus (SE) model with spontaneous recurrent seizures in which the SE is chemically induced by the injection of KA into the right hippocampus. KA is a glutamate receptor agonist, inducing hyperexcitation in neurons leading to cell damage (excitotoxicity). The injection of KA is the initial precipitating insult to the brain that triggers epileptogenesis. During the SE continuous epileptiform activity is recorded for several hours from the injected hippocampus. As a result of the KA injection and the subsequent SE the hippocampus displays the typical structural/metabolic changes as seen in human TLE such as hippocampal sclerosis (neuronal loss and gliosis), inflammation, axonal and dendritic reorganization. After a latent period, ranging from several days to several weeks, the rats display spontaneous epileptic seizures [33, 168]. The pathological process and underlying mechanisms involved in epileptogenesis are still not fully understood [220]. In fig. 5.5 the time line of the KA rat model of epilepsy is shown.

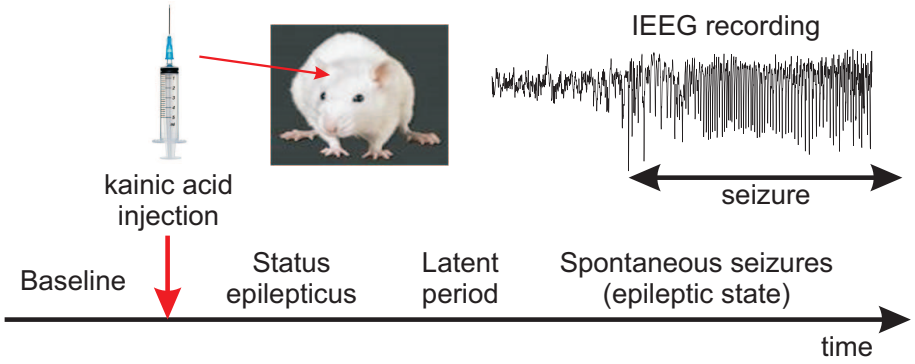


Figure 5.5: The kainic acid rat model of temporal lobe epilepsy. KA is injected into the right hippocampus of a healthy rat inducing a status epilepticus. After a latent period the rats will have spontaneous epileptic seizures.

5.4.3 Intracranial EEG recordings of seizures in rats

Kainic acid (0.4g/0.2 l) is unilaterally injected in awake rats (n=11) through a cannula implanted in the right hippocampus (AP = - 5.6 mm, ML = + 4.5 mm, DV = -5.5 mm relative to bregma). As a consequence of the KA injection the rats developed a status epilepticus and spontaneous seizures after a latency period of several weeks.

At the time of cannula implantation, two depth electrodes (separated with 0.5 mm) were implanted in the right hippocampus (dr1, dr2); one depth electrode was placed in the left hippocampus (dl) and one epidural electrode was placed over the right frontal cortex (fr) (fig. 5.6). In total 230 seizures were recorded. The EEG sampling frequency was 200 Hz. The expert electrophysiologist scored all seizures and indicated from which hippocampus (left/right) they initiated based on the IEEG.

5.4.3.1 Choice of parameters: p, WL and UC

Before the coefficients of the TVAR model can be calculated we need to define the model order p. Furthermore we need to define the WL and the UC for the sliding window technique and the Kalman filtering algorithm respectively.

The choice of these parameters is not straightforward. It can be based on the minimization of the variances of the residuals plus an additional term penalizing the number of variables that need to be estimated. Two of the most used criteria are the Akaike Information Criterion [4] and the Schwarz's

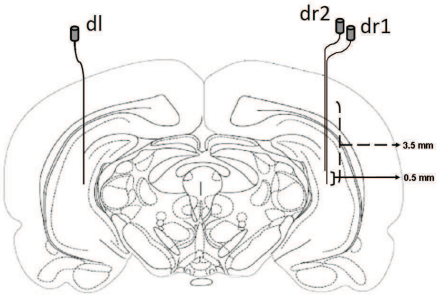


Figure 5.6: The implantation of the two depth electrode into the left (dl) and right (dr1 dr2) hippocampus shown in a coronal slice representation of the brain. The rat also had a epidural electrode over the frontal cortex (not shown in figure).

Bayesian Criterion [178] (section 3.4.1.1).

However, in this chapter we chose a different strategy. The parameters choice of both techniques is based on the inspection of the autospectra of the signals and not on a criterion. By inspecting the time-variant autospectra of the signals derived from the TVAR coefficients we can observe if the frequency information of the signals is adequately modeled.

The choice of the parameters to calculate the TVAR coefficients was based on the visual inspection of the spectrograms of an ictal IEEG recording. We calculated the autospectra based on the TVAR model using a parameter sweep (p = 5 to 10, WL = 20 to 120 in step of 20, UC from 0.0001 to 0.001 in steps of 0.0002). The spectrograms resulting from the parameters sweep during an example epoch are shown in fig. 5.7. A model order equal to 8 was sufficient to adequately model the frequency content up to 40 Hz. The WL was set to 100 (=1 s) and the UC was set to 0.0006. With these parameters the dynamics of the time series were captured without overfitting. These values are used during the remainder of this chapter.

5.4.4 SOZ localization from the ictal IEEG recordings

An example of a recorded seizure is shown in fig. 5.8. For the purpose of this study we added an electrophysiological marker depicting the time point of first spread of rhythmic activity, with fundamental frequency between 3Hz and 20 Hz, based on the spectrograms of all 4 signals. The marker indicates the presence of rhythmic epileptic activity in at least 2 channels and was used as start point of our analysis because we wanted to investigate the network during the first few seconds of the rhythmic ictal activity spread.

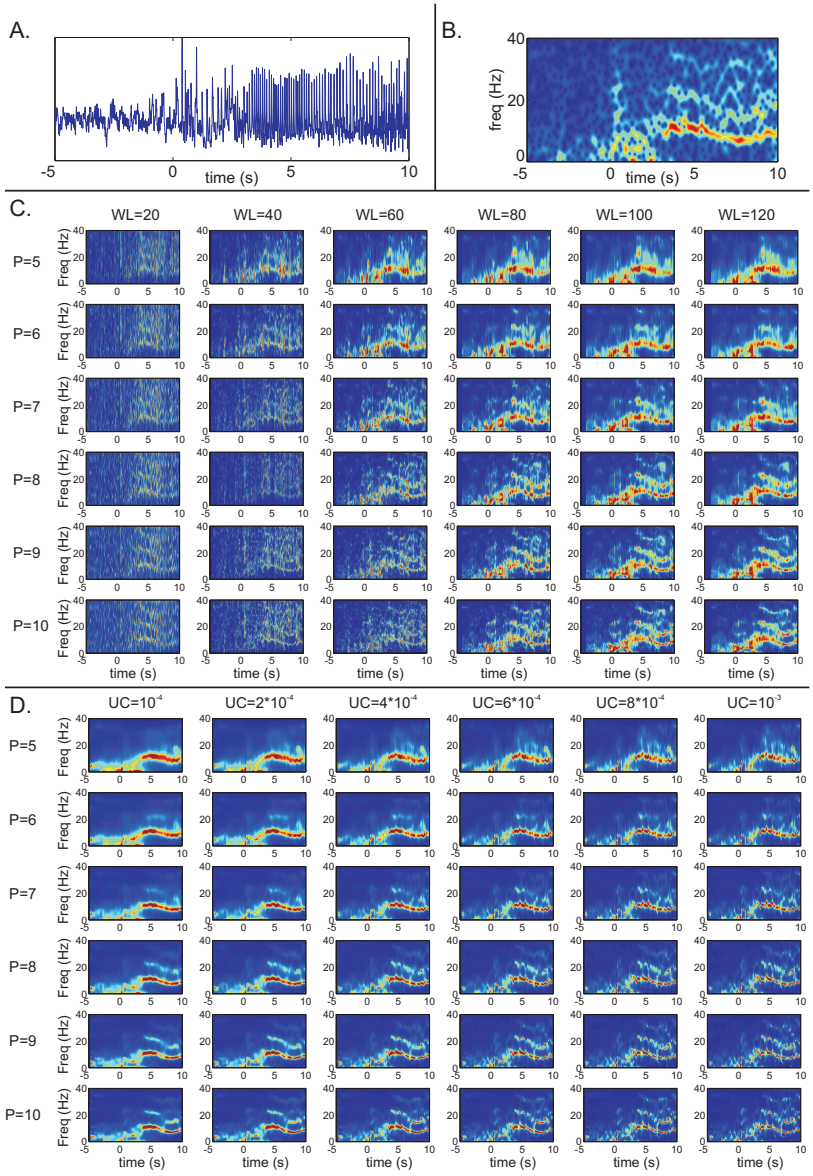


Figure 5.7: Spectrograms of an example IEEG seizure epoch estimated out of the TVAR coefficients using different parameters. Panel A: the IEEG signal recorded in a rat during a seizure; Panel B: The spectrogram of the signal using the short-time Fourier transform; Panel C: Spectrogram computed out of TVAR coefficients using the sliding window technique with different model orders (p) and window lengths (WL); Panel D. Spectrogram computed out of TVAR coefficients using the Kalman filtering technique with different model orders (p) and update coefficients (UC).

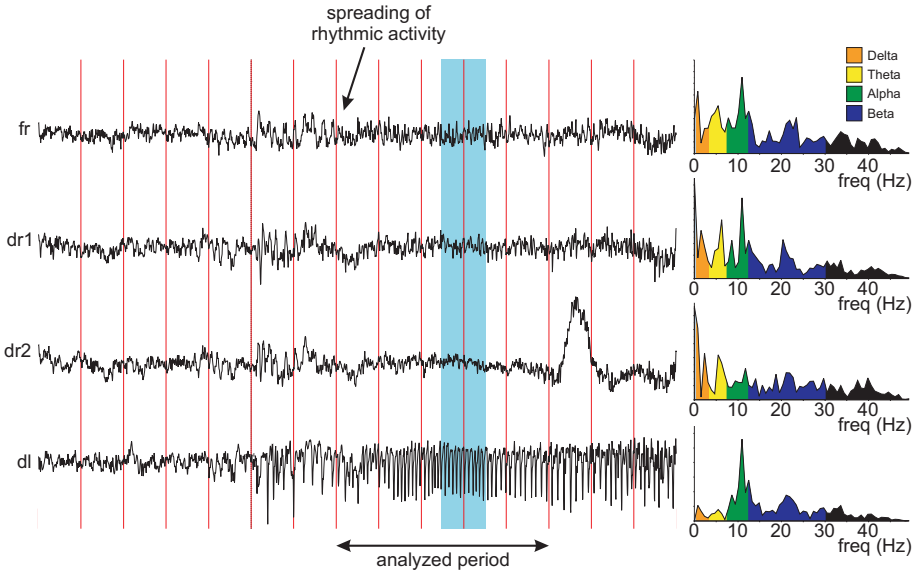


Figure 5.8: An example of a recorded seizure in the intrahippocampal kainic acid rat model of epilepsy (fr: right frontal, dr1 and dr2: right hippocampus, dl: left hippocampus). The spectra of the 4 channels during the blue window is shown on the right. The 5 s after the time point when rhythmic activity is present in more than 1 channel are used as input for the connectivity analysis.

Therefore it is necessary that this rhythmic epileptic activity is present in at least two or more channels.

We segmented for all 230 seizures the 5 s following the marked starting point. The 50 Hz power line artifact was filtered using a notch filter. The resulting signals were decimated to 100 Hz with a specific resampling procedure for time-variant autoregressive models [175] and were normalized afterwards. The iADTF, ffADTF and swADTF of the resulting signals were calculated with parameters: p = 8, WL = 100 or UC = 6*10^{-4} and the frequency band equal to [3, 40 Hz] using both the sliding window and Kalman filtering technique.

The adjacency matrices were calculated using eq.5.4 with connection specific thresholds based on connectivity analysis of interictal epochs. We selected 100 interictal epochs of 5 s and processed them in the same manner as the ictal epochs for each rat individually. The 99 percentile of each specific connection was calculation and used as threshold for that specific connection. Afterwards the integrated out-degree over the 5 s was calculated using eq.5.6 and the electrode contact with the highest out-degree was

identified as SOZ and compared to the scoring of the electrophysiologist.

5.4.5 Results

The electrophysiologist scored all 230 seizures of the 11 rats. In 6 out of the 11 rats seizures originated from both hippocampi independently. In 3 rats seizures originated from the right hippocampus and in 2 rats only from the left hippocampus. The channel with the highest out-degree was depicted as being the driver behind the seizure and was compared to the scoring of the electrophysiologist. The global results for all rats are depicted in table 5.1. It can clearly be noticed that the swADTF$_{SL}$ and swADTF$_{KF}$ have much better overall performance than the others, especially for depicting the driver of left hippocampal onset seizures. The measures based on Kalman filtering also outperform those based on the sliding window technique.

To investigate why so many left-sided onset seizures are missed by the iADTF, ffADTF and not by the swADTF we will study the seizures of rat 3 in more detail. In this rat almost none of the seizure originating from the left hippocampus were correctly localized by iADTF and ffADTF analysis. The out-degree of the 6 connectivity measures for the 7 different seizures of rat 3 are shown in fig. 5.9. It can clearly be seen that all connectivity measures have the same behavior for seizures with right hippocampal onset. However, for left hippocampal onset seizures only the swADTF$_{SL}$ and swADTF$_{KF}$ are able to correctly identify the SOZ in 3 and in 4 out of 4 seizures respectively.

To understand the basis of the large difference in left hippocampal SOZ localization between the iADTF$_{KF}$, ffADTF$_{KF}$ and the swADTF$_{KF}$ we inspected the connections in the frequency domain. fig. 5.10 shows the connections in the frequency domain for seizure 3 of rat3. The spectrogram of the signals is shown in the diagonal boxes. The off-diagonal boxes show the connections between the different channels for the different connectivity measures. The sum of the images over the frequency axis eventually leads to the corresponding iADTF$_{KF}$, ffADTF$_{KF}$ and swADTF$_{KF}$ values, meaning that the terms of the frequency sum in eq.4.25, 4.30 and 5.1 are depicted here.

We noticed spurious connections at frequencies that are not even present in the signals for the iADTF$_{KF}$ compared to the ffADTF$_{KF}$ and the swADTF$_{KF}$. For instance the connections from dr1 to dl at high frequencies from 5 to 10 s. There is much connectivity seen at frequencies between the fundamental seizure frequency and its second harmonic and in between the second and third harmonic. The ffADTF$_{KF}$ already weights the frequen-

Table 5.1: Identification of the driver of 230 seizures in 11 rats by the different connectivity measures. The numbers depict the amount of correctly localized SOZ compared to the visual classification of the electrophysiologist. The three bottom rows depict the percentage correctly localized SOZ for seizures originating from the right hippocampus (RH), the left hippocampus (LH) and overall respectively.

	iADTF$_{\mathrm{SL}}$	ffADTF$_{\mathrm{SL}}$	swADTF$_{\mathrm{SL}}$	iADTF$_{\mathrm{KF}}$	ffADTF$_{\mathrm{KF}}$	swADTF$_{\mathrm{KF}}$
	Seizures originating from right hippocampus					
rat1	3/4	4/4	4/4	4/4	4/4	4/4
rat2	6/6	6/6	6/6	5/6	5/6	6/6
rat3	2/2	2/2	2/2	2/2	2/2	2/2
rat4	1/3	1/3	2/3	2/3	2/3	3/3
rat5	7/12	7/12	12/12	5/12	7/12	12/12
rat6	-	-	-	-	-	-
rat7	10/11	10/11	10/11	10/11	8/11	8/11
rat8	-	-	-	-	-	-
rat9	8/8	8/8	8/8	7/8	7/8	7/8
rat10	13/14	13/14	14/14	14/14	14/14	13/14
rat11	3/3	3/3	3/3	3/3	3/3	2/3
	Seizures originating from left hippocampus					
rat1	-	-	-	-	-	-
rat2	1/9	2/9	3/9	3/9	4/9	9/9
rat3	0/4	0/4	3/4	1/4	0/4	4/4
rat4	0/1	0/1	0/1	0/1	0/1	1/1
rat5	-	-	-	-	-	-
rat6	0/3	0/3	2/3	0/3	1/3	3/3
rat7	-	-	-	-	-	-
rat8	1/5	1/5	2/5	2/5	2/5	4/5
rat9	0/4	0/4	0/4	2/4	2/4	1/4
rat10	5/23	6/23	9/23	7/23	7/23	11/23
rat11	62/118	60/118	116/118	75/118	78/118	116/118
	Percentage correctly classified					
RH	84,1	85,7	96,8	82,5	82,5	90,5
LH	41,3	41,3	80,8	53,9	56,3	89,2
all	53,0	53,5	85,2	61,7	63,5	89,6

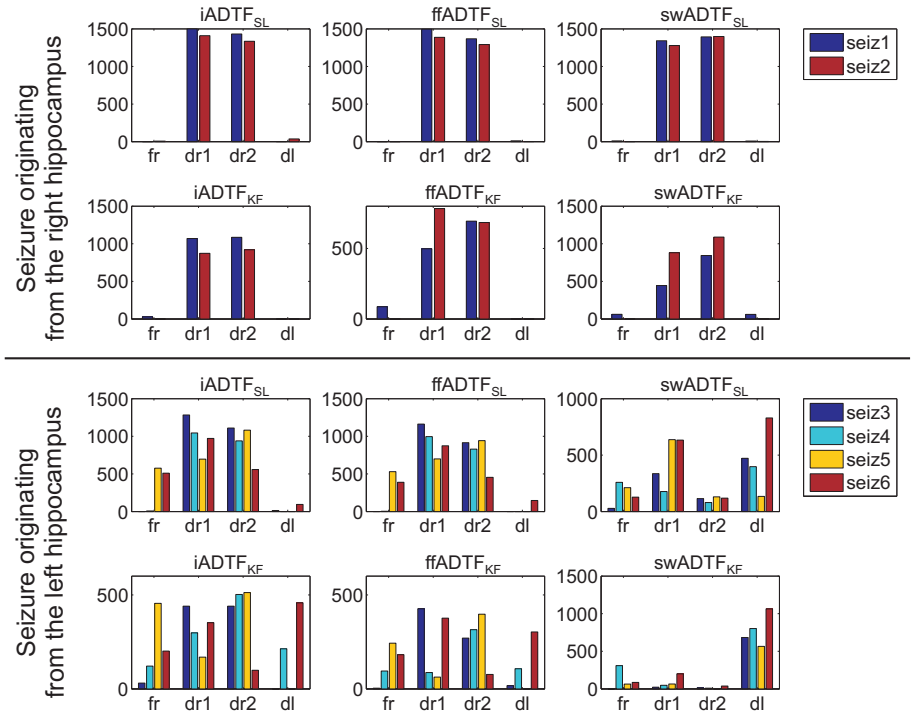


Figure 5.9: The out-degrees for the different connectivity measures for all seizures of rat3 (fr: frontal cortex; dr1, dr2: right hippocampus; dl: left hippocampus). The upper panel depicts the seizures originating from the right hippocampus, the lower panel the seizures originating from the left hippocampus. The electrode contact with highest out-degree is depicted as being the driver behind the seizure. For seizures originating from the right hippocampus all measures have similar behavior and are able to correctly localize the SOZ. For seizures originating from the left hippocampus the swADTF outperforms both the iADTF and the ffADTF.

cies more appropriately: there are only connections at frequencies that are present in the power spectrum of the receiving signal. Nevertheless it is still not able to pinpoint the correct driver behind the seizure. The swADTF$_{KF}$ on the other hand, has a weighting respecting both the frequencies present in the sending and in the receiving signal and is therefore able to correctly estimate the driver of the seizure.

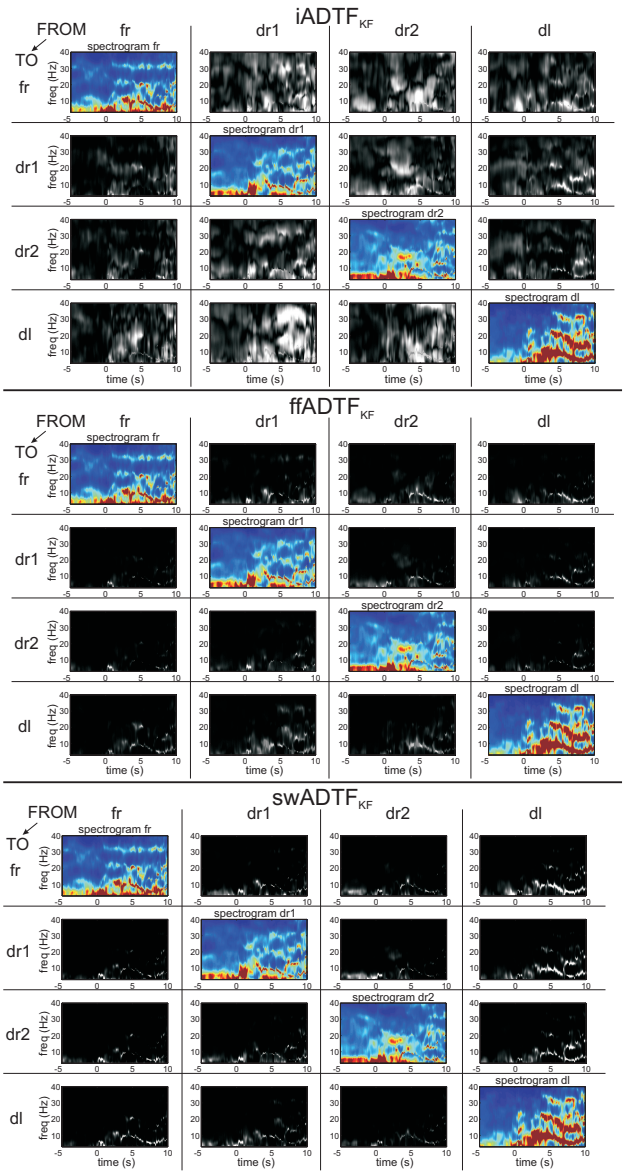


Figure 5.10: The connections in the frequency domain over time between signal fr, dr1, dr2 and dl for seizure 3 (originating from left hippocampus) of rat3. On the diagonals the spectrogram of each corresponding electrode contact is displayed. The off diagonal boxes show the connectivity pattern in the frequency domain for the iADTF$_{KF}$ (panel A), ffADTF$_{KF}$ (panel B) and swADTF$_{KF}$ (panel C). For the iADTF$_{KF}$ connections are seen at frequencies without spectral power. The ffADTF$_{KF}$ and swADTF$_{KF}$ correct for this by prioritizing connections at frequencies with high spectral power. However, the swADTF$_{KF}$ is the only one capable to correctly identify the left hippocampus as seizure onset.

5.5 Discussion

The choice of the parameters to estimate the TVAR model was based on how adequately all frequencies were represented in the signals' spectrogram. We performed a parameter sweep and visually identified the spectrograms of the signals calculated from the TVAR coefficients to identify the parameters that are suitable to adequately model the signals. This is more subjective then other criteria, but leads to more control and insight on how the frequency information is represented in the model. Other criteria like minimizing the root mean square error of the residuals [175], the Akaike information criterion [4] or the Schwarz Bayesian criterion [178] are obviously more objective. But this could also introduce erroneous calculation of connectivity measures in a frequency band that is not adequately modeled. Furthermore, one also needs to check whether the dynamic behavior of the signals is adequately captured. If the order is too low, the model misses the dynamic nature of the signals, whereas if it is too high overfitting mainly emphasizes noise [171].

Ding et al. proposed to use the sliding window technique for dealing with non-stationary ERP time series [57]. Although the sliding window technique is able to model the time series dynamics, it still considers each epoch as being stationary. The Kalman filtering algorithm on the other hand is capable of modeling non-stationary signals. This was reflected in the results of the simulations, where the sliding window technique connectivity measures performed worse than their Kalman filtering variants. As this was the case for the iADTF, ffADTF and swADTF, this had nothing to do with the weighting of the different measures but everything with how well the model coefficients were estimated.

Before using the variants of the ADTF in a certain frequency band it is useful to inspect the spectrograms of the signals. If there is no signal power at certain frequencies, the connections observed at those frequencies could be and most likely are spurious. The TVAR coefficients are estimated to optimally fit the signals. This means that the frequencies containing most power are best represented by the TVAR coefficients and not the other frequencies. For this sake, the proposed normalizations are very important. The ffADTF and the swADTF do incorporate a weighting with respect to the spectrogram of the receiving signal. The swADTF even goes one step further by also including the spectrogram of the sending signal and not only that of the receiving signal.

When the connectivity pattern of frequencies with higher spectral power

than the other frequencies in the considered frequency band is desired, the normalization of the ffADTF and swADTF will improve these connectivity estimations. Because the fundamental frequency of seizures and its harmonics have higher spectral power than the other frequencies, the ffADTF and the swADTF seem more appropriate. In this way we know that, if the seizure's fundamental frequency and harmonics lie within the considered frequency band, they will always be prioritized in the calculation of both ffADTF and swADTF with respect to the frequencies without power. The ffADTF only incorporates the frequency content of the receiving signal. This means that a flow can be observed even if there is no signal power at the sending side at those frequencies. The swADTF corrects for this matter and is therefore recommended for SNRs above 2 dB. Our simulation results confirmed this.

The fact that indirect (cascade) flows are stressed by the DTF is the reason why DTF analysis is appropriate for SOZ localization. Furthermore, it also facilitates the graph analysis. There is no need for more advanced graph measures like the betweenness centrality, the path length, global and local efficiency, the rich club coefficient or others [187, 191], because we only want to know the origin of information flow. This can easily be identified by just calculating the out-degree for each electrode contact. The interpretation of the different graph measures can also differ for different connectivity measures the network was based upon. For example, the out-degree has a different meaning when the underlying network was computed with either the DTF (that stresses indirect flows) or the PDC (that stresses direct flows).

In 2006 Eichler et al. [61] showed that the DTF does not indicate multivariate or bivariate Granger causality, but that it is closely related to the concept of the impulse response function and can be viewed as a spectral measure for the total causal influence from one component to another. The DTF method seems to be the most suitable as a spectral measure explaining the total causal influence that one component exerts over another component. It does not express Granger causality as in its definition, but tends to model the indirect connections and therefore not all direct connections.

All derived versions of the DTF in this chapter, i. e. the iADTF, ffADTF and swADTF have the same behavior and do therefore not express Granger causality as in its definition. However, this can be considered a major advantage of the measures if we are looking for the origin of information flow.

In many of the performed studies investigating SOZ localization from ictal

IEEG recordings using the DTF, only one or two windows were analyzed [71, 70, 231, 112]. In all those cases the seizure was said to be stationary in the considered time window. However, seizures are intrinsically non-stationary, i. e. they spread over time to different regions and individual spreading patterns are unpredictable in nature. Furthermore, the considered time intervals were not always chosen during seizure onset, although this part is clinically most important. The first few seconds of a seizure could originate from a different brain structure than that during a later time window.

In the real dataset the overall performance of the Kalman filtering measures was also better than those of the sliding window technique. This indicates that the Kalman filtering algorithm is the preferred technique to estimate time-variant connectivity patterns from non-stationary signals. In the analyzed rat seizures we saw a tendency of the iADTF and ffADTF to depict the right hippocampus as driver during seizure episodes. This is because connections are seen from the right to left hippocampus, right frontal electrode or to the other electrode contact in the right hippocampus at frequencies that are not present in the sending signal's power spectrum (see fig. 5.10). The swADTF corrects for this matter. In the simulation the difference between the Kalman filtering and the sliding window technique seems more important than the difference in normalization. For the real dataset the normalization is much more important than the way the TVAR coefficients are modeled. However, here also the Kalman filtering technique outperforms the sliding window technique.

5.6 Conclusion

In this chapter we proposed a new effective connectivity measure, the swADTF, that is able to derive the connectivity pattern of non-stationary signals and to prioritize frequencies with high spectral power in the connectivity analysis. We showed that Kalman filtering is the preferred technique to model non-stationary signals compared to the sliding window technique. Furthermore, we showed the added value of the swADTF compared to the iADTF and ffADTF in simulations and to localize the SOZ in a small animal model of epilepsy.

5.7 Original contributions

The work presented in this chapter resulted in 1 national [196], 1 international conference contribution [207] and a A1 paper submitted to *NeuroImage*, that is currently under review [200].

Chapter 6

Seizure onset zone localization in 8 patients

6.1 Introduction

In chapter 4 we introduced the framework capable of localizing the SOZ from ictal IEEG recordings and already showed the applicability in 1 patient. In chapter 5 we extended the framework by introducing a new measure, the spectrum weighted Adaptive Directed Transfer Function and showed the applicability to a small animal model of epilepsy. The swADTF calculated using the Kalman filtering algorithm outperformed the other connectivity measures. In this chapter we will apply the developed methodology to localize the SOZ from ictal IEEG recordings in 8 patients who were rendered seizure free after resective surgery. We will compare the results obtained by our method with the visual analysis of the epileptologist and with the location of the surgically removed brain area.

6.2 Dataset and Method

6.2.1 Patient data

The IEEG dataset was obtained from a series of 8 patients included in the presurgical evaluation protocol at the Reference Center for Refractory Epilepsy at Ghent University Hospital in Belgium. The study was approved by ethics committee and all patients signed informed consent.

The patients included in the study were selected based on the following

criteria: focal ictal onset on IVEM and subsequent resective surgery rendering the patient seizure-free (Engel class I outcome [64] during a minimum follow-up of 2 years). The clinical patient characteristics are described in table 6.1.

The details of the IVEM are found in table 6.2. The IEEG was recorded using a monopolar reference electrode located on the right mastoid and with a ground electrode located on the left mastoid.

6.2.2 From IEEG to out-degree

The IEEG of all the habitual seizures in all 8 patients was selected. The starting point for the effective connectivity analysis was the moment where epileptiform rhythmical IEEG activity, with a frequency between 3Hz and 20 Hz, was observed at the onset of the seizure.

For each patient we selected the ictal IEEG from 5 s before until 20 s after the marked starting point. The epochs were filtered (low-pass filter (0.5Hz, 40 Hz), with a notch filter at 50 Hz) and normalized (mean set to 0 and standard deviation to 1). The normalization is required to treat every signal equally and in this way avoid biasing the results based on the amplitude of the signals. Afterwards the seizures were resampled from 200 Hz to 100 Hz and from 512 Hz and 256 Hz to 128 Hz with a specific resampling procedure for time-variant autoregressive models [175]. The resampling allows the use of a smaller model order while maintaining the time window used to estimate the coefficient matrices. The resampling also allows coping with computational memory issues and resulted in a significant decrease of analysis time. For each resampled seizure the TVAR coefficients were estimated with an update coefficient (UC) equal to 10^{-3} and the model order p equal to 8 and 10 for $f_s = 100$ Hz and 128 Hz, respectively. A detailed discussion on the parameters can be found in chapter 4. We discarded the coefficient matrices from the first 5 s before the marked starting point. This 5 s time frame was only used to allow the Kalman filter to adapt to the data.

Table 6.1: Clinical patient characteristics. The columns represent: the patient number, sex, age at the time of IVEM, type of epilepsy, ictal onset defined based on scalp EEG recording, notable MRI findings, type of surgery, surgical outcome and duration of follow-up since the surgery (in years).

Patient number	sex	age	epilepsy type	scalp EEG	MRI
pat.1	M	44	mTLE	L FT	L HS and scar with gliosis L angular gyrus
pat.2	F	26	mTLE	bilat FT	DNET R inf T gyrus
pat.3	F	49	n and mTLE	L FT	multifocal posttraumatic damage but mainly L T
pat.4	M	40	mTLE	L T	L HS and L P dysplasia
pat.5	M	20	mTLE	bilat T	bilat damaged hippocampi
pat.6	F	32	n extra-TLE	no clear ictal onset	R insular FCD
pat.7	F	50	mTLE	bilat T	L HS
pat.8	F	41	mTLE	L $>$ R FT	small heterotopia L lat ventricle and L HS

Patient number	surgery	surgical outcome	follow-up (years)
pat.1	L SAH	Engel I	3
pat.2	R ant T lobectomy and AH-omy	Engel I	3
pat.3	L ant T lobectomy, AH-omy and Tbasal topectomy	Engel I	2
pat.4	L SAH	Engel I	7
pat.5	L SAH	Engel I	9
pat.6	R perisylvian topectomy and lesionectomy	Engel I	3
pat.7	L SAH	Engel I	6
pat.8	L ant T lobectomy and AH-omy	Engel I	4

abbreviations: pat=patient, M=male, F=female, mTLE=mesial temporal lobe epilepsy, n=neocortical, L=left, F=frontal, T=temporal, bilat=bilateral, HS=hippocampal sclerosis, DNET=dysembryoplastic neuroepitheliale tumor, inf=inferior, P=parietal, lat=lateral, FCD=focal cortical dysplasia, SAH=selective amygdalohippocampectomy, ant=anterior, AH-omy=amygdalohippocampectomy.

Table 6.2: Details of the IVEM data. The columns represent: the patient number; the number of analyzed seizures; the number of electrode contacts; the implanted depth electrodes; the implanted subdural strips and grids; the electrode contacts omitted due to visually identified artifacts; sampling frequency; available imaging of implanted electrodes and available post-operative imaging.

Patient number	# seizures	# contacts	depth electrodes	strip and grid electrodes
pat.1	3	50	LH1-10: left hippocampus	LG1-40: left gyrus angularis
pat.2	3	36	RH1-8: right hippocampus	RATB1-4: right temporo anterior RPTB1-4: right temporo posterior RTL1-6: right temporo lateral LTL1-6: left temporo lateral LATB1-4: left temporo anterior LPTB1-4: left temporo posterior
pat.3	3	34	LH1-8: left hippocampus	LFFA1-6: left basal posterior temporal LTL1-6: left lateral temporal LTA1-4: left basal anterior temporal RTA1-4: right basal anterior temporal RFFA1-6: right basal posterior temporal
pat.4	1	48	LA0-3: left amygdala LH0-3: left hippocampus RA0-3: right amygdala RH0-3: right hippocampus	LG1-32: left temporo posterior
pat.5	3	36	LA0-3: left amygdala LH0-3: left hippocampus RA0-3: right amygdala RH0-3: right hippocampus	LATS1-6: left temporo anterior RATS1-6: right temporo anterior LPTS1-4: left temporo posterior RPTS1-4: right temporo posterior
pat.6	5	60	RD1-12: insular lesion	TG1-32: right temporal lobe SSG1-16: right suprasylvian

Patient number	# seizures	# contacts	depth electrodes	strip and grid electrodes
pat.7	4	40	LH1-12: left hippocampus RH1-12: right hippocampus	LTA1-4: left temporo basal LTM1-4: left temporo medial LTP1-6: left temporo lateral RTA1-4: right temporo anterior RTM1-4: right temporo medial RTP1-6: right temporo lateral
pat.8	5	64	LD1-8: left hippocampus (LD1-4) and trough heterotopy (LD7-8)	LG1-56: temporal and parietal (LG1-8 lateral temporal and LG49-56 parietal)

Patient number	omitted electrode contacts	sampling frequency (Hz)	electrode images	post-op images
pat.1	LG36	256	CT and MRI	MRI
pat.2	RATB1 and LATB4	256	CT and MRI	MRI
pat.3	none	512	CT and MRI	MRI
pat.4	LG25	200	CT and MRI	MRI
pat.5	none	200	not available	not available
pat.6	none	256	CT and MRI	MRI
pat.7	RH5-6 and RH11-12	256	CT and MRI	MRI
pat.8	none	256	MRI	MRI

Out of the TVAR coefficients the swADTF was calculated in the frequency band (3Hz, 40 Hz) based on eq.5.1. This band is chosen to remove the background electrical activity up to 3Hz. Due to the 1/f nature of the spectrum of the IEEG we tried to limit the influence of background activity by setting the lower bound of the frequency interval as high as possible. The upper bound of the frequency interval was set to 40 Hz based on the applied low-pass filter. All ictal rhythmical seizure activity was observed within the chosen frequency band.

The swADTF-values were thresholded by a connection specific threshold based on connectivity analysis of interictal segments. For each patient we selected 10 interictal epochs of 25 s and processed them in the same manner as the ictal epochs. We derived the 99^{th} percentile for each connection between each pair of electrode contacts and used this as the threshold for that specific connection. In this way we expect to see connections during only 1% of the analysis of an IEEG epoch.

The adjacency matrix of each seizure was calculated using these thresholds according to eq.5.4. The time-variant out-degree of each node was derived from this adjacency matrix in each patient according to eq.5.5. The seizure specific out-degree (SSO) is the sum of the out-degrees over the 20 s of each seizure epoch according to eq.5.6. This depicts how many outgoing connections arise from each contact during the considered seizure. The total out-degree is the sum of the SSO over all seizures per individual patient. The higher this total out-degree of one electrode contact, the more connections arose from this contact during all analyzed seizures.

6.2.3 The outcome parameters

We compared the electrode contact with the highest total out-degree with the electrode contacts showing ictal onset based on the visual identification of the IEEG performed by the epileptologist. Furthermore, we also compared the location of the electrode contact with the highest total out-degree with respect to the location of the resected brain area derived from the post-operative MRI. The SSO's are analyzed to evaluate whether the results are consistent over multiple seizures.

6.3 Results

First we will discuss the overall results of the considered patient group, afterwards we will present the results for each patient individually.

6.3.1 Overall results

The total out-degree results of all patients are depicted in table 6.3. In all 8 patients the electrode contact with the highest total out-degree was amongst the electrode contacts that, visually defined by the epileptologist, showed the ictal onset on IEEG. The electrode contact with highest total out-degree also laid within the resected brain region in all patients in whom post-operative images were available ($n = 7/8$). We can conclude that the localization based upon our method corresponded in all patients with the visual analysis of the epileptologist.

The highest SSO are also shown in table 6.3. The highest SSO was consistent over multiple seizures. In the majority of seizures from one individual the highest SSO came from one specific or immediately neighboring contacts. In 62% of all seizures the SSO was equal to the highest total out-degree. In 33% the electrode contact with the highest SSO was a neighboring contact (maximum distance of 2 contacts) of the one with the highest total out-degree. We can conclude that total out-degree corresponds very well with the SSO. This means that most seizures of the same patient had the same driving brain region during the analyzed epochs.

6.3.2 Individual patient results

Below we will address the patient specific results in more detail.

Table 6.3: Seizure specific results of all patients. The 3 electrode contacts with the highest out-degree for each seizure individually are shown. The columns represent: the patient number, the result of the visual analysis of the IEEG, the electrode contacts lying in the resected area (if post-operative images are available), the highest total out-degree and the seizure specific out-degree for the individual seizures.

Patient number	visual analysis	resected region	highest total outdegree
pat.1	LH1-2	LH1-4	LH2
pat.2	RPTB4	RH1-3, RPTB1-4, RATB1-4	RPTB4
pat.3	LTA4	LH1-2, LTA1-4	LTA4
pat.4	LA0-3 and LH0-3	LA0-3 and LH0-3	LA2
pat.5	LH0-3	left amygdala and hippocampus*	LH2
pat.6	RD3-8, TG28-30, TG21-23, SSG6-8	RD3-7, TG21-22, TG29-30, SSG6-7	RD3
pat.7	LH1-6	LH1-6	LH5
pat.8	LD1-3	LD1-3, LG1-3, LG9-11, LG17-19	LD2

Patient number	SSO seizure 1	SSO seizure 2	SSO seizure 3	SSO seizure 4	SSO seizure 5
pat.1	LH2 > LH3 > LH1	LH1 > LH5 > LH3	LH2 > LH3 > LG25	/	/
pat.2	RPTB4 > RATB4 > RTL3	RPTB4 > RTL3 > RH6	RPTB4 > RH3 > RH4	/	/
pat.3	LH8 > LTA4 > LFFA3	LTA4 > RFFA3 > LH2	LTA4 > LFFA6 > LH8	/	/
pat.4	LA2 > LA1 > LA3	/	/	/	/
pat.5	LH2 > LH1 > LA3	LH1 > LH2 > LH0	LA3 > LH2 > RPTS3	/	/
pat.6	RD3 > RD2 > RD6	RD1 > RD3 > RD2	RD3 > RD4 > RD1	RD3 > RD6 > RD1	RD5 > RD3 > RD6
pat.7	LH4 > LH5 > LH3	LH5 > LH4 > LH2	LH4 > LH5 > LH6	LH5 > LH4 > LH6	/
pat.8	LD2 > LD3 > LG41	LD3 > LD2 > LD1	LD2 > LD1 > LD8	LD1 > LD2 > LD6	LD2 > LD1 > LD6

6.3.2.1 Patient 1

The structural MRI investigation revealed left hippocampal sclerosis and a scar with gliosis in the left angular gyrus. The SVEM showed that the seizures started from the left frontotemporal brain region. Because of the multiple MRI anomalies the patient was admitted for IVEM. One depth electrode was implanted in the left hippocampus (LH1-10) and a grid of 40 contacts covered the left gyrus angularis. The patient had 3 habitual seizures during the IVEM. The first ictal activity was noticed on contacts LH1-2 before it spread to the contacts of the grid. During seizure 2 epileptiform discharges were seen on contact LH1-2 but there was no spread of ictal activity to the grid. The IVEM indicated that the seizures started from the left hippocampus and not from the scar in the left gyrus angularis. This resulted in a selective amygdalohippocampectomy, which rendered the patient seizure free (follow-up: 3 years). The upper panel of fig.6.1 shows the electrode contacts and their position with respect to the resected brain tissue.

The bottom panel depicts the SSO and the total out-degree. In seizure 1 and 3, LH2 had the highest SSO. During seizure 2 there was not much spreading resulting in a low out-degree at all contacts. The highest total out-degree was seen at electrode contact LH2, which corresponds both with the visual analysis of the epileptologist and the resected brain area. In fig.6.2 the connectivity pattern during seizure 3 is shown. The seizure is divided in 4 time-windows of 5 s (A, B, C and D) after the marked starting point for visualization purposes only. This revealed that during the whole 20 s epoch LH2 was the driver behind the seizure activity during that seizure.

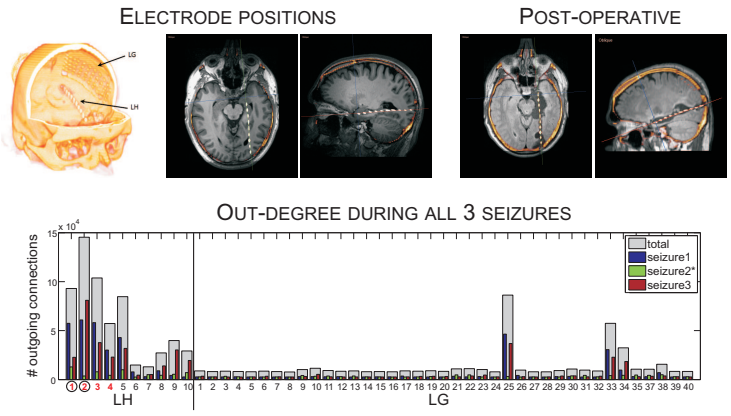


Figure 6.1: Results of the connectivity analysis in pat. 1.

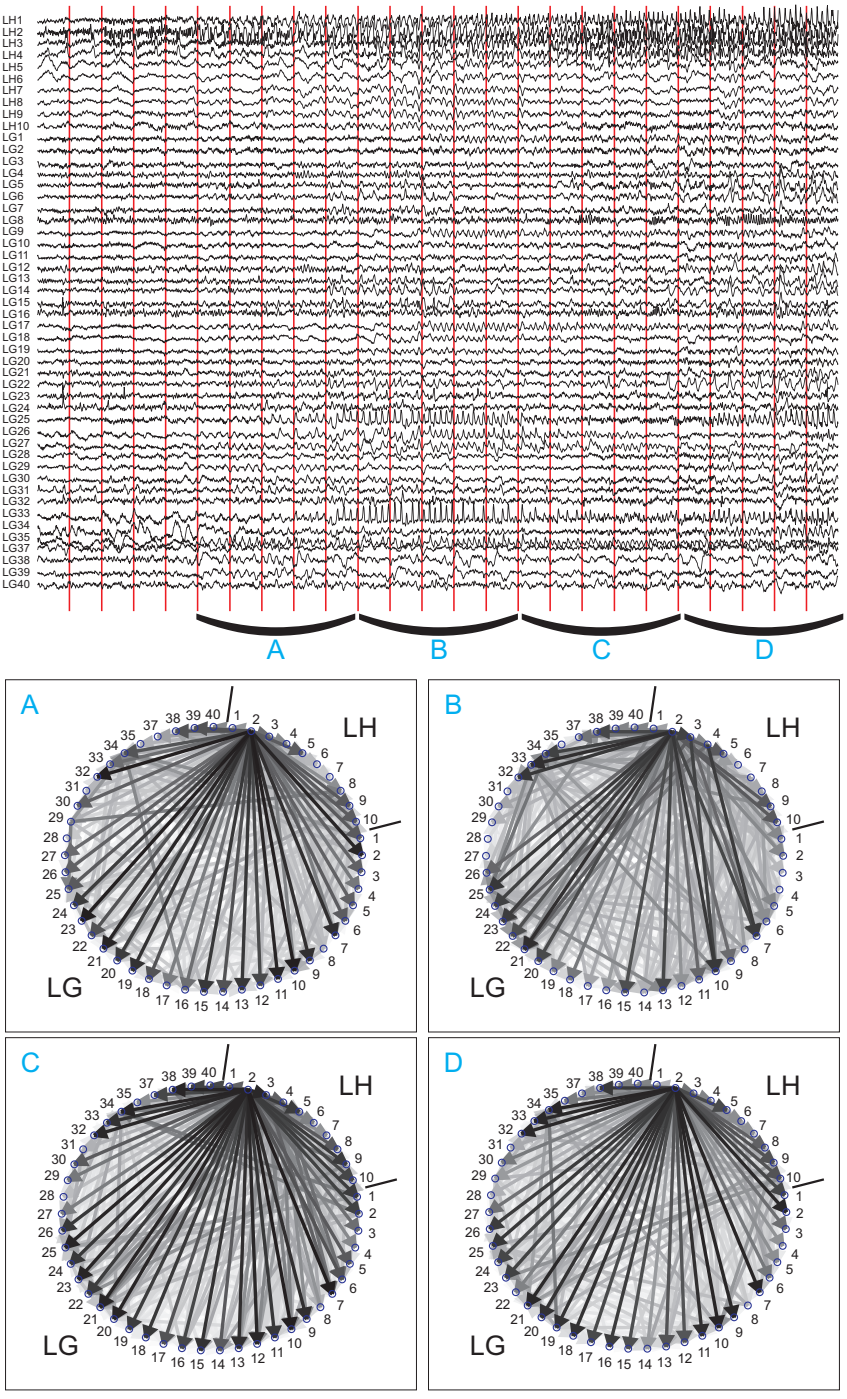


Figure 6.2: Connectivity patterns during seizure 3 in pat. 1.

6.3.2.2 Patient 2

The MRI investigation showed a dysembryoplastic neuroepithelial tumor in the right inferior temporal gyrus and the SVEM showed bilateral frontotemporal ictal onset. Because of these discongruent findings the patient was admitted for IVEM. A depth electrode was implanted in the right hippocampus and 3 strips covered the right and left temporal lobe. During the IVEM, 3 habitual seizures were recorded that started from contact RPTB4 (right temporal lobe strip) according to the visual analysis of the epileptologist. A right anterior temporal lobectomy and amygdalo-hippocampectomy rendered the patient seizure free (follow-up: 3 years). The upper panel of fig.6.3 shows the electrode positions and how they were located with respect to the later on resected brain area.

In the bottom panel the SSO and total out-degree are depicted. We can clearly observe that RPTB4 had the highest SSO during all 3 seizures. This resulted in the highest total out-degree for this contact, which corresponded with the visual analysis of the epileptologist and the subsequently resected brain area. In fig.6.4 the results of the connectivity analysis of seizure 1 are displayed. During the first 10 s most connections arose from contact RPTB4. During time window C from RPTB4 and RATB4 and during window D from RATB4.

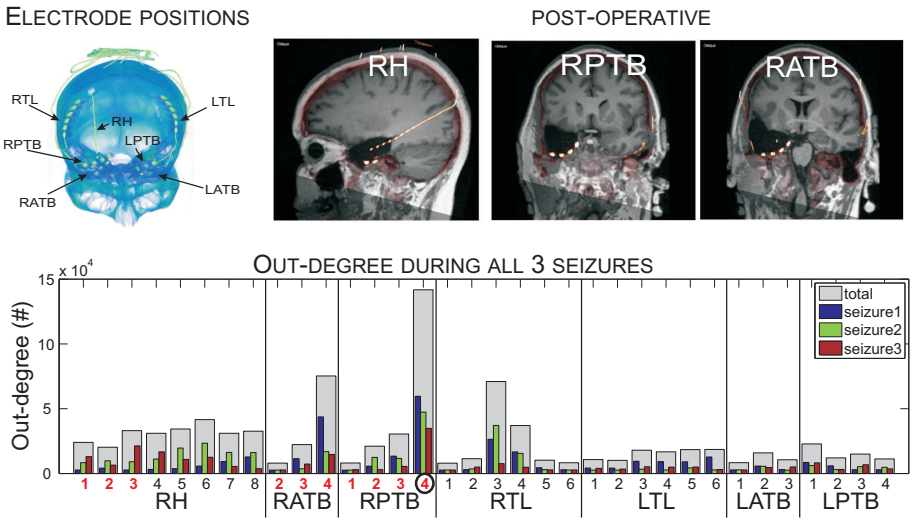


Figure 6.3: Results of the connectivity analysis in pat. 2.

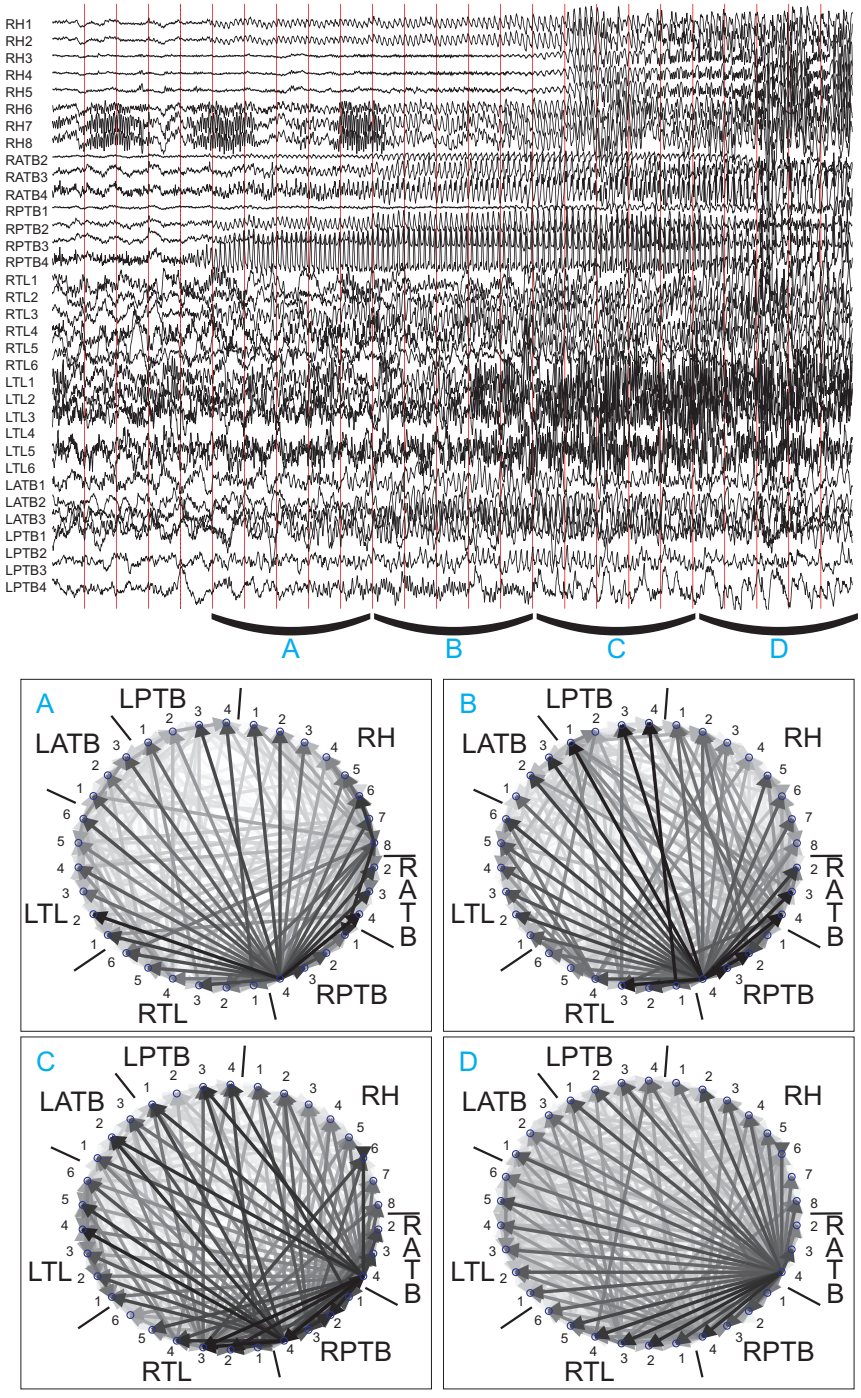


Figure 6.4: Connectivity patterns during seizure 1 in pat. 2.

6.3.2.3 Patient 3

The structural MRI investigation revealed multifocal post-traumatic damage, but mainly in the left temporal lobe. The SVEM showed that the ictal onset was found left frontotemporal. During the IVEM a depth electrode monitored the electrical activity of the left hippocampus. Five strips were also implanted, 3 covering the left and 2 the right temporal lobe (see table 6.2). The patient had 3 habitual seizures during the IVEM. During the seizures the first ictal activity was seen at contact LTA4 before it spread to other contacts in the left hemisphere. The patient had a left anterior temporal lobectomy, an amygdalohippocampectomy and a temporal basal topectomy. The patient has been seizure free since 2 years after operation. In the upper panel of fig.6.6 the electrode contacts and their relation to the later on resected area is shown.

The total out-degree and the SSO's are depicted in the bottom panel. The highest total out-degree was seen for contact LTA4. During seizure 2 and 3 LTA4 was found to have the highest SSO, only for seizure 1 we found LH8 to have the highest SSO. Although for seizure 1 the maximum out-degree is seen from LH8, we notice that for all 3 seizure many connections arose from LTA4. This electrode contact corresponds with the resected brain area and was pinpointed as the electrode contact at which first signs of ictal epileptic activity was seen based on the IVEM. The connectivity pattern over time of seizure 3 is shown in fig.6.6.

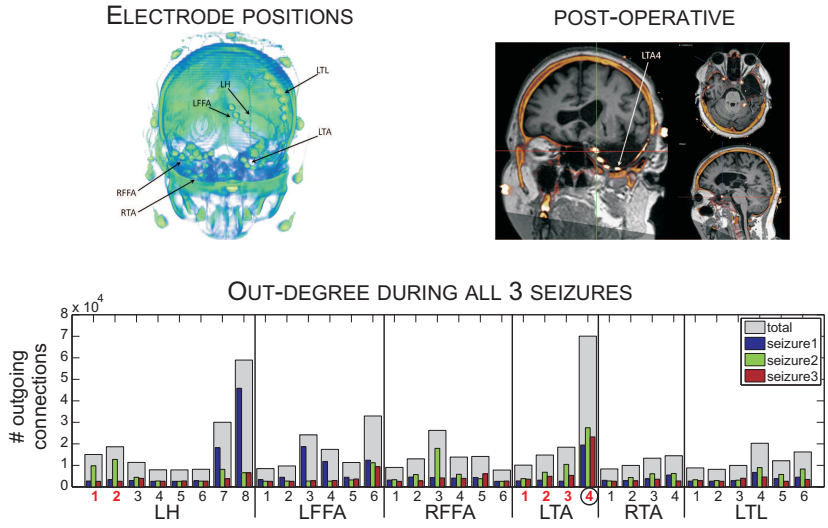


Figure 6.5: Results of the connectivity analysis in pat. 3.

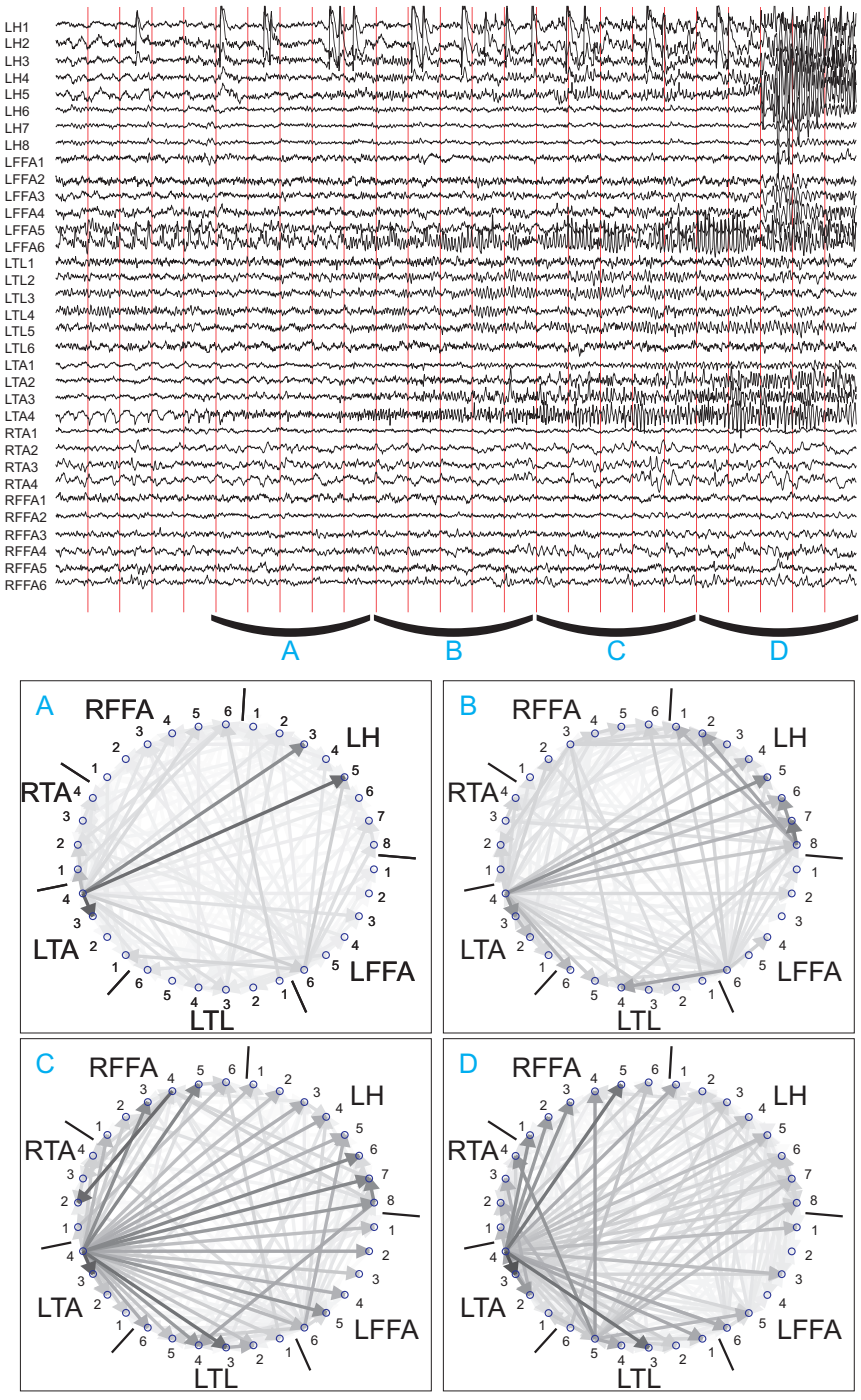


Figure 6.6: Connectivity patterns during seizure 3 in pat. 3.

6.3.2.4 Patient 4

The structural MRI investigation indicated left hippocampal sclerosis and left parietal dysplasia. The SVEM depicted the left temporal lobe as SOZ. IVEM was needed to better localize and delineate the SOZ. Four depth electrodes were implanted to monitor both amygdalae and hippocampi. A subdural grid was also implanted to monitor the left temporo posterior brain region. The patient had 10 similar habitual seizures. Unfortunately only 1 seizure was available of this patient in the hospital records. During the seizures the ictal activity started in the left hippocampus and amygdala before it spread to the neocortical grid. The patient had a left selective amygdalohippocampectomy and has been seizure free since (follow-up: 7 years). The upper panel of fig.6.7 shows the depth electrodes and the resected brain area.

Because we only had 1 seizure available, the total out-degree is equal to the SSO. We found the highest total out-degree at contact LA2. A high out-degree was also seen at other contacts in the left amygdala. In fig.6.8 the connectivity pattern during the seizure is depicted. Most information flow is coming from the left amygdala.

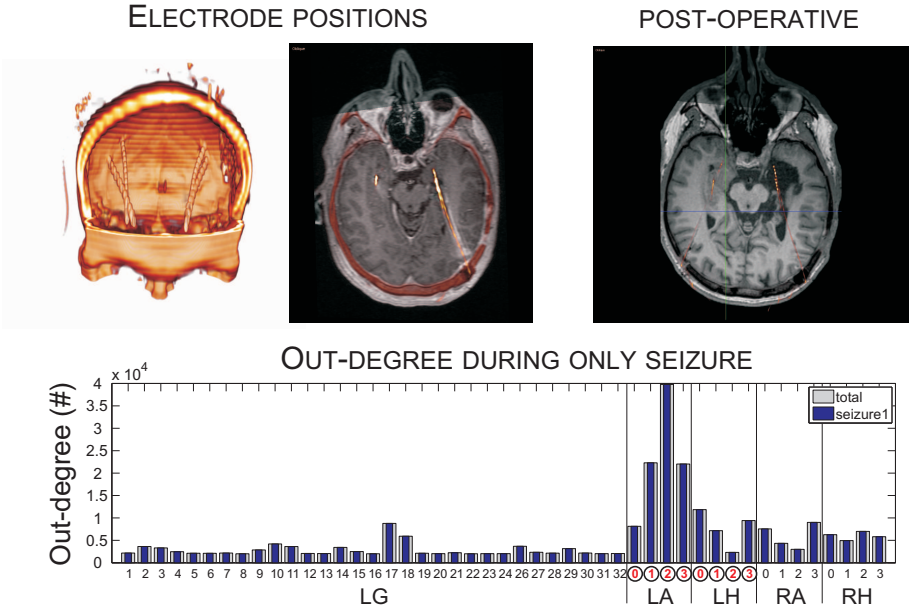


Figure 6.7: Results of the connectivity analysis in pat. 4.

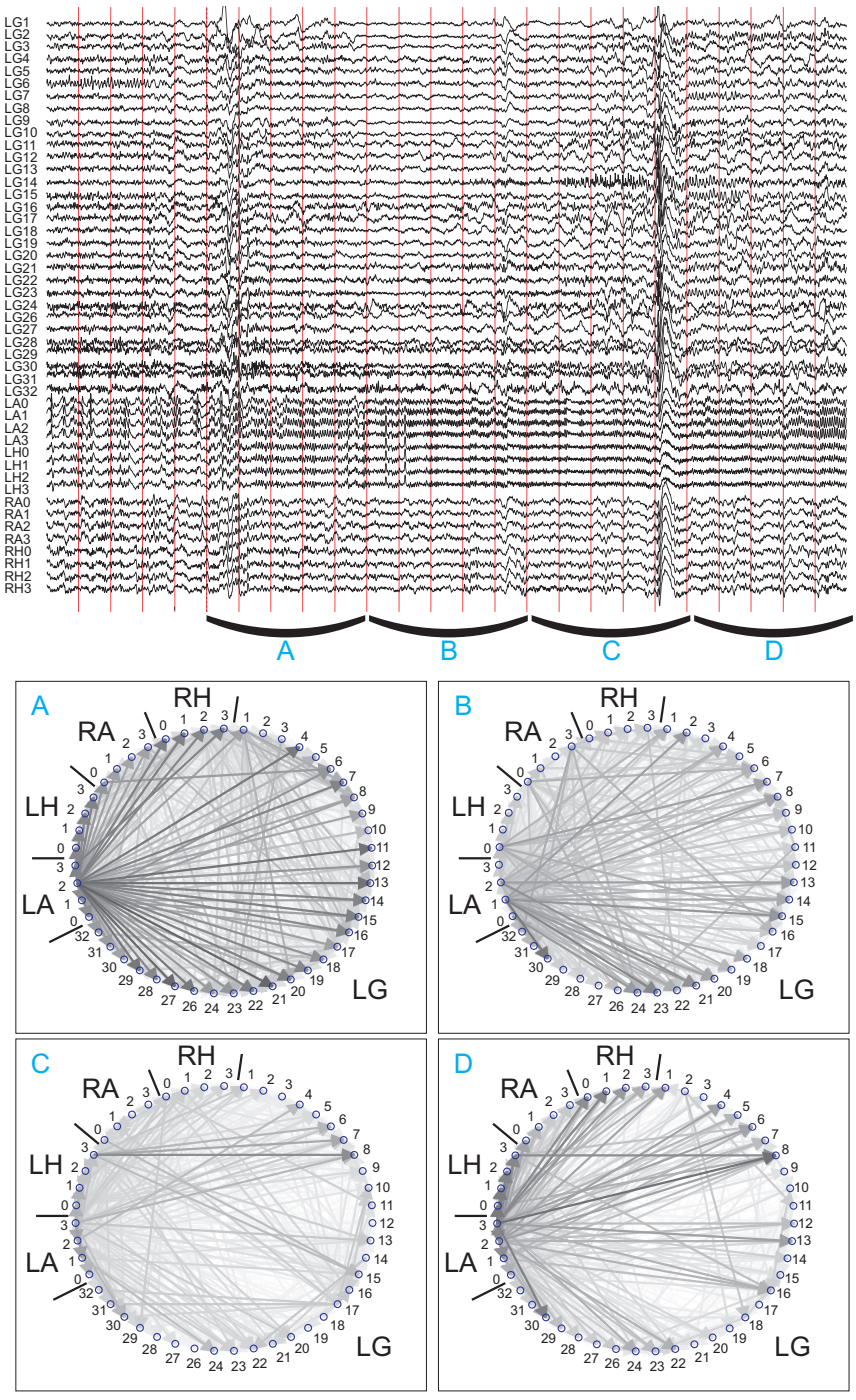


Figure 6.8: Connectivity patterns during seizure 1 in pat. 4.

6.3.2.5 Patient 5

The MRI investigation revealed bilateral damaged hippocampi. The SVEM concluded that there was bilateral temporal lobe ictal onset. Due to these bilateral findings, the patient was admitted for IVEM. Four depth electrodes were placed to monitor both hippocampi and amygdalae and 4 strips to monitor the anterior and posterior part of the left and right temporal lobe. The patient had 3 habitual seizures. During the seizures the first ictal signs were seen at contacts LH0-4 in the left hippocampus with later on spreading to the parahippocampal gyrus and the right hippocampus. The patient had a selective amygdalo-hippocampectomy and has been seizure free since (follow-up: 9 years). Unfortunately no imaging of the electrode positions as well as post-operative imaging was available for this patient.

The SSO's and the total out-degree are shown in fig.6.9. The total out-degree was the highest for LH2. The out-degree is also high for contacts in the close approximation of LH2. This was concordant with the visual analysis of the epileptologist. In fig.6.10 the connectivity pattern of seizure 2 is depicted. Most spreading is seen from LH2 to the other contacts in the left hippocampus and to the contacts of the left strips.

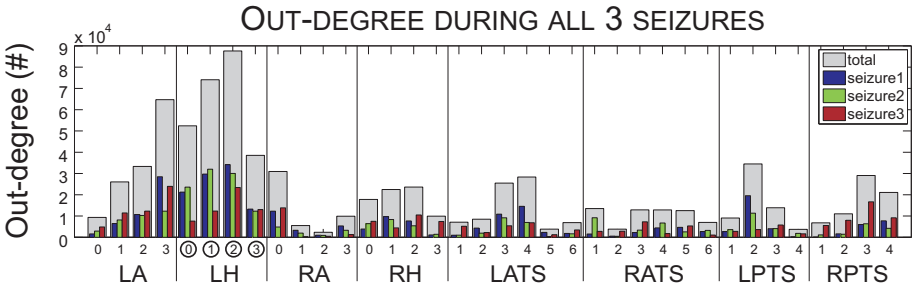


Figure 6.9: Results of the connectivity analysis in pat. 5.

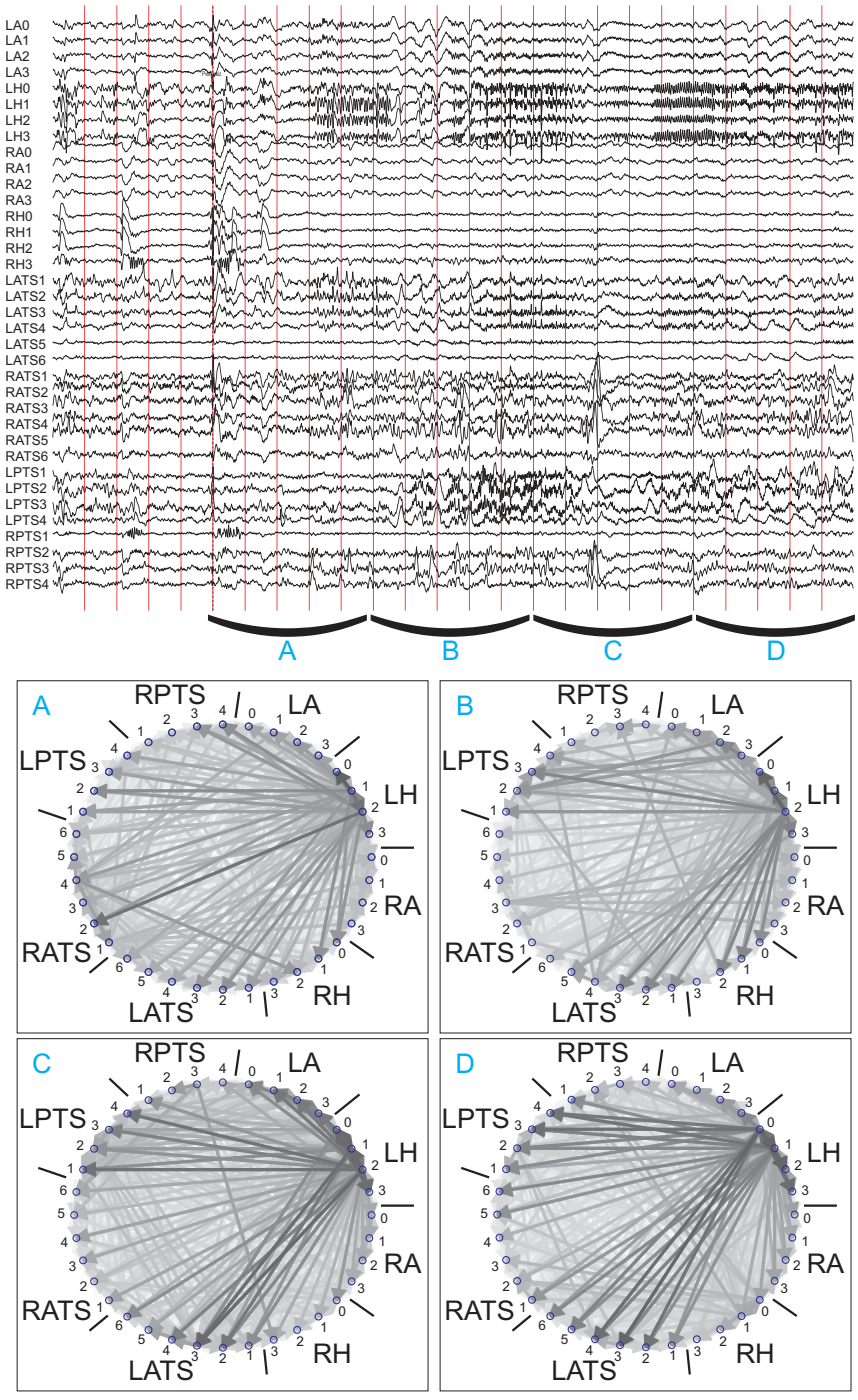


Figure 6.10: Connectivity patterns during seizure 2 in pat. 5.

6.3.2.6 Patient 6

The structural MRI investigation revealed right insular focal cortical dysplasia. During the SVEM the SOZ could not be localized and the patient was therefore admitted for IVEM. A depth electrode with 12 contacts was implanted to monitor the insular lesion. Furthermore 2 grids with 32 and 16 contacts each monitored the right temporal lobe and the right suprasylvian brain region respectively. Five habitual seizures were recorded during the IVEM. The seizures started from contacts RD3-8, TG28-30, TG21-23 and SSG6-8. This confirmed that the seizure originated from the insular lesion. The patient underwent a right perisylvian topectomy and lesionectomy and has been seizure free since (follow-up: 3 years). The electrode contacts and their position with respect to the resected brain are shown in the upper panel of fig.6.11.

The SSO's and total out-degree are depicted in the bottom panel. The highest total out-degree is found for RD3. During 3 seizures (1, 3 and 4) this contact had the highest SSO, during the other 2 seizures (2 and 5) it had the second highest SSO. In fig.6.12 the connectivity pattern during seizure 1 is shown.

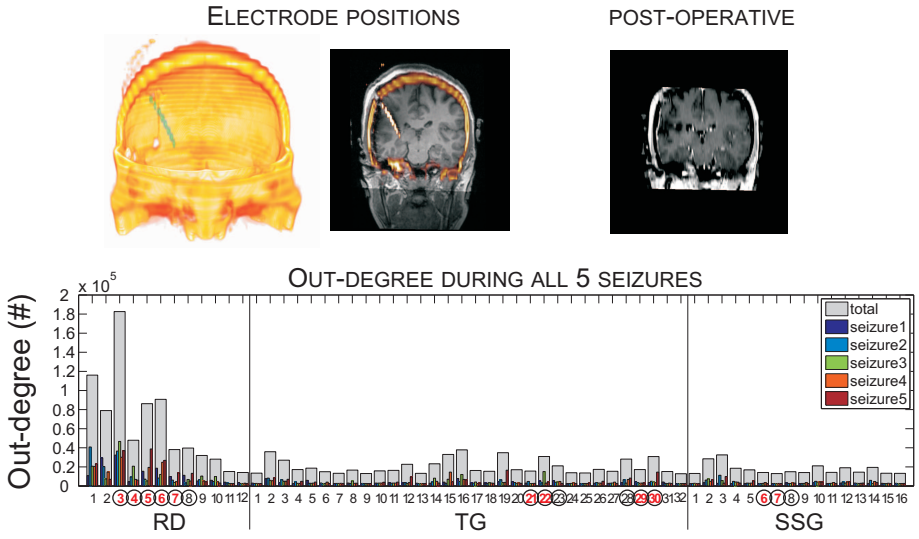


Figure 6.11: Results of the connectivity analysis in pat. 6.

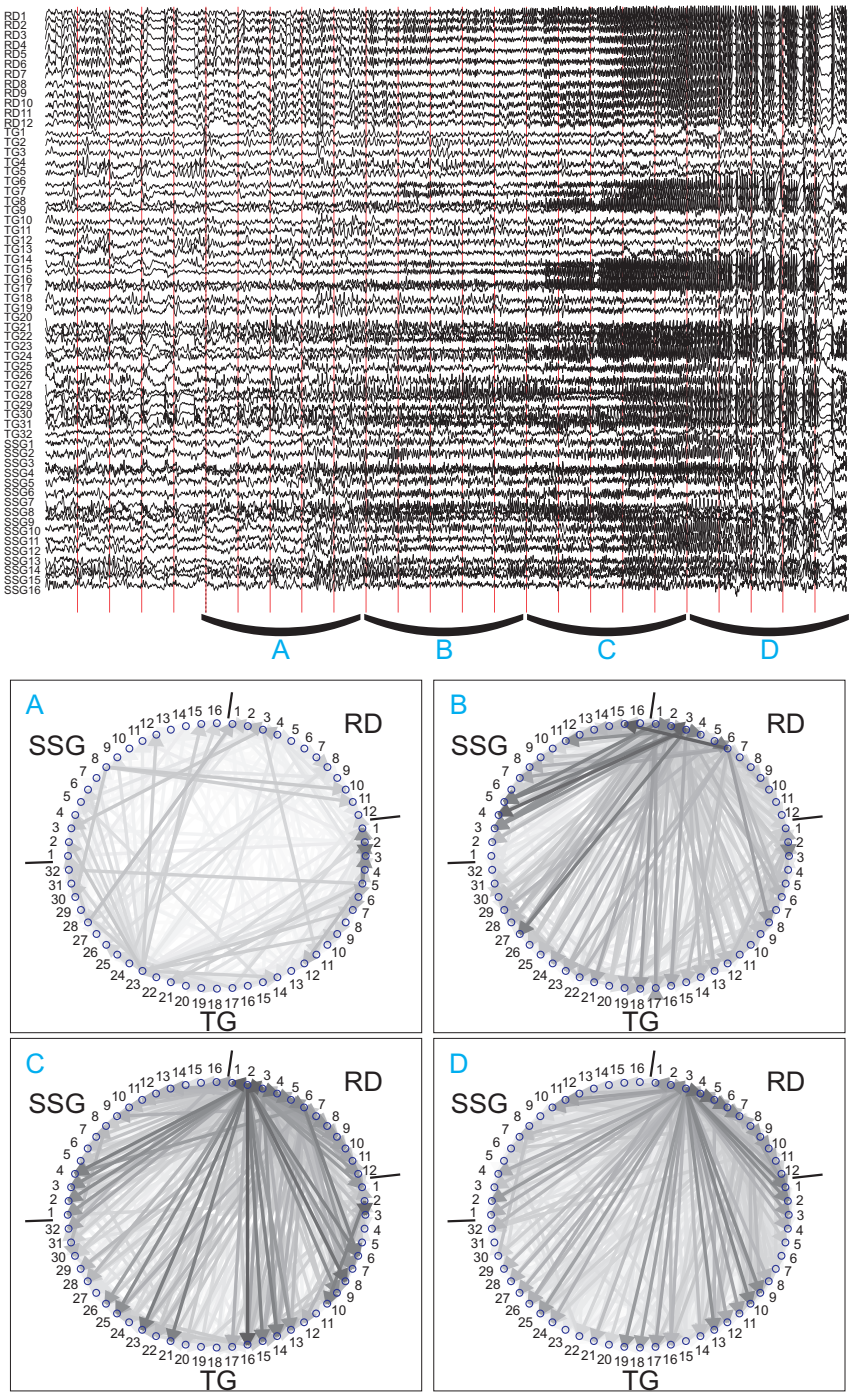


Figure 6.12: Connectivity patterns during seizure 1 in pat. 6.

6.3.2.7 Patient 7

This patient is the same patient that was investigated in chapter 4. The structural MRI showed left hippocampal sclerosis, while the SVEM was indicative for bilateral temporal lobe ictal onset. Due to the non-conclusive SVEM, the patient was admitted for IVEM. Two depth electrodes with each 12 contacts were implanted to monitor the left and right hippocampus. The patient had 4 habitual seizures during the IVEM. First ictal activity is seen at contacts LH1-LH6 before it spreads to the contacts anterior of the left hippocampus and to the contacts of the temporal basal strip LTM. The patient had a left selective amygdalohippocampectomy and has been seizure free since (follow-up: 6 years). The electrode positions and the resected brain region are shown in the upper panel of fig.6.13.

In the bottom panel the total out-degree and the SSO's are depicted. The highest SSO are seen for contacts LH5 (seizures 2 and 4) and LH4 (seizures 1 and 3). Contact LH5 had the highest total out-degree. This corresponds with the findings of chapter 4. As an example the connectivity pattern during seizure 4 is shown in fig.6.14. First connections are seen within the hippocampus and from the hippocampus to LTM and LTA. Afterwards the seizure activity spread to the other contacts with origin of information flow LH5.

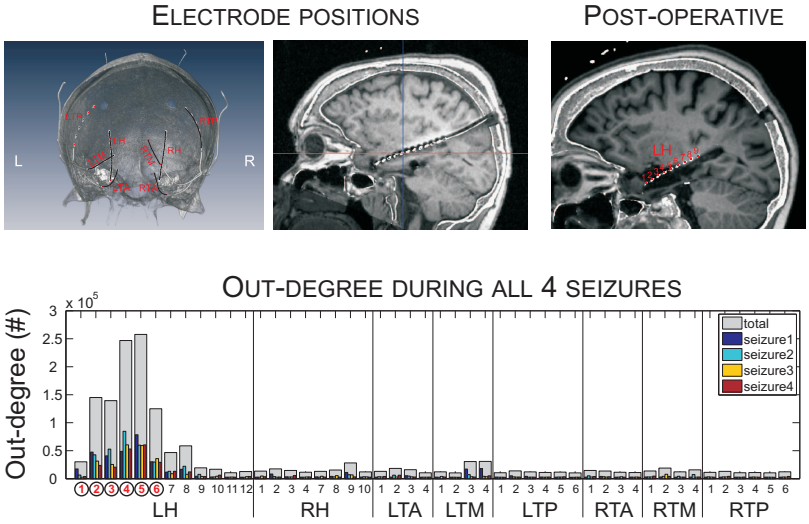


Figure 6.13: Results of the connectivity analysis in pat. 7.

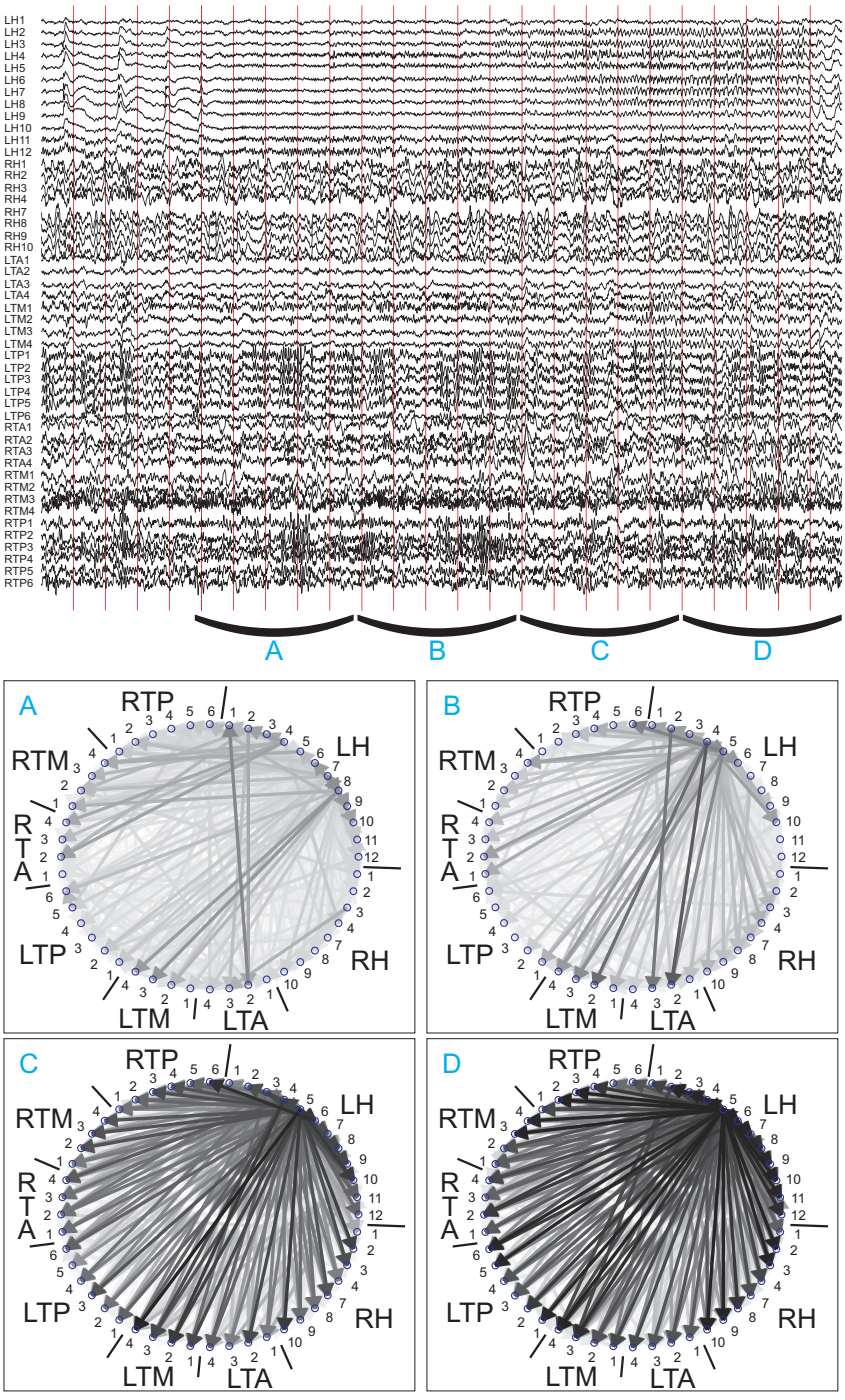


Figure 6.14: Connectivity patterns during seizure 4 in pat. 7.

6.3.2.8 Patient 8

The MRI investigation revealed a small heterotopy near the left lateral ventricle and left hippocampal sclerosis. The SVEM indicated left and right frontotemporal lobe ictal onset, with the left side the most prominent side. Because of the bilateral seizure onset noticed during the SVEM the patient was admitted for IVEM. One depth electrode with 8 contacts was placed to cover both the hippocampus (LD1-4) and the heterotopy (LD7-8). A big subdural grid with 56 contacts covered the left temporal and parietal brain lobe. The patient had 5 habitual seizures. During the seizures first ictal activity is seen at contacts LD1-3 with later on spreading toward the neocortical grid. The patient had a left anterior temporal lobectomy and amygdalohippocampectomy and is now seizure free for 4 years. The position of the electrodes and the resected brain tissue is shown in the upper panel of fig.6.15.

The highest total out-degree and the SSO's are depicted in the bottom panel. The highest SSO's are found for contact LD1 (seizure 4), LD2 (seizure 1, 3 and 5) and LD3 (seizure 2). This resulted in the highest total out-degree for LD2. In fig.6.16 the connectivity pattern of seizure 2 is shown. The first spread is seen from contacts LD2 and LD3.

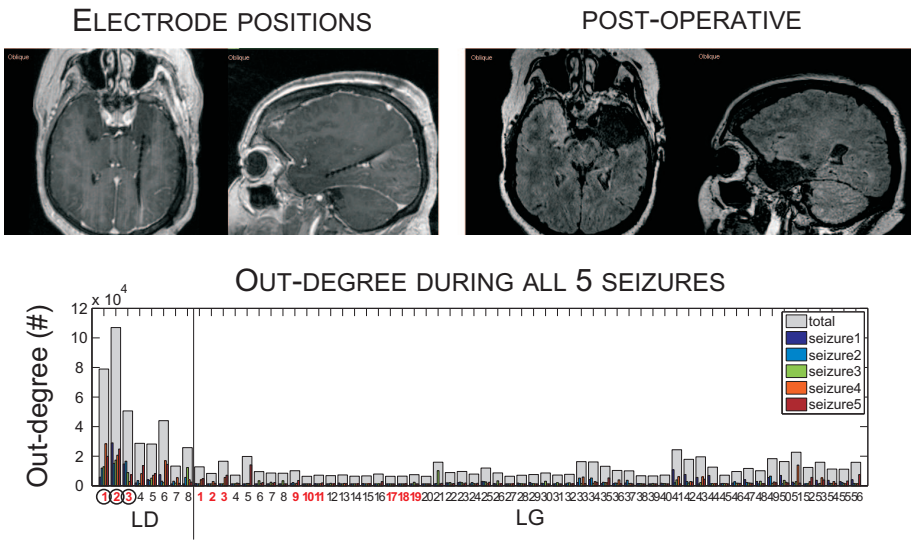


Figure 6.15: Results of the connectivity analysis in pat. 8.

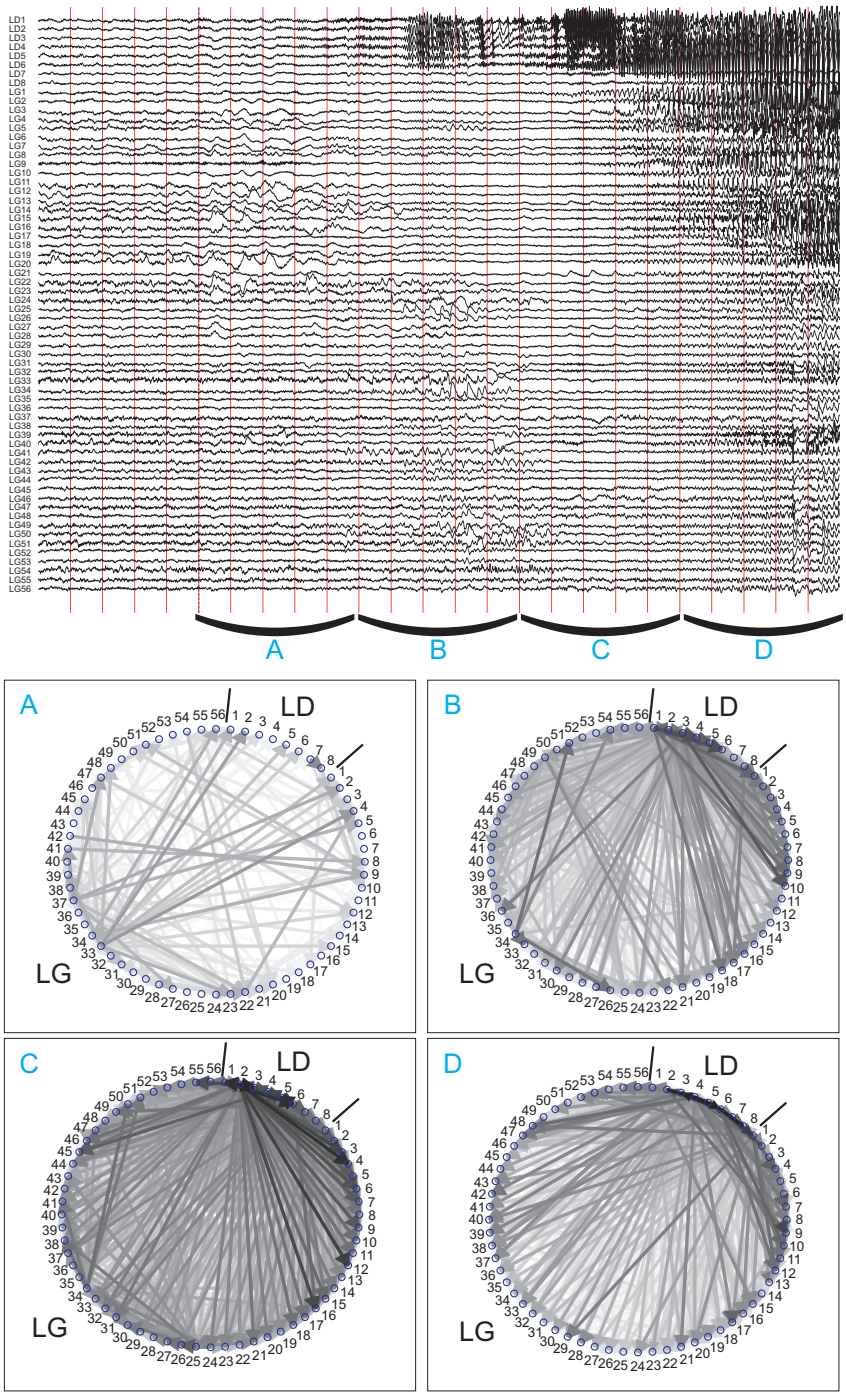


Figure 6.16: Connectivity patterns during seizure 2 in pat. 8.

6.4 Discussion

In this chapter we investigated how swADTF analysis can be used to localize the SOZ from ictal IEEG recordings. The results corresponded to the SOZ as defined by the visual analysis of the IEEG by the epileptologist and to the resected area in all patients. The method only investigated the causal relations between the signals without taken any form of prior knowledge about the electrode contact locations into account. This framework is user independent and can readily be applied in a clinical setting. In an initial stage this method can support epileptologists in SOZ localization and may significantly reduce the time spent to search for the earliest visually identifiable changes in the numerous simultaneously recorded channels observed one dimensionally but reflecting 3D-brain regions.

The method uses a mere 20 seconds of IEEG starting from when ictal rhythmical activity, between 3 and 20 Hz, was seen at multiple electrode contacts at the beginning of a seizure. We did not look at the patterns corresponding with low amplitude rapid discharges above 25Hz, during which a decorrelation between the brain regions was found [224]. In this chapter we showed that during the first 20 s of ictal rhythmical activity, we are capable of identifying the electrode contact at which the first signs of ictal activity were observed. This means that the earliest spreading pattern contained information about the seizure initiator. The analysis of the 20 s of rhythmical activity identified the same electrode contacts as the analysis of hours of IEEG by the epileptologist.

Other connectivity studies based on Granger causality [71, 70, 229, 112] localized the SOZ on the basis of stationary ictal IEEG epochs. The brain region 'driving' the seizure during a specific stationary epoch is not necessarily the region where the seizure started. There is also no guarantee that the signals were stationary in the analyzed window. In our study we used an effective connectivity measure (the swADTF) capable of analyzing non-stationary spread of ictal rhythmical activity. Since the onset of the spread is not-stationary, our method is preferred to analyze these epochs.

Wilke et al. [229, 232] showed promising results in localizing the primary sources of interictal spikes from an epilepsy patient based on a non-stationary multivariate connectivity measure. Although the localization of interictal epileptic events has proven to be valuable, some studies [5, 104, 47] have concluded that the brain region showing interictal activity (the irritative zone) is larger than the area that is involved in seizure generation. In this study we only considered the ictal epileptic activity and did not take

the interictal epileptic discharges into account, because accurate localization and determination of the ictal networks is the prerequisite for defining the subsequent therapeutic strategy, precisely aimed at suppressing seizures by the annihilation of epileptogenic networks [225].

The seizure specific analysis of individual patients led to comparable results over the majority of seizures. This is concordant with the findings of Gnatkovsky et al. [82], who were able to identify reproducible ictal patterns in patients based on quantified frequency analysis of intracranial IEEG signals. In this study we can extend these findings to connectivity patterns, meaning that the connectivity patterns were consistent over most seizures in all patients. This could be an indication that most seizures of the considered patients started within the same brain area. We suspect this explains why all patients are seizure free after resection of the ictal onset zone. Successive studies in patients with unsuccessful surgery outcome are needed to determine whether there is more variability in the connectivity pattern that may explain why they were not rendered seizure-free.

The framework was designed with the sole purpose of localizing the SOZ based on the origin of the epileptiform rhythmical activity during a seizure. How good other connectivity measures such as the non-linear correlation coupled with the direction index [223] or non-linear granger causality measures [134] would perform in localizing the SOZ still needs to be assessed. However, these measures are bivariate, meaning that all pairwise combination need to be investigated and a new framework that defines the SOZ based on these connections needs to be constructed. This will require the need for more advanced graph analysis, such as the betweenness centrality [186].

Our method is obviously limited by the spatial resolution and sampling of the implanted electrodes. Due to the difficulties in obtaining broad cortical coverage by means of implantable electrodes, it is not unlikely that invasive electrodes do not cover the entire SOZ [169].

Besides seizure freedom, there is an increasing interest for more global outcome parameters such as cognitive and psychiatric outcome and health-related quality of life [185]. A more precise and accurate localization of epileptogenic tissue could allow for resection of even smaller brain regions preserving more functionality. This has already been shown in studies comparing lobectomy to selective amygdalo-hippocampectomy, where most authors found similar seizure outcome and evidence for better neuropsychological outcome [176].

How SOZ delineation based on connectivity could affect the cognitive

and psychiatric outcome as well as the health-related quality of life of the patient after resective surgery still needs to be assessed. The connectivity measures have the potential to more precisely localize the SOZ with respect to the visual analysis of epileptologist and could therefore affect the outcome parameters. However, there will always be a trade-off between resecting a broad area that certainly encompasses all epileptogenic tissue and a smaller resection that preserves more functionality with the higher probability of leaving epileptogenic tissue [176]. Can a more limited resection yield seizure freedom rates similar to those afforded by wider/more aggressive resection? If not, is the quality of life better or worse than that with a wider resection that increases seizure freedom rate but yields a higher complication rate? One thing we do know is that as imaging and mathematical techniques advance, limited resection will become the more attractive option [154].

How connectivity measures can play a role in planning the extent of resection needs to be assessed. The potential of the connectivity analysis is promising, but studies using resection strategies based on effective connectivity measures need to be conducted. The potential benefits include the ability of connectivity analysis to pinpoint a part of a structure (e.g. anterior hippocampal region) allowing a smaller resection or even ablation around the 'driving' electrode contact. Here we need to keep in mind the poor spatial sampling of the implanted electrodes. Another potential benefit is the mapping of the spreading pattern of seizure activity that could guide subpial transections. Increased spatial resolution identification of the SOZ based on effective connectivity analysis could also be used in the more rational design of deep brain simulation protocols to treat epilepsy. Even if surgery is not an option, a deep brain stimulation system could be developed that stimulates at the electrode depicted as driver by the connectivity analysis.

However, many clinical and pre-clinical studies are needed to understand the added value of the connectivity measures over the visual analysis of the epileptologist. There is a growing need for studies showing how connectivity analysis can be used in clinical practice to ultimately ameliorate the quality of life of refractory epilepsy patients.

6.5 Conclusion

In this chapter the applicability of effective connectivity analysis to localize the SOZ from ictal IEEG recordings during early ictal rhythmical activity was investigated in a series of 8 patients. We showed that the SOZ defined by our method corresponded with the results of the standard visual analysis

performed by the epileptologist in all 8 patients. Moreover, our results also corresponded with the later on resected brain tissue that rendered the patients seizure free. The framework does not require any type of a priori knowledge and can readily be used in clinical practice.

6.6 Original contributions

The work presented in this chapter resulted in 2 national conference contributions [204, 195] and various international conference contributions [203, 205, 198, 208]. The results are published in the A1 journal *Epilepsia* [197].

Chapter 7

Seizure onset zone localization from scalp EEG recordings

7.1 Introduction

In the previous chapter connectivity analysis was applied to IEEG recordings to localize the SOZ. In this chapter we will investigate the feasibility to detect the SOZ from ictal scalp EEG recordings. Scalp EEG should be interpreted as the combined activity of different cerebral electrical sources due to volume conduction effects. Each cerebral source will contribute to each EEG channel. To investigate which specific regions are active during an epoch, EEG source imaging (ESI, see section 2.4.5) can be applied. In this chapter we investigate the added value of incorporating connectivity analysis into ESI to localize the SOZ.

ESI estimates one or several cerebral sources from scalp EEG recordings. The algorithms used to solve the inverse problem can be divided into the spatial and the spatio-temporal approaches (that are described in section 2.4.5). The spatial approaches allow a sample based analysis of the EEG. For each time point a source distribution is calculated. Examples of this approach are the Weighted Minimum Norm (WMN) [95], LORETA [161], sLORETA [160] and FOCUSS [84]. On the other hand spatio-temporal techniques calculate source distributions based on the temporal characteristic of the EEG epoch. The multiple signal classification (MUSIC) algorithm [149] belongs to this category (section 2.4.5.2). Unfortunately, most EEG

source localization techniques have difficulties in separating highly correlated sources and therefore produce large localization errors when such sources are present [128]. During a seizure the neuronal activity of different brain regions is highly correlated, making it difficult to estimate the sources.

During a focal seizure the epileptic activity start in the SOZ and afterwards spreads to other brain areas. However, the onset of the seizure is not always noticeable in the EEG. When the SOZ is a deep brain region or when the SOZ is not extensive enough to result in measurable scalp potentials. This means that by the time the seizure is visually observed in the scalp EEG, the epileptic activity can originate from a network of brain areas instead of from a single brain area. The underlying epileptic network can be simplified as a network that consists of synchronous sources and in which the SOZ was the initiator of the epileptic activity.

This chapter investigates the feasibility of detecting the driver of the brain network during an epileptic seizure from scalp EEG recordings. First the source locations and corresponding time series are estimated using ESI. Afterwards the effective connectivity pattern between the estimated brain waveforms is used to identify the driver of the brain network. This information is then used to localize the SOZ.

7.2 Method

We will combine ESI and connectivity analysis to estimate the SOZ from ictal scalp EEG recordings. First we will introduce a source localization technique capable of localizing synchronous sources. Afterwards we will apply connectivity analysis to the time series of the estimated sources to reveal the underlying brain network.

7.2.1 Estimating multiple synchronous sources from scalp EEG recordings

As explained in section 2.4.5.2, the MUSIC and the RAP MUSIC algorithms can be used to localize multiple sources. These algorithms look for independent topographies (IT) with linearly independent time series. This suggests that multiple synchronous sources can be found if the dipoles are combined in the same IT and if the time series are perfectly correlated. However, it is very computational expensive to investigate all possible combinations of dipoles. In practice the algorithms first look for single dipole sources and only look for multi-dipole IT's if the correlation between the signal subspace

and the estimated single dipole is below a certain threshold. One problem is to set this threshold and another one to deal with the computational complexity. For a source space existing out of 4000 voxels, over 8 million combinations of possible dipole pairs need to be investigated. This makes looking for synchronous sources with MUSIC or RAP-MUSIC cumbersome.

7.2.1.1 Precorrelated and orthogonally projected multiple signal classification

A technique, the precorrelated and orthogonally projected MUSIC (POP-MUSIC) algorithm, that deals with these issues was proposed by Liu and Schimpf [128]. The POP-MUSIC algorithm is designed to improve the reconstruction of synchronous sources based on the integration of the spatio-temporal (RAP-MUSIC) and spatial-only approaches (WMN) in a way to preserve both of their advantages. It is comprised out of 5 steps as depicted in fig. 7.1:

1. Iteratively search for k single-source independent topographies (IT) using RAP-MUSIC, where k is the rank of the measurements. Find the neighbors of those k source locations.

2. Reduce the source space to the source set found by step 1, including the neighboring voxels. Estimate the source waveform for each source in this space by applying WMN at each time sample.

3. For each source, find the N largest correlated companions, thus forming a collection of "correlated groups," excluding nearest neighbors. This procedure is based on a correlation threshold. The correlation threshold defines the minimal correlation needed between the time series of the sources to be grouped.

4. Perform RAP-MUSIC to find r ITs from these "correlated groups".

5. Calculate the inverse using the model parameters derived in step 4.

The algorithm results in several locations of possible sources. At each of these locations the brain waveform is estimated by using the WMN approach. This leads to time-variant source waveforms at each of the locations estimated by POP-MUSIC algorithm. The estimated brain waveforms are depicted as $s_i(n)$ with $i = 1 \ldots K$, where K is the number of sources found by the POP-MUSIC algorithm.

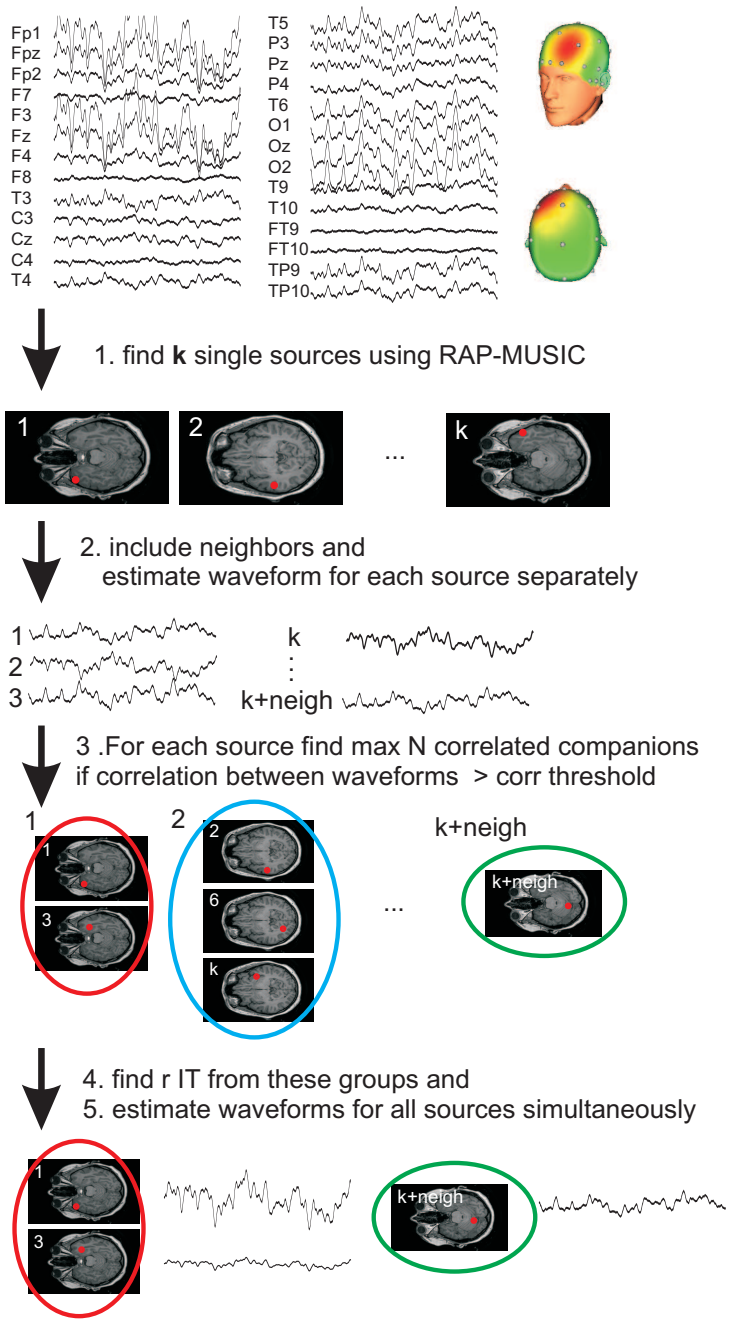


Figure 7.1: The steps in the POP-MUSIC algorithm. From EEG to the estimated sources and corresponding waveforms.

7.2.2 Source selection

To select which of the previously derived sources is considered to be the driver behind the brain network we will investigate two techniques. A first approach is based on the energy contained in the estimated brain waveforms. We select the source with the highest energy. The corresponding time series of this source has the highest standard deviation. Another technique investigates the connectivity pattern between the source time series. We will use the previously developed framework to estimate the iADTF, ffADTF and swADTF based connectivity patterns.

7.3 Simulations

First, we will perform simulations to assess the added value of performing connectivity analysis on the source time series to localize the SOZ. We will describe how the simulated scalp EEG was generated based on an underlying ictal network. Second, we will describe how to estimate multiple sources and their corresponding time series using the POP-MUSIC algorithm. In a third phase the source selection techniques will be investigated.

7.3.1 From simulated brain network to EEG

We simulated a simple seizure network existing of 2 simultaneously active sources in the brain (fig. 7.2). Here source 1 is the SOZ, it 'drives' source 2. The seizure activity is mimicked by a 10 Hz sinusoid with corresponding 20 Hz and 30 Hz harmonics plus additional 1/f noise. The length of the time course is 1 s with a sampling frequency of 512 Hz. We will call this resulting time series *s1*. The SNR of the seizure activity compared to the 1/f noise is set to 0 dB. The activity of source 1 is passed to source 2 with a delay equal to 5 samples. Additional 1/f noise is added to the delayed time course. We will call this time series *s2*.

The EEG is constructed based on a realistic patient specific head model. The head model is constructed from a T1-weighted MR image. The different tissue types: gray matter, white matter, CSF, skull and scalp are segmented with the Statistical Parametric Mapping toolbox (Wellcome Trust Center for Neuroimaging, University College London, UK). We consider 27 electrodes with standard positions. The head model has a resolution of 1 x 1 x 1 mm. The conductivity of the soft tissue types (scalp, CSF, gray matter and white matter) is set to 0.33 S/m and the conductivity of the skull is set

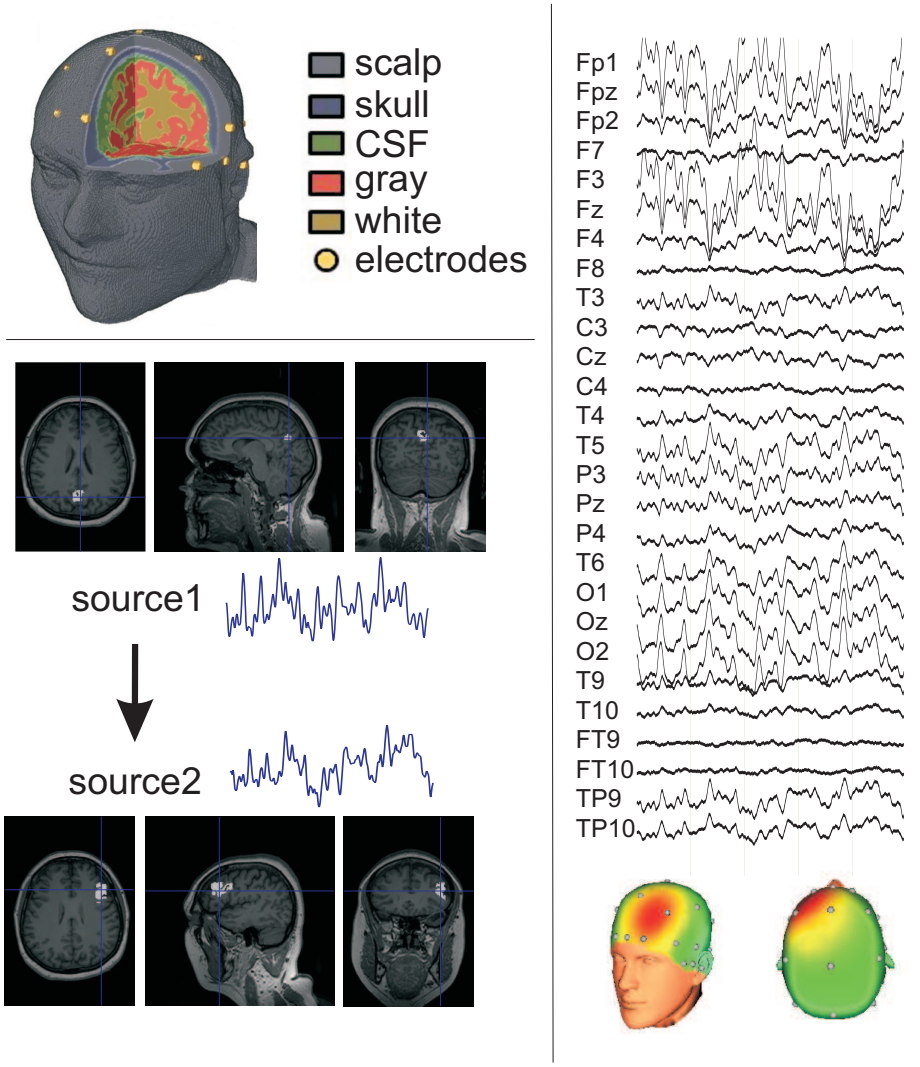


Figure 7.2: The simulation setup to generate the EEG. The underlying epileptic network exists of two sources with different size in which source 1 is the SOZ, it drives source 2. The EEG is constructed out of the source by using a complex head model. In all other voxels 1/f brain activity is simulated. The resulting EEG and corresponding scalp voltage map are shown on the right side.

to 0.0206 S/m. All tissue types are considered to be isotropic. Additional measurement noise is added to each EEG channel with a SNR equal to 30 dB.

The head model comprises in total 606.465 gray matter voxels. In each voxel a dipole is considered. The orientation of the dipole is chosen orthogonal to the gray matter surface. To build the source space we sampled this gray matter space at a resolution of 5 x 5 x 5 mm. This resulted into 4847 source space voxels. Source 1 and source 2 are randomly chosen in this source space with minimum 3 cm interdistance. We will call these positions: *p1* and *p2*. Around each position we defined a patch. The size of the patch varied from 1000 voxels to 7000 voxels. The patch is build by iteratively incorporating neighboring voxels. For patch 1, we start by adding *p1* and the neighboring voxels of it. Afterwards we add their neighbors and so forth until the patch size is equal to the desired size. The same procedure is used to construct patch 2. Only gray matter voxels are added to the patches.

The activity of each voxel in patch 1 is set to time series *s1* and those of patch 2 to time series *s2*. In all other gray matter voxels 1/f brain activity is added with a SNR of 0 dB compared to the seizure activity. The complete simulation setup with used head model, brain sources and resulting EEG and corresponding 3D scalp voltage map is shown in fig. 7.2. In this example, source 1 and source 2 comprise 2000 and 4000 voxels respectively. We clearly notice high rhythmical activity in the electrodes covering the left and central frontal brain region, Fp1, Fpz, F3 and Fz, where source 2 is located. Furthermore we also see increased rhythmic activity in electrodes covering the occipital region, O1, Oz and O2, close to source 1.

7.3.2 From EEG to source locations

If we would apply distributed source analysis like LORETA to the simulated EEG to localize the underlying sources, we would see most activation in the left frontal regions as is depicted in fig. 7.3. This is because source 2 has more active voxels compared to source 1.

We will investigate a different strategy to localize the SOZ. First we will apply POP-MUSIC to the EEG to extract several possible sources and their corresponding activity over time. For the POP-MUSIC algorithm the rank of the measurements is set to the number of simulated sources. The number of largest correlated companions is set to 5 with correlation threshold equal to 0.85 (threshold based on [128]) and the number of ITs to find in step 4 of the algorithm is set to 2.

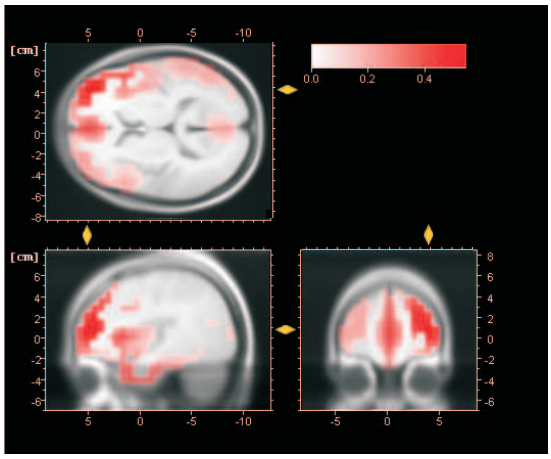


Figure 7.3: Loreta analysis of simulated EEG. The analysis was performed using Brain products analyzer software.

7.3.3 Source location selection

We will investigate two techniques to localize the SOZ from the resulting sources. The first technique is based on the amplitude of the time series of the sources. The source with highest energy is chosen as the SOZ. The other technique is based on connectivity analysis of the time series of all sources. The iADTF, ffADTf and swADTF are calculated in the frequency domain [3, 30 Hz]. We select the source with highest out-degree as the SOZ. The resulting positions are compared to the the origin of patch1, namely *p1*, by calculating the distance between them, namely the localization error.

7.3.4 Setup

We investigated the effect of different patch sizes of the sources of the epileptic network. The sizes of patch1 and patch2 varied from 1000 voxels to 7000 voxels. For each case, for example patch1 has 1000 voxels and patch2 has 3000 voxels, we performed 500 simulations. For each simulation we estimated the source locations and their corresponding time courses using the POP-MUSIC algorithm. We then applied the energy based and connectivity based source selection to localize the SOZ. This location was then compared to the simulated SOZ (position *p1*) by calculating the localization error.

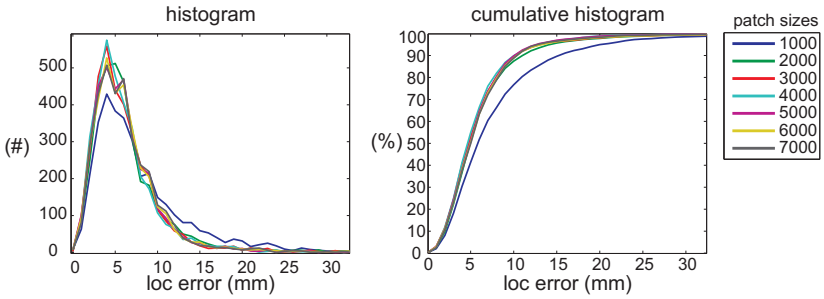


Figure 7.4: Source localization results with POP-MUSIC. The left panel shows the histograms of the localization error for different patch sizes. The right panel shows the cumulative histogram for the different patch sizes. 90 % of the sources with a patch size higher or equal to 2000 voxels are estimated with a localization error less than 10 mm. The sources with a patch size equal to 1000 voxels are more difficult to estimate.

7.3.5 Results

7.3.5.1 Localization of sources

The POP-MUSIC algorithm results in a number of sources. The maximum number of found sources is $r \times N$, or in our case $2 \times 5 = 10$. Out of this set of sources we calculated the minimal localization error to source1 at position *p1*. This means we calculated the distance between source1 and the closest estimated source. In fig. 7.4 the histogram and cumulative histogram of the localization errors are shown for the different patch sizes. We notice that the smallest patch consisting of 1000 voxels is more difficult to estimate. Overall we notice that the POP-MUSIC algorithm is able to estimate a source within 1cm in approximately 90% of the time for sources bigger than 2000 voxels.

7.3.5.2 Source selection

Out of the source set with maximal 10 sources we estimated the SOZ based on the amount of energy in the source time series and based on the connectivity pattern. We calculated the localization error between the selected source and source 1 at position *p1*. The cumulative histogram of the localization error derived with both methods is shown in fig. 7.5 for different patch sizes. The results indicate that incorporating connectivity analysis into EEG source imaging to localize the SOZ is advantageous. In almost all cases the three connectivity measures iADTF, ffADTF and

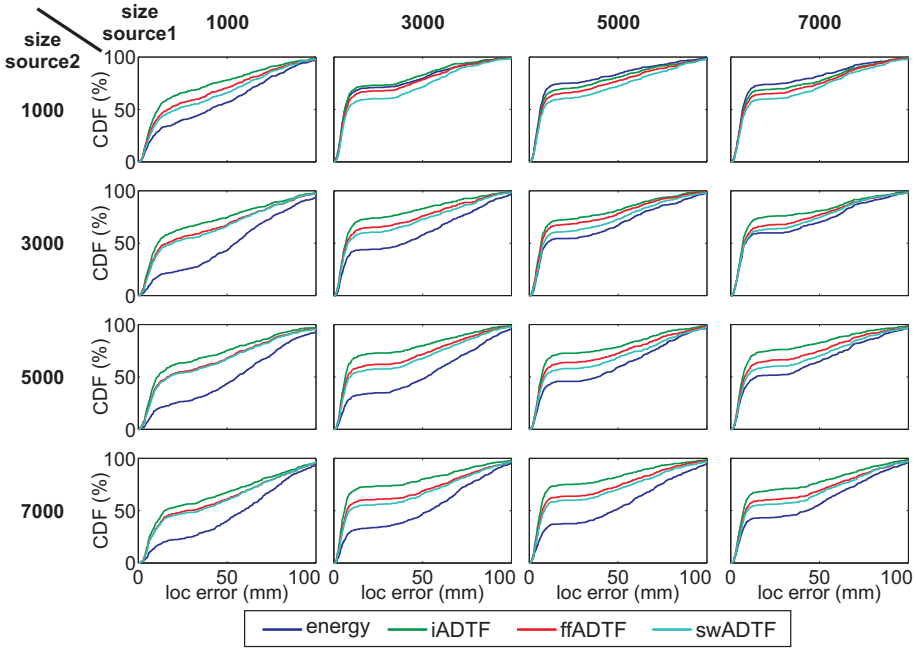


Figure 7.5: Source selection results. Source selection is based on energy or on connectivity measures (iADTF, ffADTF and swADTF).

swADTF outperform the energy based selection method. The method based on the iADTF leads to the best results in all cases but 2. In those case the driving source is at least 5 times larger than the second source. Here the energy based method performs slightly better than the method based on the iADTF.

7.4 Patient data

As a proof of concept we applied the previously described algorithm in 1 patient. The patient that we consider here, was already discussed in previous chapter, namely pat.2. The patient had 3 seizures during the SVEM recorded with 27 electrodes. According to the epileptologists the SVEM showed bilateral frontotemporal ictal onset. Afterwards, the patient underwent IVEM that led to a right anterior temporal lobectomy and amygdalohippocampectomy that rendered the patient seizure free.

In the EEG, two electrode contact O1 and TP10 were omitted due to visible identified artifacts over their complete time course. The data was

average referenced and low-pass filtered (0.5 - 40 Hz). Because many ocular artifacts were present in the data, we applied ICA analysis to remove them [125]. Afterwards we selected in each seizure an 10 s long epoch in which rhythmical activity was clearly visible and the data was not corrupted by movement or other artifacts.

The POP-MUSIC algorithm was applied to the separate epochs to derive the sources and their corresponding time series. The rank was set to 10, the number of synchronous sources to 5 with a correlation threshold equal to 0.85 (based on [128]) and the number of ITs to 10. By setting these parameters a maximum of 50 sources could be found. However, due to the correlation threshold a maximum of 20 sources was found. Some of the sources were located very close to each other. We clustered the sources based on their position using k-means clustering to reduce the source space. This led to a maximum of 8 sources. Using the positions of these sources the source time series were constructed based on step 5 in the POP-MUSIC algorithm.

Once the source locations and time series were calculated we performed source selection using the energy based method and the connectivity based method. The standard deviation of the source time series was calculated and the source having highest standard deviation was depicted as the SOZ in the energy method. For the connectivity analysis the source time series were resampled to 128 Hz using the resampling procedure as described in [175]. A TVAR model was constructed from these time series with an order set to 10 and UC equal to 10^{-3}. The iADTF, ffADTf and swADTF were calculated in the frequency band [3, 30 Hz] based on the TVAR coefficients. The seizure specific out-degree was calculated using a threshold value equal to 0.15, 0.175 and 0.2 for the iADTF, ffADTF and swADTF respectively. The source with the highest seizure specific out-degree was depicted as SOZ of that seizure.

The results for seizure 1 are shown in fig. 7.6. The seizure is depicted in the upper panel. Clear rhythmical activity around 5 Hz can be noticed in many channels. The source locations and corresponding time series are depicted in the middle panel. Seven sources were obtained after the clustering step. The corresponding time series are shown next to the sources. Source selection was applied to these time series based on the standard deviation of the signals and on the connectivity pattern between them. Based on the energy source 1 was selected which is located in the right temporal lobe. The connectivity analysis resulted in source 6 for the iADTF and swADTF and source 2 for the ffADTF which both are located in the right temporal

lobe. We can conclude that the SOZ was localized in the right temporal lobe by all methods.

For seizure 2 the results are shown in fig. 7.7. POP-MUSIC followed by clustering analysis resulted into 7 sources. The source with the highest energy, source 1, is located in the right temporal lobe. However a source with slightly less energy, source 5, is located in the cerebellum. The connectivity analysis based on the iADTF and ffADTF reveals source 1 and source 2 as the SOZ. Both sources are found in the right temporal lobe. The swADTF wrongly indicated source 5 as driver.

The results of seizure 3 are depicted in fig. 7.8. Here POP-MUSIC followed by clustering resulted into 8 possible sources. The method based on energy localized the SOZ in the cerebellum, followed by two sources in the right and left frontal lobe respectively. The connectivity measures uniformly defined source 2 and source 3 as SOZ. These sources are located in the right temporal lobe.

In general we noticed that the iADTF gives more reliable results compared to the ffADTF, swADTF and the energy of the source time series. In all three seizures the SOZ was correctly estimated by the method. Furthermore, the source with the second highest out-degree using the iADTF analysis also always laid in the right temporal lobe. This suggests that during the analyzed epoch the driving area can be assessed by using connectivity analysis and that the results are consistent over multiple seizures.

7.5 Discussion

In this chapter we investigated the added value of incorporating connectivity analysis in ESI to localize the SOZ from scalp EEG recordings. First we used simulations to test the designed method and afterwards we applied it to 1 patient as a proof of concept.

The simulated epileptic network in this chapter only consists of two sources. During an epileptic seizure the number of brain regions which are active are patient and even seizure dependent. We only used two sources to show the feasibility of finding the driver of simple networks by applying source localization algorithms followed by connectivity analysis.

For the source localization we used a state-of-the-art spatio-temporal technique, POP-MUSIC, to find correlated sources. Here, the source localization is based on the temporal characteristics of the EEG epoch. Other inverse solution techniques (for example WMN [95], LORETA [161],

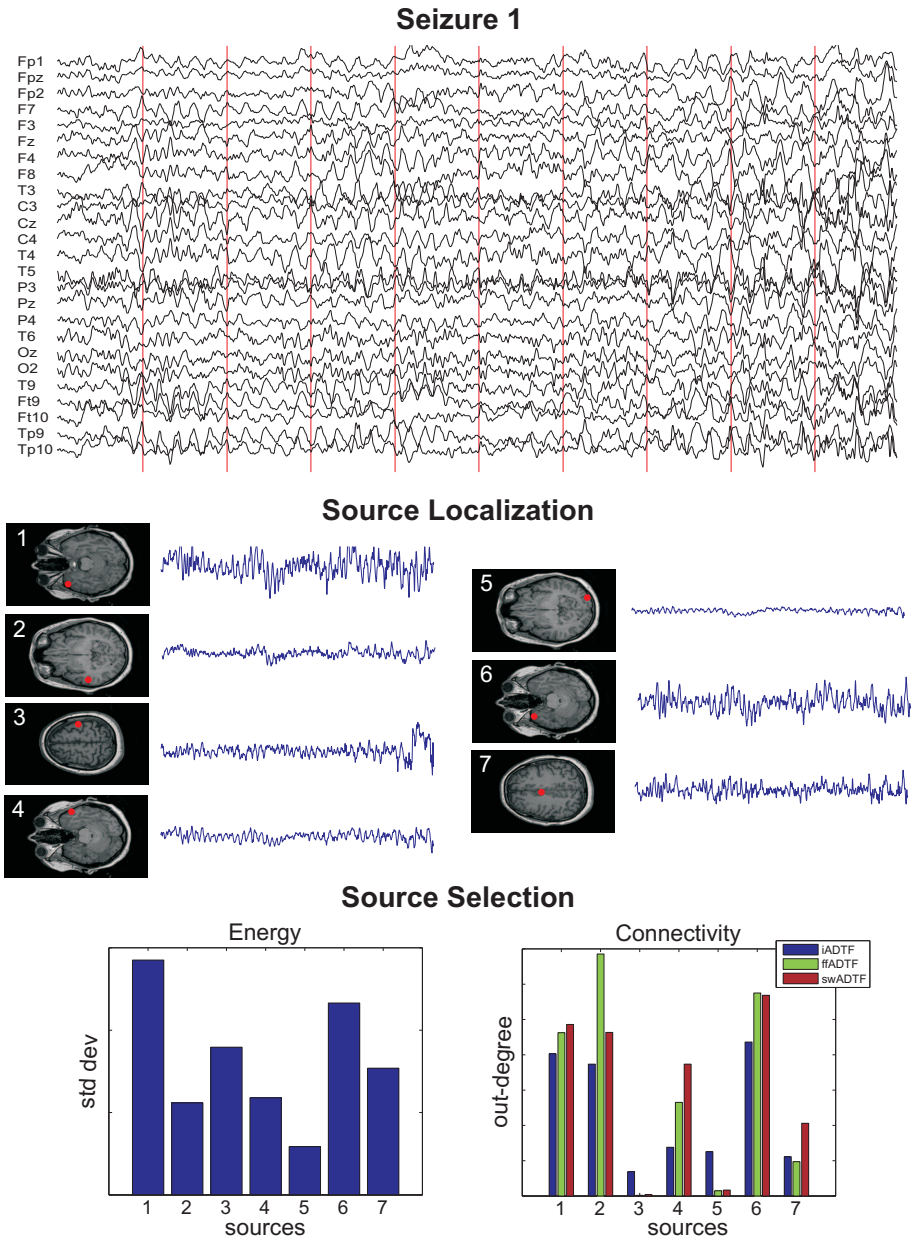


Figure 7.6: SOZ localization from scalp EEG recordings during seizure 1. In the top panel the EEG is shown. The middle panel shows the source locations and corresponding time courses derived from EEG source localization with the POP-MUSIC algorithm. In the bottom panel the source selection is depicted. Both the energy based technique and the connectivity based analysis depict the right temporal lobe as SOZ.

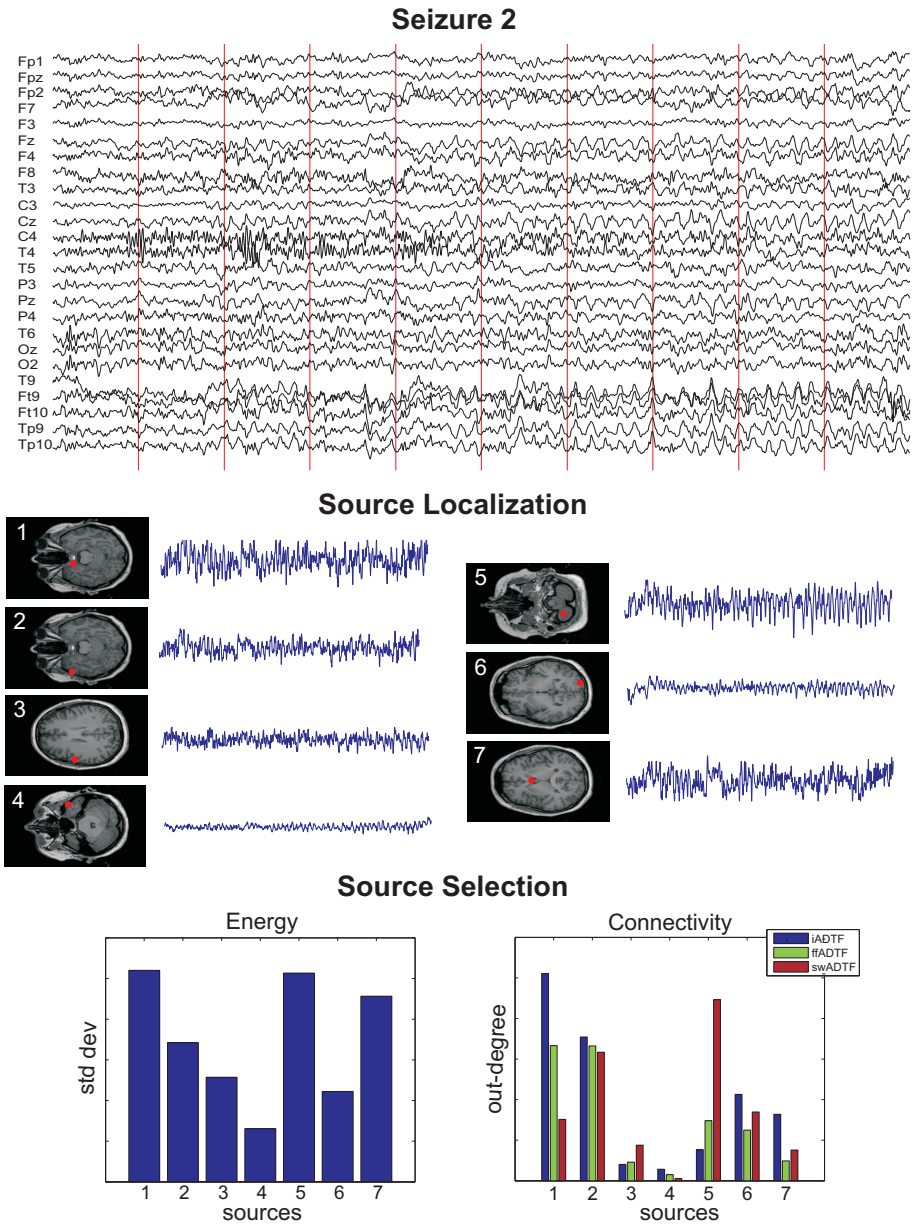


Figure 7.7: SOZ localization from scalp EEG recordings during seizure 2. The sources with highest energy are found in the right temporal lobe and the cerebellum. The connectivity iADTF and ffADTF connectivity analysis depicts two sources in the right temporal lobe as SOZ. According to swADTF analysis the SOZ is found in the cerebellum and in the right temporal lobe.

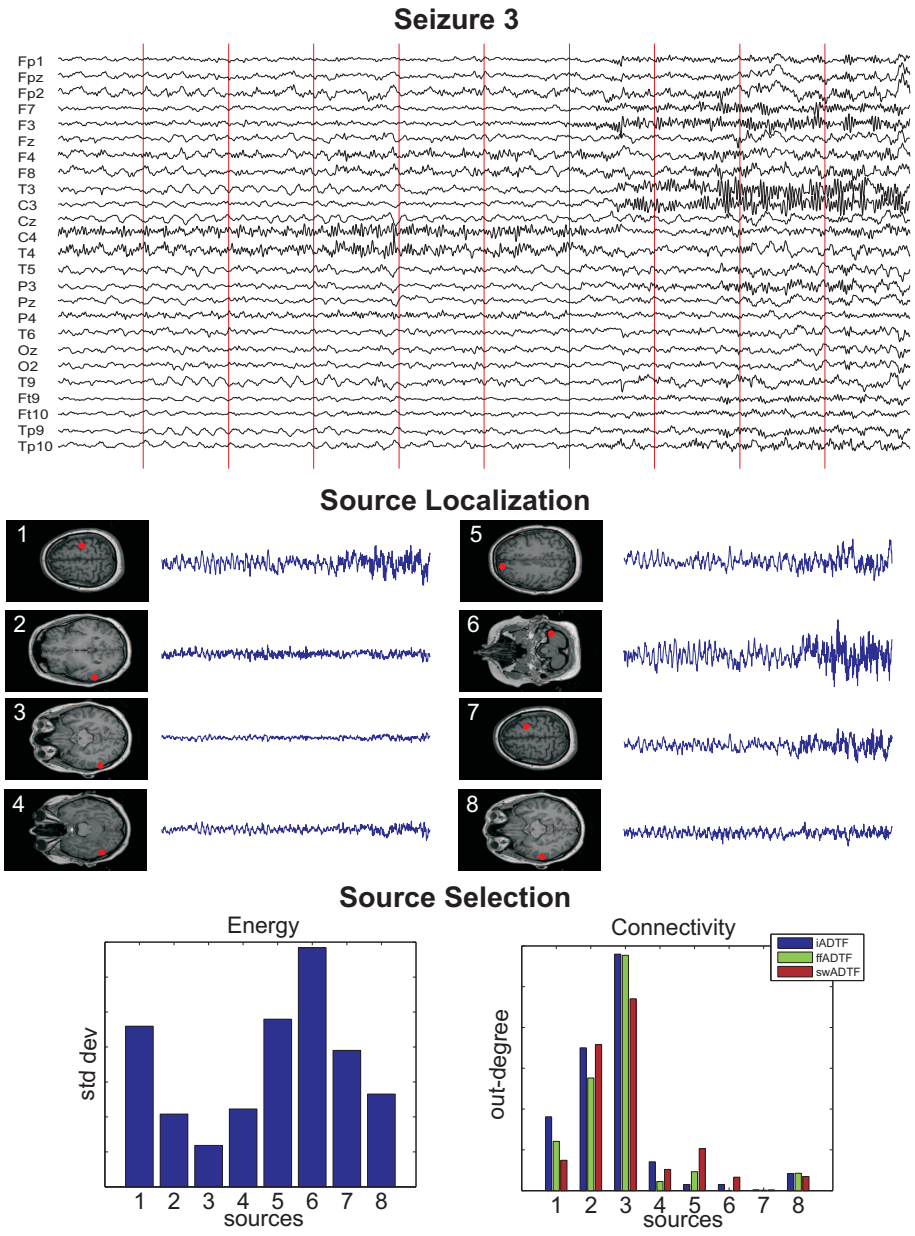


Figure 7.8: SOZ localization from scalp EEG recordings during seizure 3. The SOZ is localized in the cerebellum based on the energy of the sources. The three connectivity measures uniformly localize the SOZ in the right temporal lobe.

sLORETA [160] or FOCUSS [84]) use a spatial-only approach. They process the data on a single time sample basis, leading to higher localization errors for correlated sources.

The POP-MUSIC algorithm was designed to find correlated sources. By using this algorithm we were able to reduce the source localization space to less than 10 locations in the patient dataset. Reducing the size of the set of possible locations from 4847 to 10 or less allowed us to perform connectivity analysis on the time series of the sources.

By simulations we have shown that source localization followed by connectivity analysis can identify the driver of a simple epileptic network. The measures used to investigate the effective connectivity between the signals have the intrinsic capacity to model the indirect flows. Meaning that if the EEG recorded during a seizure originates from a network of sources, the connectivity measures have the intrinsic capabilities to identify the driver.

Overall the iADTF had the best performance compared to the other connectivity measures. This is due to the low SNR ratio of the analyzed source time series. In each gray matter voxel $1/f$ brain activity is simulated making the EEG noisy. The estimated source time series have a low SNR at which the iADTF outperforms the ffADTF and the swADTF. This is concordant with the findings in chapter 5 where for low SNR the iADTF showed the best performance as can be seen in fig. 5.2.

The method was also applied to the retrospective data of 1 epileptic patient to investigate the feasibility to localize the SOZ from ictal scalp EEG recordings. We have shown that the iADTF provides a reliable estimate for the SOZ that corresponds with post-operative findings. Hereby we showed that performing connectivity analysis to the time series of brain sources can provide useful information to localize the SOZ.

Recently two other studies have also showed the added value of combining ESI with connectivity analysis to localize the SOZ [55, 131]. Both studies use FINES [234] as source localization method. This is a MUSIC based method that performs better than RAP-MUSIC when the noise level is high and/or correlations among dipole sources exist. The sources were estimated with this technique and afterwards connectivity analysis was applied on the corresponding time courses using MVAR modeling. The DTF was calculated out of the MVAR coefficients. However, a seizure is non-stationary and therefore using the ADTF and its variants, the iADTF, ffADTF and swADTF are preferred. How FINES coupled with ADTF analysis can be used to localize the SOZ needs to be assessed.

To localize the SOZ we looked at the out-degree of the different sources

because this reflects the amount of information sent from that source during the analyzed period. However, the method is not restricted to this. The iADTF, ffADTf and swADTF can also be used to investigate the non-stationary time-variant connectivity pattern between several sources. This could not only lead to insights in how seizures spread in the brain, but also to how brain regions intercommunicate to perform complex tasks.

In this case the POP-MUSIC algorithm was used because in epilepsy many sources are simultaneously active. In other (non-epilepsy) research applications the inverse solution method can be adjusted. The resulting time series can always be investigated using the designed connectivity framework. However, for these other application the iADTF, ffADTF and swADTF might not be the most suitable measures. Still the concept remains in which sources are first localized and afterwards the connectivity pattern between the sources is assessed. The choice of inverse solution method and connectivity technique depend on the application and should be chosen carefully.

7.6 Conclusion

In this chapter we investigated the feasibility to incorporate connectivity analysis into ESI to localize the SOZ from ictal scalp EEG recordings. We have shown that the connectivity analysis can add information about the underlying cortical network that can be useful to localize the SOZ. Furthermore, we have tested the proposed framework in 3 seizures recorded in 1 patient during the SVEM. By using connectivity analysis we could better localize the SOZ than by looking at the energy of the sources. Therefore, we have shown the potential of the proposed method to localize the SOZ from ictal scalp EEG, although more research in this domain is necessary.

7.7 Original contributions

The work presented in this chapter resulted in 2 international conference contributions [210, 206].

Chapter 8

General conclusions

In this chapter we summarize the main contributions of the work in this dissertation and draw general conclusions. We also discuss possible future research directions. In the end a final conclusion is made.

8.1 Summary

The purpose of this dissertation was to investigate how effective connectivity patterns derived from ictal EEG recordings can help to localize the SOZ in epilepsy patients. Our approach consisted of the following steps. First, a framework capable of investigating the effective connectivity pattern between non-stationary EEG signals was described. Several connectivity measures were implemented in the framework and were validated using simulations. We showed the added value of using effective connectivity patterns derived from ictal IEEG recordings to localize the SOZ in a small animal model of epilepsy and in 8 patients. Next, we showed the feasibility to couple the developed framework to ESI to localize the SOZ from ictal scalp EEG recordings.

In chapter 2 the necessary background about the brain, EEG and epilepsy was given. The anatomy of the brain was described starting from microscale to macroscale. First, the anatomy and physiology of the basic building block of the brain, the neuron, was discussed. Second, the different brain lobes and their functionality were addressed. In a next section we explained how to investigate the electrical field generated by neuronal communication by using EEG. Special attention was given to EEG source imaging, that estimates the electrical source distribution inside the brain given the measured

scalp potentials. In the next section epilepsy is discussed. Special attention is paid to the treatment and presurgical evaluation for patients with refractory epilepsy. The eligibility for a patient to have a surgical resection is investigated using different modalities. Especially MRI, SVEM and IVEM are discussed in detail.

In chapter 3 brain connectivity is introduced. In a first part we introduce structural connectivity, that depicts how the brain regions are structurally connected. Later we explained functional and effective connectivity that investigate the non-directional and directional information flows between the signals respectively. Special focus was put on Granger causality and how to derive effective connectivity measures from autoregressive models. In a last part the literature dealing with the localization of the SOZ from EEG and IEEG signals is extensively discussed. Most of these studies used bivariate measures, meaning that each pairwise combination of signals needs to be investigated separately. Another issue in previous studies is that the analyzed seizure epochs are considered to be stationary, while seizures and especially the onset are intrinsically non-stationary.

In chapter 4 we introduced the framework that is capable of localizing the SOZ from ictal IEEG recordings. The proposed framework was designed to be applicable to non-stationary signals. A multivariate TVAR model allowed to simultaneously investigate multiple non-stationary signals and is therefore suited to investigate the network during seizure onsets from many recorded IEEG signals. The simulations showed that the ffADTF outperformed the two other proposed measures (the iADTF and the mADTF) with a sample based sensitivity and specificity higher than 90% for SNRs above 0dB. The applicability to localize the SOZ in 1 patient from ictal IEEG recordings was shown. The results corresponded with the post-operative findings and were consistent over seizures and subclinical seizures.

In chapter 5 two techniques, the sliding window technique and the previously introduced Kalman filtering algorithm, to estimate the TVAR coefficients were compared. A new effective connectivity measure, the swADTF, that more appropriately incorporated the frequency content of the signals into the connectivity pattern was introduced. The performance of the iADTF, ffADTF and swADTF calculated using the sliding window technique or the Kalman filtering were investigated by means of simulations. The swADTF calculated using Kalman filtering clearly outperformed the other effective connectivity measures for SNRs above 0dB. This showed that the way we incorporated the frequency content into the connectivity pattern was advantageous for signals with SNR above 0dB. Furthermore the

performance of the measures to localize the SOZ in a small animal model of epilepsy was investigated. The iADTF, ffADTF and swADTF were applied to the 320 ictal IEEG epochs recorded in 11 rats. The IEEG electrode contact with highest out-degree was depicted as SOZ and was compared to the scoring of the electrophysiologist. The swADTF calculated using Kalman filtering outperformed the others for localizing the SOZ in a small animal model of epilepsy. Hereby we showed that the swADTF is the preferred measure to be used to localize the SOZ from IEEG recordings.

In chapter 6 we applied the swADTF based on Kalman filtering to ictal IEEG recordings in 8 patients to localize the SOZ. The patients had focal ictal onset and were rendered seizure free following resective surgery. We compared the SOZ localized with our method with the results of the visual analysis by the epileptologist and the resected brain tissue. In all 8 patients the SOZ localized by our method corresponded with the one of the epileptologist and with the resected brain tissue. Furthermore, the connectivity patterns were consistent over the majority of the seizures. Overall we showed that our method is capable of localizing the SOZ in these patients from multichannel IEEG recordings. Our method does not require any prior knowledge about electrode positions and is readily applicable in clinical practice.

In the next chapter, chapter 7, we investigated the possibility to extend the framework to localize the SOZ from ictal scalp EEG. We coupled the EEG source localization technique capable of imaging multiple correlated source, POP-MUSIC, with effective connectivity analysis. The POP-MUSIC algorithm was used to estimate dipoles and their corresponding time courses during the seizure. These dipoles were clustered and the connectivity pattern between the time course was investigated using the iADTF, ffADTF and swADTF. By simulations we showed that incorporating connectivity analysis into the source localization improved SOZ localization. The applicability of the method to localize the SOZ from ictal scalp EEG recordings in a patient was shown. The results corresponded with the resected brain region. Furthermore, the results were consistent over the 3 seizures. Hereby we showed the feasibility of incorporating connectivity analysis into EEG source localization to localize the SOZ from ictal scalp EEG.

8.2 Future research possibilities

Further research is necessary to investigate the role of connectivity analysis during the presurgical evaluation in patients with refractory epilepsy. In our

dissertation we considered a patient group that was rendered seizure free after resective surgery to be able to have a gold standard where the seizures originated from. Other patient populations need to be investigated. We need to asses the difference in connectivity patterns between those who are rendered seizure free and those who were not. Differences between these two patient groups could shed light on possible markers suggestive or not for resective surgery.

Another unpaved path is the use of connectivity analysis to define the size of the surgical resection. The connectivity analysis can be indicative or not for surgery as mentioned in previous paragraph, but also the relation between the extend of resected brain area and the derived connectivity pattern needs to be assessed. Can the connectivity analysis lead to a smaller resection with the same seizure reduction outcome while preserving more functionality?

Connectivity analysis could not only be used for SOZ localization as in this dissertation, but also to detect seizures. The brain network dramatically changes during the seizures which is reflected in the connectivity pattern. Even in the pre-ictal period characteristic changes can occur in the brain network. Detecting those changes could warn the patients for upcoming seizures so that necessary precautions can be taken.

Connectivity analysis could also play a role in a deep brain stimulation setup. Chronic stimulation can be applied to the electrode contacts where the seizure activity originates from. Another strategy is to investigate the connectivity pattern at the end of a seizure and stimulate at the involved contacts. Another option would be to build a closed loop DBS setup, where seizure activity is detected and correspondingly a stimulation pulse is send to the electrode contact where the seizure activity originated from.

In this dissertation only (I)EEG signals are used to investigate the connectivity pattern due to their excellent temporal resolution. However, this implies a limited spatial sampling. By combining (I)EEG and fMRI, brain networks could be investigated with a high temporal and high spatial resolution.

8.3 Final conclusion

As final conclusion we can state that the developed framework in this dissertation is capable of localizing the SOZ from IEEG recordings and can be readily applied in clinical practice. We have shown this in a small animal model of epilepsy and in 8 patients with refractory epilepsy. The method

can assist the epileptologist to localize the SOZ and requires no prior knowledge. Furthermore, it has the potential to improve the accuracy of SOZ localization from IEEG recordings in refractory patients during the presurgical investigation. In the last part of this thesis we showed the feasibility of incorporating connectivity analysis to localize the SOZ from ictal scalp EEG recordings.

References

[1] Proposal for revised classification of epilepsies and epileptic syndromes. Commission on Classification and Terminology of the International League Against Epilepsy. *Epilepsia*, 30(4):389–99, 1989.

[2] Randomised study of antiepileptic drug withdrawal in patients in remission. Medical Research Council Antiepileptic Drug Withdrawal Study Group. *Lancet*, 337(8751):1175–80, May 1991.

[3] H. Akaike. A new look at the statistical model identification. *IEEE Transactions on Automatic Control*, 19(6):716–723, December 1974.

[4] H. Akaike. A new look at the statistical model identification. *IEEE Transactions on Automatic Control*, 19(6):716–723, December 1974.

[5] G Alarcon, J J Garcia Seoane, C D Binnie, M C Martin Miguel, J Juler, C E Polkey, R D Elwes, and J M Ortiz Blasco. Origin and propagation of interictal discharges in the acute electrocorticogram. Implications for pathophysiology and surgical treatment of temporal lobe epilepsy. *Brain : a journal of neurology*, 120 (Pt 1:2259–82, December 1997.

[6] M S Aldrich and B Jahnke. Diagnostic value of video-EEG polysomnography. *Neurology*, 41(7):1060–6, July 1991.

[7] P J Allen, S J Smith, and C A Scott. Measurement of interhemispheric time differences in generalised spike-and-wave. *Electroencephalography and clinical neurophysiology*, 82(1):81–4, January 1992.

[8] M Arnold, W H Miltner, H Witte, R Bauer, and C Braun. Adaptive AR modeling of nonstationary time series by means of Kalman filtering. *IEEE transactions on bio-medical engineering*, 45(5):553–62, May 1998.

[9] Sara Assecondi, Hans Hallez, Steven Staelens, Anna M Bianchi, Geertjan M Huiskamp, and Ignace Lemahieu. Removal of the ballistocardiographic artifact from EEG-fMRI data: a canonical correlation approach. *Physics in medicine and biology*, 54(6):1673–89, March 2009.

[10] L Astolfi, F Cincotti, D Mattia, F De Vico Fallani, A Tocci, A Colosimo, S Salinari, M G Marciani, W Hesse, H Witte, M Ursino, M Zavaglia, and F Babiloni. Tracking the time-varying cortical connectivity patterns by adaptive multivariate estimators. *IEEE transactions on bio-medical engineering*, 55(3):902–13, March 2008.

[11] L Astolfi, F Cincotti, D Mattia, F De Vico Fallani, A Tocci, A Colosimo, S Salinari, M G Marciani, W Hesse, H Witte, M Ursino, M Zavaglia, and F Babiloni. Tracking the time-varying cortical connectivity patterns by adaptive multivariate estimators. *IEEE Transactions on Biomedical Engineering*, 55(3):902–13, 2008.

[12] Frederico A C Azevedo, Ludmila R B Carvalho, Lea T Grinberg, José Marcelo Farfel, Renata E L Ferretti, Renata E P Leite, Wilson Jacob Filho, Roberto Lent, and Suzana Herculano-Houzel. Equal numbers of neuronal and nonneuronal cells make the human brain an isometrically scaled-up primate brain. *The Journal of comparative neurology*, 513(5):532–41, April 2009.

[13] F. Babiloni, F. Cincotti, C. Babiloni, F. Carducci, D. Mattia, L. Astolfi, A. Basilisco, P.M. Rossini, L. Ding, Y. Ni, J. Cheng, K. Christine, J. Sweeney, and B. He. Estimation of the cortical functional connectivity with the multimodal integration of high-resolution EEG and fMRI data by directed transfer function. *NeuroImage*, 24(1):118–31, 2005.

[14] L A Baccalá and K Sameshima. Partial directed coherence: a new concept in neural structure determination. *Biological Cybernetics*, 84(6):463–474, 2001.

[15] LA Baccala and Sameshima K. Methods for Neural Ensemble Recordings. In MAL Nicolelis, editor, *Methods for neural ensemble recordings*, pages 179–192. CRC Press, 1998.

[16] Luiz A. Baccalá and Koichi Sameshima. Partial directed coherence: a new concept in neural structure determination. *Biological Cybernetics*, 84(6):463–474, May 2001.

[17] S. Baillet, J.C. Mosher, and R.M. Leahy. Electromagnetic brain mapping. *IEEE Signal Processing Magazine*, 18(6):14–30, 2001.

[18] Prasanta Kumar Banerjee. *The Boundary Element Methods in Engineering*. Mcgraw-Hill College, 1994.

[19] Adam B Barrett, Lionel Barnett, and Anil K Seth. Multivariate Granger causality and generalized variance. *Physical review. E, Statistical, nonlinear, and soft matter physics*, 81(4 Pt 1):041907, April 2010.

[20] F Bartolomei, F Wendling, J J Bellanger, J Régis, and P Chauvel. Neural networks involving the medial temporal structures in temporal lobe epilepsy. *Clinical neurophysiology : official journal of the International Federation of Clinical Neurophysiology*, 112(9):1746–60, September 2001.

[21] F Bartolomei, F Wendling, J Régis, M Gavaret, M Guye, and P Chauvel. Pre-ictal synchronicity in limbic networks of mesial temporal lobe epilepsy. *Epilepsy research*, 61(1-3):89–104, 2004.

[22] F Bartolomei, F Wendling, J P Vignal, S Kochen, J J Bellanger, J M Badier, R Le Bouquin-Jeannes, and P Chauvel. Seizures of temporal lobe epilepsy: identification of subtypes by coherence analysis using stereo-electro-encephalography. *Clinical neurophysiology : official journal of the International Federation of Clinical Neurophysiology*, 110(10):1741–54, October 1999.

[23] Fabrice Bartolomei, Mouhamad Khalil, Fabrice Wendling, Anna Sontheimer, Jean Régis, Jean-Phillipe Ranjeva, Maxime Guye, and Patrick Chauvel. Entorhinal cortex involvement in human mesial temporal lobe epilepsy: an electrophysiologic and volumetric study. *Epilepsia*, 46(5):677–87, May 2005.

[24] P.J. Basser, J. Mattiello, and D. LeBihan. MR diffusion tensor spectroscopy and imaging. *Biophysical Journal*, 66(1):259–267, 1994.

[25] S B Baumann, D R Wozny, S K Kelly, and F M Meno. The electrical conductivity of human cerebrospinal fluid at body temperature. *IEEE transactions on bio-medical engineering*, 44(3):220–3, March 1997.

[26] Anne T Berg, Samuel F Berkovic, Martin J Brodie, Jeffrey Buchhalter, J Helen Cross, Walter van Emde Boas, Jerome Engel, Jacqueline

French, Tracy A Glauser, Gary W Mathern, Solomon L Moshé, Douglas Nordli, Perrine Plouin, and Ingrid E Scheffer. Revised terminology and concepts for organization of seizures and epilepsies: report of the ILAE Commission on Classification and Terminology, 2005-2009. *Epilepsia*, 51(4):676–85, April 2010.

[27] Hans Berger. Über das Elektrenkephalogramm des Menschen. *Archiv für Psychiatrie und Nervenkrankheiten*, 87(1):527–570, December 1929.

[28] David R. Bickel and Rudolf Frühwirth. On a fast, robust estimator of the mode: Comparisons to other robust estimators with applications. *Computational Statistics & Data Analysis*, 50(12):3500–3530, August 2006.

[29] Warren T. Blume, Hans O. Lüders, Eli Mizrahi, Carlo Tassinari, Walter Van Emde Boas, Jerome Engel Jr., and Ex-officio. Glossary of Descriptive Terminology for Ictal Semiology: Report of the ILAE Task Force on Classification and Terminology. *Epilepsia*, 42(9):1212–1218, 2001.

[30] P Boon, T Vandekerckhove, E Achten, E Thiery, L Goossens, K Vonck, M D'Have, G Van Hoey, B Vanrumste, B Legros, L Defreyne, and J De Reuck. Epilepsy surgery in Belgium, the experience in Gent. *Acta neurologica Belgica*, 99(4):256–65, December 1999.

[31] M A Boose and J L Cranford. Auditory event-related potentials in multiple sclerosis. *The American journal of otology*, 17(1):165–70, January 1996.

[32] N Boutros, M W Torello, E M Burns, S S Wu, and H A Nasrallah. Evoked potentials in subjects at risk for Alzheimer's disease. *Psychiatry research*, 57(1):57–63, June 1995.

[33] Anatol Bragin, Avetis Azizyan, Joyel Almajano, Charles L Wilson, and Jerome Engel. Analysis of chronic seizure onsets after intrahippocampal kainic acid injection in freely moving rats. *Epilepsia*, 46(10):1592–8, October 2005.

[34] M A Brazier. Spread of seizure discharges in epilepsy: anatomical and electrophysiological considerations. *Experimental neurology*, 36(2):263–72, August 1972.

[35] M A Brazier, P H Crandall, and W J Brown. Long term follow-up of EEG changes following therapeutic surgery in epilepsy. *Electroencephalography and clinical neurophysiology*, 38(5):495–506, May 1975.

[36] Steven L Bressler and Anil K Seth. Wiener-Granger causality: a well established methodology. *NeuroImage*, 58(2):323–9, September 2011.

[37] Martin J Brodie and Patrick Kwan. Staged approach to epilepsy management. *Neurology*, 58(8 Suppl 5):S2–8, April 2002.

[38] K Brodmann. Vergleichende Lokalisationslehre der Grosshirnrinde in ihren Prinzipien dargestellt auf Grund des Zellenbaues. 1909.

[39] Richard A Bronen. Review Article Epilepsy : The Role of MR Imaging. *Seizure*, 1992.

[40] C. Brown and P. Hagoort. The cognitive neuroscience of language. In C.M. Brown and P. Hagoort, editors, *The Neurocognition of Language*. Oxford University Press, USA, 1999.

[41] Evelien Carrette, Kristl Vonck, Veerle De Herdt, Annelies Van Dycke, Riëm El Tahry, Alfred Meurs, Robrecht Raedt, Lut Goossens, Michel Van Zandijcke, Georges Van Maele, Vijay Thadani, Wytse Wadman, Dirk Van Roost, and Paul Boon. Predictive factors for outcome of invasive video-EEG monitoring and subsequent resective surgery in patients with refractory epilepsy. *Clinical neurology and neurosurgery*, 112(2):118–26, February 2010.

[42] Rita Carter, Susan Aldridge, Martyn Page, and Steve Parker. *The Human Brain Book*. DK ADULT, 2009.

[43] Gregory D Cascino. Video-EEG monitoring in adults., 2002.

[44] Y.K. Cheung, S.H. Lo, and A.Y.T. Leung. *Finite element implementation*. Blackwell Science, 1996.

[45] Anders M. Dale and Martin I. Sereno. Improved Localizadon of Cortical Activity by Combining EEG and MEG with MRI Cortical Surface Reconstruction: A Linear Approach. *Journal of Cognitive Neuroscience*, 5(2):162–176, April 1993.

[46] Ryan C N D'Arcy, Yannick Marchand, Gail A Eskes, Edmund R Harrison, Stephen J Phillips, Alma Major, and John F Connolly. Electrophysiological assessment of language function following stroke. *Clinical neurophysiology : official journal of the International Federation of Clinical Neurophysiology*, 114(4):662–72, April 2003.

[47] M de Curtis and G Avanzini. Interictal spikes in focal epileptogenesis. *Progress in neurobiology*, 63(5):541–67, April 2001.

[48] Luigi De Gennaro, Fabrizio Vecchio, Michele Ferrara, Giuseppe Curcio, Paolo Maria Rossini, and Claudio Babiloni. Changes in fronto-posterior functional coupling at sleep onset in humans. *Journal of sleep research*, 13(3):209–17, September 2004.

[49] Luigi De Gennaro, Fabrizio Vecchio, Michele Ferrara, Giuseppe Curcio, Paolo Maria Rossini, and Claudio Babiloni. Antero-posterior functional coupling at sleep onset: changes as a function of increased sleep pressure. *Brain research bulletin*, 65(2):133–40, March 2005.

[50] J C de Munck, B W van Dijk, and H Spekreijse. Mathematical dipoles are adequate to describe realistic generators of human brain activity. *IEEE transactions on bio-medical engineering*, 35(11):960–6, November 1988.

[51] Karel Deblaere and Eric Achten. Structural magnetic resonance imaging in epilepsy. *European Radiology*, 18(1):119–129, 2008.

[52] Atman Desai, Kimon Bekelis, Vijay M Thadani, David W Roberts, Barbara C Jobst, Ann-Christine Duhaime, Karen Gilbert, Terrance M Darcey, Colin Studholme, and Alan Siegel. Interictal PET and ictal subtraction SPECT: sensitivity in the detection of seizure foci in patients with medically intractable epilepsy. *Epilepsia*, 54(2):341–50, February 2013.

[53] Gopikrishna Deshpande, Stephan LaConte, George Andrew James, Scott Peltier, and Xiaoping Hu. Multivariate Granger causality analysis of fMRI data. *Human brain mapping*, 30(4):1361–73, April 2009.

[54] Orrin Devinsky, Pantaleo Romanelli, Darren Orbach, Steven Pacia, and Werner Doyle. Surgical treatment of multifocal epilepsy involving eloquent cortex. *Epilepsia*, 44(5):718–23, May 2003.

[55] L Ding, GA Worrell, TD Lagerlund, and B He. Ictal source analysis: localization and imaging of causal interactions in humans. *NeuroImage*, 34:575 – 586, 2007.

[56] Lei Ding, Gregory A. Worrell, Terrence D. Lagerlund, and Bin He. Ictal source analysis: localization and imaging of causal interactions in humans. *NeuroImage*, 34(2):575–86, 2007.

[57] Mingzhou Ding, Steven L. Bressler, Weiming Yang, and Hualou Liang. Short-window spectral analysis of cortical event-related potentials by adaptive multivariate autoregressive modeling: data preprocessing, model validation, and variability assessment. *Biological Cybernetics*, 83(1):35–45, June 2000.

[58] N F Dronkers, O Plaisant, M T Iba-Zizen, and E A Cabanis. Paul Broca's historic cases: high resolution MR imaging of the brains of Leborgne and Lelong. *Brain : a journal of neurology*, 130(Pt 5):1432–41, May 2007.

[59] R B Duckrow and S S Spencer. Regional coherence and the transfer of ictal activity during seizure onset in the medial temporal lobe. *Electroencephalography and clinical neurophysiology*, 82(6):415–22, June 1992.

[60] Connie C Duncan, Mary H Kosmidis, and Allan F Mirsky. Event-related potential assessment of information processing after closed head injury. *Psychophysiology*, 40(1):45–59, January 2003.

[61] Michael Eichler. On the evaluation of information flow in multivariate systems by the directed transfer function. *Biological cybernetics*, 94(6):469–82, June 2006.

[62] Paul Eling. *Reader in the History of Aphasia: From [Franz] Gall to [Norman] Geschwind*. John Benjamins Publishing, 1994.

[63] J Engel, M F Levesque, and W D Shields. Surgical treatment of the epilepsies: presurgical evaluation. *Clinical Neurosurgery*, 38:514–534, 1992.

[64] Jerome Engel and Engel. *Surgical Treatment of the Epilepsies*. Lippincott Williams & Wilkins, 1993.

[65] Luca Faes and Giandomenico Nollo. Extended causal modeling to assess Partial Directed Coherence in multiple time series with significant

instantaneous interactions. *Biological cybernetics*, 103(5):387–400, November 2010.

[66] A. J. Fawcett, A. K. Chattopadhyay, R. H. Kandler, J. A. Jarratt, R. I. Nicolson, and M. Proctor. Event-related Potentials and Dyslexia. *Annals of the New York Academy of Sciences*, 682(1 Temporal Info):342–345, June 1993.

[67] Roberto Fernandez, Voyko Kavcic, and Charles J Duffy. Neurophysiologic analyses of low- and high-level visual processing in Alzheimer disease. *Neurology*, 68(24):2066–76, June 2007.

[68] Robert S Fisher, Walter van Emde Boas, Warren Blume, Christian Elger, Pierre Genton, Phillip Lee, and Jerome Engel. Epileptic seizures and epilepsy: definitions proposed by the International League Against Epilepsy (ILAE) and the International Bureau for Epilepsy (IBE). *Epilepsia*, 46(4):470–2, April 2005.

[69] L Forsgren, E Beghi, A Oun, and M Sillanpää. The epidemiology of epilepsy in Europe - a systematic review. *European journal of neurology : the official journal of the European Federation of Neurological Societies*, 12(4):245–53, April 2005.

[70] Piotr J. Franaszczuk and Gregory K. Bergey. Application of the Directed Transfer Function Method to Mesial and Lateral Onset Temporal Lobe Seizures. *Brain Topography*, 11(1):13–21–21, 1998.

[71] Piotr J. Franaszczuk, Gregory K. Bergey, and M Kamiski. Analysis of mesial temporal seizure onset and propagation using the directed transfer function method. *Electroencephalography and Clinical Neurophysiology*, 91(6):413–427, December 1994.

[72] K. J. Friston, C. D. Frith, and R. S. J. Frackowiak. Time-dependent changes in effective connectivity measured with PET. *Human Brain Mapping*, 1(1):69–79, 1993.

[73] K J Friston, C D Frith, P F Liddle, and R S Frackowiak. Functional connectivity: the principal-component analysis of large (PET) data sets. *Journal of cerebral blood flow and metabolism official journal of the International Society of Cerebral Blood Flow and Metabolism*, 13(1):5–14, 1993.

[74] K J Friston, L Harrison, and W Penny. Dynamic causal modelling. *NeuroImage*, 19(4):1273–302, August 2003.

[75] Karl J. Friston. Functional and effective connectivity in neuroimaging: A synthesis. *Human Brain Mapping*, 2(1-2):56–78, October 1994.

[76] Karl J Friston. Functional and effective connectivity: a review. *Brain connectivity*, 1(1):13–36, January 2011.

[77] Manfred Fuchs, Michael Wagner, and Joern Kastner. Development of volume conductor and source models to localize epileptic foci. *Journal of clinical neurophysiology : official publication of the American Electroencephalographic Society*, 24(2):101–19, April 2007.

[78] W Gersch and G V Goddard. Epileptic focus location: spectral analysis method. *Science (New York, N.Y.)*, 169(3946):701–2, August 1970.

[79] J Geweke. Measurement of linear dependence and feedback between multiple time series. *Journal of the American Statistical Association*, 77(378):304–313, 1982.

[80] J Geweke. Measures of Conditional Linear Dependence and Feedback Between Time Series. *Journal of the American Statistical Association*, 79(388):907–915, 1984.

[81] J Ginter, K J Blinowska, M Kamiski, and P J Durka. Phase and amplitude analysis in time-frequency space–application to voluntary finger movement. *Journal of neuroscience methods*, 110(1-2):113–24, September 2001.

[82] Vadym Gnatkovsky, Stefano Francione, Francesco Cardinale, Roberto Mai, Laura Tassi, Giorgio Lo Russo, and Marco de Curtis. Identification of reproducible ictal patterns based on quantified frequency analysis of intracranial EEG signals. *Epilepsia*, 52(3):477–88, March 2011.

[83] Sónia I Gonçalves, Jan C de Munck, Jeroen P A Verbunt, Fetsje Bijma, Rob M Heethaar, and Fernando Lopes da Silva. In vivo measurement of the brain and skull resistivities using an EIT-based method and realistic models for the head. *IEEE transactions on bio-medical engineering*, 50(6):754–67, June 2003.

[84] I F Gorodnitsky, J S George, and B D Rao. Neuromagnetic source imaging with FOCUSS: a recursive weighted minimum norm algorithm. *Electroencephalography and clinical neurophysiology*, 95(4):231–51, October 1995.

[85] J Gotman. Interhemispheric relations during bilateral spike-and-wave activity. *Epilepsia*, 22(4):453–66, August 1981.

[86] J Gotman. Measurement of small time differences between EEG channels: method and application to epileptic seizure propagation. *Electroencephalography and clinical neurophysiology*, 56(5):501–14, November 1983.

[87] J Gotman. Interhemispheric interactions in seizures of focal onset: data from human intracranial recordings. *Electroencephalography and clinical neurophysiology*, 67(2):120–33, August 1987.

[88] Boris Gourévitch, Régine Le Bouquin-Jeannès, and Gérard Faucon. Linear and nonlinear causality between signals: methods, examples and neurophysiological applications. *Biological cybernetics*, 95(4):349–69, October 2006.

[89] C. W. J. Granger. Investigating Causal Relations by Econometric Models and Cross-spectral Methods. *Econometrica*, 37(3):424 – 438, 1969.

[90] Roberta Grech, Tracey Cassar, Joseph Muscat, Kenneth P Camilleri, Simon G Fabri, Michalis Zervakis, Petros Xanthopoulos, Vangelis Sakkalis, and Bart Vanrumste. Review on solving the inverse problem in EEG source analysis. *Journal of neuroengineering and rehabilitation*, 5:25, January 2008.

[91] Ramesh M. Gulrajani. *Bioelectricity and Biomagnetism*. Wiley, 1998.

[92] Hans Hallez. Incorporation of anisotropic conductivities in EEG source analysis, 2008.

[93] Hans Hallez, Bart Vanrumste, Roberta Grech, Joseph Muscat, Wim De Clercq, Anneleen Vergult, Yves D'Asseler, Kenneth P Camilleri, Simon G Fabri, Sabine Van Huffel, and Ignace Lemahieu. Review on solving the forward problem in EEG source analysis. *Journal of neuroengineering and rehabilitation*, 4(1):46, January 2007.

[94] M S Hämäläinen and R J Ilmoniemi. Interpreting magnetic fields of the brain: minimum norm estimates. *Medical & biological engineering & computing*, 32(1):35–42, January 1994.

[95] Matti Hämäläinen, Riitta Hari, Risto J. Ilmoniemi, Jukka Knuutila, and Olli V. Lounasmaa. Magnetoencephalographytheory, instrumentation, and applications to noninvasive studies of the working human brain. *Reviews of Modern Physics*, 65(2):413–497, April 1993.

[96] Gregory L Hanna, Melisa Carrasco, Shannon M Harbin, Jenna K Nienhuis, Christina E LaRosa, Poyu Chen, Kate D Fitzgerald, and William J Gehring. Error-related negativity and tic history in pediatric obsessive-compulsive disorder. *Journal of the American Academy of Child and Adolescent Psychiatry*, 51(9):902–10, September 2012.

[97] J Hara, T Musha, and W R Shankle. Approximating dipoles from human EEG activity: the effect of dipole source configuration on dipolarity using single dipole models. *IEEE transactions on bio-medical engineering*, 46(2):125–9, February 1999.

[98] J Haueisen, C Ramon, P Czapski, and M Eiselt. On the influence of volume currents and extended sources on neuromagnetic fields: a simulation study. *Annals of biomedical engineering*, 23(6):728–39, 1995.

[99] Olaf Hauk. Keep it simple: a case for using classical minimum norm estimation in the analysis of EEG and MEG data. *NeuroImage*, 21(4):1612–21, April 2004.

[100] Martin Havlicek, Jiri Jan, Milan Brazdil, and Vince D Calhoun. Dynamic Granger causality based on Kalman filter for evaluation of functional network connectivity in fMRI data. *NeuroImage*, 53(1):65–77, October 2010.

[101] Bin He, Lin Yang, Christopher Wilke, and Han Yuan. Electrophysiological imaging of brain activity and connectivity-challenges and opportunities. *IEEE Transactions on Biomedical Engineering*, 58(7):1918–1931, 2011.

[102] Wolf-Dieter Heiss. The potential of PET/MR for brain imaging. *European journal of nuclear medicine and molecular imaging*, 36 Suppl 1:S105–12, March 2009.

[103] J. Hu, J.B. Gao, and K.D. White. Estimating measurement noise in a time series by exploiting nonstationarity. *Chaos, Solitons & Fractals*, 22(4):807–819, November 2004.

[104] A Hufnagel, M Dümpelmann, J Zentner, O Schijns, and C E Elger. Clinical relevance of quantified intracranial interictal spike activity in presurgical evaluation of epilepsy. *Epilepsia*, 41(4):467–78, April 2000.

[105] P. Jallon. Epidemiology of epilepsies. In C P Panayiotopoulos, editor, *A practical guide to childhood epilepsies*, pages 17–20. Medicinae: Oxford, 2006.

[106] Herbert Jasper and Wilder Penfield. Electrocorticograms in man: Effect of voluntary movement upon the electrical activity of the precentral gyrus. *Archiv fr Psychiatrie und Nervenkrankheiten*, 183(1-2):163–174, 1949.

[107] Manouchehr Javidan. Electroencephalography in mesial temporal lobe epilepsy: a review. *Epilepsy research and treatment*, 2012:637430, January 2012.

[108] B Jeffs, R Leahy, and M Singh. An evaluation of methods for neuromagnetic image reconstruction. *IEEE transactions on bio-medical engineering*, 34(9):713–23, September 1987.

[109] G.M. Jenkins and D.G. Watts. *Spectral analysis and its applications*. 1969.

[110] Carrie A Joyce, Irina F Gorodnitsky, and Marta Kutas. Automatic removal of eye movement and blink artifacts from EEG data using blind component separation. *Psychophysiology*, 41(2):313–25, March 2004.

[111] Young-Jin Jung, Hoon-Chul Kang, Keom-Ok Choi, Joon Soo Lee, Dong-Seok Kim, Jae-Hyun Cho, Shin-Hye Kim, Chang-Hwan Im, and Heung Dong Kim. Localization of ictal onset zones in Lennox-Gastaut syndrome using directional connectivity analysis of intracranial electroencephalography. *Seizure : the journal of the British Epilepsy Association*, 20(6):449–57, July 2011.

[112] Young-Jin Jung, Hoon-Chul Kang, Keom-Ok Choi, Joon Soo Lee, Dong-Seok Kim, Jae-Hyun Cho, Shin-Hye Kim, Chang-Hwan Im, and Heung Dong Kim. Localization of ictal onset zones in Lennox-Gastaut syndrome using directional connectivity analysis of intracranial electroencephalography. *Seizure : the journal of the British Epilepsy Association*, 20(6):449–57, July 2011.

[113] Kitti Kaiboriboon, Hans O Lüders, Mehdi Hamaneh, John Turnbull, and Samden D Lhatoo. EEG source imaging in epilepsy–practicalities and pitfalls. *Nature reviews. Neurology*, 8(9):498–507, September 2012.

[114] M Kaminski, K Blinowska, and W Szclenberger. Topographic analysis of coherence and propagation of EEG activity during sleep and wakefulness. *Electroencephalography and Clinical Neurophysiology*, 102(3):216–227, March 1997.

[115] M Kaminski, K Blinowska, and W Szelenberger. Investigation of coherence structure and EEG activity propagation during sleep. *Acta neurobiologiae experimentalis*, 55(3):213–9, January 1995.

[116] M Kaminski and K J Blinowska. A new method of the description of the information flow in the brain structures. *Biological cybernetics*, 65(3):203–10, January 1991.

[117] G H Klem, H O Lüders, H H Jasper, and C Elger. The ten-twenty electrode system of the International Federation. The International Federation of Clinical Neurophysiology. *Electroencephalography and clinical neurophysiology. Supplement*, 52:3–6, January 1999.

[118] Anna Korzeniewska, Magorzata Maczak, Maciej Kaminski, Katarzyna J. Blinowska, and Stefan Kasicki. Determination of information flow direction among brain structures by a modified directed transfer function (dDTF) method. *Journal of Neuroscience Methods*, 125(1-2):195–207, 2003.

[119] P Kwan and M J Brodie. Early identification of refractory epilepsy. *The New England journal of medicine*, 342(5):314–9, February 2000.

[120] Patrick Kwan, Alexis Arzimanoglou, Anne T Berg, Martin J Brodie, W Allen Hauser, Gary Mathern, Solomon L Moshé, Emilio Perucca, Samuel Wiebe, and Jacqueline French. Definition of drug resistant epilepsy: consensus proposal by the ad hoc Task Force of the ILAE Commission on Therapeutic Strategies. *Epilepsia*, 51(6):1069–77, June 2010.

[121] C la Fougère, A Rominger, S Förster, J Geisler, and P Bartenstein. PET and SPECT in epilepsy: a critical review. *Epilepsy & behavior : E&B*, 15(1):50–5, May 2009.

[122] J P Lachaux, E Rodriguez, J Martinerie, and F J Varela. Measuring phase synchrony in brain signals. *Human brain mapping*, 8(4):194–208, January 1999.

[123] J.P. Lachaux, D. Rudrauf, and P. Kahane. Intracranial EEG and human brain mapping. *Journal of Physiology-Paris*, 97(4-6):613–628, 2003.

[124] Lucy Lee, Lee M Harrison, and Andrea Mechelli. A report of the functional connectivity workshop, Dusseldorf 2002. *NeuroImage*, 19(2 Pt 1):457–65, June 2003.

[125] Yandong Li, Zhongwei Ma, Wenkai Lu, and Yanda Li. Automatic removal of the eye blink artifact from EEG using an ICA-based template matching approach. *Physiological measurement*, 27(4):425–36, April 2006.

[126] H Liang, M Ding, R Nakamura, and S L Bressler. Causal influences in primate cerebral cortex during visual pattern discrimination. *Neuroreport*, 11(13):2875–80, September 2000.

[127] J P Lieb, K Hoque, C E Skomer, and X W Song. Inter-hemispheric propagation of human mesial temporal lobe seizures: a coherence/phase analysis. *Electroencephalography and clinical neurophysiology*, 67(2):101–19, August 1987.

[128] Hesheng Liu and Paul H Schimpf. Efficient localization of synchronous EEG source activities using a modified RAP-MUSIC algorithm. *IEEE transactions on bio-medical engineering*, 53(4):652–61, April 2006.

[129] F Lopes da Silva, J P Pijn, and P Boeijinga. Interdependence of EEG signals: linear vs. nonlinear associations and the significance of time delays and phase shifts. *Brain topography*, 2(1-2):9–18, 1989.

[130] Wolfgang Löscher. Critical review of current animal models of seizures and epilepsy used in the discovery and development of new antiepileptic drugs. *Seizure : the journal of the British Epilepsy Association*, 20(5):359–68, June 2011.

[131] Yunfeng Lu, Lin Yang, Gregory A Worrell, and Bin He. Seizure source imaging by means of FINE spatio-temporal dipole localization and directed transfer function in partial epilepsy patients. *Clinical neurophysiology : official journal of the International Federation of Clinical Neurophysiology*, 123(7):1275–83, July 2012.

[132] HO Luders, J Jr Engel, and Munari C. General principles. In Engel J Jr, editor, *Surgical treatment of the epilepsies*, pages 137–153. Raven Press, New York, 1987.

[133] HO Luders and GC Youssef. *Epilepsy surgery*. Lippincott Williams & Wilkins, 2001.

[134] Daniele Marinazzo, Wei Liao, Huafu Chen, and Sebastiano Stramaglia. Nonlinear connectivity by Granger causality. *NeuroImage*, 58(2):330–8, September 2011.

[135] Daniele Marinazzo, Mario Pellicoro, and Sebastiano Stramaglia. Kernel method for nonlinear granger causality. *Physical review letters*, 100(14):144103, April 2008.

[136] N J Mars and F H Lopes da Silva. Propagation of seizure activity in kindled dogs. *Electroencephalography and clinical neurophysiology*, 56(2):194–209, August 1983.

[137] N J Mars, P M Thompson, and R J Wilkus. Spread of epileptic seizure activity in humans. *Epilepsia*, 26(1):85–94, 1985.

[138] NJI Mars, FH Lopes da Silva, Van Hulten K, and JG Lommen. Computer assisted analysis of eegs during seizures; localisation of an epileptogenic area. *Electroencephalography and Clinical Neurophysiology*, 43:575, 1977.

[139] N.J.I. Mars and G.W. van Arragon. Time delay estimation in nonlinear systems using average amount of mutual information analysis. *Signal Processing*, 4(2-3):139–153, April 1982.

[140] A Medvedev and J O Willoughby. Autoregressive modeling of the EEG in systemic kainic acid-induced epileptogenesis. *The International journal of neuroscience*, 97(3-4):149–67, April 1999.

[141] Christoph M Michel, Micah M Murray, Göran Lantz, Sara Gonzalez, Laurent Spinelli, and Rolando Grave de Peralta. EEG source imaging. *Clinical neurophysiology : official journal of the International Federation of Clinical Neurophysiology*, 115(10):2195–222, October 2004.

[142] T Mima, T Matsuoka, and M Hallett. Information flow from the sensorimotor cortex to muscle in humans. *Clinical Neurophysiology*, 112(1):122–126, January 2001.

[143] Karl E. Misulis. *Spehlmann's Evoked Potential Primer*. Butterworth-Heinemann Medical, 1994.

[144] A. R. Mitchell and D. F. Griffiths. *The Finite Difference Method in Partial Differential Equations*. John Wiley & Sons, 1980.

[145] R Mohanraj and M J Brodie. Diagnosing refractory epilepsy: response to sequential treatment schedules. *European journal of neurology : the official journal of the European Federation of Neurological Societies*, 13(3):277–82, March 2006.

[146] Rajiv Mohanraj and Martin J Brodie. Pharmacological outcomes in newly diagnosed epilepsy. *Epilepsy & behavior : E&B*, 6(3):382–7, May 2005.

[147] Todd K. Moon and Wynn C. Stirling. *Mathematical Methods and Algorithms for Signal Processing*. Prentice Hall, 1999.

[148] J C Mosher, S Baillet, and R M Leahy. EEG source localization and imaging using multiple signal classification approaches. *Journal of clinical neurophysiology : official publication of the American Electroencephalographic Society*, 16(3):225–38, May 1999.

[149] J.C. Mosher, P.S. Lewis, and R.M. Leahy. Multiple dipole modeling and localization from spatio-temporal MEG data. *IEEE Transactions on Biomedical Engineering*, 39(6):541–557, June 1992.

[150] J. A. Nelder and R. Mead. A Simplex Method for Function Minimization. *The Computer Journal*, 7(4):308–313, January 1965.

[151] Ernst Niedermeyer and Fernando Lopes da Silva. *Electroencephalography: Basic Principles, Clinical Applications, and Related Fields*, volume 1. Lippincott Williams & Wilkins, 2012.

[152] Soheyl Noachtar and Jan Rémi. The role of EEG in epilepsy: a critical review. *Epilepsy behavior EB*, 15(1):22–33, 2009.

[153] S Ogawa and T M Lee. Magnetic resonance imaging of blood vessels at high fields: in vivo and in vitro measurements and image simulation. *Magnetic resonance in medicine : official journal of the Society of Magnetic Resonance in Medicine / Society of Magnetic Resonance in Medicine*, 16(1):9–18, October 1990.

[154] Saint V Okonma, Jeffrey P Blount, and Robert E Gross. Planning extent of resection in epilepsy: limited versus large resections. *Epilepsy & behavior : E&B*, 20(2):233–40, February 2011.

[155] Guillermo J Ortega, Liset Menendez de la Prida, Rafael G Sola, and Jesus Pastor. Synchronization clusters of interictal activity in the lateral temporal cortex of epileptic patients: intraoperative electrocorticographic analysis. *Epilepsia*, 49(2):269–80, February 2008.

[156] D A Overton and C Shagass. Distribution of eye movement and eyeblink potentials over the scalp. *Electroencephalography and clinical neurophysiology*, 27(5):546, November 1969.

[157] C P Panayiotopoulos. *A Clinical Guide to Epileptic Syndromes and their Treatment*. Springer London, London, 2010.

[158] J Pardey, S Roberts, and L Tarassenko. A review of parametric modelling techniques for EEG analysis. *Medical engineering & physics*, 18(1):2–11, January 1996.

[159] P.L. Parmeggiani, A. Azzaroni, and P. Lenzi. On the functional significance of the circuit of papez. *Brain Research*, 30(2):357–374, July 1971.

[160] R D Pascual-Marqui. Standardized low-resolution brain electromagnetic tomography (sLORETA): technical details. *Methods and findings in experimental and clinical pharmacology*, 24 Suppl D:5–12, January 2002.

[161] R D Pascual-Marqui, C M Michel, and D Lehmann. Low resolution electromagnetic tomography: a new method for localizing electrical activity in the brain. *International journal of psychophysiology : official journal of the International Organization of Psychophysiology*, 18(1):49–65, October 1994.

[162] E. Pereda, R.Q. Quiroga, and J. Bhattacharya. Nonlinear multivariate analysis of neurophysiological signals. *Progress in Neurobiology*, 77(1-2):1–37, 2005.

[163] J Pijn. *Quantitative Evaluation of EEG Signals in Epilepsy, Nonlinear Associations, Time Delays and Nonlinear Dynamics*. University of Amsterdam, phd book edition, 1990.

[164] A Pitkanen, PA Schwartzkroin, and SL Moshé. *Models of Seizures and Epilepsy*. Elsevier, Amsterdam, 2006.

[165] C. Plummer, A.S. Harvey, and M. Cook. EEG source localization in focal epilepsy: where are we now. *Epilepsia*, 49(2):201–218, 2008.

[166] S Prabhakar, P Syal, and T Srivastava. P300 in newly diagnosed non-dementing Parkinson's disease: effect of dopaminergic drugs. *Neurology India*, 48(3):239–42, September 2000.

[167] R Quian Quiroga, A Kraskov, T Kreuz, and P Grassberger. Performance of different synchronization measures in real data: a case study on electroencephalographic signals. *Physical review. E, Statistical, nonlinear, and soft matter physics*, 65(4 Pt 1):041903, April 2002.

[168] R Raedt, A Van Dycke, D Van Melkebeke, T De Smedt, P Claeys, T Wyckhuys, K Vonck, W Wadman, and P Boon. Seizures in the intrahippocampal kainic acid epilepsy model: characterization using long-term video-EEG monitoring in the rat. *Acta neurologica Scandinavica*, 119(5):293–303, May 2009.

[169] F Rosenow and H. Luders. Presurgical evaluation of epilepsy. *Brain*, 124(9):1683–1700, September 2001.

[170] Y Saito and H Harashima. Tracking of information within multichannel EEG record - causal analysis in EEG. In N Yamaguchi and K Fujisawa, editors, *Recent Advances in EEG and EMG Data Processing*, pages 133–146. Elsevier Science Publishing Company, Amsterdam, 1981.

[171] V Sakkalis. Review of advanced techniques for the estimation of brain connectivity measured with EEG/MEG. *Computers in biology and medicine*, 41(12):1110–7, December 2011.

[172] F Salih, A Sharott, R Khatami, T Trottenberg, G Schneider, A Kupsch, P Brown, and P Grosse. Functional connectivity between motor cortex and globus pallidus in human non-REM sleep. *The Journal of physiology*, 587(Pt 5):1071–86, March 2009.

[173] M. Scherg. Fundamentals of Dipole Source Potentials. In F. Grandori, M. Hoke, and G.L. Romani, editors, *Advances in Audiology*, pages 40–69. volume 6 edition, 1990.

[174] A Schlögl, G R Müller, R Scherer, and G Pfurtscheller. BIOSIG - an open source software package for biomedical signal processing for use with Octave and Matlab, 2004.

[175] A. Schlögl, S.J. Roberts, and G. Pfurtscheller. A criterion for adaptive autoregressive models. *Proceedings of the 22nd Annual International Conference of the IEEE on Engineering in Medicine and Biology*, pages 1581 –1582, 2000.

[176] Johannes Schramm. Temporal lobe epilepsy surgery and the quest for optimal extent of resection: a review. *Epilepsia*, 49(8):1296–307, August 2008.

[177] T Schreiber. Measuring information transfer. *Physical review letters*, 85(2):461–4, July 2000.

[178] Gideon Schwarz. Estimating the Dimension of a Model. *The Annals of Statistics*, 6(2):461–464, March 1978.

[179] Kensuke Sekihara, Kenneth E Hild, and Srikantan S Nagarajan. A novel adaptive beamformer for MEG source reconstruction effective when large background brain activities exist. *IEEE transactions on bio-medical engineering*, 53(9):1755–64, September 2006.

[180] Claude E Shannon and Warren Weaver. *The Mathematical Theory of Communication*. University of Illinois Press, 1971.

[181] John Shawe-Taylor and Nello Cristianini. *Kernel Methods for Pattern Analysis*. Cambridge University Press, 2004.

[182] Joseph R Smith, Kostas N Fountas, and Mark R Lee. Hemispherotomy: description of surgical technique. *Child's nervous system : ChNS : official journal of the International Society for Pediatric Neurosurgery*, 21(6):466–72, June 2005.

[183] Leif Sörnmo and Pablo Laguna. *Bioelectrical Signal Processing in Cardiac and Neurological Applications (Biomedical Engineering)*. Academic Press, 2005.

[184] Leif Sörnmo and Pablo Laguna. *Bioelectrical Signal Processing in Cardiac and Neurological Applications (Biomedical Engineering)*. Academic Press, 2005.

[185] Susan Spencer and Linda Huh. Outcomes of epilepsy surgery in adults and children. *Lancet neurology*, 7(6):525–37, June 2008.

[186] Olaf Sporns, Christopher J Honey, and Rolf Kötter. Identification and classification of hubs in brain networks. *PloS one*, 2(10):e1049, January 2007.

[187] Cornelis J Stam and Jaap C Reijneveld. Graph theoretical analysis of complex networks in the brain. *Nonlinear biomedical physics*, 1(1):3, January 2007.

[188] H Stefan, S Rampp, and R C Knowlton. Magnetoencephalography adds to the surgical evaluation process. *Epilepsy & behavior : E&B*, 20(2):172–7, February 2011.

[189] James Theiler, Stephen Eubank, André Longtin, Bryan Galdrikian, and J. Doyne Farmer. Testing for nonlinearity in time series: the method of surrogate data. *Physica D: Nonlinear Phenomena*, 58(1-4):77–94, 1992.

[190] Andrew J Tomarken and Niels G Waller. Structural equation modeling: strengths, limitations, and misconceptions. *Annual Review of Clinical Psychology*, 1(1):31–65, 2005.

[191] Martijn P van den Heuvel and Olaf Sporns. Rich-club organization of the human connectome. *The Journal of neuroscience : the official journal of the Society for Neuroscience*, 31(44):15775–86, November 2011.

[192] Peter Van Hese. Detection and analysis of epileptiform activity in the electroencephalogram, 2008.

[193] P Van Loo, E Carrette, A Meurs, L Goossens, D Van Roost, K Vonck, and P Boon. Surgical successes and failures of invasive video-EEG monitoring in the presurgical evaluation of epilepsy. *Panminerva medica*, 53(4):227–40, December 2011.

[194] P van Mierlo. Time-variant connectivity pattern estimation during multiple epileptic seizure onsets. In *UGent-FirW 10e Doctoraatssymposium*, 2009.

[195] P van Mierlo. Epileptogenic focus localization through functional connectivity analysis of the intracranial EEG, 2011.

[196] P van Mierlo, S Assecondi, S Staelens, P Boon, and I Lemahieu. Changes in connectivity patterns in the kainate model of epilepsy. In *IFMBE Proceedings*, pages 360–363. SPRINGER, 2009.

[197] P van Mierlo, E Carrette, H Hallez, R Raedt, A Meurs, S Vandenberghe, D Van Roost, and P Boon. Ictal onset localization through connectivity analysis of intracranial EEG signals in patients with refractory epilepsy. *Epilepsia*, (accepted).

[198] P van Mierlo, E Carrette, S Staelens, and P Boon. Intracranial EEG connectivity anallysis improves the ictal onset zone identification in patients. In *OHBM*, Bejing, 2012.

[199] P van Mierlo, H Hallez, S Assecondi, S Staelens, E Carrette, I Lemahieu, and P Boon. Feasibility study of the time-variant functional connectivity pattern during an epileptic seizure. *International journal of bioelectromagnetism*, 11(4):170–174, 2009.

[200] P van Mierlo, H Hallez, P Boon, S Vandenberghe, K Vonck, S Staelens, and R Raedt. Effective connectivity analysis of rat temporal lobe seizures to localize the seizure onset zone. *NeuroImage*, (under review).

[201] P van Mierlo, H Hallez, E Carrette, P Boon, S Staelens, and I Lemahieu. Time-variant functional connectivity pattern during epileptic seizure onset. In *4th International Summer School in Biomedical Engineering Brain connectivity and information transfer*, Leipzig, 2009.

[202] P van Mierlo, H Hallez, E Carrette, P Boon, S Staelens, and I Lemahieu. Time-variant functional connectivity pattern during epileptic seizure onset. In *EEG/fMRI workshop*, Montreal, 2009.

[203] P. van Mierlo, H. Hallez, E. Carrette, K. Vonck, P. Boon, and S. Staelens. Accurate epileptogenic focus localization through time-variant functional connectivity analysis of intracranial electroencephalographic signals. In *European journal of neurology*, page 17(suppl. 3). WILEY-BLACKWELL, 2010.

[204] P van Mierlo, H Hallez, E Carrette, K Vonck, D Van Roost, P Boon, and S Staelens. Epileptogenic focus localization through connectivity analysis of the intracranial EEG Biomedical Engineering. In *Biomedical Engineering, 9th Belgian day*, Brussel, 2011.

[205] P van Mierlo, H Hallez, E Carrette, K Vonck, D Van Roost, P Boon, and S Staelens. Epileptogenic focus localization through functional connectivity analysis of the intracranial EEG. In *NIPS Connectivity Workshop*, Granada, 2011.

[206] P van Mierlo, G Strobbe, JD Lopez, V Montes-Restrepo, H Hallez, and S Staelens. Added value of connectivity analysis on brain waveforms in EEG source localization to detect the epileptic driver during seizures. In *18th International Conference on Biomagnetism*, Paris, 2012.

[207] P van Mierlo, K Vonck, R Raedt, E Carrette, H Hallez, S Staelens, P Boon, and S Vandenberghe. Effective connectivity analysis of intracranial EEG recordings during epileptic seizures. In *OHBM*, Seattle, 2013.

[208] Pieter van Mierlo, E Carrette, H Hallez, K Vonck, D Van Roost, P Boon, and S Staelens. Epileptogenic focus localization through connectivity analysis of the intracranial EEG: A retrospective study in 2 patients. In *International IEEE EMBS Conference on Neural Engineering*, pages 655–658. IEEE, 2011.

[209] Pieter Van Mierlo, Evelien Carrette, Hans Hallez, Kristl Vonck, Dirk Van Roost, Paul Boon, and Steven Staelens. Accurate epileptogenic focus localization through time-variant functional connectivity analysis of intracranial electroencephalographic signals. *NeuroImage*, 56(3):1122–1133, 2011.

[210] Pieter van Mierlo, Victoria Montes, Hans Hallez, and Steven Staelens. Epileptic brain network from scalp EEG: Identifying the epileptic driver by connectivity analysis on brain waveforms. In *2011 8th International Symposium on Noninvasive Functional Source Imaging of the Brain and Heart and the 2011 8th International Conference on Bioelectromagnetism*, pages 114–118. IEEE, May 2011.

[211] Vladimir N. Vapnik. *Statistical Learning Theory*. Wiley-Interscience, 1998.

[212] Giulia Varotto, Laura Tassi, Silvana Franceschetti, Roberto Spreafico, and Ferruccio Panzica. Epileptogenic networks of type II focal cortical dysplasia: a stereo-EEG study. *NeuroImage*, 61(3):591–8, July 2012.

[213] Giulia Varotto, Elisa Visani, Laura Canafoglia, Silvana Franceschetti, Giuliano Avanzini, and Ferruccio Panzica. Enhanced frontocentral EEG connectivity in photosensitive generalized epilepsies: a partial directed coherence study. *Epilepsia*, 53(2):359–67, February 2012.

[214] Panu T Vesanen, Jaakko O Nieminen, Koos C J Zevenhoven, Juhani Dabek, Lauri T Parkkonen, Andrey V Zhdanov, Juho Luomahaara,

Juha Hassel, Jari Penttilä, Juha Simola, Antti I Ahonen, Jyrki P Mäkelä, and Risto J Ilmoniemi. Hybrid ultra-low-field MRI and magnetoencephalography system based on a commercial whole-head neuromagnetometer. *Magnetic resonance in medicine : official journal of the Society of Magnetic Resonance in Medicine / Society of Magnetic Resonance in Medicine*, July 2012.

[215] H.L.F. Von Helmholtz. Ueber einige Gesetze der Verteilung elektrischer Strome in korperlichen Leitern mit Anwendung auf die tierisch elektrischen Versuche. *Ann. Physik und Chemie*, 89:211–233, 354–377, 1853.

[216] K Vonck, V De Herdt, and P Boon. Vagal nerve stimulation–a 15-year survey of an established treatment modality in epilepsy surgery. *Advances and technical standards in neurosurgery*, 34:111–46, January 2009.

[217] Kristl Vonck, Mathieu Sprengers, Evelien Carrette, Ine Dauwe, Marijke Miatton, Alfred Meurs, Lut Goossens, Veerle DE Herdt, Rik Achten, Evert Thiery, Robrecht Raedt, Dirk VAN Roost, and Paul Boon. A decade of experience with deep brain stimulation for patients with refractory medial temporal lobe epilepsy. *International journal of neural systems*, 23(1):1250034, February 2013.

[218] Douglas J Wagenaar, Maciej Kapusta, Junqiang Li, and Bradley E Patt. Rationale for the combination of nuclear medicine with magnetic resonance for pre-clinical imaging. *Technology in cancer research & treatment*, 5(4):343–50, August 2006.

[219] G Wang and M Takigawa. Directed coherence as a measure of interhemispheric correlation of EEG. *International journal of psychophysiology : official journal of the International Organization of Psychophysiology*, 13(2):119–28, September 1992.

[220] Shuhua Wang, Shengjun Wang, Peiyan Shan, Zhaofeng Song, Tingjun Dai, Rong Wang, and Zhaofu Chi. Mu-calpain mediates hippocampal neuron death in rats after lithium-pilocarpine-induced status epilepticus. *Brain research bulletin*, 76(1-2):90–6, May 2008.

[221] D J Watts and S H Strogatz. Collective dynamics of 'small-world' networks. *Nature*, 393(6684):440–2, June 1998.

[222] Tim Wehner and Hans Lüders. Role of neuroimaging in the presurgical evaluation of epilepsy. *Journal of clinical neurology (Seoul, Korea)*, 4(1):1–16, March 2008.

[223] F Wendling and F Bartolomei. Modeling EEG signals and interpreting measures of relationship during temporal-lobe seizures: an approach to the study of epileptogenic networks. *Epileptic disorders : international epilepsy journal with videotape*, Special Is:67–78, July 2001.

[224] F Wendling, F Bartolomei, J J Bellanger, J Bourien, and P Chauvel. Epileptic fast intracerebral EEG activity: evidence for spatial decorrelation at seizure onset. *Brain : a journal of neurology*, 126(Pt 6):1449–59, June 2003.

[225] Fabrice Wendling, Fabrice Bartolomei, and Lotfi Senhadji. Spatial analysis of intracerebral electroencephalographic signals in the time and frequency domain: identification of epileptogenic networks in partial epilepsy. *Philosophical transactions. Series A, Mathematical, physical, and engineering sciences*, 367(1887):297–316, January 2009.

[226] Fabrice Wendling, Patrick Chauvel, Arnaud Biraben, and Fabrice Bartolomei. From intracerebral EEG signals to brain connectivity: identification of epileptogenic networks in partial epilepsy. *Frontiers in systems neuroscience*, 4:154, January 2010.

[227] Samuel Wiebe. Effectiveness and safety of epilepsy surgery: what is the evidence? *CNS spectrums*, 9(2):120–2, 126–32, February 2004.

[228] Norbert Wiener. *The Theory of Prediction*. Modern Mathematics for Engineers, McGraw-Hill, New York, 1956.

[229] C Wilke, W van Drongelen, M Kohrman, and B He. Identification of epileptogenic foci from causal analysis of ECoG interictal spike activity. *Clinical neurophysiology : official journal of the International Federation of Clinical Neurophysiology*, 120(8):1449–56, August 2009.

[230] Christopher Wilke, Lei Ding, and Bin He. Estimation of time-varying connectivity patterns through the use of an adaptive directed transfer function. *IEEE transactions on bio-medical engineering*, 55(11):2557–64, November 2008.

[231] Christopher Wilke, Wim van Drongelen, Michael Kohrman, and Bin He. Neocortical seizure foci localization by means of a directed transfer function method. *Epilepsia*, 51(4):564–72, April 2010.

[232] Christopher Wilke, Gregory Worrell, and Bin He. Graph analysis of epileptogenic networks in human partial epilepsy. *Epilepsia*, 52(1):84–93, January 2011.

[233] P Wolf. The history of surgical treatment of epilepsy in Europe. In Hans Otto Lüders and Youssef G. Comair, editors, *Epilepsy surgery*, page 1060. New York Raven Press, 1992.

[234] Xiao-Liang Xu, Bobby Xu, and Bin He. An alternative subspace approach to EEG dipole source localization. *Physics in Medicine and Biology*, 49(2):327–343, January 2004.

List of Publications

Journal papers

[1] Strobbe G, van Mierlo P, De Vos M, Mijovic B, Hallez H, Van Huffel S, Lopez JD, Vandenberghe S. Improved EEG source reconstruction using MRI based finite difference forward models *NeuroImage* under review.

[2] Montes-Restrepo V, van Mierlo P, Strobbe G, Staelens S, Vandenberghe S, Hallez H. Influence of skull modeling approaches on EEG source localization *Brain Topography* under review.

[3] van Mierlo P, Hallez H, Boon P, Vandenberghe S, Vonck K, Staelens S, Raedt R. Effective connectivity analysis of rat temporal lobe seizures to localize the seizure onset zone *NeuroImage* under review.

[4] van Mierlo P, Carrette E, Hallez H, Raedt R, Meurs A, Vandenberghe S, Van Roost D, Boon P, Staelens S, Vonck K. Ictal onset localization through connectivity analysis of intracranial EEG signals in patients with refractory epilepsy *Epilepsia* 2013; published online.

[5] Aerts A, van Mierlo P, Hartsuiker R, Hallez H, Santens P, De Letter M. Neurophysiological investigation of phonological input: aging effects and development of normative data *Brain and Language* 2013;125(3):253-263.

[6] van Mierlo P, Carrette E, Hallez H, Vonck K, Van Roost D, Boon P, Staelens S. Accurate epileptogenic focus localization through time-variant functional connectivity analysis of intracranial electroencephalographic signals *NeuroImage* 2011;56:1122-1133.

[7] Buteneers P, Verstraeten D, van Mierlo P, Wyckhuys T, Stroobandt D, Raedt R, Hallez H, Schrauwen B. Automatic detection of epileptic

seizures on the intra-cranial electroencephalogram of rats using reservoir computing *Artificial intelligence in medicine* 2011;53(3):215-223.

Conference proceedings

[1] Montes-Restrepo V, van Mierlo P, Lopez JD, Hallez H, Vandenberghe S. Influence of Isotropic Skull Models on EEG Source Localization *35th Annual International IEEE EMBS Conference*, Osaka, 2013.

[2] Strobbe G, Santens S, van Mierlo P, Hallez H, Van Opstal F, Rosseel Y, Verguts T, Vandenberghe S. Comparison of fMRI activation and EEG source localization using beamformers during motor response in the Stroop task: preliminary results; *Proceedings of the 2011 8th International Symposium on Noninvasive Functional Source Imaging of the Brain and Heart and the 2011 8th International Conference on Bioelectromagnetism (NFSI and ICBEM)*, p.98-102, Banff, 2011.

[3] van Mierlo P, Montes-Restrepo VE, Hallez H, Staelens S. Epileptic brain network from scalp EEG: identifying the epileptic driver by connectivity analysis on brain waveforms *Proceedings of the 2011 8th International Symposium on Noninvasive Functional Source Imaging of the Brain and Heart and the 2011 8th International Conference on Bioelectromagnetism (NFSI and ICBEM)*, p.114-118, Banff, 2011.

[4] van Mierlo P, Carrette E, Hallez H, Vonck K, Van Roost D, Boon P, Staelens S. Epileptogenic focus localization through connectivity analysis of the intracranial EEG: a retrospective study in 2 patients *International IEEE EMBS Conference on Neural Engineering*, p.655-658, Cancun, 2011.

[5] van Mierlo P, Assecondi S, Staelens S, Boon P, Lemahieu I. Changes in connectivity patterns in the kainate model of epilepsy *IFMBE Proceedings*, 22(1-3):p.360-363, Antwerpen, 2009.

Conference abstracts

[1] van Mierlo P, Vonck K, Raedt R, Carrette E, Hallez H, Staelens S, Boon P, Vandenberghe S. Effective connectivity analysis of intracranial EEG recordings during epileptic seizures *OHBM*, Seattle, 2013.

[2] Keereman V, van Mierlo P, Vandenberghe S. Cerebral metabolic activity mapping with continuous infusion FDG-PET: feasibility study *OHBM*, Seattle, 2013.

[3] Strobbe G, van Mierlo P, Lopez JD, de Vos M, Mijovic B, Van Huffel S, Hallez H, Vandenberghe S. Volumetric sparse priors for the EEG inverse problem *OHBM*, Seattle, 2013.

[4] Vanhove C, Descamps B, van Mierlo P, Keereman V, Van Holen R, Vandenberghe S. Magnetic resonance imaging based workflow for radiotherapy planning on a small animal radiation research platform *SNM*, Vancouver, 2013.

[5] Keereman V, van Mierlo P, Descamps B, Vandenberghe S, Raedt R, Vanhove C. Continuous infusion PET with constant input function *SNM*, Vancouver, 2013.

[6] Keereman V, van Mierlo P, Descamps B, Dauwe I, Vandenberghe S, Raedt R, Vanhove C. PET-MRI imaging in the kainic acid model of medial temporal lobe epilepsy *PSMR*, Aachen, 2013.

[7] Aerts A, van Mierlo P, hartsuiker R, Hallez H, Santens P, De Letter M. Neurophysiological investigation of phonological input: aging effects and development of normative data *Wetenschapsdag*, Gent, 2013.

[8] Aerts A, van Mierlo P, hartsuiker R, Hallez H, Santens P, De Letter M. Neurophysiological investigation of phonological input: aging effects and development of normative data *34th VVL-congres*, Berchem, 2013.

[9] Aerts A, van Mierlo P, hartsuiker R, Hallez H, Santens P, De Letter M. Elektrofysiologische analyse van fonologie in de logopedische praktijk: invloed van veroudering en ontwikkeling van Vlaamse normen *Neurowetenschappen in Taal en Spraak*, 2013.

[10] Vanhoutte S, De Letter M, Cosyns M, van Mierlo P, Strobbe G, Corthals P, Santens P, Van Borsel J. Neurophysiological dysfunctions in adults who stutter during a perception task *34th VVL-congres*, Berchem, 2013.

[11] Vanhoutte S, De Letter M, Cosyns M, van Mierlo P, Strobbe G, Corthals P, Santens P, Van Borsel J. Neurofysiologische afwijkingen bij volwassen met ontwikkelingsstotteren tijdens een perceptietaak *Neurowetenschappen in Taal en Spraak*, 2013.

[12] Vanhove C, Descamps B, van Mierlo P, Keereman V, Van Holen R, Vandenberghe S. Magnetic resonance imaging based workflow for radiotherapy planning on a small animal radiation research platform *Small animal radiotherapy Symposium*, Maastricht, 2013.

[13] Keereman V, van Mierlo P, Descamps B, Dauwe I, Vandenberghe S, Raedt R, Vanhove C. Structural and methabolic changes in the acute and subacute phase of the kainic acid model of temporal lobe epilepsy *BMIC*, Leuven, 2013.

[14] Vanhove C, Descamps B, van Mierlo P, Keereman V, Van Holen R, Vandenberghe S. Magnetic resonance imaging based workflow for radiotherapy planning on a small animal radiation research platform *BMIC*, Leuven, 2013.

[15] van Mierlo P, Keereman V, Descamps B, Dauwe I, Van Holen R, Vandenberghe S, Raedt R, Vanhove C. Multimodal imaging for the investigation of epileptogenesis in the intrahippocampal kainic acid model of epilepsy. *ESMRMB*, Lisbon, 2012.

[16] Descamps B, Bruneel S, Keereman V, van Mierlo P, Dauwe I, Vandenberghe S, Raedt R, Vanhove C. Continuous 18F-FDG infusion for dynamic PET imaging of an excitotoxic insult in the rat brain *World Molecular Imaging Congress*, Dublin, 2012.

[17] Aerts A, van Mierlo P, hartsuiker R, Hallez H, Santens P, De Letter M. Neurofysiologisch onderzoek van fonologische input: Nederlandse normen en invloed van verouderingsprocessen *Stem-, spraak- en taalpathologie* , 17(4), 2012.

[18] Vanhoutte S, De Letter M, Cosyns M, van Mierlo P, Strobbe G, Corthals P, Santens P, Van Borsel J. Neurofysiologische afwijkingen bij volwassenen met ontwikkelingsstotteren tijdens een perceptietaak *Stem-, spraak- en taalpathologie* , 17(4), 2012.

[19] Vanhoutte S, De Letter M, van Mierlo P, Corthals P, Santens P, Van Borsel J. Elektrofysiologisch onderzoek van perceptie van werkwoorden bij vloeiende sprekers en personen met ontwikkelingsstotteren *Logopedie 25(4). p.54-67*, Herentals, 2012.

[20] Siugzdaite R, Wu G, van Mierlo P, Descamps B, Raedt R, Marinazzo D. How lesions change resting state functional connectivity in rat brain *Front. Hum. Neurosci. Conference Abstract : Belgian Brain Council*, Lige, 2012.

[21] van Mierlo P, Strobbe G, Lopez JD, Montes-Restrepo V, Hallez H, Staelens S. Added value of connectivity analysis on brain waveforms in EEG source localization to detect the epileptic driver during seizures. *18th International Conference on Biomagnetism*, Paris, 2012.

[22] Montes-Restrepo V, van Mierlo P, Hallez H, Staelens S. Accurate skull modeling from MRI for EEG source localization. *18th International Conference on Biomagnetism*, Paris, 2012.

[23] Strobbe G, Lopez JD, van Mierlo P, Vanderperren K, Mijovic B, de Vos M, Van Huffel S, Hallez H, Vandenberghe S. Comparison of BEM and FDM head modeling in SPM for EEG source reconstruction based on free energy. *18th International Conference on Biomagnetism*, Paris, 2012.

[24] van Mierlo P, Hallez H, Carrette E, Staelens S, Boon P. Intracranial EEG connectivity anallysis improves the ictal onset zone identification in patients *OHBM*, Beijing, 2012.

[25] Strobbe G, Lopez JD, Montes-Restrepo V, van Mierlo P, Hallez H, Vandenberghe S. Comparing Finite Difference Forward Models Using Free Energy based on Multiple Sparse Priors. *OHBM*, Beijing, 2012.

[26] van Mierlo P. Epileptogenic focus localization through functional connectivity analysis of the intracranial EEG. *UGent-FirW 12e Doctoraatssymposium*, Gent, 2011.

[27] van Mierlo P, Carrette E, Hallez H, Vonck K, Van Roost D, Boon P, Staelens S. Epileptogenic focus localization through functional connectivity analysis of the intracranial EEG. *Connectivity Workshop*, Granada,2011.

[28] van Mierlo P, Carrette E, Hallez H, Vonck K, Van Roost D, Boon P, Staelens S. Epileptogenic focus localization through connectivity analysis of the intracranial EEG *Biomedical Engineering, 9th Belgian day*, Brussel, 2011.

[29] van Mierlo P, Hallez H, Carrette E, Vonck K, Boon P, Staelens S. Accurate epileptogenic focus localization through time-variant functional connectivity analysis of intracranial electroencephalographic signals *European journal of neurology*, 17(suppl. 3), Geneva, 2010.

[30] van Mierlo P. Time-variant connectivity pattern estimation during multiple epileptic seizure onsets *UGent-FirW 10e Doctoraatssymposium*, Gent, 2009.

[31] van Mierlo P, Hallez H, Assecondi S, Staelens S, Carrette E, Lemahieu I, Boon P. Feasibility study of the time-variant functional connectivity pattern during an epileptic seizure *International journal of bioelectromagnetism*,11(4). p.170-174, Rome,2009.

[32] van Mierlo P, Hallez H, Carrette E, Boon P, Staelens S, Lemahieu I. Time-variant functional connectivity pattern during epileptic seizure onset. *EEG/fMRI workshop*, Montreal, 2009.

[33] van Mierlo P, Hallez H, Carrette E, Boon P, Staelens S, Lemahieu I. Time-variant functional connectivity pattern during epileptic seizure onset *4th International Summer School in Biomedical Engineering Brain connectivity and information transfer*, Leipzig, 2009.